Uncovering the Mechanisms of Infrared Neural Stimulation In Neurons & Astrocytes

By

Wilson Robert Adams

Dissertation
Submitted to the Faculty of the
Graduate School of Vanderbilt University
in partial fulfillment of the requirements
for the degree of

DOCTOR OF PHILOSOPHY

in

Biomedical Engineering

August 31th, 2021

Nashville, Tennessee

Approved:

Anita Mahadevan-Jansen, Ph.D.

E Duco Jansen, Ph.D.

William P. Roach, Ph.D.

Lauren E. Buchanan, Ph.D.

Valentina Benfenati, Ph.D.

Peter Konrad, M.D. Ph.D.

To my wife, Katherine, for her unwavering support,
relentless encouragement, and inhuman levels of patience for me.

To my daughter Ruth, for bringing so much light into my life.

To my late Grandfather, Robert Terald “Terry” Thompson, who’s contagious curiosity, perseverance,
and drive was something I was fortunate to inherit a fraction of.
For the guidance, wisdom, support, and encouragement, I am eternally grateful.

ACKNOWLEDGEMENTS

The work in this dissertation was made possible through the financial support of the Air Force Office of Scientific Research Basic Sciences portfolio (DURIP, ASTRONIR), the Vanderbilt University Department of Biomedical Engineering, the Vanderbilt Biophotonics Center, the Vanderbilt Cell Imaging Shared Resource, Vanderbilt University Trans-Institutional Program, and the Italian Consiglio Nazionale delle Ricerche in Bologna, namely the Istituto per la Sintesi Organica e la Fotoreattività (ISOF) and the Istituto per lo Studio dei Materiali Nanostrutturati (ISMN). Much of my effort throughout this dissertation was completed with the support of the ASEE NDSEG Fellowship.

I have been fortunate to have many incredible mentors over the course of my years at Vanderbilt. Dr. Anita Mahadevan-Jansen, my dissertation advisor, has been a relentless advocate for me over the years. From giving me a chance to prove myself at first, to helping me lose and rebuild my confidence over the course more than half a decade. For giving me opportunities to grow intellectually, professionally, and personally while I find my way in a less-than-perfectly-efficient fashion, I cannot thank her enough.

I would also like to extend my sincerest thanks to Dr. Duco Jansen, Dr. Bryan Millis, Dr. William P. Roach, Dr. Valentina Benfenati, Dr. Paul Stoddart, and Dr. Kenny Tao for their invaluable conversation, perspective, patience, and guidance as I navigated my way through graduate school.

I have had the good fortune to get a lot of guidance, both professional and personal, from many in the lab, including Dr. Christine O’Brien, Dr. Jeremy Ford, Dr. Mohit Ganguly, Dr. Mohamed Tarek El-Haddad, Dr. Giju Thomas, Dr. Oscar D. Ayala, Dr. John Quan Nguyen, Dr. Daniel Gil, Dr. Nick Mignemi, John Logan Jenkins, Emmanuel Mannoh, Laura Masson, and Graham Throckmorton. I cannot begin to explain the positive impact you all have had on my graduate experience.

The contributions from four specific members of the Vanderbilt Biophotonics Center made the bulk of the work in this dissertation possible in ways that thanks cannot possibly do justice: Dr. Ana Isabella Borrachero-Conejo, Dr. Rekha Gautam, Dr. Andrea Locke, and Dr. Manqing Wang. Without the contributions from these four people, the work in this dissertation would not have been possible.

I am grateful for the sacrifices my mother, Lynn, stepfather, Patrick, and sister, Melanie, have made to get me to where I am today. The support you have provided over the years has been crucial to helping me get here. Thank you for everything.

Most importantly, I owe an immense amount of gratitude to my wife, Katherine. Words cannot begin to describe the amount of help she has been for me. Every day, I wake up striving to be a better human because of her and the life we are building together. She has waded through the difficult stretches with me and celebrated every win, small or big. I only have excitement for what the future holds for us.

TABLE OF CONTENTS

LIST OF TABLES

LIST OF FIGURES

GLOSSARY

°C – Degrees Centigrade
2-APB or 2APB – 2-Aminoethoxydiphenylborane
2PF – Two-Photon Absorption Fluorescence
AMPA – α-amino-3-hydroxy-5-methyl-4-isoxazolepropionic acid
ATP – Adenosine Triphosphate
AQP4 – Aquaporin-4
BK_{Ca} – Calcium-dependent potassium channels
BMTK – Brain Modeling Toolkit
BOLD – Blood Oxygen Level Dependent, in the context of imaging contrast
BSA – Bovine Serum Albumin
C=C – Carbon-Carbon Double Covalent Bond
C-D – Carbon-Deuterium Covalent Bond
C-H – Carbon-Hydrogen Covalent Bond
Ca^{2+} - Free Calcium Ions
$[Ca^{2+}]_i$ – Intracellular Free Calcium Ion Concentration
$[Ca^{2+}]_o$ – Extracellular Free Calcium Ion Concentration
CARS – Coherent Anti-Stokes Raman Scattering
CBX – Carbenoxolone, Gap Junction and Hemichannel Antagonist
CCD – Charge Coupled Device
CH_2 – Methylene Group
CH_3 – Methyl Group
Cl^- - Free Chloride Ions
cm – Centimeter
cm^{-1} – wavenumber, inverse centimeters
CMOS – Complementary Metal-Oxide Sensor
CRS – Coherent Raman Imaging
CTRL/Ctrl/ctrl – Control experimental condition
CW – Continuous Wave
Cx43 – Connexin-43
D_2O – Deuterated water, deuterium oxide.
DAQ – Data Acquisition Interface
dF/F – Relative Change in Fluorescence Intensity
di-4-ANNEPS – 4-(2-(6-(Dibutylamino)-2-naphthalenyl)ethenyl)-1-(3-sulfopropyl)pyridinium hydroxide
DMEM – Dulbecco's Modified Eagle Medium
DMSO – Dimethyl Sulfoxide
DNA – Deoxyribonucleic Acid
dsFLIM – Direct Sampling Fluorescence Lifetime Imaging
E – Energy, used as a variable in mathematical equations
FAD – Flavin Adenine Dinucleotide
FBS – Fetal Bovine Serum
fdFLIM – Frequency Domain Fluorescence Lifetime Imaging
Fiji – Fiji is just ImageJ, curated open source biomedical image processing software package
FLIM – Fluorescence Lifetime Imaging
fMRI – Functional Magnetic Resonance Imaging
fNIRS – Functional Near Infrared Spectroscopy
FOV – Field of View
FPGA – Field Programmable Gate Array
FRET – Förster Resonant Energy Transfer
fs - Femtosecond
GABA – γ-aminobutyric acid

GCS – Gouy-Chapman-Stern Model for lipid bilayer electrodynamics
GFP – Green Fluorescent Protein
GHz – Gigahertz
GP – General Polarization
H_2O – Hydrogen oxide, water.
HEK – Human Embryonic Kidney
hr – Hour
hsSRS – Hyperspectral Stimulated Raman Scattering
HTlc – Hydrotalcite Thin Film
Hz – hertz, cycles per second, with appropriate SI prefixes
INI – Infrared Neural Inhibition
INM – Infrared Neural Modulation
INS – infrared neural stimulation
IR – Infrared
IP_3 – Insitol-3-phosphate
IP_3R or IP3R – Insitol-3-Phosphate Receptor
J – Joule
K^+ - Free Potassium Ions
kHz – Kilohertz
kg – Kilograms
Kir4.1 – Inward Rectifying Potassium Channel Type 4.1
KO – Gene Knock Out, engineered genetic variant
Laser – Light Amplification by Stimulated Emission of Radiation
LED – Light Emitting Diode
LMP – Long Multipulse
M – Molar, moles per liter
MANTIS – Multimodal Advanced Nonlinear and Thermal Imaging System
mGluR – Metabotropic Glutamate Receptors
MPF – Multiphoton Fluorescence
mg – Milligram
mJ – Millijoule
MLV – Multilamellar Vesicle
mM – Millimolar, or Millimoles per Liter
mW – Milliwatt
NA – Numerical Aperture
Na^+ - Free Sodium Ions
NADH – Nicotine Adenine Dinucleotide (protonated)
NG108 – NG108-15 Neuroglioma Hybridoma cell line
NIR – Near Infrared
nm – Nanometer
NMDA – N-Methyl-D-aspartate
NRI – Nonlinear Raman Imaging, also Coherent Raman Imaging (CRS)
ns – Nanosecond
OCH_3 – Methoxy Group
OCH_2 – Alkoxy group
OH – Hydroxyl group
OIS – Optical Intrinsic Signal
P – Activation Probability
P2X7 – Purinergic Family 1 Ionotropic Receptor Type 7
P2Y – Purinergic Family 2 Metabotropic Receptors
PBS – Phosphate Buffered Saline

PC – Phosphatidylcholine
PDL – Poly-D-Lysine
PE – Phosphatidylethanolamine
PEF – Ultrashort Pulsed Electric Field
PI – Propidium Iodide
PMMA – Polymethylmethacrylate, acrylic
PMT – Photomultiplier Tube
ps – Picosecond
PS – Polystyrene, latex
PSF – Point Spread Function
pval – p-value, probability of observed experimental differences being due to chance.
px – Pixel
RGB – Red-Green-Blue color format
ROI – Region of Interest
RR – Ruthenium Red
RN1734 – RN-1734
RNA – Ribonucleic Acid
SEM – Standard Error of the Mean
SI – Systeme International, Global governing for base units
siRNA – Small Inhibitory Ribonucleic Acid
SHG – Second Harmonic Generation
SMP – Short Multipulse
SP – Single Pulse
SRS – Stimulated Raman Scattering
SWIR – Short Wave Infrared
t – Time
$T_{1/2}$ – Fluorescence Response Duration, Full-Width Half Maximum
TCSPC – Time Correlated Single Photon Counting
ThM – Thermal Microscopy
T_{peak} – Time-to-Peak Calcium Fluorescence Intensity
TPEN - (N,N,N′,N′-tetrakis(2-pyridinylmethyl)-1,2-ethanediamine, intracellular calcium ion chelator
TRP – Transient Receptor Protein
TRPA1 – Transient Receptor Protein Ankyrin Type 1 Receptor
TRPV1 – Transient Receptor Protein Vanniloid Type 1 Receptor
TRPV4 – Transient Receptor Protein Vanniloid Type 4 Receptor
µs – Microsecond
µm – Micrometer
µL – Microliter
µM – Micromolar
V – Volt
VBC – Vanderbilt Biophotonics Center
VU-IACUC – Vanderbilt University Institutional Animal Care and Use Committee
W – Watt
WT – wild-type genetic background

CHAPTER 1:

INTRODUCTION

1.1 Motivation

Using optical energy to modulate neural activity has gained significant traction in the last two decades due to its convenient implementation, spatial specificity, and contact-free capabilities. Infrared neural stimulation (INS) uses pulsed infrared light to heat local regions of neural tissue transiently and evoke action potentials from neurons. Since INS does not require genetic modification (1) or chemical pretreatment (2), it offers a potentially flexible neuromodulation tool for clinicians and researchers (3–5). Despite its broad-reaching utility, the fundamental mechanisms of INS remain unclear. Infrared light can impact the physiological activity (e.g., calcium responses, hemodynamic activity) of more than just neurons in the brain. Previous work in our lab showed that astrocytes contribute to cortical brain tissue calcium responses evoked by INS (6). Astrocytes are rapidly becoming recognized for their crucial involvement in neuronal signaling and overall brain health. Whether IR light directly modulates astrocytes remains to be answered. Multicellular sensitivity to infrared light suggests a biophysical mechanism that extends more generally. The lack of specific neuronal targeting by INS in brain tissue raises questions about how INS drives neural activity in the brain. A clearer understanding of INS mechanisms would help realize how to use IR light to study brain physiology from a multicellular perspective.

Irradiating cells with pulsed infrared light is believed to alter the physical dimensions of the extracellular membrane and depolarize cell membrane potential (7, 8). Direct evidence of cell membrane geometry changes during INS in live neural cell models is lacking. Characterizing cell membrane dynamics at sub-second timescales in live cells is notoriously tricky and typically relies on indirect measurement methods. If thermal-based changes in cell membrane physical dimensions underlie INS, it will provide a broadly applicable explanation for IR multicellular modulation. While previous work has demonstrated that infrared light can evoke responses in non-electrically excitable cells (6, 8–12), including those in the central nervous system (6), research into the non-neuronal impacts of INS remains unexplored. There is a growing need for tools to modulate astrocyte physiology in predictable ways to study their influence on neurophysiology more broadly. Understanding the impact of INS on astrocytes would provide mechanistic clarity into INS while demonstrating new approaches to studying astroglial physiology both *in vitro* and *in vivo*.

1.2 Goals

This dissertation aims to address two core hypotheses:

(1) **Multimodal nonlinear microscopy can be used to directly visualize chemical changes occurring in the cell membrane of live neural cells during INS.**

(2) **Astrocyte physiology can be directly and differentially modulated by INS through distinct molecular signaling pathways.**

The work laid out in this dissertation provides a basis for understanding vital mechanistic details of directed energy neuromodulation. Furthermore, this work highlights the importance of considering the impact of any neuromodulation method on astrocytes. This dissertation was organized into three specific aims to address these core hypotheses systematically.

1.3 Specific Aims

Specific Aim (1): Develop and validate a nonlinear optical imaging platform to visualize biochemical changes during INS.

Nonlinear optical imaging approaches offer flexibility in studying biochemical dynamics at sub-second temporal resolutions. Combining nonlinear optical microscopy with direct biophysical measurements of sample temperature would provide a valuable platform for studying INS-related phenomena. However, the optical detection windows for nonlinear and thermal microscopies practically limit their optical paths for simultaneous measurements. A microscopy platform that enables fast measurements of temperature and functional dynamics in live cells and animals is not readily available. Combining multimodal nonlinear and thermal microscopies would provide a helpful set of tools to study the effects of fast photothermal modulation on many facets of cellular and tissue physiology. This aim demonstrates the development and application of a multimodal nonlinear and thermal imaging system (MANTIS) to perform nonlinear and thermal microscopies in neurological model systems during INS in real-time. The MANTIS imaging platform provides a valuable basis for combining any number of optical measurement techniques that rely on unique hardware configurations challenging to combine.

Specific Aim 2: Characterize the vibrational spectroscopic changes in live neural cells during INS with hsSRS microscopy.

The phospholipid membrane is critical to every cell's existence. By compartmentalizing biologically incompatible chemical reactions, lipid membranes facilitate the chemistry necessary for cellular functions. Proteins that are responsible for initiating molecular signaling cascades are all influenced by lipid membrane structure. Probing the biochemical changes of fast photothermal processes at subcellular resolutions has been difficult. Modern advances in nonlinear Raman imaging have made studying INS more feasible. This aim uses hyperspectral stimulated Raman scattering (hsSRS) microscopy during INS in neuronal cell cultures. The resulting changes in SRS spectra provide spectroscopic insight into live cell lipid membrane biophysics. Gold standard fluorescence methods of quantifying membrane biophysical dynamics validate spectral observations. The results provide supporting evidence for the role that changes in membrane physical geometry play in INS.

Specific Aim 3: Characterize the direct effects of INS on astrocytes in vitro.

Previous work from our lab indicates that astrocytes in the rat brain are involved in the observed calcium response to INS *in vivo*. Whether astrocyte activation precedes neural activation or INS directly modulates astrocytes is not clear. This aim provides a detailed characterization of the calcium and cell volume dynamics observed in isolated astrocytes following INS *in vitro*. Widefield fluorescence imaging of relative intracellular calcium levels assessed cell responsiveness to INS. Pharmacological methods deduced the calcium-controlling pathways that shape cellular responses to INS. Different dosing strategies of INS drove distinct calcium signaling pathways and regulatory cell volume dynamics. These results highlight important considerations for deploying INS *in vivo* and highlight INS's potential utility in studying neurological water transport.

1.4 Summary of Chapters

Chapter 1 provides a broad overview of the motivation and scope of the work laid out in this dissertation.

Chapter 2 offers a detailed overview of the mechanistic, biophysical, and biochemical considerations needed to explain the current mechanistic basis of INS. Sections include details on INS mechanisms, polar membrane chemistry electrodynamics, nonlinear optical microscopy in the context of biomedical imaging, as well as astrocyte molecular biology and physiology. The discussion provides a view of the gaps in the currently known mechanisms of INS and the synthesis of broader findings across several research areas.

Chapter 3 details a novel multimodal nonlinear and thermal microscopy platform capable of achieving real-time microscopic imaging in various neurological cell models, both *in vitro* and *in vivo*. The utility of combining thermal and nonlinear microscopy is demonstrated, including key benefits and practical drawbacks to such approaches. The work outlined in this chapter is peer-reviewed and published open-access in *Scientific Reports* (13).

Chapter 4 utilizes the MANTIS platform described in Chapter 3 to study the biochemical dynamics of a live neural cell model, differentiated NG-108 neuroglioma-astrocytoma cells, during INS. Experiments made use of a novel application of hyperspectral stimulated Raman scattering (hsSRS) microscopy to resolve the vibrational spectroscopic changes related to lipids during INS. The discussion analyzes the vibrational spectra changes in the CH-stretch region of the Raman spectrum during INS. Spectroscopic observations are compared with the mechanistic predictions of the current hypothesized model of INS. Some discussion provides an outlook for nonlinear Raman imaging technology and its utility in studying cell biophysics. The work outlined in this chapter is submitted for peer review and is accessible as a preprint on BioRxiv (14).

Chapter 5 details the molecular and electrodynamic basis of isolated astrocyte responses to single pulses of infrared light *in vitro*. Primary rat cortical astrocytes respond independently to single pulse INS. Activation of inositol-3-phosphate receptors (IP_3R) primarily drives the release of intracellular calcium ion stores after IR exposure. Single-pulse INS appears to drive physiological changes in water transport mediated by transient receptor protein vanilloid type IV (TRPV4) ion channels and aquaporin-4 (AQP4) coordinated activation. Stimulation drove both cell swelling and shrinking phenomena in a spatially dependent manner. This work is peer-reviewed and published in the March 2020 issue of the *FASEB Journal* (15).

Chapter 6 shows the importance of considering IR dosing protocols when deploying INS for cellular modulation. The work in this chapter provides a direct comparison of molecular signaling pathways shaping calcium dynamics evoked by single and multipulse IR stimulation in primary rat cortical astrocytes. Multipulse stimulation recruits significantly more extracellular calcium ion flux into astrocytes compared to single-pulse stimulation. Uniquely, multipulse stimulation appears to mediate activation of receptors sensitive to glutamate, GABA, and ATP. The release of neuromodulatory molecules through hemichannels was suspected but inconclusive. The discussion details the implications of these findings and makes a case for considering multicellular dynamics during INS *in vivo*. The work in this chapter is in preparation for submission to a peer-reviewed journal and will be openly accessible as a preprint on BioRxiv.

Chapter 7 synthesizes the findings in each of the previous chapters and discusses their broader societal impact. The scientific contributions of the presented findings are discussed, and future research directions are provided.

1.5 References

1. Fenno, L., Yizhar, O., and Deisseroth, K. (2011) The development and application of optogenetics. *Annu. Rev. Neurosci.* 34, 389–412
2. Ellis-Davies, G. C. R. (2007) Caged compounds: photorelease technology for control of cellular chemistry and physiology. *Nat. Methods* 4, 619–628
3. Chernov, M. and Roe, A. W. (2014) Infrared neural stimulation: a new stimulation tool for central nervous system applications. *Neurophotonics* 1, 011011
4. Lee, J. W., Kim, D., Yoo, S., Lee, H., Lee, G.-H., and Nam, Y. (2015) Emerging neural stimulation technologies for bladder dysfunctions. *Int Neurourol J* 19, 3–11
5. Cayce, J. M., Wells, J. D., Malphrus, J. D., Kao, C., Thomsen, S., Tulipan, N. B., Konrad, P. E., Jansen, E. D., and Mahadevan-Jansen, A. (2015) Infrared neural stimulation of human spinal nerve roots in vivo. *Neurophotonics* 2, 015007
6. Cayce, J. M., Bouchard, M. B., Chernov, M. M., Chen, B. R., Grosberg, L. E., Jansen, E. D., Hillman, E. M. C., and Mahadevan-Jansen, A. (2014) Calcium imaging of infrared-stimulated activity in rodent brain. *Cell Calcium* 55, 183–190
7. Plaksin, M., Shapira, E., Kimmel, E., and Shoham, S. (2018) Thermal Transients Excite Neurons through Universal Intramembrane Mechanoelectrical Effects. *Phys. Rev. X* 8, 011043
8. Shapiro, M. G., Homma, K., Villarreal, S., Richter, C.-P., and Bezanilla, F. (2012) Infrared light excites cells by changing their electrical capacitance. *Nat. Commun.* 3, 736
9. Barnes, R. A., Roth, C. C., Beier, H. T., Noojin, G., Valdez, C., Bixler, J., Moen, E., Shadaram, M., and Ibey, B. L. (2017) Probe beam deflection optical imaging of thermal and mechanical phenomena resulting from nanosecond electric pulse (nsEP) exposure in-vitro. *Opt. Express* 25, 6621–6643
10. Beier, H. T., Tolstykh, G. P., Musick, J. D., Thomas, R. J., and Ibey, B. L. (2014) Plasma membrane nanoporation as a possible mechanism behind infrared excitation of cells. *J. Neural Eng.* 11, 066006
11. Roth, C. C., Barnes, R. A., Ibey, B. L., Glickman, R. D., and Beier, H. T. (2016) Short infrared (IR) laser pulses can induce nanoporation. presented at the SPIE BiOS
12. Walsh, A. J., Cantu, J. C., Ibey, B. L., and Beier, H. T. (2017) Short infrared laser pulses increase cell membrane fluidity. presented at the SPIE BiOS
13. Adams, W. R., Mehl, B., Lieser, E., Wang, M., Patton, S., Throckmorton, G. A., Jenkins, J. L., Ford, J. B., Gautam, R., Brooker, J., Jansen, E. D., and Mahadevan-Jansen, A. (2021) Multi-modal nonlinear optical and thermal imaging platform for label-free characterization of biological tissue. *Sci. Rep.* 11, 8067
14. Adams, W. R., Gautam, R., Locke, A. K., Borrachero-Conejo, A. I., Dollinger, B. R., Throckmorton, G. A., Duvall, C., Jansen, E. D., and Mahadevan-Jansen, A. (2021) Visualizing the Role of Lipid Dynamics during Infrared Neural Stimulation with Hyperspectral Stimulated Raman Scattering Microscopy. *BioRxiv*
15. Borrachero-Conejo, A. I., Adams, W. R., Saracino, E., Mola, M. G., Wang, M., Posati, T., Formaggio, F., Bellis, M., Frigeri, A., Caprini, M., Hutchinson, M. R., Muccini, M., Zamboni, R., Nicchia, G. P., Mahadevan-Jansen, A., and Benfenati, V. (2020) Stimulation of water and calcium dynamics in astrocytes with pulsed infrared light. *FASEB*

CHAPTER 2:

BACKGROUND AND SIGNIFICANCE

2.1 Optical Neuromodulation

The ability to selectively modulate neural activity has been a critical research tool for understanding the nervous system's structure and function over the last 150 years. Since the times of Galvani, electrical current has been one of the gold standard tools for studying the nervous system. Today, electrical stimulation is often the preferred clinical and experimental method for verifying and directing neuronal activity. Without forming a direct electrical connection with a neuron (e.g., patch clamping), the spatial specificity and extent of stimulation and recording are limited. The idea of using optical energy to modulate neural activity was first demonstrated in 1971 by Fork, who used a 488nm Argon ion continuous wave (CW) laser to increase the baseline firing rate in an *Aplysia* pleural abdominal nerve preparation (1). Following works attempted to initiate action potentials with continuous-wave irradiation, appearing as a longer-term (10's of seconds) heating effect increasing spontaneous firing rates (2, 3). Others showed inhibition of neural signals through long-term laser exposure, often resulting in photo-coagulation and photodamage (2, 4–7). These early results laid the foundation for the research to come, identifying the potential of light as a unique tool for high precision neuromodulation.

In 1993, Callaway *et al.* published methods to use photochemical uncaging of free-floating neurotransmitters to excite neurons (8). This advancement has shaped our current understandings of neurobiology, such as synapse, spine formation, and functional cortical connectivity. Caged neurotransmitters can control neuronal activity through specific molecular pathways. These uncaging events can be spatially limited to the diffraction limit, allowing for high precision control of spatiotemporal dynamics. Others have extended uncaging techniques to leverage multiphoton absorption events and caging of other neurotransmitters (9–11). Despite these advantages, the need for additional exogenous agents makes it less suitable for clinical translation but a crucial tool for neuroscience research.

In 2001, Hirase *et al.* demonstrated spatial and temporal precision of neuronal activation with a high fluence of light from an ultrafast femtosecond laser source, free of exogenous labels (12). Two apparent mechanisms appeared: one from prolonged lower-intensity exposure and one from faster high-intensity exposures. Lower-intensity multiphoton depolarization was resistant to sodium channel blockers but susceptible to antioxidant presence. These results suggested an absorption-based phenomenon mediated by reactive oxygen species formation. The faster depolarization with high-intensity light pointed towards nanoporation mechanisms from the electric-field-induced dielectric breakdown of the cell membrane. Pore formation would allow charge flux through the cell membrane. The utility and clinical translation of ultrafast lasers is difficult due to their cost and susceptibility to misalignment. Advances in fiber laser technology make it more practical to have ultrafast laser systems in the clinic. However, the multiphoton nature of the excitation phenomena requires a high degree of optical focusing power which dramatically increases the potential for damage. Ideal pulse widths, peak powers, and exposure times need to be carefully selected and focused to work effectively. Currently, label-free multiphoton stimulation remains more practically suited for research applications than clinical use.

In 2005, optogenetics debuted through an optimized iteration of Channelrhodopsin-2 (ChR2). Channelrhodopsin-2 is a blue-light sensitive cation channel natively expressed by some algae to regulate osmolarity (13). Anionic photoactivatable halorhodopsins followed soon after (14, 15). Inserting the genes for these light-sensitive ion channels into mammalian cells allows optical control of cell membrane potential with visible light. This method substantially reduces the radiant exposure needed to depolarize neurons in comparison to previous techniques. Optogenetics offers an optical neuromodulation technique that acts through a well-known biomolecular mechanism. Additionally, the ability to use relatively inexpensive incoherent light sources from LEDs or broadband lamps makes optogenetic modulation adaptable to the existing neuroscience research toolbox. The ability to target protein expression to genetic subtypes of cell populations makes optogenetics ideal for studying circuit-specific behaviors in live animals. Early clinical trials are underway using optogenetics to treat blindness from retinitis pigmentosa in humans (14, 16). The subject of genetic modification of human cells in live human subjects still poses some ethical concerns. Many challenges stand in the way of using targeted genetic modification in humans for neuromodulation clinically. As technology progresses, the chances to translate optogenetics clinically will likely follow with extensive ethical and regulatory oversight.

Alongside the debut of optogenetics, Wells and colleagues first showed pulsed infrared light to elicit neural activity in the rat sciatic nerve (17, 18). Using infrared light to excite neural activity has attractive clinical potential due to its contact-free application, lack of electrical stimulation artifact, and lack of need for exogenous compounds or genetic modification. Clinically, a turn-key compact optical neural stimulation tool would offer improved spatial precision and minimal preparation time for use. Such technology is well suited for nerve identification or intraoperative nerve mapping during spatially confined procedures (19–21). With clinical translation in mind, early work in infrared neural stimulation (INS) demonstrated that the stimulation efficacy and damage threshold radiant exposures appeared to follow the spectrum of water absorption in the short-wave infrared (SWIR) regime between 2 and 10-micron wavelengths. Interestingly, the ideal regimes of stimulation did not occur on absorption peaks of water. The radiant exposures needed to cause damage and stimulation threshold were too similar. Maximum separation in stimulation and damage radiant exposure thresholds occurred in relative absorption shoulders in the water spectrum - the separation of stimulation and damaging radiant exposures was furthest apart. Tuning the absorption coefficient via adjusting stimulation wavelengths was posed as a possible means of depth selectivity in stimulating different types of neural tissue.

2.2 Biophysical Mechanisms of INS

The follow-up to this initial work identified the mechanistic nature of INS. Experiments suggested that a photothermal mechanism was at the root of INS. Transient spatial and temporal thermal gradients were required to generate a neural response (22). However, the biophysics underlying the transient thermal gradient at the cellular level to trigger an action potential was unclear. Wells and colleagues proposed several possible molecular explanations. Temperature directly affects the cells' Nerst potentials, ultimately affecting resting membrane potential and cellular excitability. Additionally, voltage-gated ion channel kinetics are thermally governed by a Q10 factor known to affect the amplitudes and durations of stimulated action potentials. Another explanation suggested a thermal gradient to generate a localized sodium conductance increase and trigger voltage-gated sodium channel gating. Wells *et al.* made mention of the possible heat-sensitive ion channels involvement in INS mechanisms. Albert *et al.* would eventually confirm the involvement of sensitive ion channels in dissociated sensory neurons (23). Studies to follow for a decade focused on mechanistic and translational applications.

Work in the auditory system, the vagus nerve, combined electrical-optical stimulation methods, cultured cells, and live brain models further demonstrated INS as a safe, versatile tool for optical neuromodulation (24–32). The underlying mechanisms connecting the thermal gradient to a cellular and molecular explanation remained unclear. In 2012, Albert *et al.* demonstrated that temperature-sensitive ion channel transient receptor protein vanilloid family subtype 4, or TRPV4, were implicated in INS evoking sensory neuron activity in isolate spiral and vestibular ganglion cultures (23). Cationic TRPV4 channels are well known to respond to elevated temperatures relevant to INS - they are likely to play a role in the physiological responses in cells that express it. However, neurons in the nervous system do not uniformly express TRPV4, such as motor axons that were the subject of initial INS works. The lack of conserved expression across cell types suggests that TRPV4 is not a general mechanistic explanation of INS. Subsequent work from Shapiro and Homma *et al.* demonstrated that infrared radiation transiently altered cell capacitance by a universal phenomenon observable across planar bilayer preparations, non-excitable *Xenopus* oocytes, heterologous expression models, and non-excitable mammalian HEK cells (33). Of the several conclusions realized from this work, infrared light induced capacitive currents in an artificial lipid bilayer, free of TRPV4, voltage-sensitive ion channel expression, or any cellular contents (Figure 2.1**A-D**).

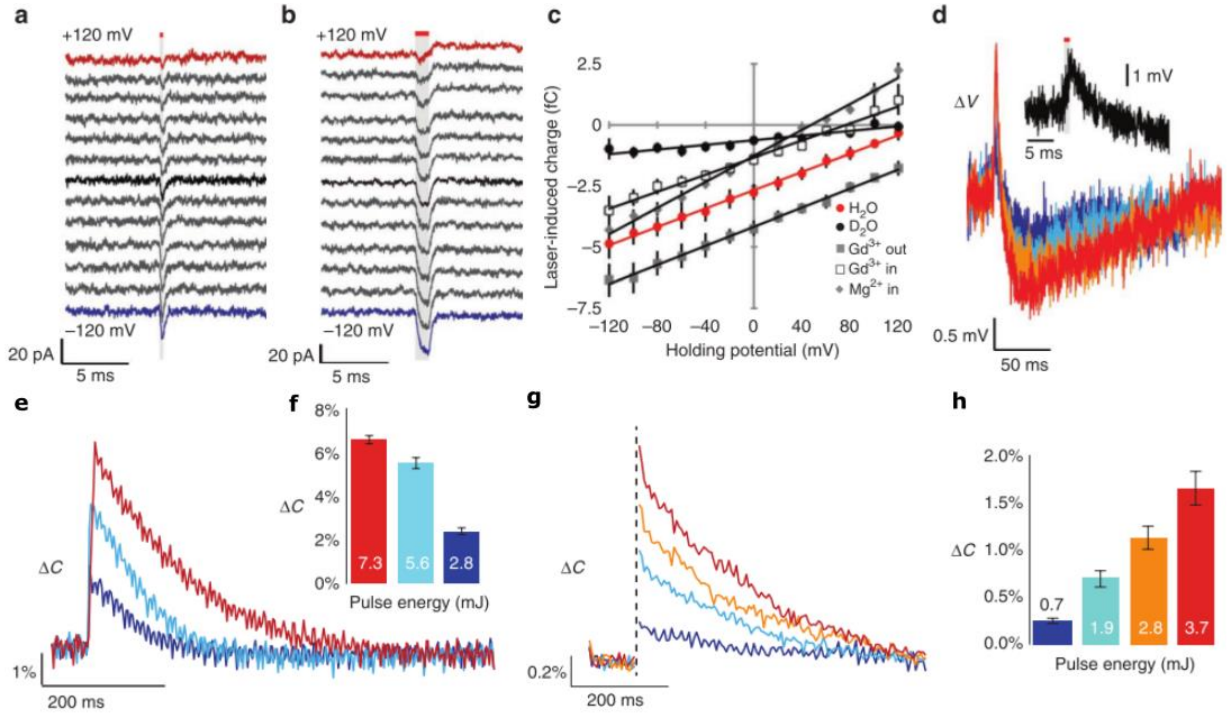

Figure 2.1: Pulsed IR exposure depolarizes cells and increases cell capacitance
I-V responses of HEK239T cells during INS to (A) 0.2ms and (B) 1ms IR pulses. (C) Q-V curves calculated for 1ms IR pulses under several different ionic conditions. (D) Voltage responses of current clamped cells to 0.5ms (blue), 1ms (cyan), 1.5ms (orange), and 2ms (red) IR exposures. Black trace is a zoomed in on first 30ms of the 1ms pulse trace. (E&F) Change in measure capacitance of an artificial PC/PE bilayer preparation irradiated with infrared light for 1ms, 2ms, and 10ms. (G&H) Change in measure capacitance of a HEK293T cell partially with 0.2ms, 0.5ms, 0.75ms, and 1ms IR pulses. Figures adapted from Ref (33).

Shapiro and Homma *et al.* concluded that depolarization of cells with infrared light is due to an increase in membrane capacitance, up to 6% in artificial bilayers and 1.6% in HEK cells *in vitro* (Figure 2.1**E-H**). Capacitance elevations appeared to decay on the order of thermal relaxation for water (Figure 2.1**E&G**). Extrapolating these results to an excitable *in vitro* condition was predicted to likely depolarize an excitable cell enough to generate an action potential. Shapiro and Homma *et al.* provide a universal explanation for depolarizing currents generated from thermal properties unique to lipid bilayers. Work to mathematically model their observations leveraged a Gouy-Chapman-Stern (GCS) model, which idealizes the cell as a fixed geometry double-layer capacitor. This GCS model reproduced experimental observations of a pure artificial bilayer well, but the molecular explanation for their results was unclear. Recent work questioned the validity of this model, demonstrating that reversing a sign convention error in the Shapiro-Homma model predicted a theoretical decrease in the cell capacitance. The GCS model employed by Shapiro and Homma *et al.* only consider a static bilayer, where the temperature dependence of charge displacements in the Stern layers and bulk water are not accounted for. Nonetheless, experimental evidence of capacitance increase is clear (Figure 2.1**E-H**), despite the validity of their biophysical model.

Plaksin *et al.* published work that revised the computational model proposed by Shapiro and Homma *et al.* and suggest a new biophysical mechanism. This revised model was benchmarked against the data from Shapiro and Homma *et al.* and accurately recreated experimental observations (33, 34). The proposed model in Plaksin *et al.* incorporated conformational changes in the lipid bilayer due to temporal temperature transients temperature-dependent membrane structure (35–39) and the ionic displacement that directly results from direct heating Figure 2.2**A**). The conformational changes in the lipid membrane derived from the literature indicate that with increased temperature, lipid bilayers in polar solvents undergo a thinning and lateral expansion (increased area per lipid molecule) around at reported rates of 0.11%/°C and 0.22%/°C, respectively Figure 2.2**A&B**) (40–43). Incorporating these physical changes in the lipid membrane dimension into their model overtakes the small decrease capacitance predicted by the previous GSC model to yield a positive change in capacitance of around 0.3%/°C. The changes in the membrane during INS alter the capacitance and depolarize the cell. If the membrane structure is changed enough, heating can depolarize cells and drive action potentials in electrically excitable cells. This dimensional change, or mechanoelectrical effect suggested by Plaksin *et al.*, relies on the premise of the hydrophobic tails of the lipid membrane undergoing a temperature-dependent *trans-gauche* rotoisomerization Figure 2.2**B**) (43). While the published data and revised model agree, **there has yet to be any direct experimental validation of their proposed mechanisms.** Electrophysiology provides an indirect observation of charge movement into and around cells. However, electrophysiology does not

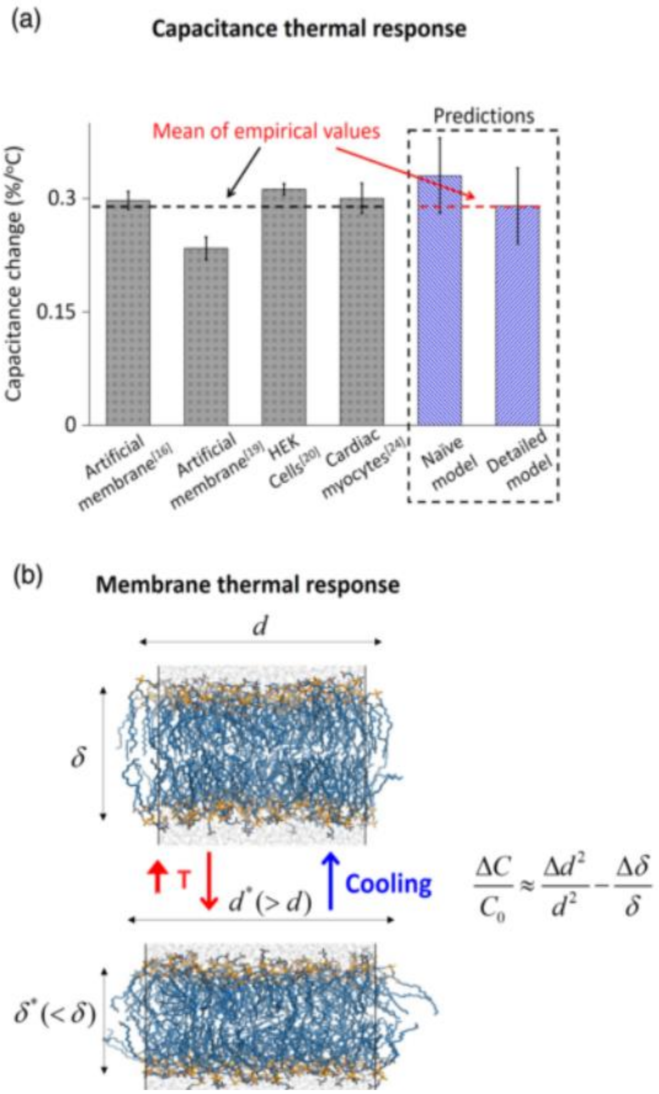

Figure 2.2: Accounting for thermally dependent bilayer structural changes in the cell membrane explains capacitance increases during INS
(A) Changes in capacitance of numerous model systems, including the detailed biophysical model accounting for physical membrane changes due to temperature. (B) Accounting for temperature-dependent physical changes in the membrane accurately predicts electrophysiological responses to INS. Figure adapted from Ref (34).

necessarily offer direct information about lipid conformational dynamics in biological models. To verify the validity of the proposed model by Plaksin *et al.*, **a method to observe lipid membrane dynamics during infrared neural stimulation is necessary**. Such a technique could answer questions about the role capacitance changes have on other non-voltage-sensitive ion channels.

Several groups have attempted to look at lipid membrane dynamics optically during infrared neural stimulation and ultrashort pulsed electric field (PEFs) exposures. Moen *et al.* demonstrated that the cell membrane undergoes some reorganization during INS, attributed to nanoporation and later disproven (44). Further work by Walsh *et al.* showed that di-4-ANNEPS indicated distinct changes in the fluidity of the cell membrane. Groups suggested nanoporation of the cell membrane was involved in the depolarization events caused by INS (45). While nanoporation appears to play more of a role in the mechanisms surrounding PEFs (44, 46, 47), this evidence does not appear to support the role of nanoporation during INS. More recently, groups are exploring the role of photomechanical effects due to thermal expansion on cellular models (48, 49). While much of the existing literature regarding changes in membrane fluidity appears to corroborate the model proposed by Plaksin *et al.*, newly emerging optical methods within nonlinear imaging have the potential to offer a more direct observation of this mechanism.

2.3 Polar Membrane Chemistry

In considering the molecular structure of a typical biological lipid membrane, the lipid membrane is composed primarily of amphipathic phospholipids. Each phospholipid molecule contains two acyl chains of variable saturation covalently linked to a hydrophilic phosphate-containing nitrogenous head group. **Figure 2.3C** shows the abbreviated chemical structures of phospholipid molecules. The amphipathic nature of lipids leads them to self-assemble into micelles or bilayers in an aqueous solution, as seen in **Figure 2.3A**. Polar head groups form the outermost portions of the membrane leaflets to interact with aqueous solvent and other polar molecules. The nonpolar aliphatic fatty acid chains are oriented between the polar headgroups to form the hydrophobic regions of each leaflet. These bilayers serve as the critical structural component for all cells. Lipid membranes separate biologically incompatible interactions within the cell to allow for the dynamic chemistry of life.

In cells, the membrane can contain proteins. Transmembrane proteins can serve as channels or transporters for passing ions or organic molecules across the cell membrane. These proteins can also act as receptors for molecular signaling or cellular communication. More recently, the more accepted model of a domain-based lipid bilayer describes that lipid bilayers in cells are composed of heterogeneous patches of

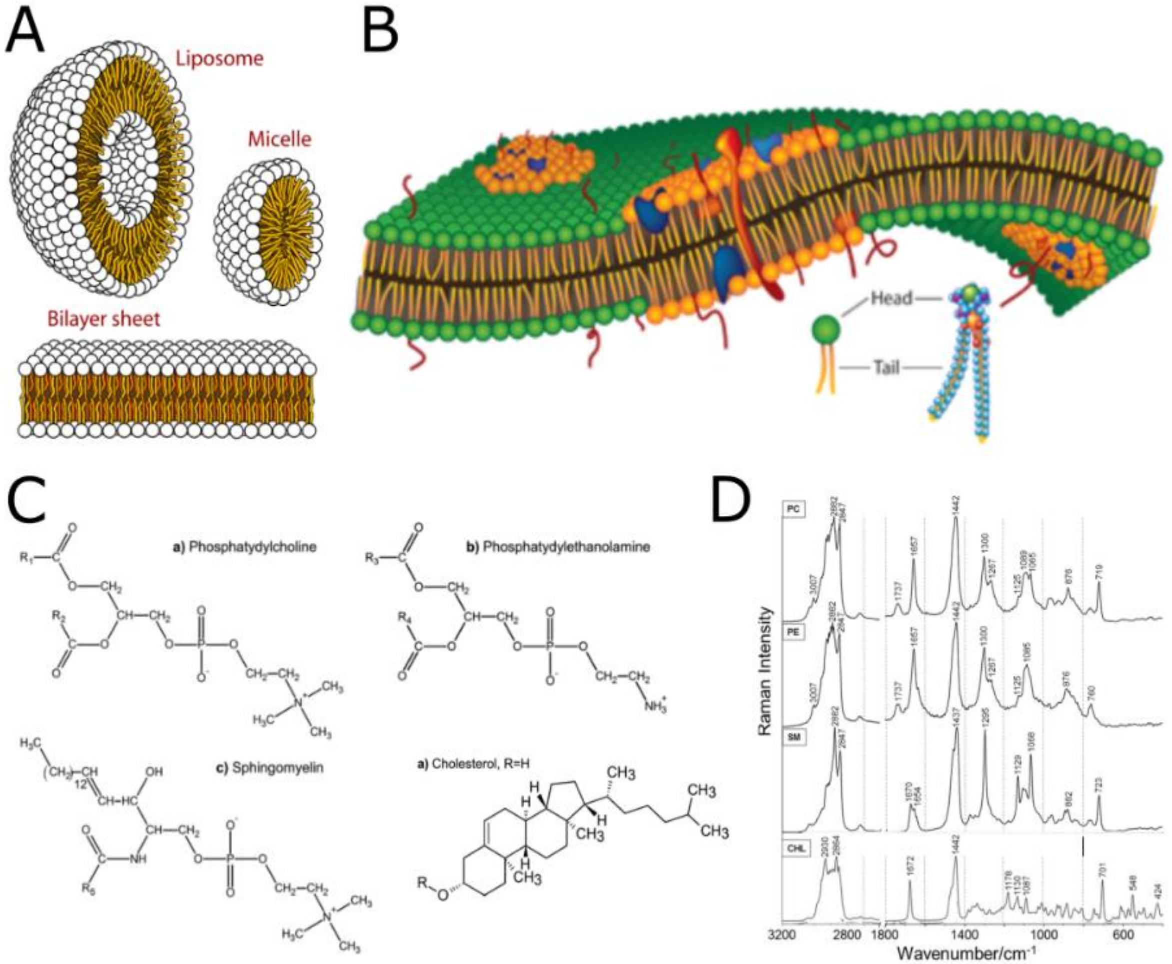

Figure 2.3: Phospholipid assemblies and their vibrational spectral properties
(A) Biologically relevant assemblies of amphipathic phospholipids. (B) Artistic rendering of lipid bilayers with microdomains of saturated lipids, cholesterol, and membrane proteins. (C) Chemical structure of commonly present phosphatydilcholine (PC), phosphatydilethanolamine (PE), Sphingomyelin (SM), and cholesterol (CHL). (D) Spontaneous Raman spectrum of each of the previous panel constituents. Adapted from Ref (76)

lipid molecules or microdomains. The lipids within these microdomains can contain varying compositions of phospholipids such as phosphatidylcholine (PC), phosphatidylethanolamine (PE), and phosphatidylinositol (PI) that tend to be more unsaturated in their fatty acid chains. Additionally, sphingolipids and cholesterol can exist in concentrated pockets within microdomains. These molecules alter the local properties of the membrane. These dense patches of lipids are referred to as “lipid rafts” within the cell membrane. Lipid rafts are important for physically stabilizing ion channels, aquaporins, and cytoskeletal projections within the cell membrane. The properties and functions of these lipid rafts are still an active area of research, appearing to play a critical role in the normal function of transmembrane proteins.

A unique feature of lipid membranes is their ability to sustain a potential difference without passing appreciable current. This property of lipid membranes gives rise to a membrane potential difference, through which electrodynamics can guide cell function. While numerous cell types undergo dynamic changes in membrane potential for their normal function, control of membrane potential is the basis of nervous system function. Transmembrane channels permeable to ions can allow for ionic currents driven by electrochemical potential differences into and out of the cell. This interplay between cell electrodynamics and protein-driven reactions drives a cascade of molecular events that ultimately lead to action potential generation in a neuron.

Lipid membranes can exist in several different structural phases driven by intermolecular interactions. Physiologically relevant membrane phases include gel, fluid, and gel-fluid transition phases (50). These phases tend to be determined by the local structural arrangement and chemical properties of the lipids, of which as well as temperature can play a crucial role (42, 51). Under physiological conditions, the membrane is never truly at a stable phase. This instability explains how lipid domains and rafts can form and disappear over a few seconds (52–54). Lipid rafts and microdomains tend to take more of a gel phase, while the edges of domains and the lipids between domains tend to live in a fluid or gel-fluid transition phase. Additionally, the role of temperature-dependent phase transitions on lipid rafts and subsequent ion channel function is limited and challenging to study. While the role of phase changes in INS is unclear (46, 55), methods to reveal phase transitions in living systems could help address such questions.

A cell becomes electrically depolarized through the application of a trans-membrane ionic current. In neurons, depolarization triggers the gating of voltage-sensitive ion channels, leading to a large and rapid change in membrane potential. These rapid shifts in membrane potential – called action potentials – propagate across the cell and form the basis of neuronal communication in the nervous system. Electrically controlling and recording cellular membrane potential has been the primary neuroscientific tool for more than a century. Practically, without direct electrical coupling to a single cell, its spatial specificity becomes limited due to the spread of electrical current in tissue. Pulsed infrared light increases the spatial specificity due to the ability to focus light and apply light in a non-contact fashion. Using light to drive neural activity circumvents the issue with current spread and collateral cell stimulation. The ability to depolarize cells optically makes optical neuromodulation a powerful research tool.

To better understand how infrared light can alter the lipid bilayer enough to generate neural activation, it is essential to consider the potential ways that optical energy can affect the lipid bilayer. In the case of the model proposed by Plaksin *et al.*, the lipid membrane changes physically where the bilayer thins and the lipid molecules expand laterally within the leafets. These assumptions derive from empirical measurements with x-ray diffraction and molecular dynamic simulations in simplified synthetic lipid preparations (37, 38, 56–59). These techniques do not translate to measuring lipid dynamics directly in live cells. Though x-ray diffraction techniques can yield more direct measurements of lipid membrane geometry, it is possible to interrogate the structure of lipid bilayers using vibrational spectroscopy (60–62). It is possible that transient heating can force phase transitions in the cell membrane and alter ion channel properties (50). Groups have observed phase transitions at physiologically relevant temperatures with vibrational spectroscopy (63), despite questions of its physiological importance. Structural information about lipid membranes is accessible from vibrational spectra, such as those seen in Figure 2.3**D** for biological membrane constituents. Optical techniques such as Raman spectroscopy are well suited to image living systems easier than x-ray diffraction. More modern approaches using nonlinear optics have the potential to make such observations in real-time.

Spectroscopic analysis of lipid membrane structures based on Raman spectroscopy dates back to the late 1970s. Raman spectroscopy relies on the inelastic scattering of photons incident on a sample. The molecular vibrations associated with covalent bonds exchange energy with incident photons and cause a red-shift in photon energy. The relative shift in scattered photon wavelength matches bond energies of covalent bonds interacting with the scattered photons (64). The chemical origins and local molecular environmental factors can significantly impact chemical bond vibrations. The finer details of these bond vibrations provide unique insight into the chemistry of biological systems. summarizes relevant vibrational spectra bands related to lipid bilayer structure. Common lipid functional groups, seen in Figure 2.3**C**, include C-H bonds in the phospholipid head groups and the fatty acid tails. C-H bonds vibrations are present in several Raman spectral regions. The 2800-3100cm^{-1} band of the Raman spectrum reveals numerous C-H stretch vibrations largely tied to fatty acid tails of phospholipids. CH_2 stretching peaks occur at 2850 and 2880cm^{-1}, indicating symmetric and asymmetric oscillations, respectively.

Table 2.1: Lipid-Related Raman Bands of Interest

2800-3100cm^{-1}	C-H related moieties, native to proteins, lipids, and carbohydrates	(60, 61, 76)
3400-3800cm^{-1}	Water Band. Hydrogen bonding information. High signal.	(82, 105, 141)
1000-1150cm^{-1}	Triple peak indicative of *trans* and *gauche* isomerization in aliphatic chains.	(60, 61)
1667cm^{-1}	Symmetric C=C stretch in aliphatic chains	(76)
1447cm^{-1}	CH_2 scissoring mode, dominantly present in lipids.	(76)

This CH_2 signal is dominated by methylene moieties in the fatty acid tails of lipids. CH_3 peaks at 2930 and 2960cm^{-1} are also observable as terminals to fatty acid chains and head groups. Several Fermi resonances exist for CH_2 and CH_3 bonds (60, 61, 65). Peaks associated with sp^2 C-H bonds, more dominant in sugars, aldehydes, and unsaturated fats, can present closer to 3010cm^{-1}. Aromatic sp^2 C-H peaks from nonpolar amino acids present around 3060cm^{-1} (65). Subtle changes in each of these bands correlate to protein and lipid structure changes. Lateral packing of fatty acid chains is particularly noticeable in the lower energy side of the C-H stretch region of the Raman spectrum (62). However, the amount of information convolved in the C-H stretching region can make interpreting lipid-specific changes difficult. Considering alternative lipid-specific signatures can be helpful. Specifically relating to INS mechanisms, the 1000-1150cm^{-1} region contains three peaks whose relative proportions describe rotational conformations of fatty acid skeletal chains about C-C bonds. Spectral changes in this skeletal carbon vibration window offer a view into the *trans-gauche* isomerization thought to drive membrane thinning in the model proposed by Plaksin *et al.* (34). Additional information regarding lateral packing of aliphatic chains present as spectral broadening or shoulder appearances within the 1447cm^{-1} peak. The 1667cm^{-1} band offers complementary information to the 1000-1150cm^{-1} band. In sum, Raman spectroscopy can describe the structure of biologically relevant lipid bilayers.

2.4 Nonlinear Imaging

Technologies enabling nonlinear imaging have advanced substantially over the past 60 years. The breadth and availability of turn-key ultrafast laser sources have had a tremendous impact on biomedical research. Neuroscientists have come to rely on multiphoton fluorescence as a means of deep tissue imaging of neural activity in anything from acute slice preparations to awake and behaving animals. While fluorescence has become one of the most useful applied optical tools in neuroscience, nonlinear imaging can bring even more practical tools to the neuroscientists' toolbox.

Nonlinear imaging is a class of imaging techniques that leverage nonlinear optical processes as a mechanism of contrast to reconstruct spatial or volumetric maps of samples. Nonlinear optics describe optical processes that occur when induced dipoles in a sample do not respond linearly to the incident electric field. Generally, the nonlinear behavior of a medium only occurs at high electric field strengths achievable with high-powered lasers. Biologically, achieving nonlinear optical contrast required the use of ultrafast lasers, which concentrate the average photon output into short sub-nanosecond pulses. The result is kilowatt level instantaneous powers achieved during each pulse while maintaining a milliwatt level average power that reduces the risk of damaging biological samples. The high instantaneous power pulse-to-pulse improves the statistical likelihood of a nonlinear optical process occurring – which scales quadratically with peak laser power. While dozens of possible nonlinear optical processes occur more-or-less simultaneously, narrowing spectral bands of detection at the photodetector can allow for preferential selection of nonlinear contrast mechanisms. For this dissertation, the optical processes of interest are multiphoton fluorescence (MPF), second harmonic generation (SHG), coherent anti-Stokes Raman scattering (CARS), and stimulated Raman scattering (SRS).

Multiphoton fluorescence is an optical process similar to single-photon fluorescence, where a higher energy photon is absorbed by a fluorophore and emitted in the form of a lower energy photon (**Figure 2.4**). These lower-energy photons can be filtered and detected with a photodetector. With MPF, the simultaneous absorption of two or more lower-energy photons can drive the same electronic transition as the single-photon fluorescence process. The resulting fluorescence of a higher energy photon can be filtered and detected similarly to single-photon fluorescence (**Figure 2.4**) (66). The practical benefits of multiphoton-driven optical processes are that scattering effects fall off as a function of $1/\lambda^4$. Using longer wavelengths to excite optical contrasts enables deeper imaging into tissue while drastically reducing photobleaching and phototoxicity. The drawbacks are that the multiphoton absorption has a low statistical probability of occurrence, requiring reasonably high powers from ultrafast laser sources under tight optical focus. These intensities can adversely impact samples, especially in biological samples. Recent work into the collateral effects of ultrafast illumination for multiphoton imaging showed that temperature rises during imaging are not a reason for concern below 200mW of power at the sample with a typical femtosecond laser (67). Over time, multiphoton fluorescence has evolved to be a standard technique for imaging live tissue with an array of different indicators (68). Standard methods for observing neural activity such as patch clamping, local field potential measurements, and multielectrode arrays are useful; they lack the spatial information and genetic/molecular specificity of fluorescence-based imaging methods.

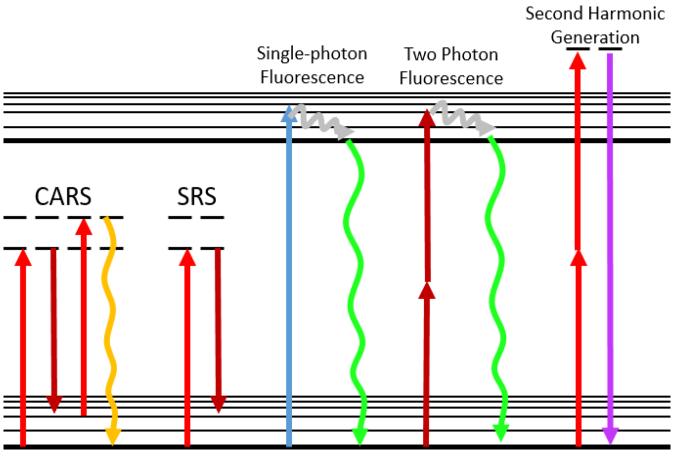

Figure 2.4: Jablonski Diagrams for nonlinear processes

Second-harmonic generation (SHG) is a parametric generation process that uses frequency doubling incident laser light using non-centrosymmetric crystals. While multiphoton fluorescence drives an electronic absorption event twice the energy of incident photons, higher harmonic generation phenomena generate a new wavelength of light at some harmonic frequency of the incident light under certain physical conditions (69). For SHG, the optical process is selective for repetitive and ordered chemical structures that lack inversion symmetry. Only a handful of biologically relevant molecules meet the selection criteria for second harmonic generation endogenously, including critical tissue structural components such as collagen, myosin, tubulin, spindle fibers, and actin (70). In the context of lipid membranes, aryl dyes such as di-4-ANNEPS can be used to observe cell membrane dynamics to gain insight into membrane order (55, 71, 72). Neurologically, SHG is useful in mapping microtubule networks in mouse brains (73, 74) as well as highlighting connective tissue in peripheral nerves (75). While SHG primarily offers a means of structural contrast, the ability to use probes of lipid membrane molecular dynamics makes it a potentially helpful tool for studying the biophysics behind INS.

Lipids are well known to have a relatively high Raman scattering cross-section, which measures how readily a molecule inelastically scatters incident light (76). In biological tissues, lipids are present in cell membranes, organelle membranes, and neutral lipid stores. These cellular and tissue lipids are well known to contribute to bulk tissue Raman signals. However, applying spontaneous Raman spectroscopy to fast photothermal events at subcellular resolution is infeasible. The single-point sampling rates for confocal Raman microspectroscopy of live cultured cells can approach 0.02 Hz (77, 78). Infrared light exposures for INS occur on the order of milliseconds and thus would necessitate sampling rates approaching 1kHz. Coherent Raman imaging can integrate into existing nonlinear imaging systems using the same ultrafast lasers and laser-scanning nonlinear microscopy technology for SHG and MPF. Nonlinear approaches to Raman can increase signals by several orders of magnitude and enable the sampling rates necessary for high-speed imaging.

Coherent Raman imaging (CRI) relies on the nonlinear interactions of multiple ultrafast laser pulses where the laser beat frequencies can coherently excite vibrational bond motion in a four-wave mixing process. While several permutations exist, the most frequently utilized methods for CRI are coherent anti-Stokes Raman scattering (CARS) and stimulated Raman scattering (SRS). The CARS signal relies on the interaction of a pump (E_P) and Stoke (E_S) beam to drive multiple stages of virtual absorption before generating a blue-shifted optical frequency (E_{CARS}) from the incident beams. This blue-shifted signal, or CARS signal, is only generated when the difference between the two incident electric field frequencies match a vibrational peak present in the sample's Raman spectrum ($E_P - E_S = \Omega$). By tuning one of the incident beam's energies, or wavelength, it is possible to obtain spectral Raman information limited by the tuning speed of the laser. SRS, unlike CARS, uses a pump-probe method of detecting the same four-wave mixing process generating coherent Raman contrast. The SRS process relies on the modulation transfer between an incident pump and probe beam, where one beam has undergone known intensity modulation. The transfer of the known modulation frequency between beams occurs more strongly when the beat frequency between the beams matches a vibrational resonance in the sample. While CARS and SRS are detected quite differently, the optical processes co-occur. As such, CARS and SRS can be detected simultaneously. While the hardware and software configurations for CRI can become complicated, MPF and SHG imaging can be readily adapted by adjusting optical detection filters.

Ford Motor Company realized spectroscopic CARS in the 1960s to analyze gas combustion and rubber production processes (79). Its translation into a laser scanning microscopy format for biomedical imaging began when Zumbusch *et al.* adapted CARS contrast to a laser-scanning multiphoton microscope platform in 1999 (80). CARS has been used primarily in the 2800-3100cm^{-1} regime of the Raman spectrum due to its strong signal and ubiquitous presence in organic samples (Figure 2.5**A&B**). CARS has been effective in imaging the phases of lipid membranes (81), the ordering of water molecules between layers of multilamellar vesicles (82), and lipid composition within cells *in vitro* (83). While work thus far aimed to characterize lipids spatially and spectrally, high temporal resolution was not a major consideration in these applied studies. To date, most applications of CARS and SRS focus on the high wavenumber C-H stretch region of the Raman spectrum (2800-3100cm^{-1}). Some have successfully observed lipid signals at 1450 and 1647 cm^{-1} with CARS - nonresonant background processes can drown out other weaker CARS signals in the fingerprint region of the Raman spectrum (400-1700cm^{-1}). Many additional peaks specific to lipid bilayer conformational changes lie in the fingerprint region of the Raman spectrum. The fingerprint window contains more fine spectral features than the high wavenumber regime. Probing these peaks during INS would provide crucial insight into the biochemical changes in neural cells during INS.

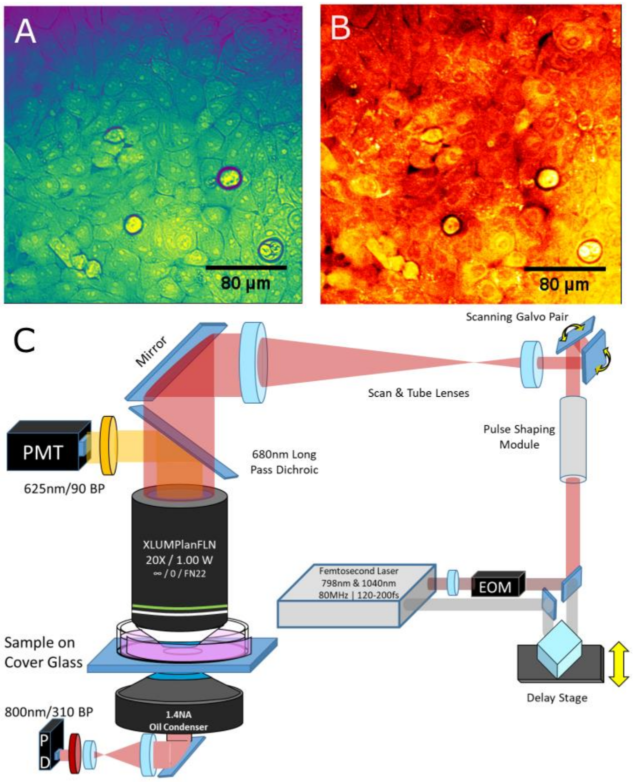

Figure 2.5: CARS and SRS of Human Mammary Cells -
Example applications of (A) CARS and (B) SRS imaging of MCF10A human mammary cells. C) An example imaging schematic of a femtosecond-based coherent Raman scattering microscope.

Beyond detection complications, one of the key issues of employing CARS in the fingerprint Raman spectral regime is nonresonant background. Background signals from other nonlinear optical processes – unrelated to the basis of CARS signal - can overwhelm CARS signal and make retrieving vibrational spectra difficult. Several strategies can circumvent this problem, including broadband CARS techniques (84–90). CARS spectra tend to differ substantially from spontaneous Raman spectra. Stimulated Raman scattering (SRS) imaging gets around these issues due to different detection techniques. Pump-probe-based lock-in detection decouples relevant Raman signals from competing background processes. The result yields nonlinear Raman spectra that are more analogous to spontaneous Raman spectra, making interpretation easier. The main drawback to SRS is that its hardware implementation is more complicated than CARS (Figure 2.5**C**). Resolving fingerprint Raman peaks with SRS is gradually improving (91–95). Additionally, stimulated Raman scattering can visualize spectroscopic signatures relating to changes in neuronal membrane potential (96). Though requiring more elaborate balanced detection strategies to mitigate system noise, SRS detected spectral changes correlated with action potentials. Others used SRS to visualize the release of acetylcholine from nerve terminals at neuromuscular junctions (95). Video-rate SRS shows drug diffusion and blood flow processes (97, 98). Deuterated lipids and proteins can highlight protein and DNA synthesis. Libraries of vibrational dyes designed to resonate in the silent window of the Raman spectrum allow multiplexing dozens of histological labels simultaneously (99–102). SRS offers many distinct advantages over CARS which are helpful in many research applications. Not only can CARS and SRS offer chemical-specific information at a high spatial resolution, but they can do so at relatively high imaging speeds. Therefore, nonlinear Raman imaging can yield new insight into the biochemical dynamics of fast processes such as INS. Changes in certain Raman bands relating to lipid membrane structure (103, 104), water hydrogen bonding dynamics (82, 105), or indicators of protein structure changes (96, 106), could yield new insight into the biophysical mechanisms of INS.

While nonlinear imaging can help understand functional and biochemical dynamics in biology, the optical design of such imaging systems leaves them susceptible to perturbation. In INS, where transient heating due to water absorption is a critical part of its mechanism (22), the induced temperature gradient can introduce a thermal lensing phenomenon that defocuses ultrafast laser excitation. This phenomenon serves as the basis for several types of imaging, such as photothermal microscopy (107, 108). Roth and Barnes *et al.* have demonstrated how probe beam deflection can visualize this thermal lensing process in real-time (48, 49). In the context of nonlinear imaging, where defocusing of the excitation laser can lead to decreases in numerical aperture and loss of nonlinear contrast, this can pose a problem for imaging during INS. The optical system used to observe INS will need to accommodate such optical perturbations.

2.5 Astrocyte Neurobiology

Neurons account for 20 to 50% of the cells in most mammalian brains (109). The remainder of those cells falls into the broad classes of either vascular cells or glial cells. The dense network of vascular and glial cells is responsible for coordinating the nutrients, oxygen, and microenvironmental stability critical for neuronal function. Blood flow throughout the brain is a dynamic balance dependent on the local energetic demands of any neurons or glial cells at any given point in time throughout the brain (110, 111). Blood flow in the brain is a tertiary indicator of local neuronal activity. For more than a century, glial cells were thought to serve structural and passive roles in the central nervous system enabling neurons to function normally (112). While this thought is true, it only tells part of the story. The additional roles of glial cells are rapidly emerging in the neuroscience community (113).

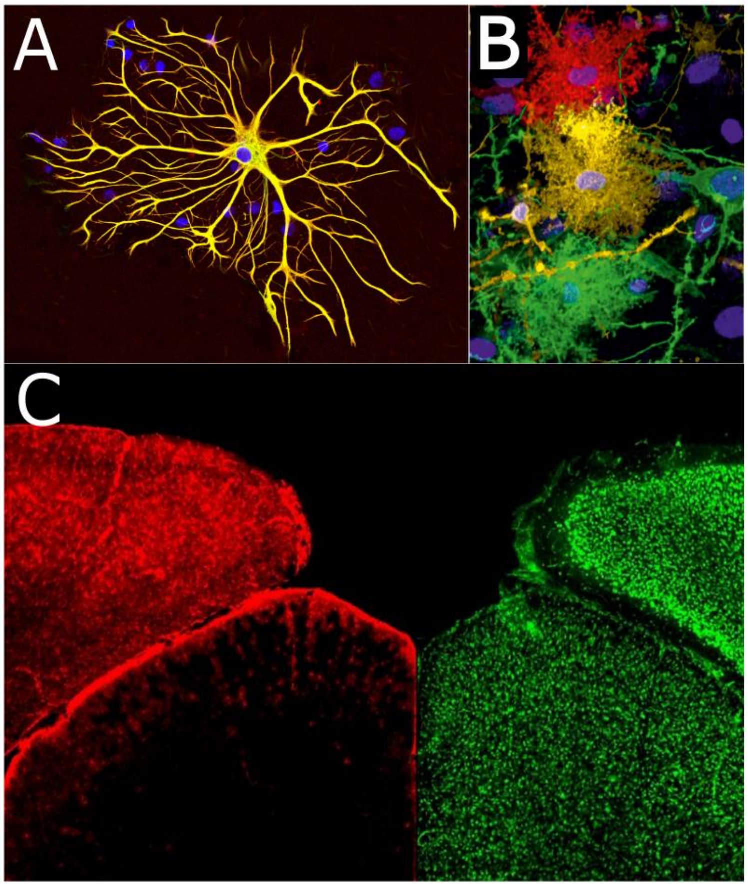

Figure 2.6: Structure and location of astrocytes in murine cortical brain tissue -
(A) Fibrous Astrocyte stained with DAPI (blue) and GFAP (yellow). Image from Rodrigo Garcia, MIT. (B) protoplasmic astrocytes stained individually via patch perfusion. DAPI highlighting nuclei. (C) GFAP expressing protoplasmic astrocytes (red) and NeuN expressing neurons (green) in the mouse visual cortex. Image from Robel Lab, Virginia Tech

Glial cells are present in the brain in varying ranges of population. Estimates put glia at ratios between 1:1 and 5:1 relative to neurons. Microglia, oligodendrocytes, and astrocytes are the three primary cell populations classified as glia. Microglia are responsible for carrying out immune functions in the brain, often referred to as the brain's macrophages. These cells are constantly traversing the brain’s interstitial space, responding to inflammatory signals and neutralizing foreign bodies. Oligodendrocytes are responsible for forming myelin in the brain's white matter, critical for relaying action potentials at high speeds over long distances.

Astrocytes are emerging as one of the most multifaceted cells in the central nervous system (113). They tend to be significantly smaller than neurons, with numerous leaflet-like projections that extend from the cell body. The bushy extensions from astrocytes reach to contact neuronal cell bodies, dendrites, axons, and synapses, as well as local pericytes, blood vessels, and other astrocytes locally in the brain. Fibrous astrocytes reside in white matter, or fiber tracts, of the brain and tend to take on a smaller, more differentiated dendritic morphology, as seen in Figure 2.6**A**. Reactive or gliotic astrocytes can present with similar dendritic morphology and play an essential role in brain immune function. Protoplasmic astrocytes that reside in the brain's grey matter tend to exhibit expansive “bushy” projections, depicted in Figure 2.6**B**. The distal ends of protoplasmic astrocytes projections that contact synapses, vessels, and other cells are called ‘endfeet’ and are critical for the functional capacities of astrocytes (114, 115). For the concern of this dissertation, protoplasmic astrocytes are the subtype of astrocytes considered. Their spatial location superficially in the neocortex is most relevant to previous INS work *in vivo*.

Astrocytes maintain hydrosaline and chemical homeostasis in the perisynaptic and perivascular spaces of the brain (116). They maintain homeostasis by multiple mechanisms: potassium buffering (117), volume regulation (118), and neurotransmitter uptake and release (119). During an action potential, neurons expel potassium into the extracellular space. Accumulation of potassium in the local extracellular space raises the neuron's resting membrane potential. If potassium concentrations go unregulated, it can lead to sustained depolarization, tetanic neuronal response, and ultimately neuronal death (120). To counteract the osmotic gradient, active potassium cotransporters and inward rectifying potassium channels (e.g., Kir4.1) in astrocytes help to siphon K^+ from extracellular space. Removal of K^+ balances the local osmotic gradient and stabilizes neuronal resting membrane potential. In astrocytes, this intake of potassium, actively or passively, depolarizes the astrocyte. Depolarization propagates to other astrocytes via gap junctions (117) and initiates neurovascular responses (111). The potassium uptake and diffusion by astrocyte networks is a mechanism known as K^+ spatial buffering. Kir4.1 channels localize in astrocytic endfeet surrounding synapses and blood vessels, owing to their functional significance in homeostasis. Neurovascular coupling, or the increase in local blood perfusion in active brain areas, serves as the basis of detection for blood-oxygen-level-dependent functional magnetic resonance imaging (BOLD fMRI), optical intrinsic signal imaging (OIS), and functional near-infrared spectroscopy (fNIRS) (110).

Astrocytes regulate perisynaptic and perineuronal homeostasis during periods of elevated neuronal activity. Osmolarity changes during periods of high neuronal activity can lead to potentially dangerous levels of water diffusion and potassium accumulation. Astrocytes are also responsible for buffering the local osmotic balance around neurons by adjusting their cell volume via AQP-4 mediated water flux (121). AQP-4 colocalizes with Kir4.1 in the endfeet of protoplasmic astrocytes. They appear to work collaboratively in maintaining perisynaptic homeostasis. Interestingly, transient receptor protein vanilloid family subtype 4, or TRPV4, channels have been implicated in osmoregulation (122). TRPV4 colocalizes in astrocytic endfeet with AQP-4 (122). The activation of TRPV4 can give rise to a swelling-induced cation influx, particularly Ca^{2+} and K^+ (118, 122–124). Together, these channels help guide the homeostasis of the synaptic and neuronal microenvironment.

Astrocytes envelop synapses to uptake potassium and recycle neurotransmitters to prune synaptic transmission (125). More recently, mechanisms of gliotransmission are the subject of debate (126, 127). Evidence suggests that astrocytes can release neuromodulatory molecules and directly influence neuronal function. Whether gliotransmission impacts neuronal signaling under physiological conditions is still in question. Experimentally, elevated Ca^{2+} causes the release of neurotransmitters, such as glutamate, from astrocytes – through mechanisms of which are not clear (127–129). Perturbing astrocyte calcium signaling has yielded mixed outcomes on neuronal signaling (130, 131), though evidence points to endfoot-directed perisynaptic mechanisms (114, 132). Vesicular-based gliotransmitter release may be possible (133), but the lack of canonical synaptic scaffolding and fusion protein expression in astrocytes (134). Volume-regulated anion channel (VRAC) and hemichannels-mediated passive release of modulatory molecules have also been hypothesized (113, 127, 135, 136).

The way astrocytes mediate much of their cellular functions is through changes in intracellular calcium concentration. Calcium is a tightly regulated ion in astrocytes and is involved in many aspects of their physiology (137). Rapid increases in intracellular calcium levels in astrocytes *in vivo* can be coupled with activation of neurotransmitter receptors expressed by astrocytes, mediating calcium-dependent potassium release via BK_{Ca} channels to mediate vascular dilation (116). Additionally, Ca^{2+} can trigger the release of intracellular calcium stores to activate secondary messenger pathways and osmotic responses (116, 122, 127). Strong concerted calcium responses in astrocytes can mediate modulatory molecule release (127, 129). The physiological relevance of such strong induced astrocyte calcium events is often questioned.

In the context of infrared neural stimulation, astrocytes appear to play a role in the evoked calcium responses observed *in vivo* (138). Considering the cortical distribution of astrocytes, dominantly occupying the superficial layers of the cortex and pial surface (Figure 2.6**C)**, it seems reasonable that astrocytes would take the primary portion of the thermal load during INS. Additionally, astrocytes are known to express TRPV4 (123). In astrocytes, TRPV4 serves a functional role in volume regulation (122). It is also a temperature-sensitive channel that is involved in sensory neuron sensitivity to INS (23). With the postulated universal mechanisms of thermal cellular depolarization (33, 34), it is conceivable that pulsed infrared light could modulate astrocytes directly through multiple potential mechanisms. If astrocytic responses to INS can directly modulate neural activity, INS could be a valuable tool for studying astrocyte physiology. These conjectures serve as the basis for the latter portion of this dissertation.

2.6 Impact

Understanding the mechanisms of INS on a biochemical and physiological level will enable its optimization for clinical and research applications. Furthermore, understanding the mechanisms responsible for INS lays the groundwork for developing innovative neuromodulation tools that are faster, more precise, and impactful. Optimizing neuromodulation technologies towards clinical treatments could improve patient outcomes by avoiding complications of existing technologies.

The potential for astrocytic modulation provides a unique research tool to study astrocyte physiology and function. Astrocyte-mediated disease researchers need targeted tools to drive cellular function in a spatially dependent way. Diseases such as epilepsy, encephalitis, acute morbidities related to concussions, ischemia all have known astrocyte involvement. Approaching cases of debilitating depression or post-traumatic stress may offer a paradigm-shifting approach in future psychiatric interventions. The impact of astrocytes on human behavior and neuropathology is just now being realized (128, 139, 140). Tools for direct control over astrocyte molecular dynamics are not as readily available as tools for neuronal modulation. A label-free optical tool in the scientists' toolbox can help the neuroscience and glial biology communities better understand and improve human health.

2.7 Innovation

Only a handful of work to date has used nonlinear Raman imaging to observe fast biochemical changes in neural model systems (95, 96). Even fewer have utilized nonlinear Raman imaging to observe fast photothermal perturbations in biological model systems (105). Using nonlinear Raman imaging to characterize and analyze chemical changes during fast photothermal events, such as INS, is unprecedented in the current literature. Demonstration of nonlinear Raman imaging for studying the biochemical changes during INS would provide some of the first direct measurements of lipid dynamics in neural models during INS. No work before this dissertation sought to characterize the mechanistic nature of astrocyte sensitivity to INS. Furthermore, detailed work on the molecular signaling processes elicited by different IR dosing strategies has not been demonstrated until now. The ability to selectively modulate astrocytic activity in a safe label-free format brings new potential in studying astrocyte physiology. In sum, this dissertation addresses multiple gaps in knowledge by combining methods across multiple disciplines to answer impactful questions in biomedicine.

2.8 References

1. Fork, R. L. (1971) Laser stimulation of nerve cells in Aplysia. *Science* 171, 907–908
2. Walker, J. (1983) Relief from chronic pain by low power laser irradiation. *Neurosci. Lett.* 43, 339–344
3. Janiszewski, J. (1986) The effect of temperature changes on the spontaneous activity in the neural ganglia of the cockroach, Periplaneta americana. *J Therm Biol* 11, 191–197
4. Hopp, F. A., Zuperku, E. J., Coon, R. L., and Kampine, J. P. (1980) Effect of anodal blockade of myelinated fibers on vagal C-fiber afferents. *Am. J. Physiol.* 239, R454–62
5. Klumpp, D. and Zimmermann, M. (1980) Irreverisble differential block of A- and C-fibres following local nerve heating in the cat. *J. Physiol. (Lond.)* 298, 471–482
6. Tsuchiya, K., Kawatani, M., Takeshige, C., Sato, T., and Matsumoto, I. (1993) Diode laser irradiation selectively diminishes slow component of axonal volleys to dorsal roots from the saphenous nerve in the rat. *Neurosci. Lett.* 161, 65–68
7. Tsuchiya, K., Kawatani, M., Takeshige, C., and Matsumoto, I. (1994) Laser irradiation abates neuronal responses to nociceptive stimulation of rat-paw skin. *Brain Res. Bull.* 34, 369–374
8. Callaway, E. M. and Katz, L. C. (1993) Photostimulation using caged glutamate reveals functional circuitry in living brain slices. *Proc. Natl. Acad. Sci. USA* 90, 7661–7665
9. Kramer, R. H., Chambers, J. J., and Trauner, D. (2005) Photochemical tools for remote control of ion channels in excitable cells. *Nat. Chem. Biol.* 1, 360–365
10. Kramer, R. H., Fortin, D. L., and Trauner, D. (2009) New photochemical tools for controlling neuronal activity. *Curr. Opin. Neurobiol.* 19, 544–552
11. Gee, K. R., Wieboldt, R., and Hess, G. P. (1994) Synthesis and photochemistry of a new photolabile derivative of GABA-neurotransmitter release and receptor activation in the microsecond time region. *J. Am. Chem. Soc.* 116, 8366–8367
12. Hirase, H., Nikolenko, V., Goldberg, J. H., and Yuste, R. (2002) Multiphoton stimulation of neurons. *J. Neurobiol.* 51, 237–247
13. Nagel, G., Szellas, T., Huhn, W., Kateriya, S., Adeishvili, N., Berthold, P., Ollig, D., Hegemann, P., and Bamberg, E. (2003) Channelrhodopsin-2, a directly light-gated cation-selective membrane channel. *Proc. Natl. Acad. Sci. USA* 100, 13940–13945
14. Klapper, S. D., Swiersy, A., Bamberg, E., and Busskamp, V. (2016) Biophysical properties of optogenetic tools and their application for vision restoration approaches. *Front. Syst. Neurosci.* 10, 74
15. Essen, L.-O. (2002) Halorhodopsin: light-driven ion pumping made simple? *Curr. Opin. Struct. Biol.* 12, 516–522
16. Allergan. (2015) RST-001 Phase I/II Trial for Advanced Retinitis Pigmentosa.
17. Wells, J., Kao, C., Mariappan, K., Albea, J., Jansen, E. D., Konrad, P., and Mahadevan-Jansen, A. (2005) Optical stimulation of neural tissue in vivo. *Opt. Lett.* 30, 504–506
18. Wells, J., Kao, C., Jansen, E. D., Konrad, P., and Mahadevan-Jansen, A. (2005) Application of infrared light for in vivo neural stimulation. *J. Biomed. Opt.* 10, 064003
19. Teudt, I. U., Nevel, A. E., Izzo, A. D., Walsh, J. T., and Richter, C.-P. (2007) Optical stimulation of the facial nerve: a new monitoring technique? *Laryngoscope* 117, 1641–1647
20. Lee, J. W., Kim, D., Yoo, S., Lee, H., Lee, G.-H., and Nam, Y. (2015) Emerging neural stimulation technologies for bladder dysfunctions. *Int Neurourol J* 19, 3–11
21. Cayce, J. M., Wells, J. D., Malphrus, J. D., Kao, C., Thomsen, S., Tulipan, N. B., Konrad, P. E., Jansen, E. D., and Mahadevan-Jansen, A. (2015) Infrared neural stimulation of human spinal nerve roots in vivo. *Neurophotonics* 2, 015007
22. Wells, J., Kao, C., Konrad, P., Milner, T., Kim, J., Mahadevan-Jansen, A., and Jansen, E. D. (2007) Biophysical mechanisms of transient optical stimulation of peripheral nerve. *Biophys. J.* 93, 2567–2580

23. Albert, E. S., Bec, J. M., Desmadryl, G., Chekroud, K., Travo, C., Gaboyard, S., Bardin, F., Marc, I., Dumas, M., Lenaers, G., Hamel, C., Muller, A., and Chabbert, C. (2012) TRPV4 channels mediate the infrared laser-evoked response in sensory neurons. *J. Neurophysiol.* 107, 3227–3234

24. Wells, J. D., Thomsen, S., Whitaker, P., Jansen, E. D., Kao, C. C., Konrad, P. E., and Mahadevan-Jansen, A. (2007) Optically mediated nerve stimulation: Identification of injury thresholds. *Lasers Surg Med* 39, 513–526

25. Izzo, A. D., Walsh, J. T., Ralph, H., Webb, J., Bendett, M., Wells, J., and Richter, C.-P. (2008) Laser stimulation of auditory neurons: effect of shorter pulse duration and penetration depth. *Biophys. J.* 94, 3159–3166

26. Albert Y. Rhee, Gong Li, Jonathon Wells, and Joseph P. Y. Kao. (2008) Photostimulation of sensory neurons of the rat vagus nerve. presented at the SPIE BiOS

27. Duke, A. R., Cayce, J. M., Malphrus, J. D., Konrad, P., Mahadevan-Jansen, A., and Jansen, E. D. (2009) Combined optical and electrical stimulation of neural tissue in vivo. *J. Biomed. Opt.* 14, 060501

28. Cayce, J. M., Kao, C. C., Malphrus, J. D., Konrad, P. E., Mahadevan-Jansen, A., and Jansen, E. D. (2010) Infrared neural stimulation of thalamocortical brain slices. *IEEE J. Select. Topics Quantum Electron.* 16, 565–572

29. Feng, H.-J., Kao, C., Gallagher, M. J., Jansen, E. D., Mahadevan-Jansen, A., Konrad, P. E., and Macdonald, R. L. (2010) Alteration of GABAergic neurotransmission by pulsed infrared laser stimulation. *J. Neurosci. Methods* 192, 110–114

30. Jenkins, M. W., Duke, A. R., Gu, S., Chiel, H. J., Fujioka, H., Watanabe, M., Jansen, E. D., and Rollins, A. M. (2010) Optical pacing of the embryonic heart. *Nat. Photonics* 4, 623–626

31. Katz, E. J., Ilev, I. K., Krauthamer, V., Kim, D. H., and Weinreich, D. (2010) Excitation of primary afferent neurons by near-infrared light in vitro. *Neuroreport* 21, 662–666

32. Tozburun, S., Lagoda, G. A., Burnett, A. L., and Fried, N. M. (2010) Gaussian versus flat-top spatial beam profiles for optical stimulation of the prostate nerves. presented at the BiOS

33. Shapiro, M. G., Homma, K., Villarreal, S., Richter, C.-P., and Bezanilla, F. (2012) Infrared light excites cells by changing their electrical capacitance. *Nat. Commun.* 3, 736

34. Plaksin, M., Shapira, E., Kimmel, E., and Shoham, S. (2018) Thermal Transients Excite Neurons through Universal Intramembrane Mechanoelectrical Effects. *Phys. Rev. X* 8, 011043

35. Akabori, K. and Nagle, J. F. (2014) Comparing lipid membranes in different environments. *ACS Nano* 8, 3123–3127

36. Kopelevich, D. I. and Nagle, J. F. (2015) Correlation between length and tilt of lipid tails. *J. Chem. Phys.* 143, 154702

37. Kucerka, N., Nagle, J. F., Sachs, J. N., Feller, S. E., Pencer, J., Jackson, A., and Katsaras, J. (2008) Lipid bilayer structure determined by the simultaneous analysis of neutron and X-ray scattering data. *Biophys. J.* 95, 2356–2367

38. Nagle, J. (2017) Mechanical properties of lipid bilayers. *European Pharmaceutical Journal* 64, 22–23

39. Pan, J., Tristram-Nagle, S., Kucerka, N., and Nagle, J. F. (2008) Temperature dependence of structure, bending rigidity, and bilayer interactions of dioleoylphosphatidylcholine bilayers. *Biophys. J.* 94, 117–124

40. Pan, J., Mills, T. T., Tristram-Nagle, S., and Nagle, J. F. (2008) Cholesterol perturbs lipid bilayers nonuniversally. *Phys. Rev. Lett.* 100, 198103

41. Kucerka, N., Perlmutter, J. D., Pan, J., Tristram-Nagle, S., Katsaras, J., and Sachs, J. N. (2008) The effect of cholesterol on short- and long-chain monounsaturated lipid bilayers as determined by molecular dynamics simulations and X-ray scattering. *Biophys. J.* 95, 2792–2805

42. Szekely, P., Dvir, T., Asor, R., Resh, R., Steiner, A., Szekely, O., Ginsburg, A., Mosenkis, J., Guralnick, V., Dan, Y., Wolf, T., Tamburu, C., and Raviv, U. (2011) Effect of temperature on the structure of charged membranes. *J. Phys. Chem. B* 115, 14501–14506

43. Zhuang, X., Makover, J. R., Im, W., and Klauda, J. B. (2014) A systematic molecular dynamics simulation study of temperature dependent bilayer structural properties. *Biochim. Biophys. Acta* 1838, 2520–2529

44. Moen, E. K., Beier, H. T., Ibey, B. L., and Armani, A. M. (2016) The role of membrane dynamics in electrical and infrared neural stimulation. presented at the SPIE BiOS

45. Beier, H. T., Tolstykh, G. P., Musick, J. D., Thomas, R. J., and Ibey, B. L. (2014) Plasma membrane nanoporation as a possible mechanism behind infrared excitation of cells. *J. Neural Eng.* 11, 066006

46. Troyanova-Wood, M., Musick, J. D., Ibey, B. L., Thomas, R. J., and Beier, H. T. (2014) Observation of changes in membrane fluidity after infrared laser stimulation using a polarity-sensitive fluorescent probe. presented at the SPIE BiOS

47. Franklin, S., Ibey, B. L., Nash, K., and Beier, H. T. (2013) Measurement of changes in plasma membrane phospholipid polarization following nanosecond pulsed electric field exposure. presented at the SPIE BiOS

48. Barnes, R. A., Roth, C. C., Beier, H. T., Noojin, G., Valdez, C., Bixler, J., Moen, E., Shadaram, M., and Ibey, B. L. (2017) Probe beam deflection optical imaging of thermal and mechanical phenomena resulting from nanosecond electric pulse (nsEP) exposure in-vitro. *Opt. Express* 25, 6621–6643

49. Roth, C. C., Barnes, R. A., Ibey, B. L., Glickman, R. D., and Beier, H. T. (2016) Short infrared (IR) laser pulses can induce nanoporation. presented at the SPIE BiOS

50. Riske, K. A., Barroso, R. P., Vequi-Suplicy, C. C., Germano, R., Henriques, V. B., and Lamy, M. T. (2009) Lipid bilayer pre-transition as the beginning of the melting process. *Biochim. Biophys. Acta* 1788, 954–963

51. Kučerka, N., Nieh, M.-P., and Katsaras, J. (2011) Fluid phase lipid areas and bilayer thicknesses of commonly used phosphatidylcholines as a function of temperature. *Biochim. Biophys. Acta* 1808, 2761–2771

52. Reeves, V. L., Thomas, C. M., and Smart, E. J. (2012) Lipid rafts, caveolae and GPI-linked proteins. *Adv. Exp. Med. Biol.* 729, 3–13

53. Bacia, K., Scherfeld, D., Kahya, N., and Schwille, P. (2004) Fluorescence correlation spectroscopy relates rafts in model and native membranes. *Biophys. J.* 87, 1034–1043

54. Pike, L. J. (2003) Lipid rafts: bringing order to chaos. *J. Lipid Res.* 44, 655–667

55. Walsh, A. J., Cantu, J. C., Ibey, B. L., and Beier, H. T. (2017) Short infrared laser pulses increase cell membrane fluidity. presented at the SPIE BiOS

56. Boscia, A. L., Treece, B. W., Mohammadyani, D., Klein-Seetharaman, J., Braun, A. R., Wassenaar, T. A., Klösgen, B., and Tristram-Nagle, S. (2014) X-ray structure, thermodynamics, elastic properties and MD simulations of cardiolipin/dimyristoylphosphatidylcholine mixed membranes. *Chem Phys Lipids* 178, 1–10

57. Chu, N., Kucerka, N., Liu, Y., Tristram-Nagle, S., and Nagle, J. F. (2005) Anomalous swelling of lipid bilayer stacks is caused by softening of the bending modulus. *Phys. Rev. E, Stat. Nonlin. Soft. Matter. Phys.* 71, 041904

58. Kucerka, N., Liu, Y., Chu, N., Petrache, H. I., Tristram-Nagle, S., and Nagle, J. F. (2005) Structure of fully hydrated fluid phase DMPC and DLPC lipid bilayers using X-ray scattering from oriented multilamellar arrays and from unilamellar vesicles. *Biophys. J.* 88, 2626–2637

59. Nagle, J. F. and Tristram-Nagle, S. (2000) Lipid bilayer structure. *Curr. Opin. Struct. Biol.* 10, 474–480

60. Gaber, B. P., Yager, P., and Peticolas, W. L. (1978) Interpretation of biomembrane structure by Raman difference spectroscopy. Nature of the endothermic transitions in phosphatidylcholines. *Biophys. J.* 21, 161–176

61. Gaber, B. P. and Peticolas, W. L. (1977) On the quantitative interpretation of biomembrane structure by Raman spectroscopy. *Biochimica et Biophysica Acta (BBA) - Biomembranes* 465, 260–274

62. Snyder, R. G., Scherer, J. R., and Gaber, B. P. (1980) Effects of chain packing and chain mobility on the raman spectra of biomembranes. *Biochimica et Biophysica Acta (BBA) - Biomembranes* 601, 47–53

63. Lewis, R. N. A. H. and McElhaney, R. N. (2013) Membrane lipid phase transitions and phase organization studied by Fourier transform infrared spectroscopy. *Biochim. Biophys. Acta* 1828, 2347–2358

64. Austin, L. A., Osseiran, S., and Evans, C. L. (2016) Raman technologies in cancer diagnostics. *Analyst* 141, 476–503

65. Syed, A. and Smith, E. A. (2017) Raman Imaging in Cell Membranes, Lipid-Rich Organelles, and Lipid Bilayers. *Annu. Rev. Anal. Chem. (Palo Alto, Calif.)* 10, 271–291

66. Denk, W., Delaney, K. R., Gelperin, A., Kleinfeld, D., Strowbridge, B. W., Tank, D. W., and Yuste, R. (1994) Anatomical and functional imaging of neurons using 2-photon laser scanning microscopy. *J. Neurosci. Methods* 54, 151–162

67. Podgorski, K. and Ranganathan, G. (2016) Brain heating induced by near-infrared lasers during multiphoton microscopy. *J. Neurophysiol.* 116, 1012–1023

68. Chen, T.-W., Wardill, T. J., Sun, Y., Pulver, S. R., Renninger, S. L., Baohan, A., Schreiter, E. R., Kerr, R. A., Orger, M. B., Jayaraman, V., Looger, L. L., Svoboda, K., and Kim, D. S. (2013) Ultrasensitive fluorescent proteins for imaging neuronal activity. *Nature* 499, 295–300

69. Campagnola, P. J. and Loew, L. M. (2003) Second-harmonic imaging microscopy for visualizing biomolecular arrays in cells, tissues and organisms. *Nat. Biotechnol.* 21, 1356–1360

70. Campagnola, P. J., Millard, A. C., Terasaki, M., Hoppe, P. E., Malone, C. J., and Mohler, W. A. (2002) Three-dimensional high-resolution second-harmonic generation imaging of endogenous structural proteins in biological tissues. *Biophys. J.* 82, 493–508

71. Owen, D. M., Rentero, C., Magenau, A., Abu-Siniyeh, A., and Gaus, K. (2011) Quantitative imaging of membrane lipid order in cells and organisms. *Nat. Protoc.* 7, 24–35

72. Campagnola, P. J., Wei, M. D., Lewis, A., and Loew, L. M. (1999) High-resolution nonlinear optical imaging of live cells by second harmonic generation. *Biophys. J.* 77, 3341–3349

73. Kwan, A. C., Dombeck, D. A., and Webb, W. W. (2008) Polarized microtubule arrays in apical dendrites and axons. *Proc. Natl. Acad. Sci. USA* 105, 11370–11375

74. Kwan, A. C., Duff, K., Gouras, G. K., and Webb, W. W. (2009) Optical visualization of Alzheimer’s pathology via multiphoton-excited intrinsic fluorescence and second harmonic generation. *Opt. Express* 17, 3679–3689

75. Huff, T. B. and Cheng, J. X. (2007) In vivo coherent anti-Stokes Raman scattering imaging of sciatic nerve tissue. *J. Microsc.* 225, 175–182

76. Czamara, K., Majzner, K., Pacia, M. Z., Kochan, K., Kaczor, A., and Baranska, M. (2015) Raman spectroscopy of lipids: a review. *J. Raman Spectrosc.* 46, 4–20

77. Bi, X., Rexer, B., Arteaga, C. L., Guo, M., and Mahadevan-Jansen, A. (2014) Evaluating HER2 amplification status and acquired drug resistance in breast cancer cells using Raman spectroscopy. *J. Biomed. Opt.* 19, 025001

78. Große, C., Bergner, N., Dellith, J., Heller, R., Bauer, M., Mellmann, A., Popp, J., and Neugebauer, U. (2015) Label-free imaging and spectroscopic analysis of intracellular bacterial infections. *Anal. Chem.* 87, 2137–2142

79. Cheng, J. X. and Xie, X. S. (2012) Coherent Raman Scattering Microscopy. CRC Press

80. Zumbusch, A., Holtom, G. R., and Xie, X. S. (1999) Three-Dimensional Vibrational Imaging by Coherent Anti-Stokes Raman Scattering. *Phys. Rev. Lett.* 82, 4142–4145

81. Müller, M. and Schins, J. M. (2002) Imaging the Thermodynamic State of Lipid Membranes with Multiplex CARS Microscopy. *J. Phys. Chem. B* 106, 3715–3723

82. Cheng, J.-X., Pautot, S., Weitz, D. A., and Xie, X. S. (2003) Ordering of water molecules between phospholipid bilayers visualized by coherent anti-Stokes Raman scattering microscopy. *Proc. Natl. Acad. Sci. USA* 100, 9826–9830

83. Rinia, H. A., Burger, K. N. J., Bonn, M., and Müller, M. (2008) Quantitative label-free imaging of lipid composition and packing of individual cellular lipid droplets using multiplex CARS microscopy. *Biophys. J.* 95, 4908–4914

84. Camp, C. H., Lee, Y. J., and Cicerone, M. T. (2016) Quantitative, comparable coherent anti-Stokes Raman scattering (CARS) spectroscopy: correcting errors in phase retrieval. *J. Raman Spectrosc.* 47, 408–415

85. Camp, C. H., Lee, Y. J., Heddleston, J. M., Hartshorn, C. M., Hight Walker, A. R., Rich, J. N., Lathia, J. D., and Cicerone, M. T. (2014) High-Speed Coherent Raman Fingerprint Imaging of Biological Tissues. *Nat. Photonics* 8, 627–634

86. Cicerone, M. T. and Camp, C. H. (2017) Histological coherent Raman imaging: a prognostic review. *Analyst* 143, 33–59

87. Liu, Y., Lee, Y. J., and Cicerone, M. T. (2009) Broadband CARS spectral phase retrieval using a time-domain Kramers–Kronig transform. *Opt. Lett.* 34, 1363

88. Li, B., Charan, K., Wang, K., Rojo, T., Sinefeld, D., and Xu, C. (2016) Nonresonant background suppression for coherent anti-Stokes Raman scattering microscopy using a multi-wavelength time-lens source. *Opt. Express* 24, 26687–26695

89. Li, B., Charan, K., Wang, K., Sinefeld, D., and Xu, C. (2017) Multi-wavelength time-lens source and its application to nonresonant background suppression for coherent anti-Stokes Raman scattering microscopy. presented at the SPIE BiOS

90. Wang, K., Zhang, D., Charan, K., Slipchenko, M. N., Wang, P., Xu, C., and Cheng, J.-X. (2013) Time-lens based hyperspectral stimulated Raman scattering imaging and quantitative spectral analysis. *J. Biophotonics* 6, 815–820

91. Zhang, D., Slipchenko, M. N., and Cheng, J.-X. (2011) Highly sensitive vibrational imaging by femtosecond pulse stimulated raman loss. *J. Phys. Chem. Lett.* 2, 1248–1253

92. Ozeki, Y., Umemura, W., Otsuka, Y., Satoh, S., Hashimoto, H., Sumimura, K., Nishizawa, N., Fukui, K., and Itoh, K. (2012) High-speed molecular spectral imaging of tissue with stimulated Raman scattering. *Nat. Photonics* 6, 845–851

93. Yu, Z., Chen, T., Zhang, X., Fu, D., Liao, X., Shen, J., Liu, X., Zhang, B., Xie, X. S., Su, X.-D., Chen, J., and Huang, Y. (2012) Label-free chemical imaging in vivo: three-dimensional non-invasive microscopic observation of amphioxus notochord through stimulated Raman scattering (SRS). *Chem. Sci.* 3, 2646

94. Fu, D., Yu, Y., Folick, A., Currie, E., Farese, R. V., Tsai, T.-H., Xie, X. S., and Wang, M. C. (2014) In vivo metabolic fingerprinting of neutral lipids with hyperspectral stimulated Raman scattering microscopy. *J. Am. Chem. Soc.* 136, 8820–8828

95. Fu, D., Yang, W., and Xie, X. S. (2017) Label-free Imaging of Neurotransmitter Acetylcholine at Neuromuscular Junctions with Stimulated Raman Scattering. *J. Am. Chem. Soc.* 139, 583–586

96. Lee, H. J., Zhang, D., Jiang, Y., Wu, X., Shih, P.-Y., Liao, C.-S., Bungart, B., Xu, X.-M., Drenan, R., Bartlett, E., and Cheng, J.-X. (2017) Label-Free Vibrational Spectroscopic Imaging of Neuronal Membrane Potential. *J. Phys. Chem. Lett.* 8, 1932–1936

97. Wang, Z., Zheng, W., and Huang, Z. (2016) Lock-in-detection-free line-scan stimulated Raman scattering microscopy for near video-rate Raman imaging. *Opt. Lett.* 41, 3960–3963

98. Saar, B. G., Freudiger, C. W., Reichman, J., Stanley, C. M., Holtom, G. R., and Xie, X. S. (2010) Video-rate molecular imaging in vivo with stimulated Raman scattering. *Science* 330, 1368–1370

99. Wei, L., Chen, Z., Shi, L., Long, R., Anzalone, A. V., Zhang, L., Hu, F., Yuste, R., Cornish, V. W., and Min, W. (2017) Super-multiplex vibrational imaging. *Nature* 544, 465–470

100. Zhao, Z., Shen, Y., Hu, F., and Min, W. (2017) Applications of vibrational tags in biological imaging by Raman microscopy. *Analyst* 142, 4018–4029

101. Wei, L., Hu, F., Chen, Z., Shen, Y., Zhang, L., and Min, W. (2016) Live-Cell Bioorthogonal Chemical Imaging: Stimulated Raman Scattering Microscopy of Vibrational Probes. *Acc. Chem. Res.* 49, 1494–1502

102. Min, W., Freudiger, C. W., Lu, S., and Xie, X. S. (2011) Coherent nonlinear optical imaging: beyond fluorescence microscopy. *Annu. Rev. Phys. Chem.* 62, 507–530
103. Pézolet, M. and Georgescauld, D. (1985) Raman spectroscopy of nerve fibers. A study of membrane lipids under steady state conditions. *Biophys. J.* 47, 367–372
104. Mendelsohn, R., Sunder, S., and Bernstein, H. J. (1975) Structural studies of biological membranes and related model systems by raman spectroscopy. *Biochimica et Biophysica Acta (BBA) - Biomembranes* 413, 329–340
105. Beier, H. T., Noojin, G. D., and Rockwell, B. A. (2012) Coherent Raman scattering for localized thermal mapping. presented at the SPIE BiOS
106. Liu, B., Lee, H. J., Zhang, D., Liao, C.-S., Ji, N., Xia, Y., and Cheng, J.-X. (2015) Label-free spectroscopic detection of membrane potential using stimulated Raman scattering. *Appl. Phys. Lett.* 106, 173704
107. Bai, Y., Zhang, D., Li, C., Liu, C., and Cheng, J.-X. (2017) Bond-Selective Imaging of Cells by Mid-Infrared Photothermal Microscopy in High Wavenumber Region. *J. Phys. Chem. B* 121, 10249–10255
108. Eldridge, W. J., Meiri, A., Sheinfeld, A., Rinehart, M. T., and Wax, A. (2014) Fast wide-field photothermal and quantitative phase cell imaging with optical lock-in detection. *Biomed. Opt. Express* 5, 2517–2525
109. Oberheim, N. A., Wang, X., Goldman, S., and Nedergaard, M. (2006) Astrocytic complexity distinguishes the human brain. *Trends Neurosci.* 29, 547–553
110. Kozberg, M. and Hillman, E. (2016) Neurovascular coupling and energy metabolism in the developing brain. *Prog. Brain Res.* 225, 213–242
111. Metea, M. R. and Newman, E. A. (2006) Glial cells dilate and constrict blood vessels: a mechanism of neurovascular coupling. *J. Neurosci.* 26, 2862–2870
112. Volterra, A. and Meldolesi, J. (2005) Astrocytes, from brain glue to communication elements: the revolution continues. *Nat. Rev. Neurosci.* 6, 626–640
113. Verkhratsky, A. and Nedergaard, M. (2018) Physiology of Astroglia. *Physiol. Rev.* 98, 239–389
114. Bindocci, E., Savtchouk, I., Liaudet, N., Becker, D., Carriero, G., and Volterra, A. (2017) Three-dimensional Ca2+ imaging advances understanding of astrocyte biology. *Science* 356
115. Di Castro, M. A., Chuquet, J., Liaudet, N., Bhaukaurally, K., Santello, M., Bouvier, D., Tiret, P., and Volterra, A. (2011) Local Ca2+ detection and modulation of synaptic release by astrocytes. *Nat. Neurosci.* 14, 1276–1284
116. Benfenati, V. and Ferroni, S. (2015) Microdynamics of water and ion homeostasis in the brain. In *Homeostatic control of brain function* (Boison, D. and Masino, S. A., eds) pp. 3–30, Oxford University Press
117. Orkand, R. K., Nicholls, J. G., and Kuffler, S. W. (1966) Effect of nerve impulses on the membrane potential of glial cells in the central nervous system of amphibia. *J. Neurophysiol.* 29, 788–806
118. Benfenati, V. and Ferroni, S. (2010) Water transport between CNS compartments: functional and molecular interactions between aquaporins and ion channels. *Neuroscience* 168, 926–940
119. Perea, G. and Araque, A. (2010) GLIA modulates synaptic transmission. *Brain Res. Rev.* 63, 93–102
120. Witthoft, A., Filosa, J. A., and Karniadakis, G. E. (2013) Potassium buffering in the neurovascular unit: models and sensitivity analysis. *Biophys. J.* 105, 2046–2054
121. Mola, M. G., Sparaneo, A., Gargano, C. D., Spray, D. C., Svelto, M., Frigeri, A., Scemes, E., and Nicchia, G. P. (2016) The speed of swelling kinetics modulates cell volume regulation and calcium signaling in astrocytes: A different point of view on the role of aquaporins. *Glia* 64, 139–154
122. Benfenati, V., Caprini, M., Dovizio, M., Mylonakou, M. N., Ferroni, S., Ottersen, O. P., and Amiry-Moghaddam, M. (2011) An aquaporin-4/transient receptor potential vanilloid 4 (AQP4/TRPV4) complex is essential for cell-volume control in astrocytes. *Proc. Natl. Acad. Sci. USA* 108, 2563–2568

123. Benfenati, V., Amiry-Moghaddam, M., Caprini, M., Mylonakou, M. N., Rapisarda, C., Ottersen, O. P., and Ferroni, S. (2007) Expression and functional characterization of transient receptor potential vanilloid-related channel 4 (TRPV4) in rat cortical astrocytes. *Neuroscience* 148, 876–892
124. Dunn, K. M., Hill-Eubanks, D. C., Liedtke, W. B., and Nelson, M. T. (2013) TRPV4 channels stimulate Ca2+-induced Ca2+ release in astrocytic endfeet and amplify neurovascular coupling responses. *Proc. Natl. Acad. Sci. USA* 110, 6157–6162
125. Chung, W.-S., Verghese, P. B., Chakraborty, C., Joung, J., Hyman, B. T., Ulrich, J. D., Holtzman, D. M., and Barres, B. A. (2016) Novel allele-dependent role for APOE in controlling the rate of synapse pruning by astrocytes. *Proc. Natl. Acad. Sci. USA* 113, 10186–10191
126. Savtchouk, I. and Volterra, A. (2018) Gliotransmission: Beyond Black-and-White. *J. Neurosci.* 38, 14–25
127. Nimmerjahn, A. (2009) Astrocytes going live: advances and challenges. *J. Physiol. (Lond.)* 587, 1639–1647
128. Monai, H., Ohkura, M., Tanaka, M., Oe, Y., Konno, A., Hirai, H., Mikoshiba, K., Itohara, S., Nakai, J., Iwai, Y., and Hirase, H. (2016) Calcium imaging reveals glial involvement in transcranial direct current stimulation-induced plasticity in mouse brain. *Nat. Commun.* 7, 11100
129. Hirase, H., Qian, L., Barthó, P., and Buzsáki, G. (2004) Calcium dynamics of cortical astrocytic networks in vivo. *PLoS Biol.* 2, E96
130. Petravicz, J., Boyt, K. M., and McCarthy, K. D. (2014) Astrocyte IP3R2-dependent Ca(2+) signaling is not a major modulator of neuronal pathways governing behavior. *Front. Behav. Neurosci.* 8, 384
131. Petravicz, J., Fiacco, T. A., and McCarthy, K. D. (2008) Loss of IP3 receptor-dependent Ca2+ increases in hippocampal astrocytes does not affect baseline CA1 pyramidal neuron synaptic activity. *J. Neurosci.* 28, 4967–4973
132. Yu, X., Taylor, A. M. W., Nagai, J., Golshani, P., Evans, C. J., Coppola, G., and Khakh, B. S. (2018) Reducing astrocyte calcium signaling in vivo alters striatal microcircuits and causes repetitive behavior. *Neuron* 99, 1170–1187.e9
133. Bezzi, P., Gundersen, V., Galbete, J. L., Seifert, G., Steinhäuser, C., Pilati, E., and Volterra, A. (2004) Astrocytes contain a vesicular compartment that is competent for regulated exocytosis of glutamate. *Nat. Neurosci.* 7, 613–620
134. Fiacco, T. A. and McCarthy, K. D. (2018) Multiple Lines of Evidence Indicate That Gliotransmission Does Not Occur under Physiological Conditions. *J. Neurosci.* 38, 3–13
135. Suadicani, S. O., Brosnan, C. F., and Scemes, E. (2006) P2X7 receptors mediate ATP release and amplification of astrocytic intercellular Ca2+ signaling. *J. Neurosci.* 26, 1378–1385
136. Benfenati, V., Caprini, M., Nicchia, G. P., Rossi, A., Dovizio, M., Cervetto, C., Nobile, M., and Ferroni, S. (2009) Carbenoxolone inhibits volume-regulated anion conductance in cultured rat cortical astroglia. *Channels* 3, 323–336
137. Guerra-Gomes, S., Sousa, N., Pinto, L., and Oliveira, J. F. (2017) Functional roles of astrocyte calcium elevations: from synapses to behavior. *Front. Cell Neurosci.* 11, 427
138. Cayce, J. M., Bouchard, M. B., Chernov, M. M., Chen, B. R., Grosberg, L. E., Jansen, E. D., Hillman, E. M. C., and Mahadevan-Jansen, A. (2014) Calcium imaging of infrared-stimulated activity in rodent brain. *Cell Calcium* 55, 183–190
139. Maiolo, L., Guarino, V., Saracino, E., Convertino, A., Melucci, M., Muccini, M., Ambrosio, L., Zamboni, R., and Benfenati, V. (2021) Glial interfaces: advanced materials and devices to uncover the role of astroglial cells in brain function and dysfunction. *Adv Healthc Mater* 10, e2001268
140. Fabbri, R., Saracino, E., Treossi, E., Zamboni, R., Palermo, V., and Benfenati, V. (2021) Graphene glial-interfaces: challenges and perspectives. *Nanoscale* 13, 4390–4407
141. Rabasovic, M. D., Sisamakis, E., Wennmalm, S., and Widengren, J. (2016) Label-Free Fluctuation Spectroscopy Based on Coherent Anti-Stokes Raman Scattering from Bulk Water Molecules. *ChemPhysChem* 17, 1025–1033

CHAPTER 3:

MULTI-MODAL NONLINEAR OPTICAL AND THERMAL IMAGING PLATFORM FOR LABEL-FREE CHARACTERIZATION OF BIOLOGICAL TISSUE

Text adapted from:

Wilson R Adams, Brian Mehl, Eric Lieser, Manqing Wang, Shane Patton, Graham A Throckmorton, J Logan Jenkins, Jeremy B Ford, Rekha Gautam, Jeff Brooker, E. Duco Jansen, Anita Mahadevan-Jansen. *Multi-modal Nonlinear Optical and Thermal Imaging Platform for Label-Free Characterization of Biological Tissue*. Scientific Reports. Apr 2021. https://doi.org/10.1038/s41598-021-86774-2 Abstract

The ability to characterize the combined structural, functional, and thermal properties of biophysically dynamic samples is needed to address critical questions related to tissue structure, physiological dynamics, and disease progression. Towards this, we have developed an imaging platform that enables multiple nonlinear imaging modalities to be combined with thermal imaging on a common sample. Here we demonstrate label-free multimodal imaging of live cells, excised tissues, and live rodent brain models. While potential applications of this technology are wide-ranging, we expect it to be especially useful in addressing biomedical research questions aimed at the biomolecular and biophysical properties of tissue and their physiology.

3.2 Introduction

With increased focus on high-speed biological processes at molecular, chemical, and biophysical levels, there has come a critical need to develop tools that can keep pace with the number of active research areas in biomedicine. Technical developments in nonlinear optical microscopy have revolutionized our ability to study biophysical and biochemical properties of tissues, both in terms of the wide range of samples, improved contrast modalities, and unprecedented speeds at which imaging is now possible. However, combining direct spatial temperature measurements alongside multiphoton modes of contrast have not been widely adopted. Multiphoton imaging approaches have enabled deep-tissue imaging across numerous model systems, gleaning important insights on the structure and function of cells and tissues (1, 2) while thermal imaging can yield complementary information to relate to study metabolism, circulation, and immune response. Temperature plays a crucial role in biology yet has yet to be extensively demonstrated in any substantial capacity towards biological microscopy applications. Thus, instrumentation to explore the structural, functional, and thermal properties of tissue would prove useful in studying biophysical dynamics in tissue physiology.

Multiphoton fluorescence (MPF) and second harmonic generation (SHG) are particularly useful in highlighting tissue structure and function (3, 4). Calcium, voltage, and molecule-sensitive reporters continue to push the boundaries of multiphoton applications in biomedical research. Vibrational spectroscopic contrast using nonlinear Raman imaging (NRI), namely coherent anti-Stokes Raman scattering (CARS) and stimulated Raman scattering (SRS), has shown particularly wide-ranging applicability. These include rapid identification of tumor margins (5), high-dimensional structural labeling (6), other biological processes such as drug delivery (7), neurotransmitter release (8), and electrophysiological dynamics (9). Such imaging can highlight the molecular organization and biochemical composition of tissue over time– offering a glimpse into sub- and inter-molecular dynamics without using exogeneous labels. Multiplexing functional, biochemical, and biophysical (e.g. temperature) contrast in cells and tissues can offer a unique tool in evaluating and imaging biological and physiological processes that may not be possible with the same degree of exploratory power in separate instruments (1).

Nonlinear optical microscopy is inherently suitable for multimodal imaging applications. Integrating the different modalities that fall under nonlinear microscopy can help alleviate unnecessary system complexity while providing complementary information about tissue structure and function. Notably, CARS, SRS, MPF, and SHG are all optical processes that can occur and be detected simultaneously or sequentially by selecting the appropriate filters and detectors for the techniques used. Several groups have demonstrated selective combinations of nonlinear imaging strategies to address a range of biological questions, *in vitro* and *in vivo* (10), particularly sensing fast biological processes such as neuronal action potentials and calcium activity with combined SRS and calcium-sensitive MPF (9). Integration of SRS with optical coherence tomography (OCT) has been shown to augment nonspecific scattering-based contrast with vibrational specificity to image lipid distributions in excised human adipose tissue (11). More recently, researchers have employed four or more nonlinear imaging modalities, including CARS, MPF, SHG, and third harmonic generation for live tissue and intravital imaging towards wound healing and cancer metastasis (12, 13). While most of these demonstrated approaches have been applied towards observing biological processes over the span of multiple hours at the molecular and biochemical levels, they are limited in their ability to observe snapshots of sub-second functional, biochemical, and thermal processes.

The influence of temperature in physiological and biochemical processes – particularly surrounding sample damage and physiological modulation - has recently become an area of prominence across biomedical research disciplines (14–16). As optical imaging and perturbation technologies continue to advance biomedical research, it becomes critical to consider thermodynamic effects particularly on live specimens albeit practically difficult. A flexible imaging system that incorporates molecular, biochemical, and biophysical information from cells to tissues, *in vitro* to *in vivo,* would enable the study of rapid and dynamic biophysical processes from multiple perspectives.

Measuring temperatures in biological samples at high resolutions spatially and temporally has proven difficult and continues to be an active area of research. Groups have multiplexed blackbody thermal imaging and fluorescence microscopy at cellular resolutions *in vitro* (17, 18), however water absorption generally obscures the ability to visualize cell morphology with thermal imaging alone. Moreover, optical components that suffice for use between 0.4 and 14 µm wavelengths to encompass visible optical and thermal infrared imaging are not readily available. Finite element heat transfer modeling and Monte Carlo simulations of photon transport in scattering media is often regarded as the benchmark approach for temperature estimation of dynamic photothermal processes in biological samples with high water concentrations (19). Several indirect approaches have been demonstrated including temperature-dependent changes in fluorophore emission, and probe beam deflection microscopy (16, 19, 20). While point-based methods (utilizing thermocouples, customized miniature sensors, or intrinsic fluorescence of rare-earth doped glass waveguides) are more direct, they sacrifice spatial information obtained with temperature mapping (21). Previous work has utilized thermal imaging with laser speckle imaging to study cerebral blood flow changes during different methods of anesthesia (22). However, despite the potential utility of combining thermal imaging with multimodal nonlinear microscopy, such a combination has not been previously reported. A system that can combine multimodal nonlinear microscopy with thermal imaging would offer unprecedented flexibility to study biological processes in real time.

The goal of this project is to integrate multiple nonlinear imaging methods with thermal imaging so that biophysical, biochemical, and molecular information from dynamic biological processes may be imaged with micron level spatial resolution and millisecond level temporal resolution. Towards this effort, we present an imaging platform that integrates single-band CARS, SRS, MPF, SHG, and wide field thermal microscopy (ThM) for characterizing tissues at varying time scales. Applications of our imaging system are demonstrated imaging both *in vitro* with neural cell cultures and tissue specimen as well as *in vivo* with acute craniotomy rat preparations. Our platform offers a novel approach enabling imaging techniques with otherwise incompatible optical paths (due to physical limitations of hardware) to be applied on a common sample. We demonstrate that this platform provides a robust tool for researchers to probe the physiology of dynamic biological systems, through the unique integration of vibrational spectroscopic, functional fluorescence, and thermal contrast.

3.3 System Design

The framework of the Multimodal Advanced Nonlinear and Thermal Imaging System, or MANTIS, is a three-armed imaging turret (Customized Bergamo II Platform, Thorlabs Imaging Research, Sterling, VA, USA) that respectively images a sample with either nonlinear imaging, thermal imaging, or widefield white light reflectance imaging which is reconfigurable to adapt additional measurement approaches (**Figure 3.1A**). The mechanical arrangement of distinct imaging arms allows for modalities with incompatible optical instrumentation (e.g. ultrafast near infrared imaging with endogenous shortwave infrared measurements) to be performed sequentially without disturbing or repositioning the sample. A FLIR SC8300-series high-speed indium-antimonide CCD camera equipped with a 4X germanium imaging objective (FLIR Systems Inc., Nashua, NH, USA | **Figure 3.1B**) is attached to the thermal imaging arm of the microscope. The thermal camera relies on the endogenous black/grey body emission of a sample between 3-5 µm wavelength under the assumption of homogenous emissivity to infer sample temperatures.

The nonlinear imaging section of MANTIS, depicted in **Figure 3.1C** with a simplified schematic, is coupled to two nonlinear laser sources supplying femtosecond (Insight DS+, Spectra Physics, Fremont, CA, USA) and picosecond (picoEmerald S, A.P.E, Berlin, DE) laser lines. Higher spectral bandwidth (~15 nm) femtosecond laser pulses provides high peak powers necessary for optimal multiphoton and higher harmonic generation *in vivo* (1). The picosecond laser has narrower bandwidth (~0.5 nm, or 10 cm^{-1}), which is critical for maintaining the spectral resolution necessary for single-band nonlinear Raman imaging while minimizing power at the sample for safe *in vivo* applications (<20 mW average power) (23). Both laser systems operate with a pulse repetition rate of 80MHz and output two beams necessary for pump and Stokes excitation of NRI contrast processes. The shorter wavelength tunable laser line undergoes a tunable path length delay while the longer wavelength laser line is intensity-modulated at 20 MHz via an electro-optical modulator (Thorlabs, Newton, NJ, USA) to facilitate SRS. Each laser's output is spatially and temporally co-linear and directed with a series of mirrors into the scan head of the nonlinear imaging arm of MANTIS. The imaging optics of the nonlinear imaging arm are based on conventional upright laser-scanning microscopy. The scanning optics consist of a pair of galvanometric mirrors (Thorlabs, Newton, NJ, USA), which are imaged onto the back focal plane of a commercial objective lens (Olympus XLUMPLFLN, 20X 1.0NA | Nikon CFI Apochromat NIR 60X, 1.0NA) via a 4f optical relay. This scan relay performs a fixed 4X magnification of the laser beam diameter to accommodate the back-aperture pupil size of the largest objective lenses we use relative to the entrance beam diameter (SL50-2P2 & TL200-2P2, Thorlabs, Newton, NJ, USA). Two epi-detection ports with a photomultiplier tube (CARS/MPF/SHG | GaAsP Amplified

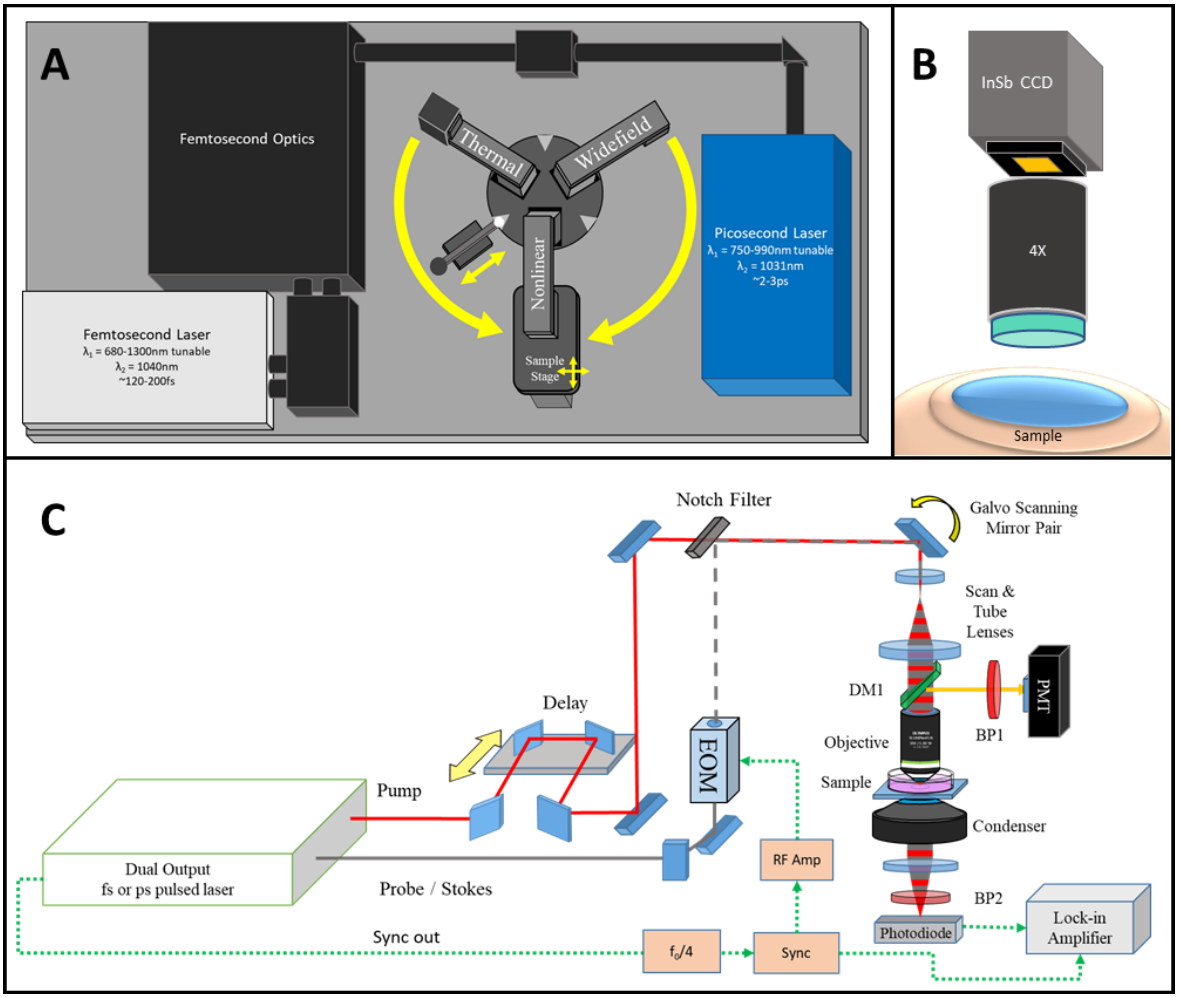

Figure 3.1: MANTIS System Design
A) The layout of MANTIS. The system is capable of performing multimodal nonlinear and thermal imaging over the same sample. Additionally, white light imaging on a third imaging arm is available for further expansion of the system. B) Schematic of wide-field thermal microscopy, which infers the temperature of a sample based on the blackbody emission observed between wavelengths of 3 and 5µm. C) General optical schematic of a multimodal nonlinear imaging system capable of integrating CARS, SRS, MPF and SHG imaging. DM – dichroic mirror, BP – bandpass filter, PMT – photomultiplier tube, EOM – electro-optical modulator, InSb CCD – indium antimonide charge coupled device.

PMT, Thorlabs, USA) and a large area 50-V reverse-biased photodiode (SRS | A.P.E. GmbH, Berlin, DE) are used for imaging epi-detected contrast. Two additional detachable forward detection ports were also built to accommodate coherent imaging modalities in transparent samples in transmission mode. All reported SRS images are acquired in transmission mode with the exception of *in vivo* imaging data. Stimulated Raman loss for SRS was demodulated via a commercial lock-in-amplifier (A.P.E. Gmbh, Berlin, DE). All emission filters and excitation wavelengths included with the system are in Table 3.1 (Semrock, Brattleboro, VT, USA). Scanning and detection hardware for imaging is controlled through ThorImageLS version 2.1, 3.0, or 3.2 (Thorlabs Imaging Research, Sterling, VA, USA). All images shown are raw with linear intensity rescaling, with all analysis being performed in FIJI (24).

Table 3.1: Summary of emission filters and excitation wavelengths used for multimodal imaging.
All filters obtained from Semrock (Brattleboro, VT, USA).

Contrast	Filter (Center/Passband FWHM)	Excitation Wavelengths
CH-band CARS	625nm/90nm	792-803nm & 1040nm
SRS	890nm/310nm	792-803nm & 1040nm
NADH/Blue Fluorescence	460nm/30nm	780nm
FAD/Green Fluorescence	525nm/30nm	934nm
SHG	460nm/30nm	900nm
Propidium Iodide / Orange Fluorescence	625nm/90nm	1040nm

The third imaging arm of MANTIS initially features a color complementary metal oxide semiconductor (CMOS) camera (Thorlabs Inc., Newton, NJ, USA) with a variable focal length lens (Navitar Inc., Rochester, NY, USA) for widefield white-light reflectance imaging of samples (**Figure 3.1A**). However, this arm was built into the imaging system to readily enable integration of additional contrast modalities that may be further incompatible with multimodal nonlinear microscopy – such as interferometric contrast or stereoscopic surgical guidance. Each arm is locked into position by a custom-designed spring-loaded locking system against the rotating turret base (**Figure 3.1A**). The maximum fields of view of each imaging arm is ~800 µm-x-800 µm for nonlinear microscopy with a 20X objective, 3mm-x-4mm for thermal microscopy with a 4X objective, and 50 mm-x-50 mm for widefield white light reflectance imaging.

3.4 System Performance

To achieve high-speed imaging at subcellular resolution, MANTIS was designed to resolve at least 1 µm lateral resolution in the nonlinear imaging arm. Performance was verified on a series of standards, (**Figure 3.2A**), with measured axial and lateral resolutions for each modality summarized in (with full data summary in). Images of 0.5 µm diameter polystyrene (PS, latex, Polysciences Inc. Warrington, PA, USA) beads with CARS and SRS were obtained to generate a point spread function (PSF), which is reported here as the full-width half-maximum intensity cross-section of

Table 3.2: Summary of measured system resolutions across multiple imaging modalities.

Modality	Lateral Resolution (µm)	Axial Resolution (µm)
CARS	0.632	3.009
SRS	0.833	3.136
MPF	0.359	1.502
SHG	0.388	X
Thermal	6.9	X

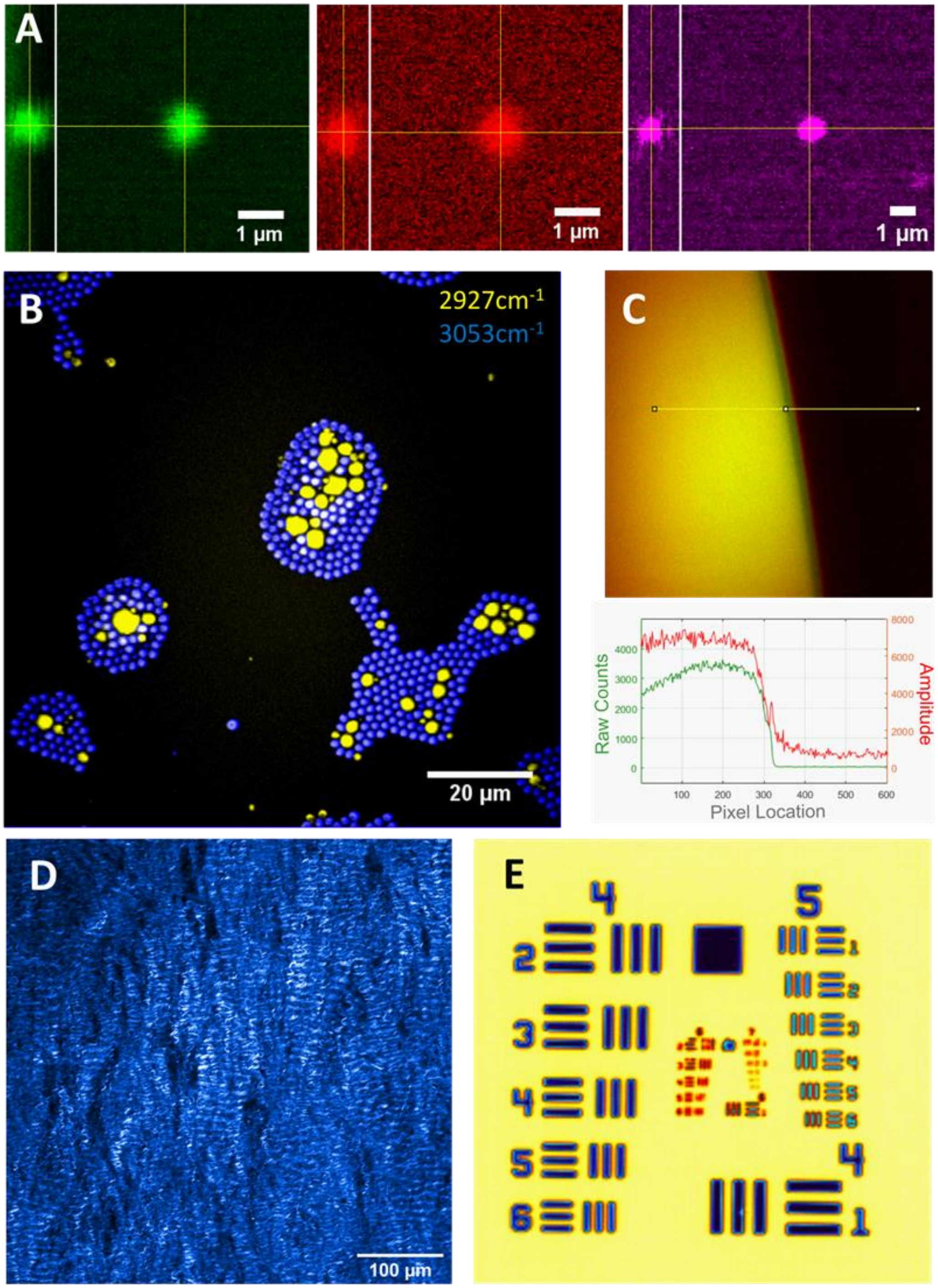

Figure 3.2: MANTIS System Performance
A) Resolution of CARS (Green), SRS (Red) with a 1 µm polystyrene bead, and Multiphoton Fluorescence (Magenta) with a 500 -nm yellow-fluorescent polystyrene bead. Measured resolutions summarized in . B) Preparation of mixed beads containing 2 µm polystyrene beads (blue, 2927 cm^{-1}) with 1-10 µm PMMA beads (yellow, 3053 cm^{-1}). Peaks specific to each bead type C) CARS (Green) and SRS (Red) of signal-to-noise profile measured at a vegetable oil – air meniscus at 2927 cm^{-1}. E) Thermal Imaging of a 1951 U.S. Air Force Target..

Inc. Warrington, PA, USA) were used to measure the PSF of MPF. All PSF calculations were performed using the MetroloJ plugin in FIJI (25). Measured resolutions, reported in , are on par with results published in literature when imaging with numerical apertures approaching 1.0 (3, 23, 26). Spectral separation of polymethyl-methacrylate (PMMA, acrylic, Polysciences Inc. Warrington, PA, USA)) and PS beads with single-band SRS are shown in **Figure 3.2B**. Acrylic (PMMA) beads are depicted using the 2927 cm^{-1} band – an asymmetric CH$_3$ resonance- (yellow), and latex (PS) beads are depicted spectrally separate with the 3053 cm^{-1} band– an asymmetric CH$_2$ resonance- in blue. The signal-to-noise ratio (SNR), measured at the edge of a vegetable oil meniscus at the 2927 cm^{-1} band with SRS (**Figure 3.2C**, **Figure 3.3**), was calculated to be 34.6 (27).

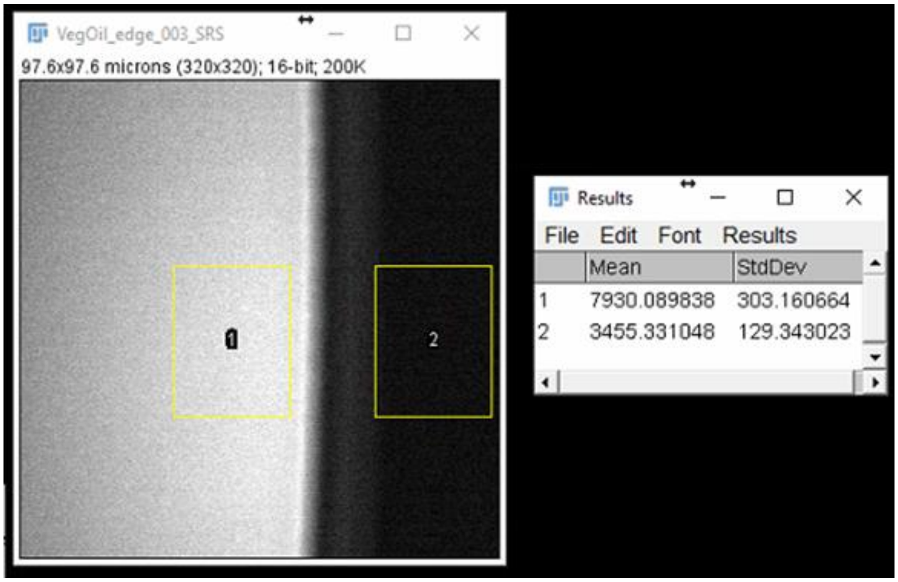
VegOil_edge_003_SRS

97.6x97.6 microns (320x320); 16-bit; 200K

Results

	Mean	StdDev
1	7930.089838	303.160664
2	3455.331048	129.343023

Figure 3.3: Signal to Noise calculation with a Vegetable Oil meniscus in FIJI.
SNR was calculated to be 34.6.

Resolution standards to verify SHG imaging resolution are not commercially available. In place of a controlled standard, a collagen-rich biological sample (a porcine mitral valve) was imaged at a high spatial

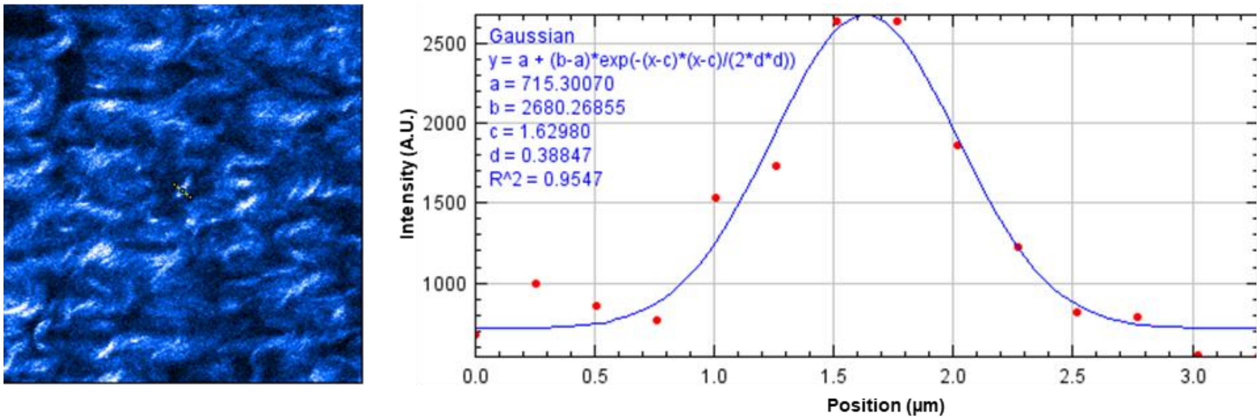

Figure 3.4: Sample Lateral Resolution Characterization for SHG imaging in a porcine mitral valve sample.
Gaussian fitting performed in FIJI**.**

sampling density (250 nm/px) and the finest resolvable fibrillar structures were measured as a proxy for lateral resolution. Sample images of mitral valve collagen are shown in **Figure 3.2D** and **Figure 3.8**. Example calculations of fibril diameter are show in **Figure 3.4**. Fibrillar collagen bundles and quaternary structure are clearly visualized. While fibrillar structures vary substantially in diameter (3), the resolving power of SHG on MANTIS () is well within our targeted resolution goals being able to resolve sub-micron spatial features.

The FLIR thermal camera resolution was estimated by identifying the smallest resolvable group on a 1951 United States Air Force resolution target (**Figure 3.2E**). Resolving group 6, element 4 equates to a lateral resolution of 6.9 µm. The depth of focus of the thermal camera is about 40 µm, based on an f/4.0 aperture stop of the objective lens in the thermal camera. Since the depth of focus of the thermal camera is substantially larger than the depth of focus of the nonlinear imaging system, registration of the focal planes axially was not an issue. The factory measured temperature resolution is specified to be 0.1°C. The nonlinear and thermal microscopy field view were independently adjusted to centrally registered the corner of a 10 µm grid target. Switching between thermal and nonlinear microscopy fields of view was found to repeatable within 1 µm radial to imaging turret rotation and 10 µm tangent to imaging turret rotation (**Figure 3.1A**, yellow arrows). Since field of view of the thermal camera is nearly four times that of the nonlinear microscopy field of view – making the coincidence of each modality's field of view with each other straight-forward (**Figure 3.5**). Once aligned, the fields of view were observed to remain well registered for more than a week following initial alignment. It takes about 90-180 seconds to switch between nonlinear and thermal imaging arms over the same sample. The sub-millimeter repeatability of positioning multiple imaging

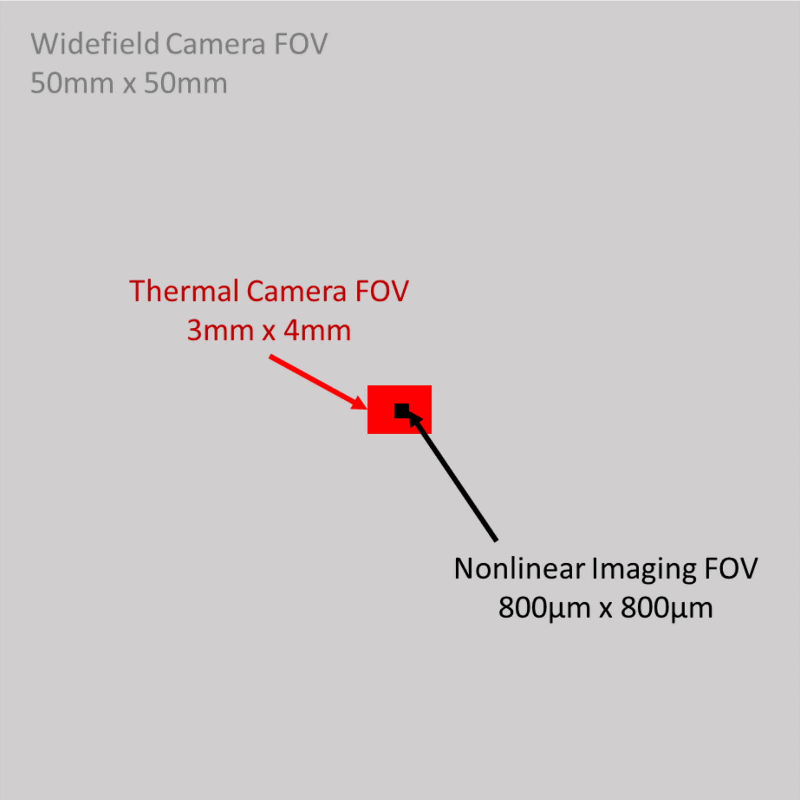

Figure 3.5: MANTIS Fields of View
To-scale representation of the overlap of multimodal imaging fields of view for the 3 imaging arms of MANTIS.

arms readily enables multiplexing of thermal and nonlinear microscopy on the same field of view without needing to reposition the sample.

3.5 *In vitro* Imaging

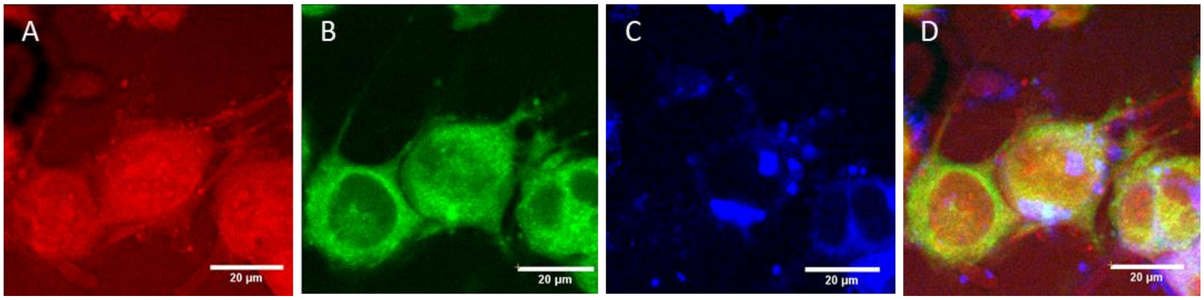

Figure 3.7: *in vitro* imaging capabilities of MANTIS
NG108 cells observed with CARS (A) at 2830cm^{-1}, a protein-dominant peak, NADH autofluorescence (B), FAD autofluorescence (C), and as a composite overlay of the three channels (D). Images were acquired separately and coregistered together with a rigid transformation.

To verify the capability of MANTIS to perform *in vitro* imaging, cultured NG108 cells – a spiking neuron-astrocytoma hybridoma cell line - were imaged with CARS and MPF, as seen in **Figure 3.7D**. Briefly, cells were plated on poly-D-lysine coated cover glass for 48hr prior to imaging and maintained in Dulbecco's Modified Eagle Medium (DMEM) supplemented with 10%v/v fetal bovine serum and 5mM L-glutamine. 12-hours prior to imaging, medium was replaced with DMEM containing 3%v/v FBS to morphologically differentiate adherent cells. Performing CARS imaging at 2830 cm^{-1} resonance highlights a lipid-dominant CH_2 symmetric

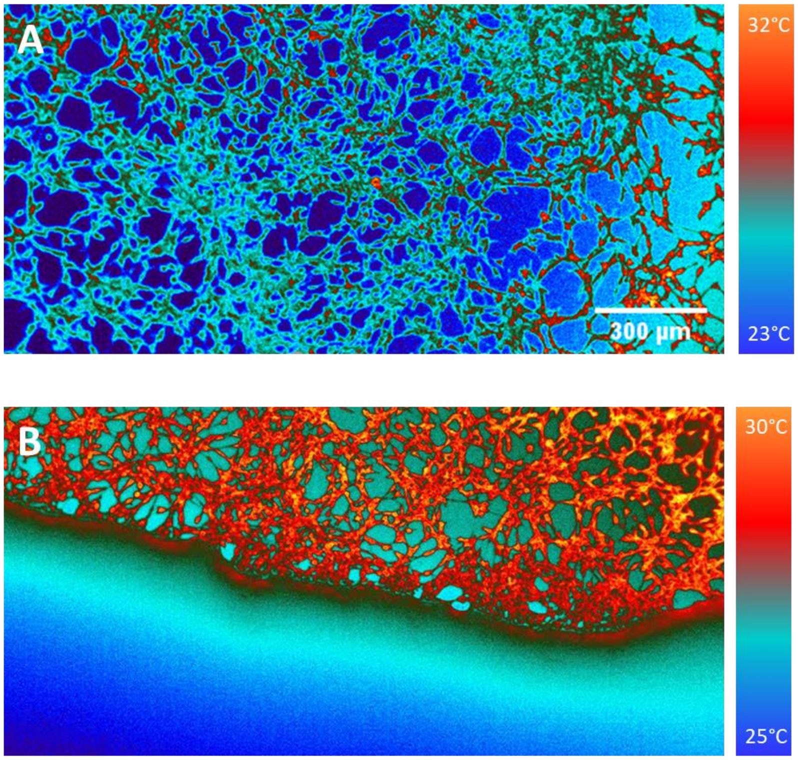

Figure 3.6: Thermal images of cultured 3T3 Fibroblasts.
A) Cells imaged without any aqueous medium. B) Image of aqueous medium front advancing over cells. The absorption of water in the short-wave infrared is high, making cell culture medium difficult to image through with blackbody thermal contrast.

stretch mode, which relates to cellular projections and lipid-rich intracellular contents such as organelles, lipid droplets, and vesicles (**Figure 3.7A**). Autofluorescence from NADH and FAD can be used to extrapolate metabolic information relating to relative aerobic metabolism dynamics and metabolic cofactor distribution throughout the cell, Together, combined CARS and MPF demonstrate the structural and functional capacities of multimodal nonlinear imaging *in vitro* (**Figure 3.7B&C**). Blackbody thermal imaging of cells in media in an upright configuration was not feasible due to the strong absorption of water in the wavelength range measured by the thermal camera (3 to 5-µm). Imaging with cellular resolution with thermal microscopy is possible in an upright configuration (**Figure 3.6A**), with the ability to resolve cellular temperature distribution. However, once medium is introduced to the imaging field of view (**Figure 3.6B**), cellular morphology is occluded due to strong water absorption of the sensed wavelength range. This has been addressed by others by utilizing inverted imaging configurations (17, 28, 29) , however resolvable cellular morphology were not demonstrated. Imaging of cells through glass coverslips is possible, however strong water absorption still occluded cellular morphology.

Combined SHG and MPF was demonstrated on fresh *ex vivo* porcine mitral valve samples (**Figure 3.8**). Tissue samples were harvested from porcine cardiac tissue postmortem and stored in phosphate buffered saline for 72hrs prior to imaging. Samples were mounted on a standard microscopy slide and imaged through leveled and supported cover glass in contact with the tissue surface. Simultaneous autofluorescence and SHG under 930 nm illumination with the femtosecond laser source yielded high resolution microstructure of endogenous elastin and collagen, free of exogenous labeling (30). Changes in

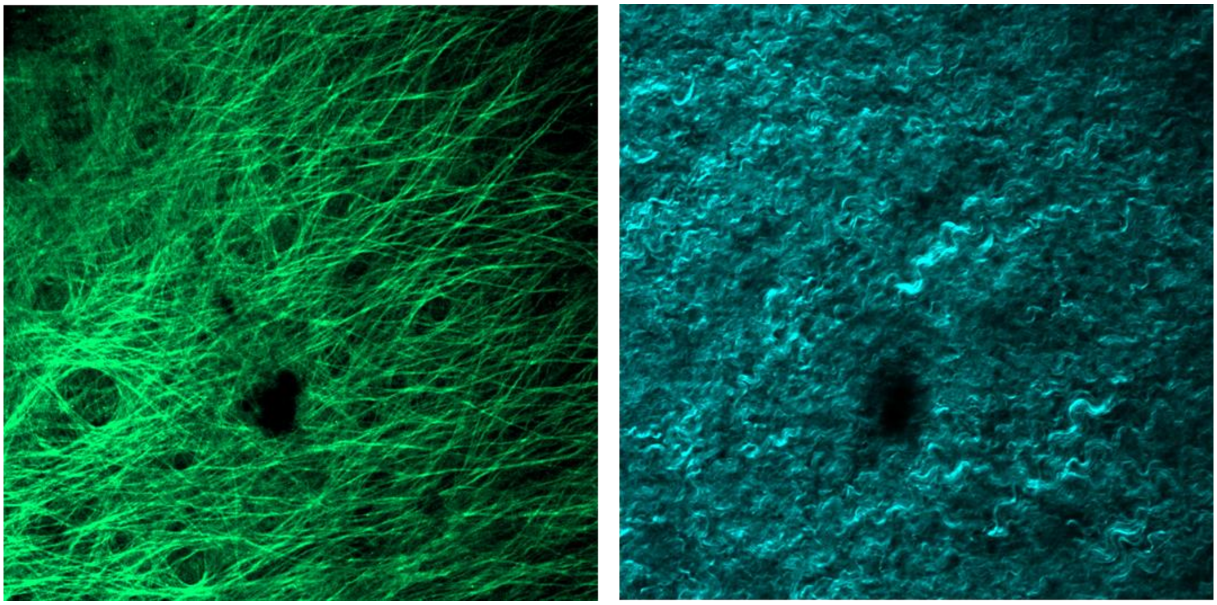

Figure 3.8: Porcine Mitral Valve Imaging
Endogenous autofluorescence from elastin (left) and collagen SHG (right). Image width is 520-µm.

collagen and elastin can dangerously disrupt the structure and function of heart valves (31). Having methods to study new interventions to improve heart valve function could be valuable to cardiac biomechanics researchers. Combining SHG with SRS at 2880 cm^{-1} to broadly highlight lipids allows for the visualization of tissue architecture in unfixed frozen sections of murine cervix (**Figure 3.9**). Distinct chemical and structural differences are notable between the epithelium and stroma of the cervix. The stroma is dense with collagen and low in cellular content, while the epithelium is rich in lipids and proteins due to cellularization. The lamina propria of blood vessels are also discernable with SHG, appearing as fine tubular structures with strong SHG signal, providing an indication of tissue vascularization. Visualizing the changes in vasculature, cellular, extracellular matrix protein distribution throughout cervix shows potential for studying parturition processes and cancer progression in the cervix without the need for exogenous labelling.

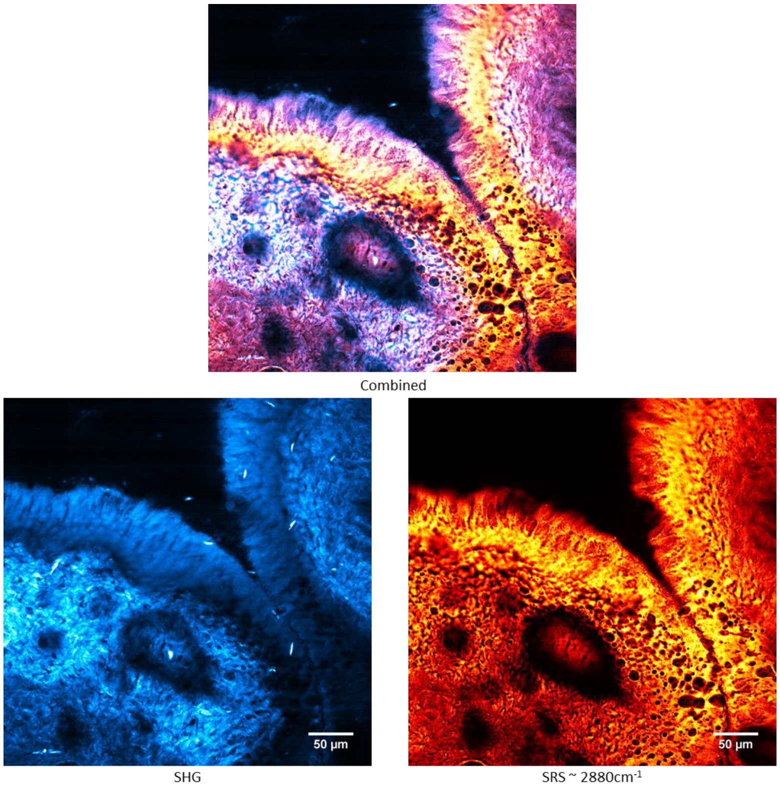

Figure 3.9: Murine Cervix Section Imaging

Simultaneous SHG (cyan) and SRS (2880-cm-1, lipid dominant resonance, orange) imaging of an unstained murine cervix unfixed frozen section. The stroma (dense in collagen) and epithelium are easily discernable based on relative concentrations on ratio of SHG and SRS signals. Blood vessels lamina propria are also visible with SHG contrast.

Figure 3.10, **Figure 3.11**, and **Figure 3.12** demonstrate multimodal nonlinear imaging with CARS, SRS, SHG, and MPF in an ex vivo rat sciatic nerve preparation. Nerves were harvested from Sprague-Dawley rats and imaged immediately postmortem. Contrast from CARS and SRS primarily highlights myelin (Figure B&C). The CARS and SRS images correspond well with the MPF images of FluoroMyelin green (ThermoFisher Inc | **Figure 3.11E**, **Figure 3.12C&D**) but are less prone to heterogeneous dye uptake. While myelin plays a major functional role in nerve signal conduction, collagen is a major structural component of the sciatic nerve that provides a protective exterior sheath and additional

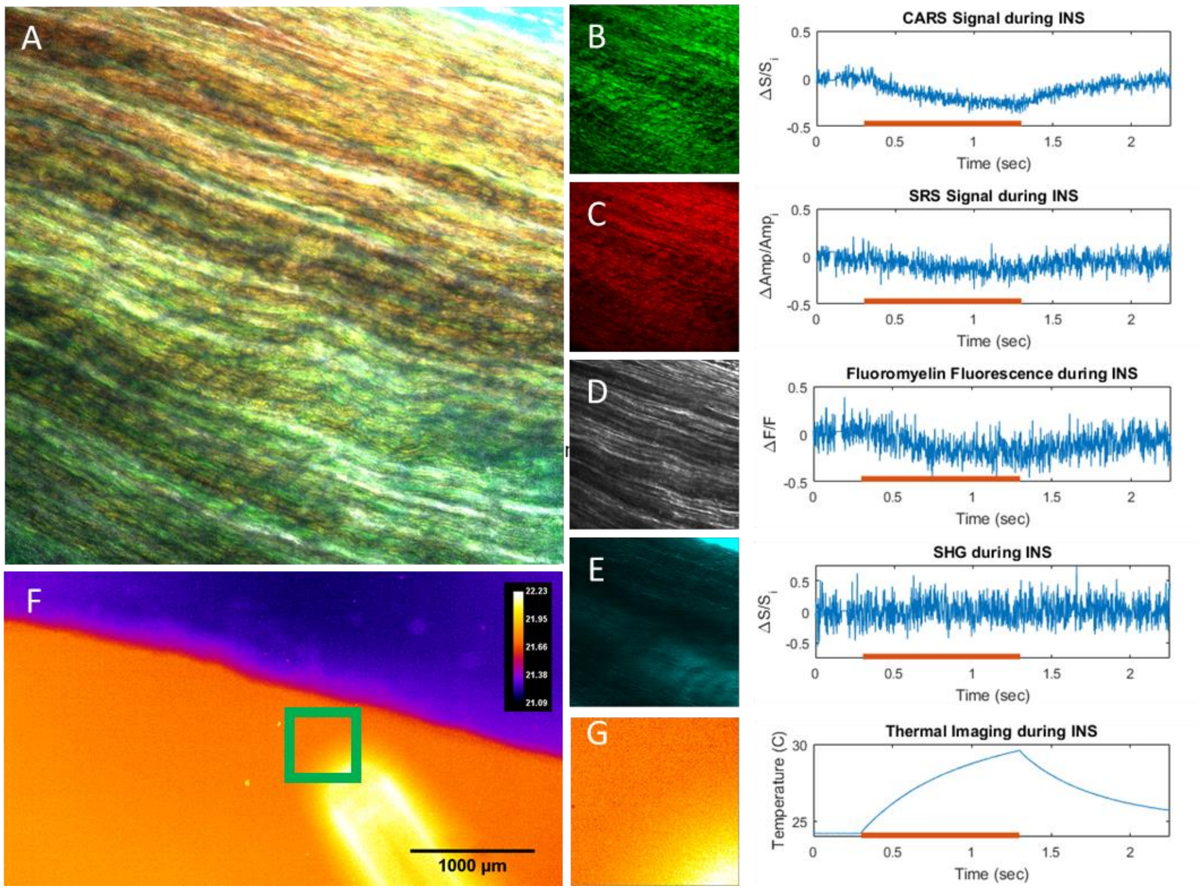

Figure 3.10: Ex vivo rat sciatic nerve samples imaged with high-speed multimodal nonlinear and thermal microscopy
A) Combined image of B-E. Images and corresponding high-speed line scans through the centers of the fields of view with B) CARS at 2880-cm^{-1}. C) SRS at 2880cm^{-1}, D) FluoroMyelin Green, E) SHG. Red lines on graphs indicate the exposure of the tissue to 1875nm light from an optical fiber. Light exposure causes a local temperature increase over 1 second (thermal images, F& G) yielding a corresponding decrease in nonlinear signals.

mechanical stability within the nerve. Collagen contrast from SHG can be used to visualize the epineurium and fascicle-residing collagen (**Figure 3.13**). These four modalities together therefore offer key structural insight to the sciatic nerve and can be used to study nerve injury, regeneration, and disease. Furthermore, the ability to flexibly apply these techniques to different sample types, between live cells and excised tissue specimen, highlights a key design goal of the imaging platform.

The key advancement allowed by the MANTIS platform is the ability to multiplex optically incompatible imaging techniques such as thermal imaging with nonlinear optical microscopy. Thermal imaging can be used to evaluate fast photothermal processes (**Figure 3.10F&G**), such as infrared neural stimulation (INS) (32, 33), with coregistered contrast from nonlinear imaging modalities to study real time

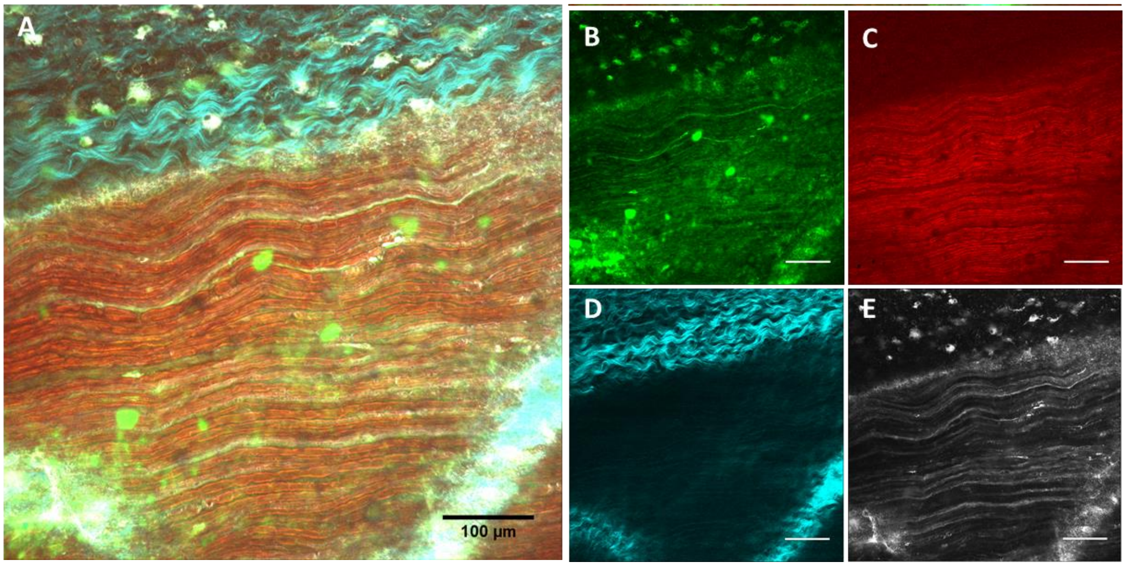

Figure 3.11: Rat Sciatic Nerve Imaging
Composite multimode image of an *ex vivo* rat sciatic nerve.(A) CARS signal at 2927cm-1 (B, green), SRS signal at 2927cm-1 (C, red), SHG signal (D, cyan), and multiphoton fluorescence of FluoroMyelin Green (E, Grey). All scale bars are 100um.

biophysical dynamics (**Figure 3.10A&F**). To assess the multimodal capabilities of MANTIS, readout of multimodal nonlinear contrast was directly correlated with high-speed temperature changes during infrared neural stimulation in a fresh *ex vivo* sciatic nerve preparation (**Figure 3.10**). Point-scanned line repeats through the center of the images fields of view were employed to obtain high speed (488 Hz) nonlinear signals during IR stimulation. Average intensities across the entire acquired line scan at each timepoint are reported for each modality. Reported temperature data is a the average temperature of the entire FOV denoted in **Figure 3.10G** acquired at 180 Hz. Intriguingly, our results show a notable decrease in nonlinear signals from CARS (**Figure 3.10B**), SRS (**Figure 3.10C**), and MPF (**Figure 3.10D**) that tracks closely with temperature increases (**Figure 3.10G**) over the period of one second. Notably, SHG signals (**Figure 3.10E**) did not exhibit a discernable decrease in signal, which is attributable to the lack of collagen present through where line scans were acquired (center of the field of view, **Figure 3.10**). However, decreases in SHG signal during IR stimulation have been verified in other FOVs, suggesting this signal decrease is a more general physical phenomenon. Decreases in nonlinear signal were found to be caused by a defocusing artifact induced by the spatial thermal gradient inherent to infrared neural stimulation in the microscope’s field of view. Resolving photothermal effects of IR heating in biological tissues at high speed, such as during INS, will provide invaluable information in studying *in vivo* applications of INS.

3.6 *In vivo* Imaging

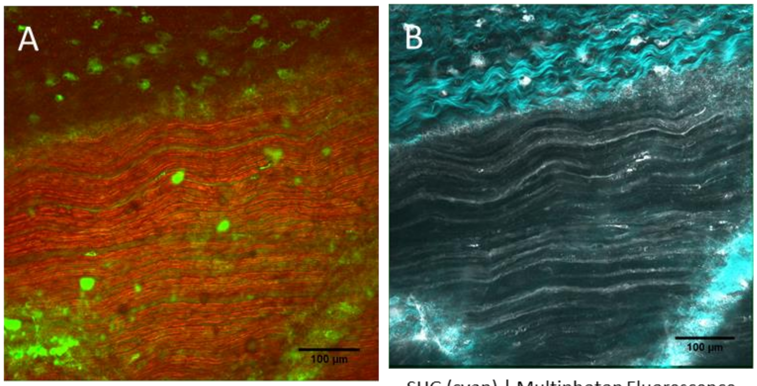

CARS (green) |SRS at 2927-cm^{-1} (red)

SHG (cyan) | Multiphoton Fluorescence of FluoroMyelin Green (grey)

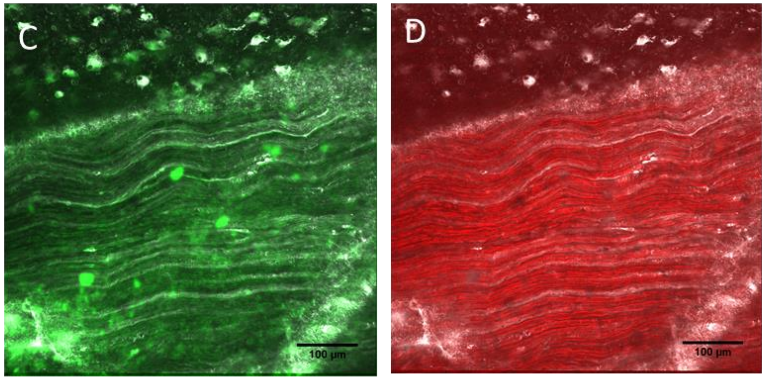

CARS at 2927-cm^{-1} (green) | Multiphoton Fluorescence of FluoroMyelin Green (grey)

SRS at 2927-cm^{-1} (red) | Multiphoton Fluorescence of FluoroMyelin Green (grey)

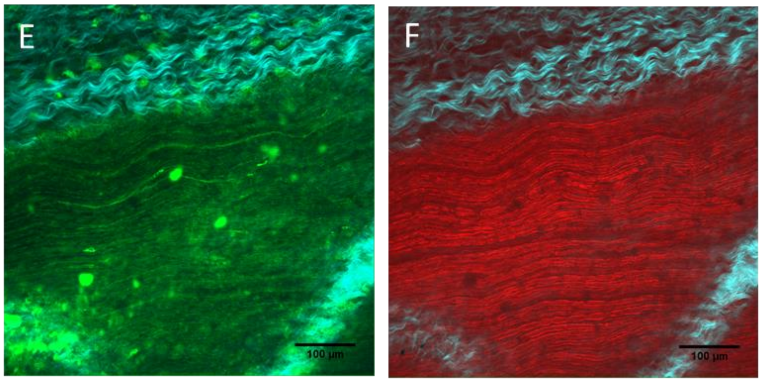

CARS at 2927-cm^{-1} (greed) |.SHG (cyan)

SRS at 2927-cm^{-1} (red) | SHG (cyan)

Figure 3.12: Rat Sciatic Nerve Multimode Composites

Ex vivo rat sciatic nerve samples imaged with multimodal nonlinear imaging from Figure 3.11. Two different modalities can be combined in different ways to visualize tissue structure.

All protocols using live animals were performed in accordance with and are approved by Vanderbilt University Institute for Animal Care and Use Committee (VU-IACUC, Protocol M1600084). All protocols using live animals were performed in accordance with ARRIVE guidelines for animal use. An acute craniotomy preparation in an anesthetized rat model was utilized to validate the *in vivo* capabilities of MANTIS. Sprague-Dawley rats were anesthetized with intraperitoneal injections of ketamine (40-80

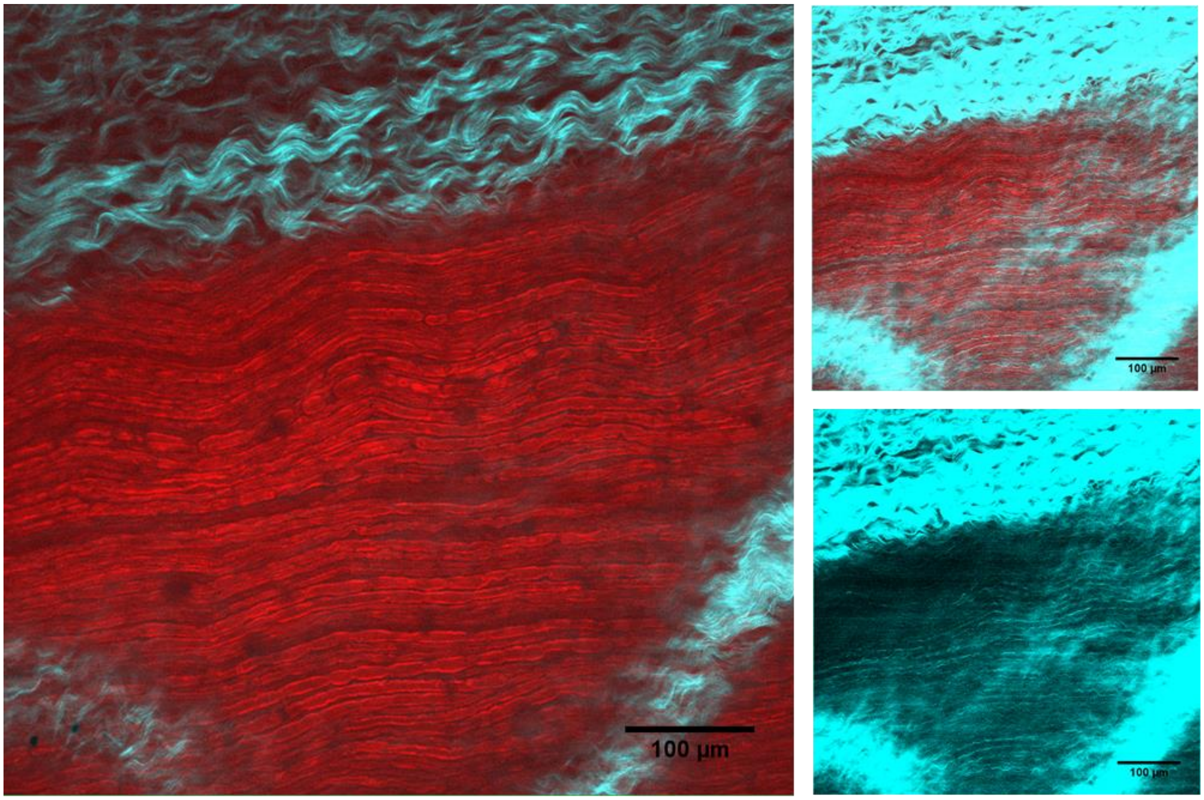

SRS at 2927cm^{-1} vs. SHG

SHG contrast adjusted to show intrafasicular collagen structures

Figure 3.13: Sciatic Nerve Collagen

Ex vivo rat sciatic nerve samples imaged with SRS (red, myelin at 2927cm-1) and SHG (cyan, collagen). Rescaled SHG images are shown to highlight intrafasicular collagen, which is in lower abundance and overall signal then epineurial collagen.

mg/kg) and xylazine (10 mg/kg) for 40 minutes prior to surgery. Anesthetic depth was monitored every 10 minutes and maintained with follow-up half-dose anesthetic injections every 90-120 minutes as needed. Animals were mounted in a stereotaxic frame under the microscope objective while a 2 mm-x-2 mm section of skull and dura mater overlying the somatosensory cortex was carefully removed. Tissue hydration was maintained with sterile saline throughout imaging. Animals were sacrificed by anesthetic overdose and cervical dislocation following experiments. During imaging experiments, pixel dwell times needed to be increased to 8 µs to account for signal loss in moving the SRS detection path into an epi-detection configuration. Epi-SRS detection was implemented by replacing the dichroic mirror immediately preceding to the objective in the incident light path with a polarizing beam splitter cube and quarter wave plate (23). Images were initially acquired at a high spatial sampling density (0.5 µm/px, 800x800 px) with a 0.2 Hz framerate. However, by reducing the spatial sampling density and overall image sizes (3 µm/px, 256x256 px) over a comparable field of view, we were able to achieve 2 Hz framerates. Subsequently, repeated

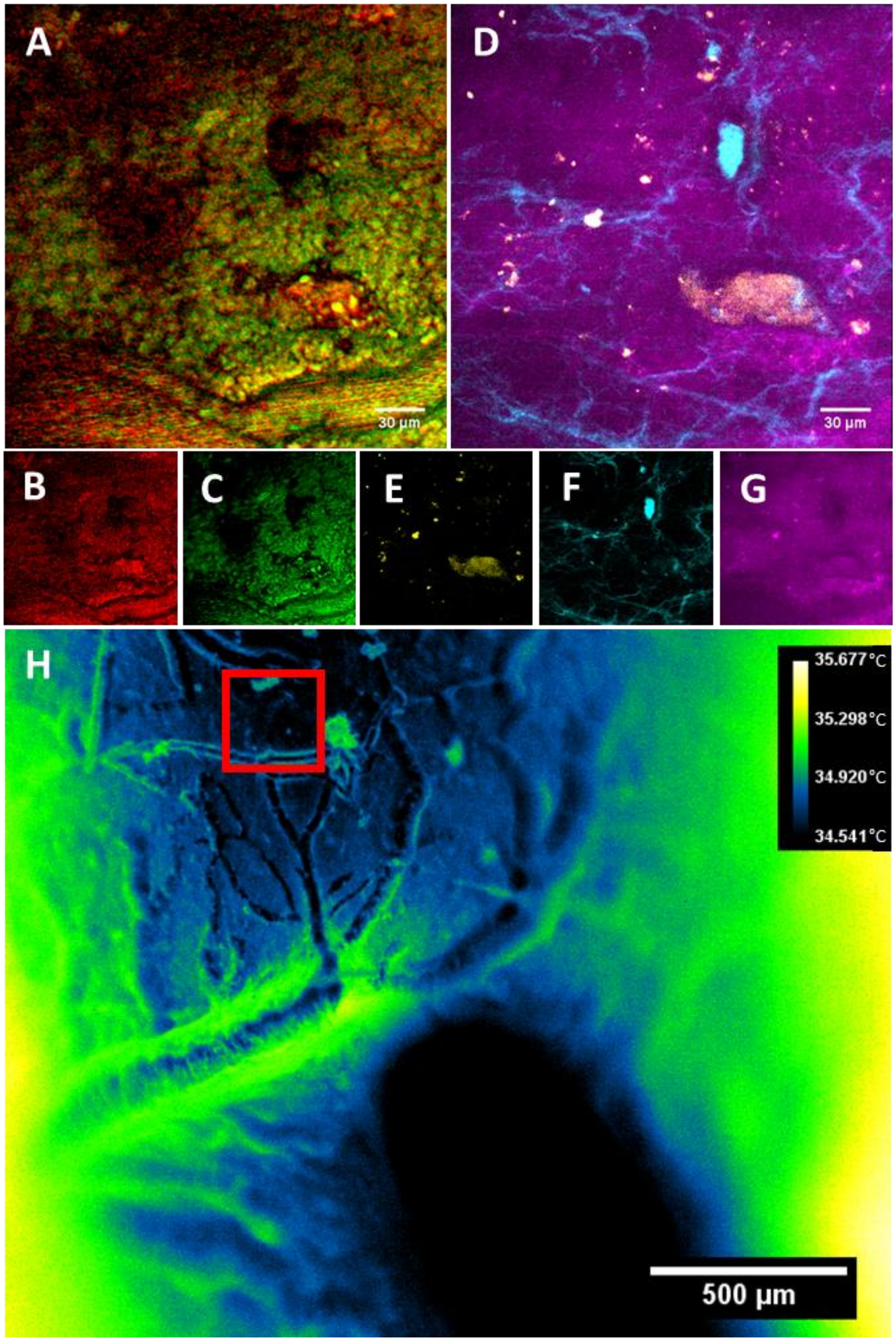

Figure 3.14: Multimodal images from a rat brain in vivo.
A) Composite image of B (SRS, 2930cm^{-1}) and C (CARS, 2850cm^{-1}) highlighting lipid and protein-dominated signals, respectively. D) Composite image of the same field of view in A of E (Green autofluorescence), F (SHG signal), and G (Blue autofluorescence, likely NADH). (H) Thermal images of the brain surface, temperatures shown in °C.

dynamics. This flexibility emphasizes the trade-offs between spatial and temporal sampling in nonlinear microscopy approaches *in vivo*. Acquiring images using CARS, MPF, or SHG needed to be performed sequentially, due to the availability of only one PMT detector at the time of experiments. However, any one of the three PMT-requiring modalities can be multiplexed with SRS contrast, since SRS uses a separate detector in an adjacent detection path. Excitation and detection wavelengths are summarized in Table A1.

Examples of *in vivo* images can be seen in **Figure 3.14**. A protein-dominant SRS resonance at 2930 cm^{-1} (**Figure 3.14B**) and a lipid-rich CARS resonance at 2850 cm^{-1} (**Figure 3.14C**) and appears to highlight superficial cellular features as well as vascular perfusion within blood vessels. Autofluorescence contrast from blue and green detection channels are most commonly used to measure endogenous NADH (**Figure 3.14D&G**, **Table A1**) and FAD **(Figure 3.14D&E**, **Table A1**). This diffuse NADH signal is likely arising from the neuropil at the pial surface of the cortex, while FAD tends to present more sparsely superficially in the outer cortex *in vivo*; this weak fluorescence is often spectrally indistinct from other biological autofluorescence (34, 35). Contrast from SHG (**Figure 3.14F**) revealed unknown morphologies, which may be due to cytoskeletal structures across the pial surface, but is more likely to be residual collagen from the dura mater after surgical preparation. Thermal imaging (**Figure 3.14H**) of the brain surface appears to reveal mostly topographical contrast - vasculature is clearly visible. The lack of optical penetration depth of measured wavelengths of the thermal camera are likely responsible for the brain surface topographical contrast. Temperature fluctuations across the surface of the brain appear to be minimal, even with breathing, heart rate, and motion artifacts. Larger vessels appear slightly warmer than smaller vessels. Focusing artifacts appeared to have some effect on the accurate approximation of the brain surface temperature within 1°C – particularly noticeable at the edges of the field of view, which likely arise from out of focus signal from underlying bulk tissue due to the high degree of surface curvature in the sample (**Figure 3.14H**). Cellular morphologies were not apparent in thermal images of the brain surface. Thermal imaging of the brain surface was capable of acquisition speeds approaching 180 Hz framerates with a full field of view. This imaging rate can be substantially increased to 500 Hz or more by cropping the image sensor readout without loss in spatial resolution or pixel binning without reduction in field of view. The vessel morphologies visible between thermal and CARS/SRS contrast made fine registration of thermal and nonlinear imaging fields straightforward with rigid registration of manually labelled image features.

3.7 Fast Multimodal Nonlinear and Thermal Microscopy of Photothermal Cell Damage

Infrared neural stimulation utilizes pulsed short-wave infrared laser light to transiently invoke a thermal gradient in neural tissue resulting in activation of neural cells. One of the major concerns about neuromodulation with rapid targeted thermal gradients is that the change in temperature could cause cell or

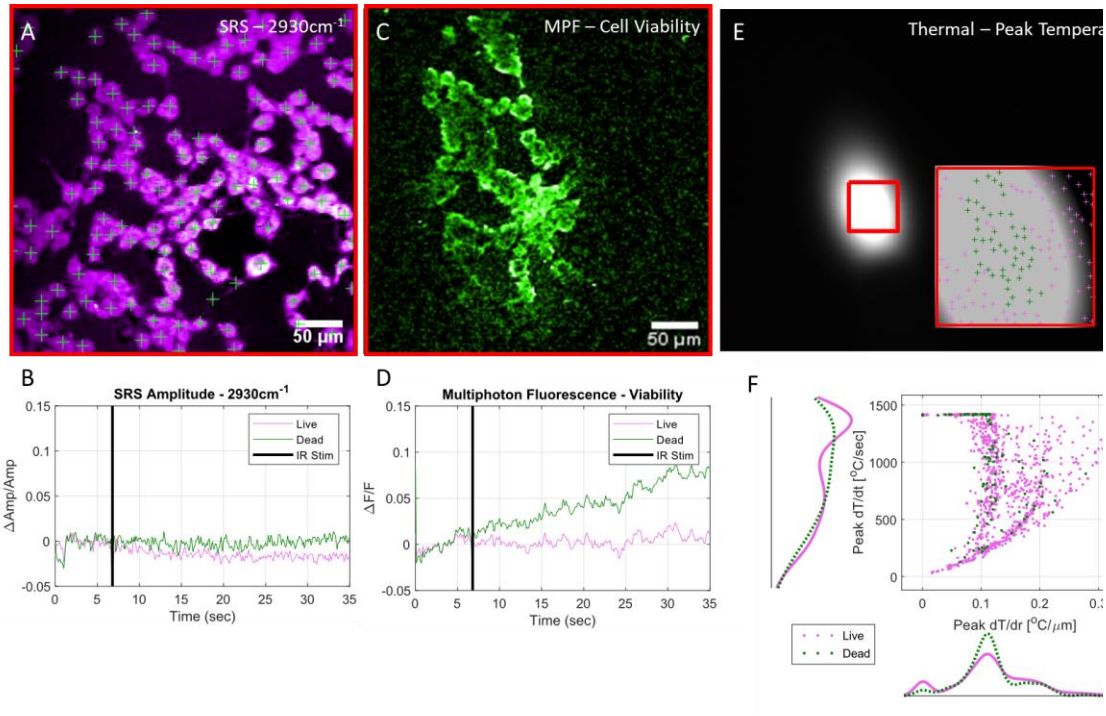

Figure 3.15: Fast Multimodal Nonlinear and Thermal Microscopy of NG108 cells during in infrared neural stimulation

Examples of an A) SRS average intensity projection image of cells with indicated centroids and (B) pooled average SRS timeseries of live (magenta) and damaged (green) cells during IR stimulation across all observed cells. (C) Example of a normalized sum intensity projection of cell viability image timeseries used to indicate cell viability via uptake and fluorescence of propidium iodide. (D) Average pooled MPF timeseries of all observed live and damaged cells during INS. Increases in MPF signal after INS above 3% dF/F over 30 seconds were considered damaged/dead. (E) Thermal images of NG108 sample preparation during peak temperatures of INS. Registration of thermal and nonlinear fields of view (E, inset) allows for precise spatial temperature mapping. Cellular details are not observable due to strong absorption by the aqueous imaging medium. Coupled with high-speed thermal imaging, (F) high resolution temporal and spatial thermal observations can be directly correlated with functional cellular outcomes such as cell viability. Data shows results of 10 different experiments including 3 different INS intensity conditions, n = 1144 cells.

tissue damage. Generally, damage from IR exposure is verified with histology, immunohistochemistry, or staining with cell damage indicators well after exposure, introducing notable lag times to results. Cells are naturally prone to damage at elevated temperatures; however, the role of temperature-time history is often underappreciated in the context of biological thermodynamics. Integrating fast nonlinear and thermal microscopy offers a particularly useful platform for studying the physical and functional impacts of INS on neural cell in the context of cell activation or damage in real time.

The ability to correlate high resolution temporal and spatial thermal information (**Figure 3.15E&F**) with the functional information afforded by nonlinear imaging (**Figure 3.15A-D**), available in the MANTIS platform offers a unique opportunity to visualize biochemical, biophysical, and biomolecular dynamics of cultured NG108 cells during INS. An 8 ms pulse of 1875 nm infrared light was delivered to the cells via a 400 µm diameter optical fiber at average radiant exposures spanning 0.5 (stimulating) and 3 J/cm^2 (damaging) while imaging at 10 Hz framerates. Multiphoton fluorescence of cells imaged in saline containing a damage indicator, propidium iodide (PI, 1uM concentration, Fig. 6C, Table A1), differentiated healthy and damaged cells due to IR exposure. Increases in relative fluorescence greater than 3% were presumed to be indicative of cell damage. Simultaneously, SRS imaging at a CH_3 resonance (2930 cm^{-1}, lipid/protein) provides endogenous biochemical information of cells during INS. In this study, SRS images were primarily used to segment cell morphologies to extract viability status (MPF) and interpolate thermodynamics (thermal imaging). Since the stimulating IR light (1875nm) is strongly absorbed by water, the immersion medium required for nonlinear imaging had a substantial impact on the heating of cells, leading to potentially large discrepancies in thermal imaging measurements. To minimize optical absorption of 1875nm stimulation light by the aqueous immersion medium necessary for the nonlinear microscopy objective (Olympus XLUMPLNFL 20X, 1.0NA), spectroscopic-grade deuterated water (Sigma Aldrich, St. Louis, MO, USA) was used as an immersion medium (33). Cells remained immersed in normal imaging media and were separated from heavy water by the coverslip on which the cells were mounted. The reduction in IR absorption in the objective lens immersion media was enough to allow for representative spatial thermal measurements of INS on aqueous cellular samples with the thermal camera. Functional observations of cell death aligned well with peak spatial temperature maps (**Figure 3.15E**, inset). It is expected that absolute temperature measurements at the sample are likely to differ with and without the presence of deuterated immersion medium during INS, however the spatial and temporal dynamics of IR-induced cellular thermal gradients are expected to remain consistent and comparable across all exposure conditions. With this assumption, physiological comparisons can be effectively drawn with the understanding that the observed absolute temperatures are likely slightly higher than during nonlinear image experiments where immersion medium may impact INS.

Thermal images during INS were acquired at 34 Hz framerates after all nonlinear imaging and stimulation experiments were completed. Temperature information is not simultaneously available with nonlinear observations due to physical limitations. Since the thermal properties of cells mounted in imaging saline behave thermodynamically like water upon INS, cell position data was registered to thermal imaging videos acquired after IR stimulation experiments while holding the stimulation geometry constant. Based on alignment against a fluorescent target performed immediately before cell imaging experiments, the translation matrix needed to register nonlinear spatial coordinate to thermal spatial coordinates was applied to cell centroid positions and used to obtain spatial thermodynamic information for each cell. Registration was performed with an iterative closest point algorithm implemented in MATLAB to register manually selected features of a fluorescent target (Chroma, Rochester, NY, USA) observable in both nonlinear and thermal imaging modes. Cell centroids were calculated from cell morphologies identified with SRS (**Figure 3.15A**) in Fiji utilizing a seeded watershed segmentation algorithm (24, 36). Cell positions coordinates in the thermal camera field of view were used to interpolate temperature-time and temperature-space thermal data on a per-cell basis using built-in 2D interpolation functions in MATLAB.

Since the stimulating IR light (1875 nm) is strongly absorbed by water, the immersion medium required for nonlinear imaging had a substantial impact on the heating of cells, leading to potentially large discrepancies in thermal imaging measurements. To minimize optical absorption of 1875 nm stimulation light by the aqueous immersion medium necessary for the nonlinear microscopy objective (Olympus XLUMPLNFL 20X, 1.0NA), spectroscopic-grade deuterated water (Sigma Aldrich, St. Louis, MO, USA) was used as an immersion medium (33). Cells remained immersed in normal imaging media and were separated from heavy water by the coverslip on which the cells were mounted. The reduction in IR absorption in the objective lens immersion media was enough to allow for representative spatial thermal measurements of INS on aqueous cellular samples with the thermal camera. Functional observations of cell death aligned well with peak spatial temperature maps (**Figure 3.15E**, inset). It is expected that absolute temperature measurements at the sample are likely to differ with and without the presence of deuterated immersion medium during INS, however the spatial and temporal dynamics of IR-induced cellular thermal gradients are expected to remain consistent and comparable across all exposure conditions. With this assumption, physiological comparisons can be effectively drawn with the understanding that the observed absolute temperatures are likely slightly higher than during nonlinear image experiments where immersion medium may impact INS.

Spatially registered observations of cell functional, chemical, and temperature dynamics is only made possible by a combined and accurately coregistered nonlinear and thermal imaging platform such as the MANTIS platform. From these multimodal imaging experiments, we observed that cells that experience more rapid changes in temperatures as a function of time were more likely to be damaged (**Figure 3.15E&F**). Damaged cells are more likely to be located near low spatial thermal gradient values, which correspond to local maxima in spatial heating profiles (Fig. 6E, inset). However, cells outside the fiber illumination would be expected to present similar spatial thermal gradients as cells at peak levels of heating - introducing some heterogeneity in the spatial thermal gradient information. Considering spatial and temporal thermal gradient information together clarifies the thermodynamic difference between heated and unheated cells. Numerous cells appear to survive rapid temperature changes while others do not, however damaged cells are far more likely to undergo rapid heating. This observation demonstrates the variability in cell physiological responses due to INS. Distinct increases in mean multiphoton fluorescence timeseries indicate cell damage within 30 seconds of IR exposure. Cell damage appears to coincide with stable mean SRS CH_3 amplitude following IR stimulation, while live cells present a decrease in 2930 cm^{-1} SRS amplitude. The basis for SRS signal increase is currently unclear, though we speculate attribution to a balance between cell swelling and morphological changes triggered by cell damage. Currently, there remains to be extensive validation of changes in endogenous SRS signal in the context of live cell imaging and damage beyond lipid storage and cell membrane dynamics. Experimentally, SRS images were primarily used in **Figure 3.15** to identify, segment, and locate cells for temperature and viability data calculations. However, this platform readily enables such explorations into the molecular basis of SRS signal changes simultaneously with commonly used live cell fluorescence imaging probes.

3.8 Discussion

We demonstrate the first imaging system that combines CARS, SRS, MPF, SHG, and thermal imaging into a single microscope for biomedical imaging applications. The similarities in illumination and detection instrumentation needed for nonlinear excitation has been exploited in the past to design multimodal imaging platforms. But as demonstrated here, our novel system design includes a movable turret that allows for overlaying these different modalities to achieve a more complete picture of biological processes to be imaged. This logically suggests that another imaging modality that typically could not be integrated into a nonlinear optical microscopy path may be similarly incorporated. Such flexibility of optical microscopy design provides the opportunity to study physiology in unique and dynamic ways.

The proposed imaging system, MANTIS, was built with modularity and expandability in mind. On the nonlinear imaging arm, the current configuration has four optional detection ports - two each in the epi- and forward detection configurations. Additional channels can easily be added to expand simultaneous imaging capabilities based on research needs. Lock-in detection arms can be refitted with the appropriate optical filters for transient absorption imaging. Sum-frequency generation imaging can also be readily integrated for studying ordered molecular orientation and interfacial phenomena in biological samples. The widefield reflectance imaging arm may be useful for integrating laser speckle, diffuse reflectance, optical coherence tomography and microscopy, or spatial frequency domain imaging with the correct illumination optics to map tissue blood flow, oxygenation, and optical properties. Furthermore, the widefield reflectance and thermal imaging arms were built on detachable 96-mm optical rails so that other imaging methods may be integrated based on future research needs. The multi-armed imaging concept can also yield more utility out of a condensed instrument footprint, which may be useful in places where laboratory floorspace is limited.

The scanning optics used in nonlinear imaging arm can achieve 1 kHz scan rates. A galvo-scanning pair was chosen over a faster galvo-resonant scanning pair, which typically offer an order of magnitude increase in scanning rates. By doing so, improved control over image sampling densities can be achieved to readily span subcellular and multicellular scales. This is exemplified by the difference in sampling density observed between **Figure 3.7** and **Figure 3.14**. As demonstrated in **Figure 3.10**, our imaging system can perform nonlinear imaging with line scans approaching 0.5 kHz with detectable amounts of signal. This is enough to resolve high-speed biophysical dynamics, such as during neural modulation or optogenetic stimulation, from a functional, chemical, and physical standpoint. Kilohertz bandwidth scanning rates are sufficient to achieve visualization of neuronal action potentials as demonstrated by Lee *et al.* with balanced detection SRS and calcium fluorescence microscopy (9).

Both femtosecond and picosecond lasers were included in the design of MANTIS for signal and spectral resolution considerations. The bandwidth of the picosecond laser source (around 0.5 nm) allows for higher spectral resolutions (around 10 cm^{-1}) which is critical for nonlinear Raman imaging (37). However, the peak powers of the picosecond source are orders of magnitude lower than that of the femtosecond laser, yielding less signal during multiphoton fluorescence and higher harmonic imaging. At the time of construction, the use of broadband nonlinear Raman techniques, such as pulse shaping and spectral focusing had yet to be realized for fast imaging *in vivo* (38). As such, design considerations to optimize narrow band spectral resolution and *in vivo* imaging speed were a priority. A number of broadband spectral NRI techniques have since been described (39, 40), with a handful demonstrated *in vivo* (10). The flexibility of the existing instrumentation on MANTIS readily allows for the integration such broadband approaches.

Using blackbody thermal microscopy to characterize sample temperatures in conjunction with nonlinear imaging, or any laser-scanning microscopy approach, has yet to be previously published. Estimating temperature with a thermal camera provides a more direct measurement than other approaches, such as fluorescence-based methods. The ability to measure thermal information alongside the functional and structural information offered by nonlinear microscopy provides a unique instrument to explore new questions in biophysics, particularly *ex vivo* and *in vivo*. Practically, thermal microscopy presents some advantages and drawbacks depending on the model systems being imaged. We have found that high resolution fluorescence microscopy can be difficult to interpret in highly thermally dynamic systems with high numerical apertures at high imaging speeds, which became apparent in applying infrared neural stimulation in sciatic nerve (**Figure 3.10**) as well as in cells. Having thermal information to contrast and systematically compensate for thermally induced effects is something that our imaging platform lends itself to accomplish. Since imaging depth with thermal microscopy is limited due to the optical penetration depth of water in the 3-5 µm wavelength spectral regime, this means that SWIR based imaging methods are ideally suited for measuring surface temperatures in water-dominant samples such as biological tissues. This is even more apparent *in vitro,* where imaging through any amount of aqueous medium occludes cellular morphology (**Figure 3.6**). While others have demonstrated blackbody thermal imaging of cells via inverted microscopy through cover glass (17, 18), visualizing cell morphology with thermal imaging has not been previously demonstrated - our observations support the previous work. Thermal microscopy on MANTIS can be performed readily and reliably on tissues *ex vivo* (**Figure 3.10F**) and *in vivo* (**Figure 3.14H**). Topographical features such as blood vessels tissue surfaces are clearly visible in the brain. The pronounced topography of these anatomical features can be helpful when performing fine registration nonlinear and thermal imaging fields. However in tissue samples with limited visibility of morphology (e.g. **Figure 3.10F**) thermal imaging is limited to providing purely temperature information. Temperature at aqueous interfaces are useful in approximating spatial temperature distributions *in vitro*. Combining surface temperatures with finite element heat transfer modeling and precise control over sample thermodynamics can be used to render volumetric estimates of temperature *in vitro* (18). In combination with fluorescence or other nonlinear imaging modalities, imaging the thermodynamics of adherent cells *in vitro* or in tissues with thermal microscopy could be quite useful. Consequently, multimodal methods almost become an essential requirement to correlate temperature and real-time cellular observations. Our microscopy platform readily allows such observation to be made and flexibly configured to address a wide range of biological and physiological questions.

As expected, cell viability at elevated temporal thermal gradients values is more likely to result in cell death than at lower gradient values (**Figure 3.15F**, axes histograms). However, as evident by the overlap in cell viability as a function of thermodynamics in **Figure 3.15F**, peak thermal gradients are not absolutely predictive (Figure 3.15**F**, scatter plot). While cells heated quickly are more likely to become damaged, rapid heating is not necessarily a death sentence for cells. The variability in thermally evoked cell damage illustrates the need for tools to study underlying functional and biomolecular dynamics evoked by IR light on a cell-to-cell basis. Exposure time and time after exposure becomes a crucial dimension of cellular physiology to explore in the context of infrared neural stimulation. Endogenous lipid/protein SRS signals are stable (**Figure 3.15A&B**) and a fluorescence marker for cell damage (**Figure 3.15C&D**) increases following damaging levels of INS. Intriguingly, live cells show a decrease in SRS amplitude and stable fluorescence intensities. Cell swelling could cause CH_3 related SRS amplitudes to decrease to the increase in cell volume, though the reasoning for this observation is unclear. Regardless, the unique ability to correlate temperature, cell function, and cell biochemistry together shows that this imaging platform can be a powerful research tool in certain research applications. Having temperature information to correlate directly with cell physiology or damage allows for more detailed characterization of safety and damage levels for INS applications. Registration of thermal and nonlinear imaging fields within a couple of microns is key to enable direct correlation of temperature-time dynamics with cell functionality since cells are not readily visible with thermal imaging.

To practically extend this imaging platform, cell viability markers like that shown in Figure 6 can readily be substituted for calcium sensors, voltage probes, FRET constructs, or gene transcription assays. Using hyperspectral or bio-orthogonal SRS alongslide functional contrast, it is possible to correlate endogenous contrast metrics with functional information to improve optical tools in studying cellular physiology. SRS often provides relatively nonspecific biomolecular information relative to fluorescence imaging strategies; combining functional fluorescence and SRS imaging during INS can expand the current understanding of the impact of cellular physiological dynamics on SRS signals. Similar approaches can be used to understand the effects of rapid temperature changes on more specific aspects of cellular physiology to improve our general understanding of the impact of thermodynamics on cells. Such multidimensional data set can make further use of multivariate statistics and machine learning based analyses to integrate and observe the interplay of biochemical, biomolecular, and biophysical dynamics in unprecedented ways.

Beyond INS, similar approaches as demonstrated in **Figure 3.15** may readily be adapted to study laser tissue interactions associated with optogenetic or nanoplasmonic neuromodulation, laser preconditioning of immunological response, or photodynamic therapy of infectious or cancerous model systems where temperature changes may be involved. These types of experiments are enabled only by an imaging platform that integrates nonlinear and thermal microscopy with high enough spatial and temporal resolution capabilities to study the processes at hand. While neuroscientific questions provide a valuable benchmark in terms of evaluating imaging speed, this platform is just as applicable to other areas of biomedical research.

Undoubtedly, an imaging platform that simultaneously integrates thermal and nonlinear imaging would be practically important in answering many questions in the aforementioned disciplines. It becomes technically difficult to accommodate the disparity in optical detection wavelengths for use in a broad range of cellular, tissue, and live animal preparations. Tradeoffs between sample flexibility and optical access were major considerations in the imaging system's three-armed design. Inherent hardware limitations prevent the design a truly simultaneous multimodal nonlinear and thermal imaging system. Nonetheless, the MANTIS platform offers a novel approach to creatively answer fundamental and translationally relevant questions about biology and thermodynamics which are applicable broadly to biomedical research.

3.9 Conclusion

We present a novel and flexible multimodal optical imaging system that combines nonlinear and thermal microscopies for biomedical imaging applications. Our platform can be used to overlay functional, structural, and biochemical information from a single specimen tracked over time at high speed and spatial resolution. Such approaches can be applied to study dynamic biophysical processes in cells and tissues, in vitro and in vivo. In conjunction with continually expanding molecular biology tools, this instrument and related imaging methods will aid in studying physiological and biochemical processes from multiple perspectives in many fields including neuroscience, cancer biology, metabolic disease, tissue biomechanics, and much more.

3.10 Funding

Funding for this work was provided by the following grants: AFOSR DURIP FA9550-15-1-0328, AFOSR FA9550-14-1-0303, AFOSR FA 9550-17-1-0374. WRA was supported through the ASEE NDSEG Fellowship.

3.11 Acknowledgements

The authors would also like to thank Dr. Bryan Millis, Dr. Christine O'Brien, and Dr. Andrea Locke for their feedback and guidance on the manuscript. The authors would also like to thank Dr. Matthew Bersi, Joshua Bender, and Dr. W David Merryman for providing the porcine mitral valve samples.

3.12 Author Contributions

AMJ, EDJ, and JB conceived the idea for the manuscript. WRA, BM, EL, SP, JB and AMJ designed, and built the imaging system. AMJ and EDJ secured funding support for the published work. MW performed *in vivo* surgical preparations and assisted in imaging. RG, GT, JLJ, and JBF provided samples and experimental guidance imaging tissue samples. WRA assisted in all sample preparations, performed all imaging experiments, image processing, data analysis, and prepared the manuscript. All authors contributed to editing manuscript.

3.13 Data Access

Any raw data and processing scripts are readily available from the corresponding authors upon request.

3.14 Conflicts of Interest Statement

BM, EL, SP, and JB are employees of Thorlabs Imaging Research, LLC. The remaining authors report no additional conflicts of interest.

3.15 Additional Data

Table 3.3: Detailed summary of point spread function calculations for nonlinear imaging modalities.

		CARS				
					Mean	STD
x	0.646	0.615	0.636	**x**	**0.6323**	0.0158
y	0.773	0.69	0.772	**y**	**0.7450**	0.0476
z	2.758	3.282	2.986	**z**	**3.0087**	0.2627
		SRS				
x	0.849	0.743	0.906	**x**	**0.8327**	0.0827
y	0.896	0.793	0.86	**y**	**0.8497**	0.0523
z	3.36	2.813	3.235	**z**	**3.1360**	0.2866
		MPF				
x	0.379	0.272	0.426	**x**	**0.3590**	0.0789
y	0.286	0.413	0.377	**y**	**0.3587**	0.0655
z	1.473	1.432	1.601	**z**	**1.5020**	0.0882
		SHG				
L	0.388	0.383	0.433	**L**	**0.4013**	0.0275

3.16 References

1. Yue, S., Slipchenko, M. N., and Cheng, J.-X. (2011) Multimodal nonlinear optical microscopy. *Laser Photon. Rev.* 5
2. Zipfel, W. R., Williams, R. M., and Webb, W. W. (2003) Nonlinear magic: multiphoton microscopy in the biosciences. *Nat. Biotechnol.* 21, 1369–1377
3. Campagnola, P. J., Millard, A. C., Terasaki, M., Hoppe, P. E., Malone, C. J., and Mohler, W. A. (2002) Three-dimensional high-resolution second-harmonic generation imaging of endogenous structural proteins in biological tissues. *Biophys. J.* 82, 493–508
4. Helmchen, F. and Denk, W. (2005) Deep tissue two-photon microscopy. *Nat. Methods* 2, 932–940
5. Ji, M., Lewis, S., Camelo-Piragua, S., Ramkissoon, S. H., Snuderl, M., Venneti, S., Fisher-Hubbard, A., Garrard, M., Fu, D., Wang, A. C., Heth, J. A., Maher, C. O., Sanai, N., Johnson, T. D., Freudiger, C. W., Sagher, O., Xie, X. S., and Orringer, D. A. (2015) Detection of human brain tumor infiltration with quantitative stimulated Raman scattering microscopy. *Sci. Transl. Med.* 7, 309ra163
6. Wei, L., Chen, Z., Shi, L., Long, R., Anzalone, A. V., Zhang, L., Hu, F., Yuste, R., Cornish, V. W., and Min, W. (2017) Super-multiplex vibrational imaging. *Nature* 544, 465–470
7. Lee, M., Tipping, W. J., Serrels, A., Hulme, A. N., and Brunton, V. G. (2017) New approaches to intracellular drug imaging by stimulated Raman scattering microscopy. presented at the SPIE BiOS

8. Fu, D., Yang, W., and Xie, X. S. (2017) Label-free Imaging of Neurotransmitter Acetylcholine at Neuromuscular Junctions with Stimulated Raman Scattering. *J. Am. Chem. Soc.* 139, 583–586
9. Lee, H. J., Zhang, D., Jiang, Y., Wu, X., Shih, P.-Y., Liao, C.-S., Bungart, B., Xu, X.-M., Drenan, R., Bartlett, E., and Cheng, J.-X. (2017) Label-Free Vibrational Spectroscopic Imaging of Neuronal Membrane Potential. *J. Phys. Chem. Lett.* 8, 1932–1936
10. Robles, F. E., Zhou, K. C., Fischer, M. C., and Warren, W. S. (2017) Stimulated Raman scattering spectroscopic optical coherence tomography. *Optica* 4, 243–246
11. Tu, H., Liu, Y., Marjanovic, M., Chaney, E. J., You, S., Zhao, Y., and Boppart, S. A. (2017) Concurrence of extracellular vesicle enrichment and metabolic switch visualized label-free in the tumor microenvironment. *Sci. Adv.* 3, e1600675
12. Boppart, S. A., Brown, J. Q., Farah, C. S., Kho, E., Marcu, L., Saunders, C. M., and Sterenborg, H. J. C. M. (2017) Label-free optical imaging technologies for rapid translation and use during intraoperative surgical and tumor margin assessment. *J. Biomed. Opt.* 23, 1–10
13. Owen, S. F., Liu, M. H., and Kreitzer, A. C. (2019) Thermal constraints on in vivo optogenetic manipulations. *Nat. Neurosci.* 22, 1061–1065
14. Picot, A., Dominguez, S., Liu, C., Chen, I.-W., Tanese, D., Ronzitti, E., Berto, P., Papagiakoumou, E., Oron, D., Tessier, G., Forget, B. C., and Emiliani, V. (2018) Temperature Rise under Two-Photon Optogenetic Brain Stimulation. *Cell Rep.* 24, 1243–1253.e5
15. Podgorski, K. and Ranganathan, G. (2016) Brain heating induced by near-infrared lasers during multiphoton microscopy. *J. Neurophysiol.* 116, 1012–1023
16. Denton, M. L., Ahmed, E. M., Noojin, G. D., Tijerina, A. J., Gamboa, G., Gonzalez, C. C., and Rockwell, B. A. (2019) Effect of ambient temperature and intracellular pigmentation on photothermal damage rate kinetics. *J. Biomed. Opt.* 24, 1–15
17. Walsh, A. J., Tolstykh, G. P., Martens, S., Ibey, B. L., and Beier, H. T. (2016) Action potential block in neurons by infrared light. *Neurophotonics* 3, 040501
18. Choi, B. and Welch, A. J. (2001) Analysis of thermal relaxation during laser irradiation of tissue. *Lasers Surg Med* 29, 351–359
19. Moreau, D., Lefort, C., Burke, R., Leveque, P., and O’Connor, R. P. (2015) Rhodamine B as an optical thermometer in cells focally exposed to infrared laser light or nanosecond pulsed electric fields. *Biomed. Opt. Express* 6, 4105–4117
20. Ford, J. B., Ganguly, M., Poorman, M. E., Grissom, W. A., Jenkins, M. W., Chiel, H. J., and Jansen, E. D. (2020) Identifying the role of block length in neural heat block to reduce temperatures during infrared neural inhibition. *Lasers Surg Med* 52, 259–275
21. Suzuki, T., Oishi, N., and Fukuyama, H. (2018) Simultaneous infrared thermal imaging and laser speckle imaging of brain temperature and cerebral blood flow in rats. *J. Biomed. Opt.* 24, 1–11
22. Freudiger, C. W., Min, W., Saar, B. G., Lu, S., Holtom, G. R., He, C., Tsai, J. C., Kang, J. X., and Xie, X. S. (2008) Label-free biomedical imaging with high sensitivity by stimulated Raman scattering microscopy. *Science* 322, 1857–1861
23. Schindelin, J., Arganda-Carreras, I., Frise, E., Kaynig, V., Longair, M., Pietzsch, T., Preibisch, S., Rueden, C., Saalfeld, S., Schmid, B., Tinevez, J.-Y., White, D. J., Hartenstein, V., Eliceiri, K., Tomancak, P., and Cardona, A. (2012) Fiji: an open-source platform for biological-image analysis. *Nat. Methods* 9, 676–682
24. Matthews, C. ; C. (2010) MetroloJ: an ImageJ plugin to help monitor microscopes’ health. presented at the ImageJ User & Developer Conference
25. Xu, C., Zipfel, W., Shear, J. B., Williams, R. M., and Webb, W. W. (1996) Multiphoton fluorescence excitation: new spectral windows for biological nonlinear microscopy. Proc. Natl. Acad. Sci. USA 93, 10763–10768
26. Zhang, D., Slipchenko, M. N., and Cheng, J.-X. (2011) Highly sensitive vibrational imaging by femtosecond pulse stimulated raman loss. *J. Phys. Chem. Lett.* 2, 1248–1253

27. Choi, T. Y., Denton, M. L., Noojin, G. D., Estlack, L. E., Shrestha, R., Rockwell, B. A., Thomas, R., and Kim, D. (2014) Thermal evaluation of laser exposures in an in vitro retinal model by microthermal sensing. *J. Biomed. Opt.* 19, 97003
28. Denton, M. L., Noojin, G. D., Foltz, M. S., Clark, C. D., Estlack, L. E., Rockwell, B. A., and Thomas, R. J. (2011) Spatially correlated microthermography maps threshold temperature in laser-induced damage. *J. Biomed. Opt.* 16, 036003
29. Tilbury, K., Hocker, J., Wen, B. L., Sandbo, N., Singh, V., and Campagnola, P. J. (2014) Second harmonic generation microscopy analysis of extracellular matrix changes in human idiopathic pulmonary fibrosis. *J. Biomed. Opt.* 19, 086014
30. Prunotto, M., Caimmi, P. P., and Bongiovanni, M. (2010) Cellular pathology of mitral valve prolapse. *Cardiovasc Pathol* 19, e113–7
31. Wells, J., Kao, C., Konrad, P., Milner, T., Kim, J., Mahadevan-Jansen, A., and Jansen, E. D. (2007) Biophysical mechanisms of transient optical stimulation of peripheral nerve. *Biophys. J.* 93, 2567–2580
32. Shapiro, M. G., Homma, K., Villarreal, S., Richter, C.-P., and Bezanilla, F. (2012) Infrared light excites cells by changing their electrical capacitance. *Nat. Commun.* 3, 736
33. Stuntz, E., Gong, Y., Sood, D., Liaudanskaya, V., Pouli, D., Quinn, K. P., Alonzo, C., Liu, Z., Kaplan, D. L., and Georgakoudi, I. (2017) Endogenous Two-Photon Excited Fluorescence Imaging Characterizes Neuron and Astrocyte Metabolic Responses to Manganese Toxicity. *Sci. Rep.* 7, 1041
34. Yaseen, M. A., Sutin, J., Wu, W., Fu, B., Uhlirova, H., Devor, A., Boas, D. A., and Sakadžić, S. (2017) Fluorescence lifetime microscopy of NADH distinguishes alterations in cerebral metabolism in vivo. *Biomed. Opt. Express* 8, 2368–2385
35. Legland, D., Arganda-Carreras, I., and Andrey, P. (2016) MorphoLibJ: integrated library and plugins for mathematical morphology with ImageJ. *Bioinformatics* 32, 3532–3534
36. Lin, C.-Y., Suhalim, J. L., Nien, C. L., Miljković, M. D., Diem, M., Jester, J. V., and Potma, E. O. (2011) Picosecond spectral coherent anti-Stokes Raman scattering imaging with principal component analysis of meibomian glands. *J. Biomed. Opt.* 16, 021104
37. Fu, D., Holtom, G., Freudiger, C., Zhang, X., and Xie, X. S. (2013) Hyperspectral imaging with stimulated Raman scattering by chirped femtosecond lasers. *J. Phys. Chem. B* 117, 4634–4640
38. Dedic, C. E., Meyer, T. R., and Michael, J. B. (2017) Single-shot ultrafast coherent anti-Stokes Raman scattering of vibrational/rotational nonequilibrium. Optica 4, 563

1. Yue, S., Slipchenko, M. N., and Cheng, J.-X. (2011) Multimodal nonlinear optical microscopy. *Laser Photon. Rev.* 5
2. Zipfel, W. R., Williams, R. M., and Webb, W. W. (2003) Nonlinear magic: multiphoton microscopy in the biosciences. *Nat. Biotechnol.* 21, 1369–1377
3. Campagnola, P. J., Millard, A. C., Terasaki, M., Hoppe, P. E., Malone, C. J., and Mohler, W. A. (2002) Three-dimensional high-resolution second-harmonic generation imaging of endogenous structural proteins in biological tissues. *Biophys. J.* 82, 493–508
4. Helmchen, F. and Denk, W. (2005) Deep tissue two-photon microscopy. *Nat. Methods* 2, 932–940
5. Ji, M., Lewis, S., Camelo-Piragua, S., Ramkissoon, S. H., Snuderl, M., Venneti, S., Fisher-Hubbard, A., Garrard, M., Fu, D., Wang, A. C., Heth, J. A., Maher, C. O., Sanai, N., Johnson, T. D., Freudiger, C. W., Sagher, O., Xie, X. S., and Orringer, D. A. (2015) Detection of human brain tumor infiltration with quantitative stimulated Raman scattering microscopy. *Sci. Transl. Med.* 7, 309ra163
6. Wei, L., Chen, Z., Shi, L., Long, R., Anzalone, A. V., Zhang, L., Hu, F., Yuste, R., Cornish, V. W., and Min, W. (2017) Super-multiplex vibrational imaging. *Nature* 544, 465–470
7. Lee, M., Tipping, W. J., Serrels, A., Hulme, A. N., and Brunton, V. G. (2017) New approaches to intracellular drug imaging by stimulated Raman scattering microscopy. presented at the SPIE BiOS
8. Fu, D., Yang, W., and Xie, X. S. (2017) Label-free Imaging of Neurotransmitter Acetylcholine at Neuromuscular Junctions with Stimulated Raman Scattering. *J. Am. Chem. Soc.* 139, 583–586

9. Lee, H. J., Zhang, D., Jiang, Y., Wu, X., Shih, P.-Y., Liao, C.-S., Bungart, B., Xu, X.-M., Drenan, R., Bartlett, E., and Cheng, J.-X. (2017) Label-Free Vibrational Spectroscopic Imaging of Neuronal Membrane Potential. *J. Phys. Chem. Lett.* 8, 1932–1936
10. Zhang, D., Wang, P., Slipchenko, M. N., and Cheng, J.-X. (2014) Fast vibrational imaging of single cells and tissues by stimulated Raman scattering microscopy. *Acc. Chem. Res.* 47, 2282–2290
11. Robles, F. E., Zhou, K. C., Fischer, M. C., and Warren, W. S. (2017) Stimulated Raman scattering spectroscopic optical coherence tomography. *Optica* 4, 243–246
12. Tu, H., Liu, Y., Marjanovic, M., Chaney, E. J., You, S., Zhao, Y., and Boppart, S. A. (2017) Concurrence of extracellular vesicle enrichment and metabolic switch visualized label-free in the tumor microenvironment. *Sci. Adv.* 3, e1600675
13. Boppart, S. A., Brown, J. Q., Farah, C. S., Kho, E., Marcu, L., Saunders, C. M., and Sterenborg, H. J. C. M. (2017) Label-free optical imaging technologies for rapid translation and use during intraoperative surgical and tumor margin assessment. *J. Biomed. Opt.* 23, 1–10
14. Owen, S. F., Liu, M. H., and Kreitzer, A. C. (2019) Thermal constraints on in vivo optogenetic manipulations. *Nat. Neurosci.* 22, 1061–1065
15. Picot, A., Dominguez, S., Liu, C., Chen, I.-W., Tanese, D., Ronzitti, E., Berto, P., Papagiakoumou, E., Oron, D., Tessier, G., Forget, B. C., and Emiliani, V. (2018) Temperature Rise under Two-Photon Optogenetic Brain Stimulation. *Cell Rep.* 24, 1243–1253.e5
16. Podgorski, K. and Ranganathan, G. (2016) Brain heating induced by near-infrared lasers during multiphoton microscopy. *J. Neurophysiol.* 116, 1012–1023
17. Denton, M. L., Ahmed, E. M., Noojin, G. D., Tijerina, A. J., Gamboa, G., Gonzalez, C. C., and Rockwell, B. A. (2019) Effect of ambient temperature and intracellular pigmentation on photothermal damage rate kinetics. *J. Biomed. Opt.* 24, 1–15
18. Walsh, A. J., Tolstykh, G. P., Martens, S., Ibey, B. L., and Beier, H. T. (2016) Action potential block in neurons by infrared light. *Neurophotonics* 3, 040501
19. Choi, B. and Welch, A. J. (2001) Analysis of thermal relaxation during laser irradiation of tissue. *Lasers Surg Med* 29, 351–359
20. Moreau, D., Lefort, C., Burke, R., Leveque, P., and O’Connor, R. P. (2015) Rhodamine B as an optical thermometer in cells focally exposed to infrared laser light or nanosecond pulsed e*lectric fields. Biom*ed. Opt. Express 6, 4105–4117
21. Ford, J. B., Ganguly, M., Poorman, M. E., Grissom, W. A., Jenkins, M. W., Chiel, H. J., and Jansen, E. D. (2020) Identifying the role of block length in neural heat block to reduce temperatures during infrared neural inhibition. *Lasers Surg Med* 52, 259–275
22. Suzuki, T., Oishi, N., and Fukuyama, H. (2018) Simultaneous infrared thermal imaging and laser speckle imaging of brain temperature and cerebral blood flow in rats. *J. Biomed. Opt.* 24, 1–11
23. Freudiger, C. W., Min, W., Saar, B. G., Lu, S., Holtom, G. R., He, C., Tsai, J. C., Kang, J. X., and Xie, X. S. (2008) Label-free biomedical imaging with high sensitivity by stimulated Raman scattering microscopy. *Science* 322, 1857–1861
24. Schindelin, J., Arganda-Carreras, I., Frise, E., Kaynig, V., Longair, M., Pietzsch, T., Preibisch, S., Rueden, C., Saalfeld, S., Schmid, B., Tinevez, J.-Y., White, D. J., Hartenstein, V., Eliceiri, K., Tomancak, P., and Cardona, A. (2012) Fiji: an open-source platform for biological-image analysis. *Nat. Methods* 9, 676–682
25. Matthews, C. ; C. (2010) MetroloJ: an ImageJ plugin to help monitor microscopes’ health. presented at the ImageJ User & Developer Conference
26. Xu, C., Zipfel, W., Shear, J. B., Williams, R. M., and Webb, W. W. (1996) Multiphoton fluorescence excitation: new spectral windows for biological nonlinear microscopy. *Proc. Natl. Acad. Sci. USA* 93, 10763–10768
27. Zhang, D., Slipchenko, M. N., and Cheng, J.-X. (2011) Highly sensitive vibrational imaging by femtosecond pulse stimulated raman loss. *J. Phys. Chem. Lett.* 2, 1248–1253

28. Choi, T. Y., Denton, M. L., Noojin, G. D., Estlack, L. E., Shrestha, R., Rockwell, B. A., Thomas, R., and Kim, D. (2014) Thermal evaluation of laser exposures in an in vitro retinal model by microthermal sensing. *J. Biomed. Opt.* 19, 97003
29. Denton, M. L., Noojin, G. D., Foltz, M. S., Clark, C. D., Estlack, L. E., Rockwell, B. A., and Thomas, R. J. (2011) Spatially correlated microthermography maps threshold temperature in laser-induced damage. *J. Biomed. Opt.* 16, 036003
30. Tilbury, K., Hocker, J., Wen, B. L., Sandbo, N., Singh, V., and Campagnola, P. J. (2014) Second harmonic generation microscopy analysis of extracellular matrix changes in human idiopathic pulmonary fibrosis. *J. Biomed. Opt.* 19, 086014
31. Prunotto, M., Caimmi, P. P., and Bongiovanni, M. (2010) Cellular pathology of mitral valve prolapse. *Cardiovasc Pathol* 19, e113–7
32. Wells, J., Kao, C., Konrad, P., Milner, T., Kim, J., Mahadevan-Jansen, A., and Jansen, E. D. (2007) Biophysical mechanisms of transient optical stimulation of peripheral nerve. *Biophys. J.* 93, 2567–2580
33. Shapiro, M. G., Homma, K., Villarreal, S., Richter, C.-P., and Bezanilla, F. (2012) Infrared light excites cells by changing their electrical capacitance. *Nat. Commun.* 3, 736
34. Stuntz, E., Gong, Y., Sood, D., Liaudanskaya, V., Pouli, D., Quinn, K. P., Alonzo, C., Liu, Z., Kaplan, D. L., and Georgakoudi, I. (2017) Endogenous Two-Photon Excited Fluorescence Imaging Characterizes Neuron and Astrocyte Metabolic Responses to Manganese Toxicity. *Sci. Rep.* 7, 1041
35. Yaseen, M. A., Sutin, J., Wu, W., Fu, B., Uhlirova, H., Devor, A., Boas, D. A., and Sakadžić, S. (2017) Fluorescence lifetime microscopy of NADH distinguishes alterations in cerebral metabolism in vivo. *Biomed. Opt. Express* 8, 2368–2385
36. Legland, D., Arganda-Carreras, I., and Andrey, P. (2016) MorphoLibJ: integrated library and plugins for mathematical morphology with ImageJ. *Bioinformatics* 32, 3532–3534
37. Lin, C.-Y., Suhalim, J. L., Nien, C. L., Miljković, M. D., Diem, M., Jester, J. V., and Potma, E. O. (2011) Picosecond spectral coherent anti-Stokes Raman scattering imaging with principal component analysis of meibomian glands. *J. Biomed. Opt.* 16, 021104
38. Fu, D., Holtom, G., Freudiger, C., Zhang, X., and Xie, X. S. (2013) Hyperspectral imaging with stimulated Raman scattering by chirped femtosecond lasers. *J. Phys. Chem. B* 117, 4634–4640
39. Dedic, C. E., Meyer, T. R., and Michael, J. B. (2017) Single-shot ultrafast coherent anti-Stokes Raman scattering of vibrational/rotational nonequilibrium. *Optica* 4, 563
40. Camp, C. H., Lee, Y. J., Heddleston, J. M., Hartshorn, C. M., Hight Walker, A. R., Rich, J. N., Lathia, J. D., and Cicerone, M. T. (2014) High-Speed Coherent Raman Fingerprint Imaging of Biological Tissues. *Nat. Photonics* 8, 627–634

CHAPTER 4:

VISUALIZING THE ROLE OF LIPID DYNAMICS DURING INFRARED NEURAL STIMULATION WITH HYPERSPECTRAL STIMULATED RAMAN SCATTERING MICROSCOPY

Text adapted from:

Wilson R Adams, Rekha Gautam, Andrea Locke, Ana I. Borrachero-Conejo, Bryan Dollinger, Graham A. Throckmorton, Craig Duvall, E Duco Jansen, Anita Mahadevan-Jansen. *Visualizing the Role of Lipid Dynamics during Infrared Neural Stimulation with Hyperspectral Stimulated Raman Scattering Microscopy*. bioRxiv. May 2021. https://doi.org/10.1101/2021.05.24.444984 [In Submission]

4.1 Abstract

Infrared neural stimulation, or INS, is a method of using pulsed infrared light to yield label-free neural stimulation with broad experimental and translational utility. Despite its robust demonstration, the mechanistic and biophysical underpinnings of INS have been the subject of debate for more than a decade. The role of lipid membrane thermodynamics appears to play an important role in how fast IR-mediated heating nonspecifically drives action potential generation. Direct observation of lipid membrane dynamics during INS remains to be shown in a live neural model system. To directly test the involvement of lipid dynamics in INS, we used hyperspectral stimulated Raman scattering (hsSRS) microscopy to study biochemical signatures of high speed vibrational dynamics underlying INS in a live neural cell culture model. Findings suggest that lipid bilayer structural changes are occurring during INS *in vitro* in NG108-15 neuroglioma cells. Lipid-specific signatures of cell SRS spectra were found to vary with stimulation energy and radiant exposure. Spectroscopic observations were verified against high-speed ratiometric fluorescence imaging of a conventional lipophilic membrane structure reporter, di-4-ANNEPS. Overall, the presented data supports the hypothesis that INS causes changes in the lipid membrane of neural cells by changing lipid membrane packing order – which coincides with likelihood of cell stimulation. Furthermore, this work highlights the potential of hsSRS as a method to study biophysical and biochemical dynamics safely in live cells.

4.2 Introduction

Neuromodulation using directed energy, including optical, ultrasonic, and radio frequency, have gained notable interest recently due to their spatial precision, noninvasive implementation, and promising potential for clinical translation in therapeutic interventions. Label-free optical neuromodulation with pulsed infrared (IR) light, or infrared neural stimulation (INS), offers a spatially and temporally precise means of contact-free activation of neural cells without the need for genetic modification or exogenous mediators. Similar to most label-free directed energy methods of neuromodulation, the biophysical mechanisms underlying INS have remained elusive for more than a decade (1). In contrast to the tools derived from molecular biology, such as optogenetics or photochemical uncaging, INS appears to act through an entirely different photothermal-based mechanism (1,2). The role of lipid membrane dynamics are thought to play an important role in how IR light depolarizes neurons photothermally (3), but remains to be directly experimentally validated in a live neural model system.

Infrared wavelengths generally used for INS are strongly absorbed by water (4,5). The rapid temperature rise from brief pulses of IR light were experimentally shown to depolarize HEK cells as well as synthetic charged lipid bilayer preparations through a transient increase in membrane capacitance (2). Biomolecular explanations for these observations were unclear. A biophysical explanation of this phenomenon was described computationally by factoring in the thermal dependence of lipid bilayer geometry with a Gouy-Chapman-Stern based electrodynamic model of charged lipid bilayers (3). While the experimental data and computational model agree with each other, the role of lipid dynamics in neural models of INS remain to be directly validated. Lipid dynamics during INS have been probed through electrophysiology and fluorescent membrane structure reporters (2,6,7). However, these methods are inherently indirect to lipid molecular dynamics. There remains to be any direct observation of lipid dynamics in live neural cells during INS. Understanding the role of lipid dynamics in the mechanisms of INS would provide both valuable scientific insight and a basis for innovation towards the next generations of neuromodulation technology.

Conventional methods of directly measuring lipid bilayer geometry, such as x-ray diffraction and small angle neutron scattering, are slow and not biologically compatible (8–10). Optical methods are well suited for high resolution, biologically compatible experiments, but generally lack the spatial resolution necessary to directly resolve lipid bilayer geometry (< 3 nm thick) on millisecond timescales. Fluorescent functional lipid indicators, such as laurdan or di-4-ANNEPS (11), have been shown to be powerful tools in studying lipid membrane biophysics. However, these indicators offer latent readouts of lipid dynamics and are inherently indirect in that they rely on the molecular interaction of reporter molecules with their molecular environment rather than the lipid molecules themselves. Vibrational spectroscopic methods, such as Raman scattering and infrared absorption, can be performed label-free and offer a feature-rich molecular signature useful in studying lipid organization in live cells. Traditionally, vibrational spectroscopic methods have not been biologically compatible on sub-second timescales (12,13). Stimulated Raman scattering (SRS) microscopy combines label-free vibrational spectroscopic contrast with subcellular spatial resolution and sub-second temporal resolution enabling time resolved vibrational spectral measurements of live neural cells during INS (14,15). Others have shown that lipid molecular symmetry and ordered molecular interactions of water with lipid bilayers are observable with nonlinear Raman microscopy (16,17). Moreover, SRS can be implemented fast enough to discern signatures of neuronal action potentials at millisecond timescales (16–18). With this in mind, we set out to employ a hyperspectral SRS (hsSRS) microscopy approach to identify vibrational signatures of lipid bilayer dynamics during INS in live neural cell cultures.

The goal of this paper is therefore to identify the molecular dynamics of membrane lipids in live neural cells during INS with hsSRS microscopy. We demonstrate a time-resolved hsSRS methodology combined with focus precompensation to obtain SRS spectra of live NG108 cells. Spectra of NG108 cells show significant changes during INS which are attributable to changes in lipid packing order and solvent interactions. Validation of this approach was compared to gold-standard ratiometric fluorescence of a functional lipid packing order indicator – di-4-ANNEPS. We discuss how changes in the vibrational spectral signatures of cells during INS compare to what the current mechanistic hypothesis implies. Furthermore, we offer practical insight to performing high-resolution optical microscopy in dynamically varying optical imaging conditions during INS, as well as offer some thoughts to the potential extensions of this hsSRS methodology as SRS technology continues to develop.

4.3 Methods

4.3.1 Cell Culture and Maintenance

Methods for neuronal hybridoma cell cultures were adapted from previous work (19,20). A spiking neuroma-glioblastoma hybridoma cell line, NG-108-15 (Sigma-Aldrich, St. Louis, MO), were thawed and maintained in culture for 1 week prior to imaging experiments. Cells were maintained in Dulbecco's Modified Eagle Medium supplemented with 4.5g/L of glucose, 20mM of L-glutamine, 15%v/v fetal bovine serum and 1%v/v of penicillin/streptomycin antibiotics. Cells were incubated at 37ºC in 5% of CO_2 and 95% relative humidity. Growth medium was completely replaced every 48 hours until cells approached confluency. Once ~80% confluent, cells were mechanically dissociated and propagated onto additional cell culture flasks until experimental use. All cells were imaged within 15 rounds of passage from thawed supplier stocks. Seventy-two hours prior to imaging, cells were passaged and plated onto poly-D-lysine-coated glass-bottom petri dished (Mattek, Natick, MA) to allow for cellular adherence. Twenty-four hours prior to image experiments, the cell culture medium was replaced with an identical DMEM formulation except for the reduction of fetal bovine serum concentration (3%v/v) to promote morphological differentiation into dendritic neuronal phenotypes. During imaging experiments, cells were maintained at room temperature and humidity in neurophysiologically balanced saline free of protein and glucose with the following composition (in mM): 140 NaCl, 4 KCl, 2 $MgCl_2$, 2 $CaCl_2$, 10 HEPES, 5 glucose, pH 7.4

with NaOH and osmolarity adjusted to ~318 mOsm with mannitol (21). Cells were imaged for 45 minutes before being discarded.

4.3.2 Microscope System

The physical layout and capability of the custom-built multimodal imaging platform utilized in this study (**Figure 4.1A**) was described previously (22). Briefly, a dual output femtosecond near-infrared laser source (Insight DS+, Spectra Physics, Santa Clara, CA) was used to excite nonlinear contrast. Both output beams were spatially and temporally combined, with 20 MHz intensity modulation of the 1040 nm output and a variable linear optical path length on the 798 nm output for temporal collinearity and to facilitate hyperspectral SRS (23). The combined ultrafast laser outputs were subsequently chirped through 150mm of high-index SF11 glass rods (Newlight Photonics, Ontario, Canada) to enable spectral focusing based hsSRS microscopy(23,24). In summary, chirping the two ultrafast laser pulses though high index glass from ~200 fs to about ~2.5 ps allows for tuning of the relative temporal delay between the ultrafast laser pulses at the sample to variably evoke SRS resonances. The result is improved spectral resolution (~30 cm^{-1}) compared to using transform-limited 200 fs pulses (~300 cm^{-1}) without being limited by laser wavelength tuning speed. The result is a video rate nonlinear microscopy platform with 800 nm spatial resolution and approximately 30 cm^{-1} spectral resolution. After chirping, the beams were directed to a pair of scanning galvanometric mirrors. The face of the first scanning mirror was relayed to the back focal plane of a physiological imaging objective (Olympus XLUMPLN 20X 1.0 NA, water dipping) through a 4X magnifying 4-f imaging relay (Thorlbs SL50-2P and TL200-2P).

Detection for SRS – specifically stimulated Raman loss – was collected via transmission by a high-NA condenser lens (1.4 NA Oil, Nikon Instruments) directing light to a reverse-biased photodiode (APE, Gmbh., Berlin) behind an 850 nm centered, 310nm bandwidth optical bandpass filter (Semrock, Brattleboro, VT) to isolate the 798 nm laser line. The detected signal was subsequently demodulated with a lock-in amplifier (APE, Gmbh. Berlin) synced against the 20 MHz sinusoid signal driving the 1040 nm beam modulation. Any 20 MHz modulation transfer from the 1040 nm beam to the 798 nm beam was assumed to be attributed to stimulated Raman contrast. The temporal delay between the chirped 798 nm and 1040 nm laser pulses arriving at the sample was carefully tuned by varying the optical path length of the 798 nm laser beam with an optical delay stage (BB201, Thorlabs, Newton, NJ, USA). The relative delay between laser pulses over a span of 0.5 mm (or 1.6 ps) allowed for scanning of SRS resonance contrast over approximately 300 cm^{-1} between 2800 and 3100 cm^{-1}. Additionally, this system also allows for for

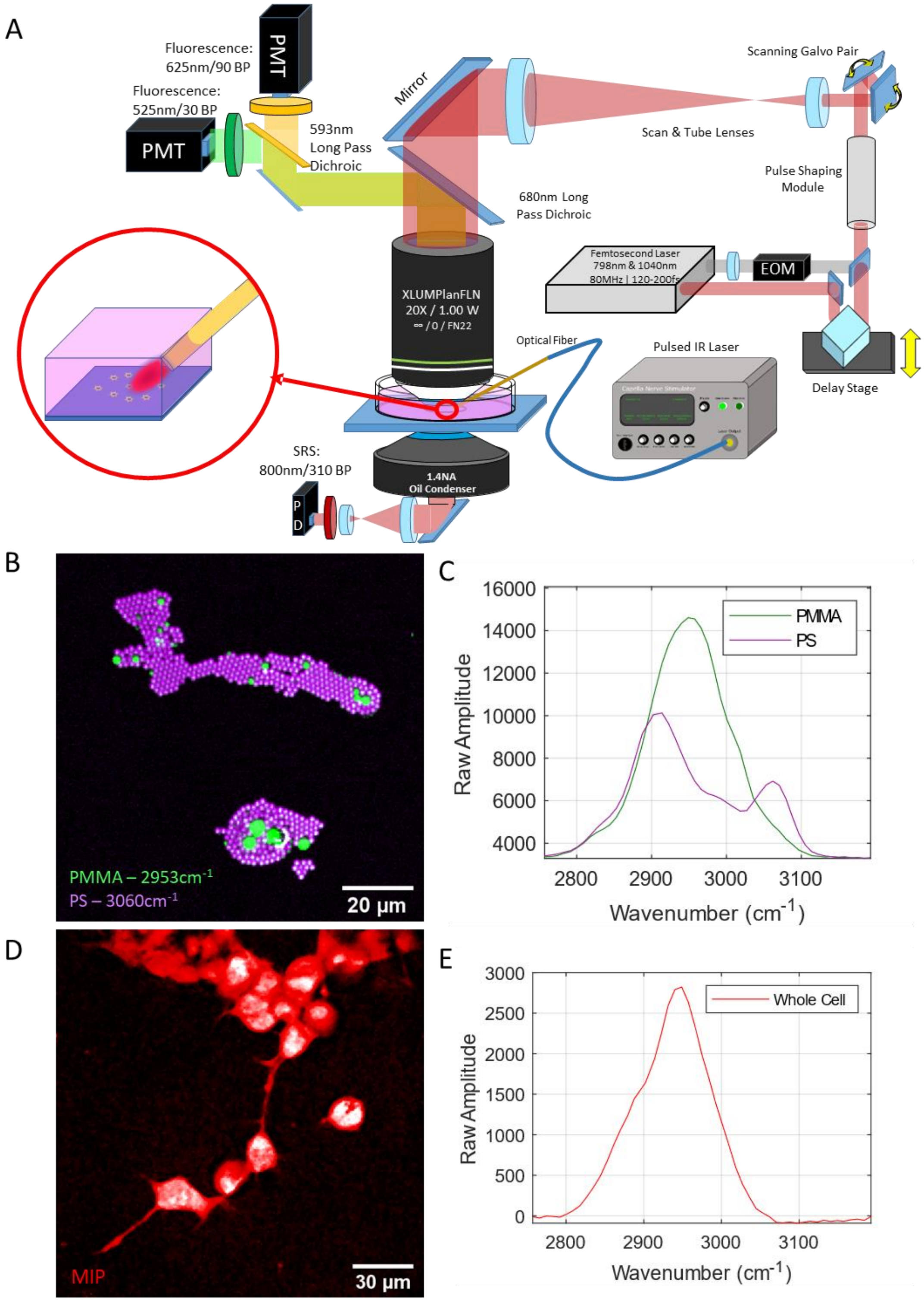

Figure 4.1: Experimental setup for SRS and fluorescence imaging of samples during IR exposure.
(A) Imaging system schematic, (B) Standard poly(methyl methacrylate) and polystyrene (PMMA | PS) monolayer demonstrating spatial and (C) spectral performance of imaging system. (D) Maximum-intensity projection of the hyperspectral SRS image stack of live NG108 cells alongside their respective (E) whole-cell SRS spectra.

nm long pass dichroic mirror (Semrock, Brattleboro, VT) behind the objective lens in a non-descanned configuration. Bandpass filters for multiphoton fluorescence microscopy were selected to collect the green (525 nm center, 50nm passband) and red (625 nm center, 90 nm passband) emission profiles of the lipophilic dye di-4-ANNEPS. Images were acquired in a bidirectional point-scanning configuration. High-speed hsSRS imaging experiments were acquired with a 96x64 px sampling profile with varying pixel sampling densities between 1 and 4 µm/px. Imaging with 2-5 µs pixel dwell time and bidirectional scanning amounts to an effective imaging framerate approaching 150 Hz. Ultrafast laser average powers at the sample plane were measured to be about 10 mW for the 798 nm laser, and 25 mW for the 1040 nm laser – corresponding to 199W/cm^2 and 497W/cm^2 irradiances at each pixel, respectively. Assuming a constant 5 µs pixel dwell time, radiant exposures per pixel amount to 1.00 mJ/cm^2 and 2.49 mJ/cm^2. The substantial increase in power necessary for imaging in this configuration are due to the decrease in peak power within each ultrafast laser pulse during the chirping stage. Live cell viability was verified with all relevant imaging conditions by cellular uptake of propidium iodide (PI) and is described in *Live Cell Hyperspectral SRS Imaging*.

4.3.3 hsSRS Spectral Focusing Calibration

A monolayer preparation of mixed polymer beads were used to calibrate the optical delay between pump and probe laser pulses as a function of SRS resonance. A mixed sample of poly(methyl methacrylate) – PMMA 1-10 µm diameter– and polystyrene – PS, 2 µm diameter – microspheres (PolySciences Ltd., Warrington, PA, USA) were diluted to a concentration of 0.002% w/v (each) in a solution of methanol (Fisherbrand, St. Louis, MO, USA). After mixing, 10 µL of diluted microbead solution were spread onto a #1.5 glass coverslip and left to evaporate for 25 minutes at room temperature. Once dried, samples were mounted dry onto a standard microscope slide and used for spectral calibration of hyperspectral SRS system by spectral focusing.

To calibrate the vibrational spectral dimension of hyperspectral imaging space, 50 sequential images were acquired of mounted polymer bead monolayers. Between each acquired image, the optical path length delay of the 798 nm laser line was stepped by 10 µm between each image, over a total of 500 µm or 1.6 ps of total optical path length delay. The peak SRS signal for the 2950 cm^{-1} resonance of PMMA was centered in the spectral scanning range to ensure sufficient spectral sampling. Manual segmentation of PMMA and PS beads from spectral stacks were performed and averaged across each spectral frame to provide high-fidelity spectra for both polymers. The known vibrational peaks of PS (2910, 3060 cm^{-1}) and PMMA (2950 cm^{-1}) were used as spectral fiducials (**Figure 4.1B&C**) to linearly interpolate a relationship between optical path delay of the chirped 798 nm laser pulse and the excited vibrational resonant mode.

$$d_{fiber} = 440\mu m \qquad r_f = 220\mu m$$

$$\theta_A = 30° \qquad sin\,\theta_A = \frac{1}{2} \qquad \cos\theta_A = \frac{\sqrt{3}}{2}$$

$$d_{cs} = 10\mu m$$

$$l = \frac{(r_f \cos\theta_A) + d_{cs}}{\sin\theta_A} = 400\mu m$$

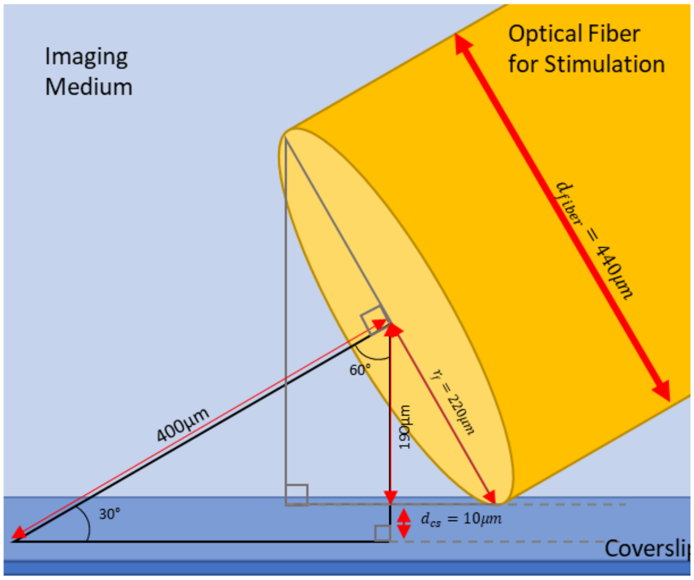

Figure 4.2: Fiber Illumination Geometry
(Right) Illumination geometry and (Left) calculation of approximate fiber distance for estimating radiant exposure – where d_{fiber} is the optical fiber diameter, r_{fiber} is the optical fiber radius, θ_A is the fiber approach angle, d_{cs+} is the fiber edge's distance off of the surface of the cover slip, and l is the normal distance from the optical fiber face to the cover slip plane.

Calibrations were performed at the beginning of each day's experiments to ensure spectral accuracy. The spectral resolution was observed to be approximately 30 cm^{-1}.

4.3.4 Infrared Neural Stimulation

Neural stimulation was performed by placing a bare 400 µm-diameter core low-OH optical fiber (Ocean Optics, FL, USA) in close proximity to samples (~450 µm) at a 30-degree approach angle into the sample plane of the microscope's field of view (**Figure 4.2**). The optical fiber used for stimulation is connected to a pulsed laser diode centered at 1875 nm (Capella Nerve Stimulator, Aculight – Lockheed-Martin, Bothel, WA, USA). During imaging experiments, samples were exposed to a pulse train of 188 pulses distributed evenly over 1500 ms). Pulses were 400 µs in duration and were delivered at a repetition rate of 125 Hz. Radiant exposures on samples were varied by adjusting the peak current delivered to the laser diode, holding all dosing and geometric configurations constant. Radiant exposure calculations for stimulation were approximated based on power measurements performed externally in air and employing Beer's law under the assumption of an absorption-dominated photon distribution – described in **Figure 4.2** and **Figure 4.3**. Infrared exposure levels for INS were selected based on their ability to elicit dynamic calcium responses (>2% increase, dF/F) in NG108 cells loaded with a calcium dye (Fluo-4-AM at 1 µM , ThermoFisher, St. Louis, MO, USA). Radiant exposures for no stimulation, sub-threshold, and threshold levels of stimulation used 0, 5.02, and 10.63 J/cm^2, respectively.

4.3.5 Phospholipid Multilamellar Vesicle Preparation

$$DC = \frac{t_{pulse}}{T_{pulse}}$$

$$P_{peak} = \frac{P_{avg}}{DC}$$

$$\begin{aligned} E_{pulse} &= t_{pulse} \cdot P_{peak} \\ E_T &= N \cdot E_{pulse} \\ E_s &= E_T \cdot e^{-\alpha \cdot d_s} \end{aligned}$$

$$\begin{aligned} D_{spot} &= D_{fiber} \cdot 2\ \delta D \\ &= D_{fiber} + 2(d_s \cdot \tan(\theta)) \end{aligned}$$

$$RE_{fiber} = \frac{E_t}{\pi \cdot \left(\frac{D_{fiber}}{2}\right)^2}$$

$$\begin{aligned} RE_{sample} &= \frac{E_s}{\pi \cdot \left(\frac{D_{spot}}{2}\right)^2} \\ &= \frac{E_T \cdot e^{-\alpha \cdot d_s}}{\pi \cdot \left(\frac{D_{fiber} + 2(d_s \cdot \tan(\theta))}{2}\right)^2} \end{aligned}$$

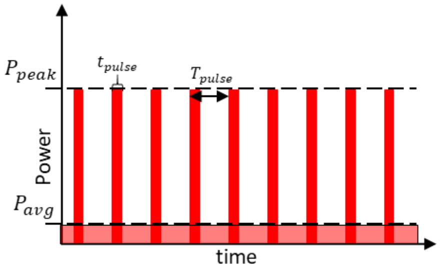

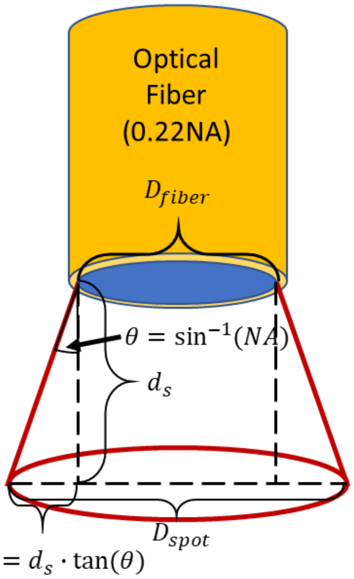

Variable	Definition	Variable	Definition
T_{pulse}	Pulse period, time between pulses	N	Number of pulses delivered
t_{pulse}	Pulse width / duration	α	Absorption coefficient of 1875nm light in water (~26cm^{-1} per Hale and Querry, 1973)
DC	Duty Cycle of IR pulses (0.05)	D_{fiber}	Optical fiber output diameter
P_{peak}	Peak Power of IR pulses	D_{spot}	Effective spot size or diameter (without absorption)
P_{avg}	Average power measured from a train of IR pulses	δD	Change in diameter between sample and fiber face, based on the NA of optical fiber output
E_{pulse}	Optical Energy per IR pulse	θ	Angle of divergence of light from the optical fiber, calculated from the NA of the optical fiber.
E_T	Total Optical Energy	RE_{fiber}	Radiant exposure calculated ex fiber
E_s	Optical Energy observed at the sample, d_s away from fiber output.	RE_{sample}	Radiant Exposure calculated at the sample positioned d_s away from fiber face.
d_s	Distance between fiber output and sample		

Figure 4.3: Estimated IR Dosage Calculation
Optical dosage calculations at the cell imaging plane based on an absorption-dominated photon distribution in homogenous medium, assuming negligible scattering and non-angled fiber approach to the sample

acids signal in a biomimetic context. Multilamellar vesicles were prepared according to protocols provided from the supplier (Avanti Polar Lipids, Alabaster, AL, USA). Phosphatidylcholine (PC) derived from porcine brain tissue arrived dissolved in chloroform at a concentration of 2.5 mg/mL. The chloroform was evaporated from the lipid mixture with a stream of dry nitrogen overnight and mechanically resolubilized in phosphate-buffered saline solution at a concentration of 1 mg/mL. Vesicle mixtures were stored at 4°C and imaged within three days of preparation. Imaging was performed at room temperature. Size distribution of the lipid vesicle preparation was verified via dynamic light scattering to contain 1 and 5 μm diameter

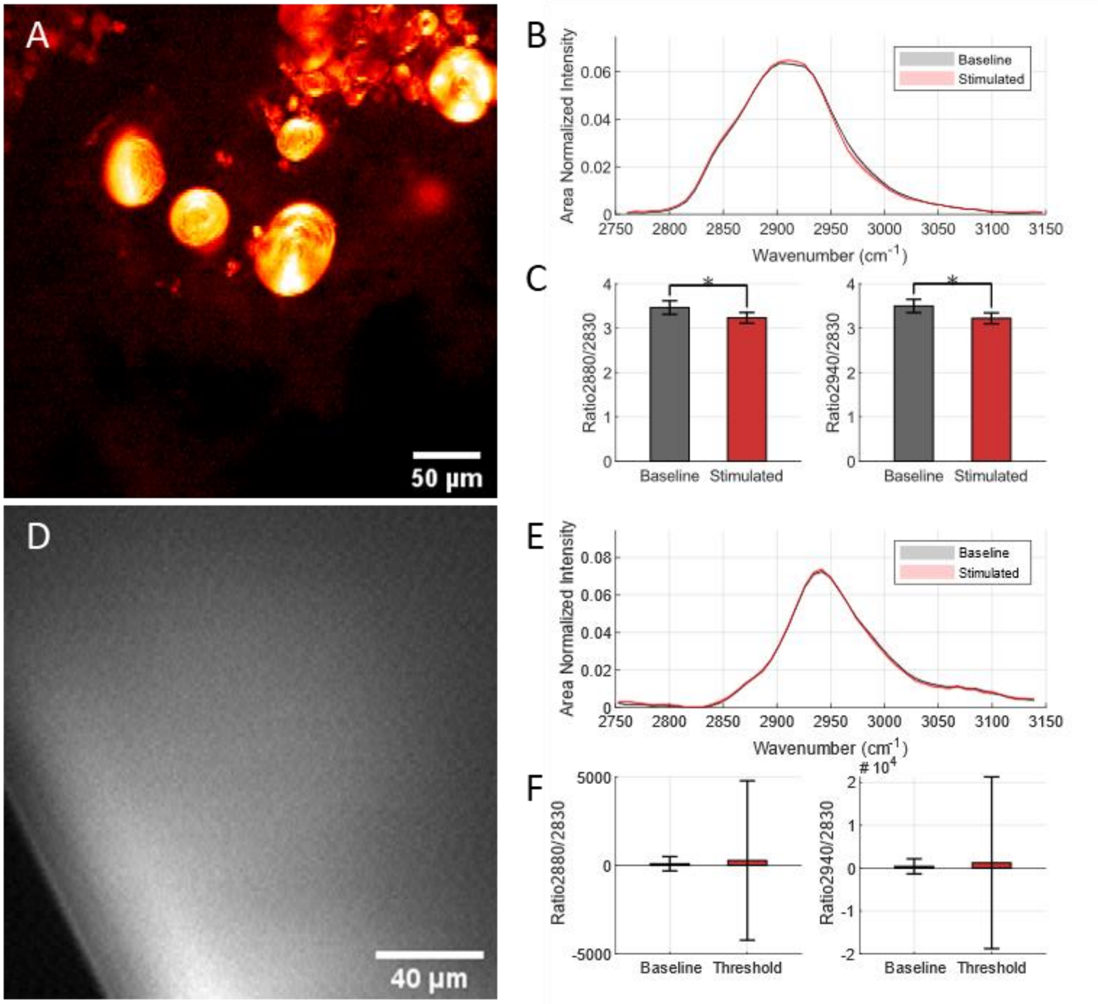

Figure 4.4: Validating IR-stimulated hsSRS images on isolated biological Raman scatterers.
(A) SRS image of a 10% bovine serum albumin (BSA) sample in phosphate buffered saline as a control sample to measure protein SRS spectra (B) baseline and IR-stimulated SRS spectra observed in BSA solution. (D) SRS image of multilamellar vesicles at 2930 cm^{-1} resonance. (E) SRS spectra of baseline and IR-stimulated MLVs. (C, F) Ratiometric comparison of BSA and MLV SRS spectra, respectively, of resonances indicative of lipid membrane biophysical dynamics.

vesicles (Malvern Panalytical, Malvern, UK). MLVs were identified as multilayered spherical structures with SRS contrast tuned to 2910cm^{-1} (**Figure 4.4A**).

4.3.6 Live Cell Hyperspectral SRS Imaging

Live cell imaging experiments of endogenous vibrational contrast with hsSRS were conducted with adherent cell preparations imaged in a physiologically balanced saline solution. Following placement of the fiber and calibration of the spectral axis against the known vibrational peaks of PS and PMMA beads, baseline hyperspectral image stacks were acquired for live cell samples. All images were acquired in a point-scanning approach with a 5 µs pixel dwell time and a spatial sampling density of ~500 nm/px. To improve signal to noise ratio of higher fidelity images, square fields of view between 320 and 512 pixels in size were acquired and 6 to 10 images were averaged together for each spectral position. For hyperspectral image stacks acquisitions, 50 images were acquired at evenly spaced intervals (10 µm) over 500 µm of optical path length delay – corresponding to a spectral range spanning approximately 2800 to 3100 cm^{-1}. The resultant spectral image stack was taken as ground-truth cellular spectra to compare high speed imaging spectra of the cells during INS in subsequent experiments.

For high-speed imaging during INS on NG108 cells, as well as control samples of multilamellar vesicles and BSA solution, 5 µs pixel dwell time were employed to obtain imaging fields 96x64 pixels in size with a sampling density between 1.5 and 4 µm per pixel - enabling framerates of 33.4 Hz. For each of the 50 spectral position, cells were imaged continuously for 5 seconds, during which a train of stimulating infrared pulses is delivered at the first second of the imaging timeframe. Image acquisition and IR stimulation was coordinated through a customized TTL-triggering protocol with an external signal digitizer (Digidata 1550B, Molecular Devices, Sunnyvale, CA, USA). The ultrafast excitation laser is observed to be defocused at the sample plane due to the thermal gradient induced by the stimulating infrared laser (**Figure 4.7A**) was observable in each imaging timeseries as an exponential decrease, and subsequent return to baseline (**Figure 4.7B&C**), of nonlinear signal on imaging photodetectors. The shift in focal length as a function of laser power was calibrated using microbead (PMMA and PS) preparations and accounted for prior to each IR-stimulation trial on cells. The defocusing phenomenon allowed for precise temporal synchronization of time series across each spectral channel. After repeating and temporally aligning simultaneous imaging and stimulation time courses on lives cells for each SRS spectral position (n = 50), the temporal evolution of live cell endogenous vibrational spectra could be observed as a function of irradiation time and deposited energy. For spectral evaluation, the final ten sampling time points within the of IR exposure were averaged and reported – which was found to help reduce high frequency spectral noise to draw conclusions from. Spectra from stimulation experiments were pooled from n = 24 cells across ten different individual experiments of IR exposure. Each cell spectrum was normalized with respect to its integrated spectral intensity, and standard deviation of the spectra across all cells in each stimulation condition were calculated. The ‘no stimulation’ conditions are obtained from initial SRS signal from cells prior to each round of IR exposure and pooled from all stimulation conditions being compared. The shape of SRS spectra acquired at high frame rates (**Figure 4.8B**) were not found to noticeably differ from higher fidelity spectra (**Figure 4.1D**).

To verify cell viability during IR exposure, NG108 cells were subject to the hsSRS and stimulation protocol described above while simultaneously monitoring for cell damage via positive fluorescence staining of cell nuclei with propidium iodide. Imaging protocols were kept identical as previously described while supplementing the cell imaging medium with 1 µM propidium iodide (Thermo-Fisher, Natick, MA, USA). Cell morphology was additionally monitored throughout the experiment by comparing high fidelity images (< 1 µm/px sampling density) of the cells before and after imaging at their peak SRS resonance contrast at 2930 cm^{-1}.

4.3.7 di-4-ANNEPS Ratiometric Fluorescence Imaging

Imaging protocols were adapted from previously published work (25). Briefly, a loading solution of 4-(2-(6-(Dibutylamino)-2-naphthalenyl)ethenyl)-1-(3-sulfopropyl)pyridinium hydroxide (or di-4-ANNEPS) was prepared by diluting an aliquot of 4mM stock solution in dimethyl sulfoxide (DMSO) in neurophysiological saline to a final loading concentration of 2 µM. NG108 cells were incubated in the dark at 37°C, 5% CO_2 and 95% relative humidity for 25 minutes, before being rinsed and maintained in fresh neurophysiological saline solution free of dye for fluorescence imaging. To image di-4-ANNEPS fluorescence, two photomultiplier tubes (PMTs) configured for non-descanned epifluorescence detection. Fluorescence emission was split by a 593nm long pass dichroic mirror and subsequently filtered with either a 525nm/25, or 625nm/45 optical bandpass filter before reaching PMT detectors (Semrock, Brattleboro, VT, USA). Ultrafast laser excitation for multiphoton fluorescence was tuned to 960 nm to optimally excite di-4-ANNEPS. For high-speed imaging, images were acquired as 96x64 pixel images between 0.5-4.0 µm/pixel sampling densities with 5 µs pixel dwell times to yield 33.4 Hz framerates. Excitation laser intensity for imaging was maintained below 10 mW at the sample plane. The SF11 glass rods used to chirp the laser pulses for hsSRS imaging were removed for ratiometric fluorescence imaging, resulting in ultrafast laser pulse width approaching 200 fs at approximately 80 MHz.

During a 5-second imaging period, stimulating IR light was delivered to di-4-ANNEPS stained NG108 cells via a 400 µm core multimode optical fiber immediately adjacent to the microscope’s field of view. Varying levels of radiant exposure were delivered to cells (0-44 J/cm^2) and the resulting fluorescence intensity changes were compared across stimulation conditions. Calculations for conventional polarization, as well as a modified version of general polarization (**Figure 4.5**), were derived to compare conventional assessments of lipid packing with that observed with hsSRS.

4.3.8 Data Processing, Analysis, and Visualization

1.4.3.8 ***Hyperspectral SRS Imaging Data***

Raw data acquired from the imaging experiments were collated and sorted into multidimensional stacks of 16-bit TIFF stacks separated by time and wavenumber using a customize processing pipeline in Fiji leveraging the Bioformats plugin (26,27). Average intensity projections of multidimensional (spectral, temporal) image stacks in time and spectral space were used to generate a mask to segment cells geometries. A general region of interest identified from the resultant masks were applied to the raw multidimensional image stack to extract spectral and temporal data from features of interest (e.g. beads, cells). To segment individual cells, a 2-pixel Gaussian blur was applied to the average intensity projection of the multidimensional image stack and contrast local histogram equalization was performed to reduce cell signal intensity variations between cells. Post-hoc flat field correction of imaging field heterogeneity of images was implemented by scaling pixel intensities relative to the average intensity projection gaussian blurred with a kernel equal to 0.25-0.5x the largest dimension of a particular image. Prominent peak locations in the image are identified. The filtered average intensity projection is subsequently segmented via Otsu segmentation. The resulting mask and previously identified peak locations are fed into an seeded watershed segmentation algorithm which reliably separates and segments induvial cells as their own ROIs with minimal cell-to-cell overlap (28). Edge maps of cells were acquired by subtracting the watershed-segmented mask from itself following an erosion operation, which reliably identifies borders in a cell-specific manner. The resultant regions of interest are applied to the raw stacks to extract the mean amplitude, standard deviation of signal or amplitude measurements, and their respective centroid locations in image-space for each spatial and temporal point. This process is automated as a macro procedure in FIJI and is freely available with raw data examples as supplementary information. Depicted images provided in the manuscript are derived either from single frames at specific wavenumbers of interest or maximum intensity projections of spectral image stacks. For visualization purposes in publication, intensity scaling for all images were adjusted linearly.

All hsSRS spectra are smoothed with a 3-point sliding Gaussian window and normalized with respect to their integrated spectral area. Since the intent of the study is to compare the relative spectral shapes of each sample, an integrated spectral normalization was chosen to facilitate this interpretation. Error associated with each plot is presented as standard deviation of all averaged spectra obtained for a given experimental trial. Each individual bead was taken as one sample, and different trials were taken as independent observations for statistical analysis purposes. For peak ratio comparisons, vibrational resonance intensities were calculated utilizing a cubic spline interpolation of the measured spectral data and it's respective standard deviation. Comparisons of peak ratios were assessed using a student's 2-sided t-test, where errors associated with ratiometric comparisons were calculated based on the propagation of error of the interpolated standard deviations (statistical significance was denoted by * for $p < 0.05$, ** for $p < 0.01$). All quantitative work was performed in MATLAB (Mathworks, Natick, MA, USA) using native functions. All bar graphs were created using the superbar package.

2.4.3.8 ***Ratiometric Fluorescence Analysis of di-4-ANNEPS Data***

Processing of ratiometric fluorescence data is derived in part from previous work (29). Raw image stacks of green (lipid membrane gel phase - ordered) and red (lipid membrane liquid phase - disordered) spectral emission channels are acquired simultaneously at a 33.4 Hz framerate. Conventional general polarization (GP_{conv}) was calculated using the following equation (29): Gwas calculated using the following equation (ref)

$$GP_{conv}(t) = \frac{(O(t) - D(t))}{(O(t) + D(t))}$$

The raw image intensity differences between the green (ordered, O(t)) and red (disordered, D(t)) imaging channels were divided by the sum of both channels for each timepoint in the image stack for each experiment. Decreases in GP_{conv} value generally suggest decreases in membrane packing order. Average GP values as a function of time were calculated and each cell's GP value was taken as an average GP of all pixels contained in each cell's ROI. Cell segmentation similar to those segmented for SRS images utilizing a seeded watershed method was performed. However, since di-4-ANNEPS labels the extracellular membrane preferentially, a Huang threshold mask of raw disordered spectral fluorescence intensity images were obtained to determine cell boundaries and a binary fill operation was employed to identify areas in the image that contained cells. The lack of lipid-stained fluorescence in cell nuclei was used to identify center points of cells. The raw disordered fluorescence channel image was smoothed with a 2-pixel Gaussian filter and local minima in the images were used to approximately localize cell center points. These cell center points, as well as the cell position mask, and a distance map calculated from the cell position mask were fed into a seeded watershed algorithm in FIJI to yield segmentation maps of individual cells in a given experiment (26,28). The regions of interest derived from the segmentation were subsequently applied to each imaging experiment, where time series of both raw fluorescence channels were obtained per cell and the resultant data was exported for processing and analysis in MATLAB (Mathworks, Natick, MA, USA). Statistical comparison of GP values across stimulation conditions was performed using a 2-sided student's t-test and the magnitudes and standard error of means across the GP values were calculated across all individual cells in a particular experimental condition (statistical significance denoted as * for $p < 0.05$).

For image visualization, adapted from previous work (29), 8-bit depth raw fluorescence intensity images from the disordered fluorescence channel were multiplied by each color channel of an color red-green-blue (RGB) format image representing the calculated GP images with the desired false-colored look-up table of preference. The resulting images yield an image where pixel brightness represents intensity and color represents calculated conventional general polarization – which are used purely for visualization purposes. All rescaling of intensities in images are linear and performed for clarity of cellular morphologies and biophysical properties in print **(Figure 4.10A**).

Due to large variations in total fluorescence measured in any given experiment due to thermal lensing during IR stimulation, the conventional method of calculating GP was found to be unreliable. Since we expect a decrease in overall fluorescence due to the decrease in effective collection efficiency during thermal lensing induced defocusing, the magnitude of changes in the denominator of the GP_{conv} equation are much larger than that of the changes in the numerator of the equation. To account for these effects, we developed an intensity invariant version of GP_{conv} to better reflect these dynamics mathematically over short experimental periods of time undergoing substantial changes in photon collection:

$$GP_{mod}(t) = \frac{[O_0 - D_0] + [O_{off}(t) - D_{off}(t)]}{[O_0 + D_0]}$$

Where O_0 represents initial ordered fluorescence levels, D_0 represents initial disordered fluorescence levels

$$O_{off}(t) = [O(t) - O_0]$$

$$D_{off}(t) = [D(t) - D_0]$$

$O_{off}(t)$ represent the net change in ordered fluorescence relative to O_0 as a function of time, and $D_{off}(t)$ represents the net change in disordered fluorescence as a function of time. O(t) and D(t) are the raw ordered and disordered fluorescence as a function of time, respectively. (**Figure 4.5B**). The alternative metric of modified GP (GP_{mod}) emphasizes the raw difference in measured fluorescence intensity between the ordered and disordered fluorescence imaging channel without dividing by the sum of both image channels over time. Assuming the defocusing artifact between both channels results in an equal amount of defocusing and signal loss from each fluorescence channel, any changes in the relative difference between

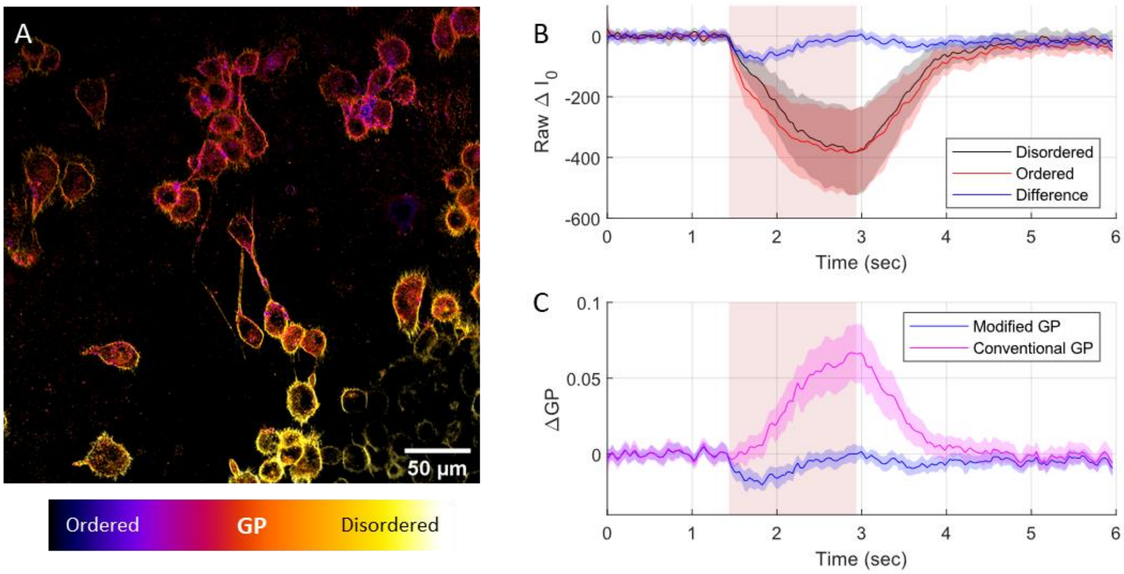

$$GP_{conv}(t) = \frac{(O(t) - D(t))}{(O(t) + D(t))} \qquad GP_{mod}(t) = \frac{[O_0 - D_0] + [O(t) - D(t)]}{[O_0 + D_0]}$$

$$O_0 = Ordered\ (Green)\ Channel\ Fluorescence$$

$$D_0 = Disordered\ (Red)\ Channel\ Fluorescence$$

Figure 4.5: An intensity-invariant metric of general polarization for di-4-ANNEPS imaging of cells during IR stimulation.
A method to account for signal loss from thermal lensing that may impacts perceived signal interpretation. (A) di-4-ANNEPS loaded NG108 cells. (B) Baseline-offset mean detected intensities of mean disordered (black line) and ordered (red line) of all cells in a given experiment, plotted alongside the difference of detected intensities (Ordered – Disordered) (C) Calculated conventional general polarization timeseries during IR stimulation alongside adapted general polarization calculation. (D) Conventional and adapted GP metric calculations alongside each other. Eliminating the time dependance of the denominator term circumvents the defocusing artifact's impact on the GP calculation.

the fluorescence signals as a function of time is indicative of functional changes in lipid bilayer packing (**Figure 4.5**). For the purposes of this study, we are interested in determining the direction of GP changes – positive or negative - rather than it's magnitude. This consideration makes GP_{mod} a convenient and applicable tool for our experimental approach.

4.4 Results

4.4.1 Thermal Lensing during IR Stimulation

Following confirmation of our instrument's ability to obtain hsSRS image stacks from live NG108 cells (**Figure 4.1D&E**), initial experiments with IR stimulation during nonlinear microscopy (i.e. any

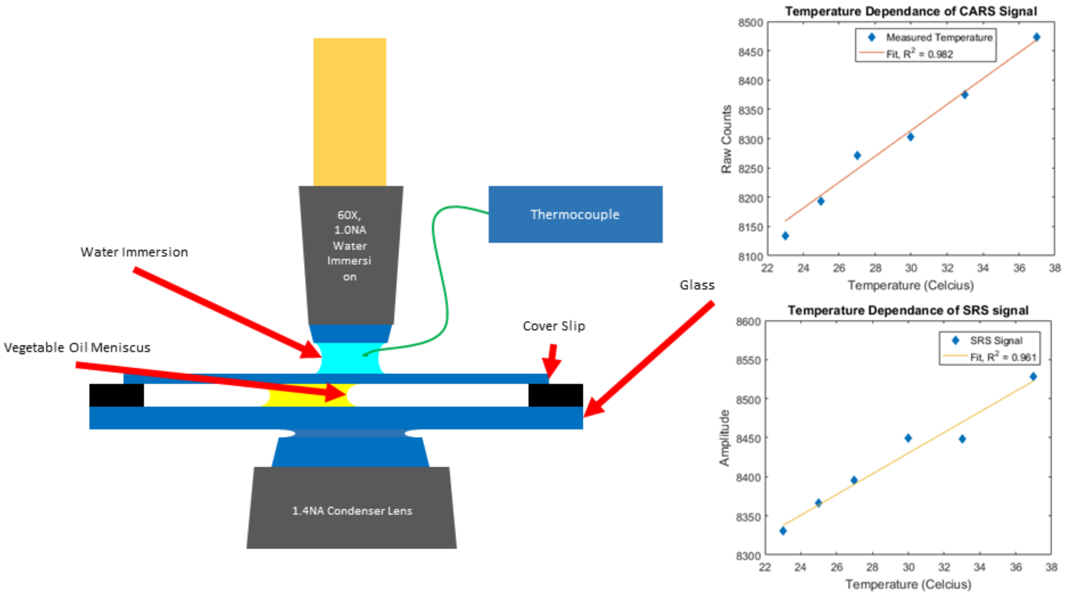

Figure 4.6: Temperature dependence of 2930 cm^{-1} CARS and SRS signal. (Left) experimental imaging and temperature measurement setup. (Right) Raw intensity measurements of vegetable oil meniscus as a function of temperature.

coherent Raman modality, multiphoton fluorescence, or higher harmonic generation) resulted in a substantial loss in measured signal during IR exposure (**Figure 4.7B&C**) (22). This was apparent in both short periods of heating from a millisecond pulse of IR light (unpublished data), or pulse trains of multiple microsecond pulses of light. The shape of the disappearance and reappearance of the nonlinear signal appears to follow the shape of the expected heating and cooling dynamics that is typically observed during IR mediated heating (30)– suggesting that a temperature related phenomenon may be responsible for the loss in signal. Considering the goal of this work is to image the high-speed chemical dynamics in live cells during IR exposure, the loss of signal during this critical time period posed a challenge. To better understand the role of this signal loss with immersion medium temperature, a vegetable oil sample was imaged with SRS (2885 cm^{-1}) through warmed immersion medium at a range of physiologically relevant temperatures. Temperature of the immersion medium was monitored by a thermocouple placed adjacent to the microscope's field of view at the coverglass-immersion medium interface (**Figure 4.6**). Warmed deionized water (approximately 50 °C) was added between the objective and sample with the edge of vegetable oil sample placed in focus. Images were acquired continuously as the immersion medium slowly cooled to room temperature (22 °C). Contrary to the signal decrease observed during rapid IR heating (**Figure 4.7B&C**), this experiment showed that changes in immersion medium temperature revealed a positive correlation with temperature and SRS signal of vegetable oil. This data suggested that changes in immersion medium temperature on its own was not sufficient to explain the decrease in nonlinear optical signal during IR heating.

y

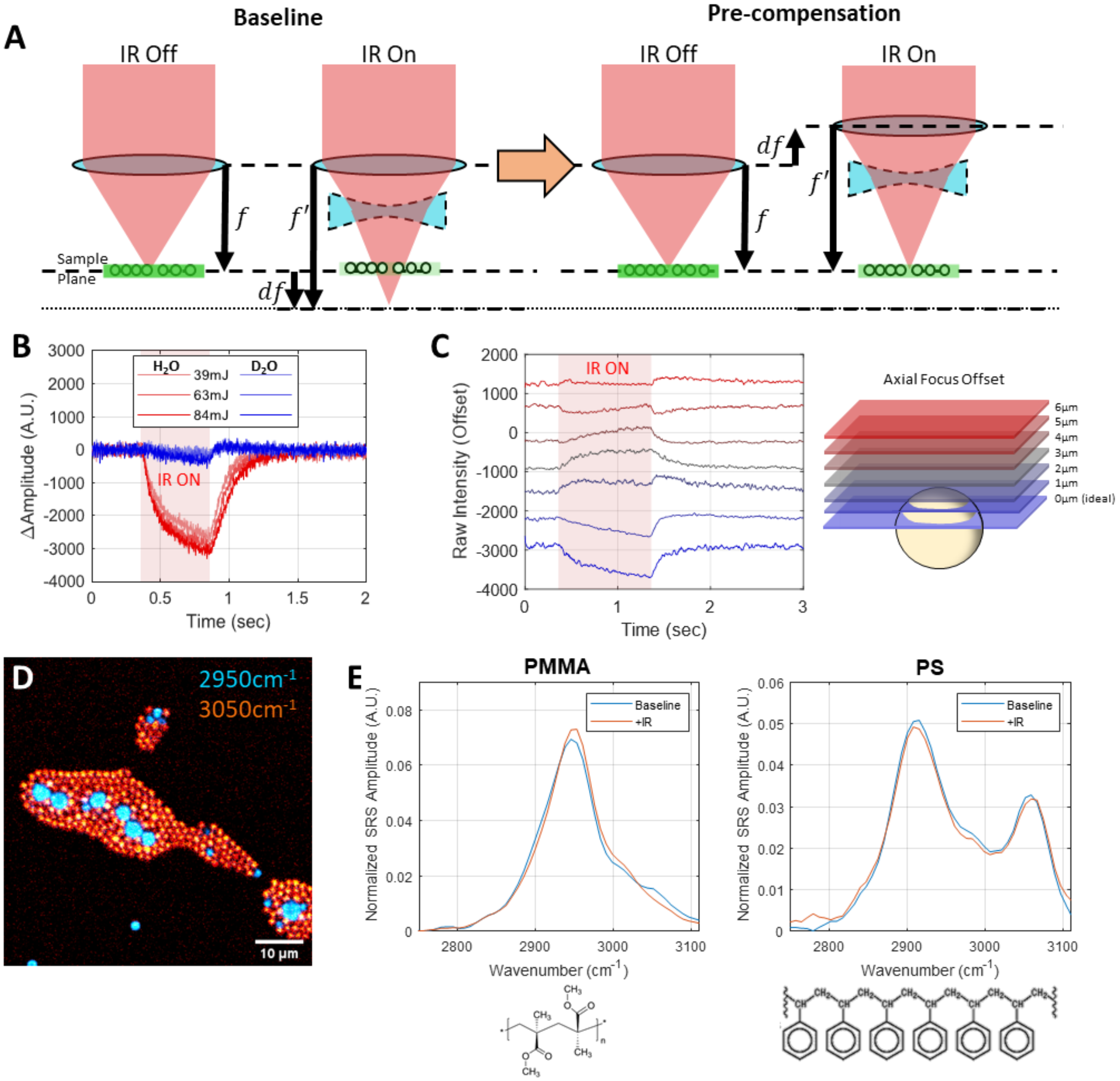

Figure 4.7: Explanation of defocusing phenomenon and an experimental approach to circumvent it.

(A) By adjusting the microscope focal plane to accommodate focal shifts induced by pulsed-IR neurostimulation within the microscope's field of view, it is possible to recover some lost nonlinear signal due to defocusing. (B) The thermal gradient and subsequent defocusing artifact generated by INS in the microscope's field of view is due to water absorption of INS light. Replacing H_2O immersion with D_2O immersion for imaging demonstrates that absorption of IR light is the driving force behind defocusing and signal loss. (C) Pre-compensating for INS-induced defocus by adjusting the focal plane position relative to our sample allows for nonlinear signal during INS. (D-F) Extrapolating this experimental approach across the wavenumber regions of interest allows for reconstruction of vibrational spectral dynamics during fast biophysical thermal events such as INS. **D)** Composite SRS image of PMMA and PS beads at 2950 and 3050 cm^{-1}, respectively. Baseline and IR-stimulated spectra for E) PMMA, and F) PS reconstructed using the focus pre-compensation approach, with respective chemical structures for reference.

correlated with temperature (31). This concept suggests that the spatial thermal gradients generated by the IR absorption from IR stimulation would defocus the ultrafast laser driving nonlinear contrast and thus reduce observed nonlinear optical signal. To test this hypothesis, the immersion medium for the objective lens was replaced with heavy water (D_2O), which has a five-fold lower absorption coefficient at 1875nm than deionized water with nearly identical refractive indices (2). If the thermal gradient causes the decrease in nonlinear signal observed in the sample, then reducing the immersion medium's IR absorption properties should reduce the magnitude of the nonlinear signal decrease during stimulation. The results shown in **Figure 4.6** validates this hypothesis (**Figure 4.7B**) suggesting that the thermal gradient from IR stimulation was defocusing the ultrafast laser source resulting in a decrease in nonlinear signal.

Since water's index of refraction is negatively correlated with temperature, the thermal gradient generated during IR stimulation in front of the stimulation fiber and within the microscope's field of view behaves like a negative lens during imaging. Imaging out of focus samples during IR stimulation would bring samples into focus (**Figure 4.7A**). This hypothesis was found to be true for both nonlinear imaging and IR transillumination imaging. By moving the microscope's focal plane above the sample by a few microns prior to IR exposure, the samples (polymer microbeads in this case) would come into focus (**Figure 4.7C**). This precompensation of defocus was applied repeatedly across numerous spectral channels to generate a time resolved hsSRS profile of samples during IR stimulation, similar to previously employed approaches with hsSRS and electrophysiology (18,32). This approach was verified by measuring several control samples: PS/PMMA microbead monolayer mixtures, 10%w/v bovine serum albumin solution in PBS, and large multilamellar vesicles of neurologically derived phosphatidylcholine (PC) and phosphatidylethanolamine (PE) in physiologically balanced neural saline solution before conducting experiments using live cellular samples.

4.4.2 Verifying pre-compensation for thermal defocusing during hsSRS

Figure 4.7D shows a representative image of mixed microbead monolayers, highlighting PMMA in cyan using the band at 2950 cm^{-1}(terminal methyl C-H resonance) and PS in orange using the band at 3050 cm^{-1} (aromatic C-H stretch resonance). The mixed bead sample was exposed to ~12 J/cm^2 IR stimulation and the resultant spectra for both bead types are shown in **Figure 4.7E&F**. Relevant spectral band assignments for polymer microbead samples are summarized in **Table 4.1**.. Infrared-exposed PMMA beads exhibit several distinct spectral changes upon heating – decreases in the 2880 and 2910 cm^{-1} resonances of skeletal C-H stretching, as well as relative increases in resonances at 3000 cm^{-1} and decreases at 3050 cm^{-1}. Shifts in PS hsSRS spectra during IR exposure show relative increased vibrational activity

Table 4.1: Raman spectral band assignments in the CH stretch region
Control (23,73,74) and cellular (36,37,43,75) samples band assignments from their respective references.

Wavenumber	Chemical	Assignment
Polymer Microbeads		
2847	PMMA	C-H stretching of O-CH_3
2885	PMMA	C-H stretching of α-CH_3
2910	PMMA	symmetric C-H of -CH_2 ; C-H stretching of O-CH_3
2950	PMMA	symmetric C-H of α-CH_3; symmetric C-H of O-CH_3; asymmetric C-H of -CH_2
3000	PMMA	asymmetric C-H of O-CH_3, asymmetric C-H of α-CH_3
3050	PMMA	asymmetric C-H of O-CH_3
2850	Polystyrene	symmetric C-H of CH_2
2915	Polystyrene	asymmetric C-H of CH_2
3050	Polystyrene	=C—H stretching of aromatic ring
Biological Lipids		
2850	Lipids	Symmetric C-H stretch of aliphatic -CH_2
2880 or 2885	Lipids	asymmetric C-H of aliphatic -CH_2; Fermi resonance between the symmetric C-H stretching mode and the overtone of the C-H bending vibrations
2970 or 2960	Lipids	Asymmetric C-H stretch of -CH_3
3015 or 3023	Lipids	Alkyl =C—H stretches
Biological Proteins		
2940 or 2930	Proteins	Symmetric C-H stretch of -CH_3 Asymmetric C-H stretch of -CH_2 2930 cm-1 corresponds to the overtone of the CH_2 scissoring (δ(CH_2)) enhanced by Fermi resonance with the v_s-(CH_2) mode.
3000 - 3060	Proteins	sp^2 C-H stretch of aromatic/vinyl amino acid residues (=C—H)

around 2850 cm^{-1}, implying the possibility of relaxed steric hinderance of skeletal sp^3 CH_2 symmetric stretching modes, while broadening the 3050 cm^{-1} peak attributable to aromatic sp^2 C-H stretching and suggesting reduced steric hinderance around aromatic side chains. These observations show that utilizing a time resolved approach to obtaining hsSRS spectra of samples heated by pulsed IR light is feasible in highly Raman active idealized chemical samples.

The dominant Raman scatterers in the 2800-3100 cm^{-1} spectral region primarily include lipids and proteins – with some marginal nucleic acid contribution (33,34). Spatially and spectrally, nucleic acids are easy to separate in cellular images (35). However, since proteins and lipids in cells do not appear as spatially distinct as the resolution of our microscope, their distinct spectral information must be used to draw conclusions about their molecular dynamics. Understanding how proteins and lipids are separately affected by IR stimulation provides insight to the spectral shifts can be attributed to each biomolecule during live cell imaging. hsSRS imaging with IR stimulation was performed on separate aqueous preparations of biomimetic multi-lamellar vesicles (phosphatidylcholine - PC, neurologically derived, porcine sourced, Avanti Polar Lipids, Alabaster, AL, USA) and bovine serum albumin (BSA, 10%w/v) solutions.

An emulsion of multilamellar vesicles (MLVs) were imaged with hsSRS and focus precompensation during radiant exposures equivalent to threshold levels (10.63 J/cm^2) of IR exposures in live cells. These vesicles serve as a coarse chemical representation of cells to provide an isolated lipid preparation, free of protein or carbohydrate contribution to vibrational spectra. Infrared-exposed MLV spectra (**Figure 4.4A&B**) show distinct shifts in lipid molecule resonances relevant to lipid molecular packing order. Relevant spectral band assignments for biological lipid samples are summarized in **Table 4.1**. The 2850 cm^{-1} symmetric aliphatic C-H stretch resonance is markedly decreased, along with its Fermi resonance at 2880 cm^{-1}. Meanwhile, sp^2 C-H stretching resonances associated with unsaturated aliphatic chain motifs at 3010 cm^{-1} are substantially decreased. Crucially, ratiometric comparison of 2880 and 2850 cm^{-1} shows reduced rotational restriction in alkane chains, or a decrease in aliphatic tail packing order within the hydrophobic region of the membrane (**Figure 4.8C**). This is further supported by the observed decrease in the ratio of 2940 to 2830 cm^{-1}, which relates to increases in the solvent interaction with lipids (**Figure 4.4C**). These observations suggest that thermodynamic changes in lipid vibrational signatures during IR stimulation are discernable with hsSRS.

To characterize protein vibrational signature changes during IR-induced heating, the edge of a 10%w/v BSA solution meniscus was imaged with hsSRS using radiant exposures equivalent to threshold levels of IR exposures in live cells (**Figure 4.4D**). Changes in protein spectra during IR exposure appear to be negligible (**Figure 4.4E).** Furthermore, the contribution of protein vibrational spectra in ratiometric comparisons that reveal significant changes in MLV samples appear to contribute negligibly to IR-exposed changes in the BSA sample (**Figure 4.4F**). It is worth noting that the amino acid constituents of BSA, a water-soluble protein, may not be directly representative of a transmembrane protein one would observe as a component of the extracellular membrane or intracellular organelles. However, the data supports previous work showing that the shape of protein spectra in the CH-band region of the Raman spectrum do not appreciably change with temperature (36,37).

4.4.3 hsSRS of Neural Cell Models during INS

With the spectral changes in biomimetic samples established, hsSRS imaging during IR stimulation was conducted in an *in vitro* neural cell model - a neuroma-glioblastoma hybridoma cell line (NG-108-15, Sigma-Aldrich, MO, USA). The NG-108 cell line was used as a practically robust and experimentally resilient neuronal cell model for hsSRS imaging. These cells are an accepted electrodynamic model of *in*

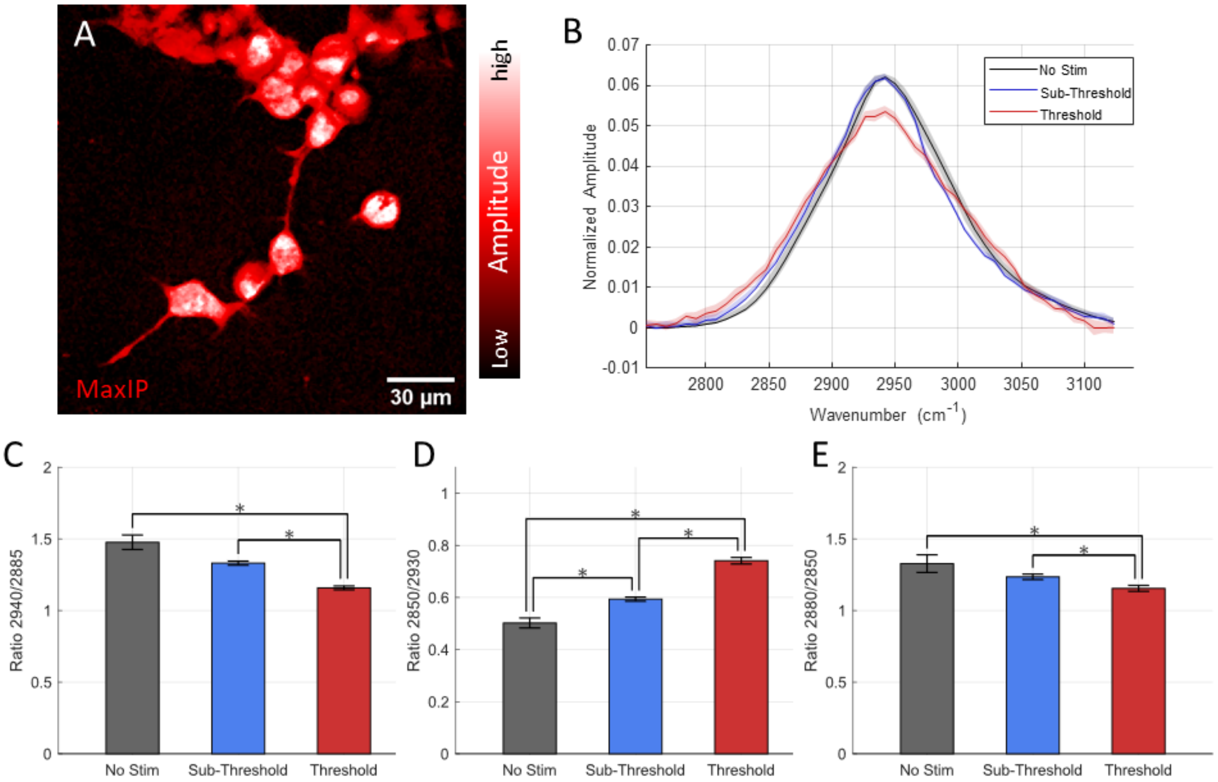

Figure 4.8: Vibrational Spectroscopic Imaging of NG108 Cells during infrared neural stimulation **(**A) Maximum Intensity projection of NG108 spectral image stack from 2800-3150 cm^{-1} [n = 50 images]. (B) Average SRS spectra obtained from NG108 cells during infrared neural stimulation of at and above activation threshold radiant exposures [n = 10-24 cells per group]. Peak ratio comparisons indicative (C) asCH_2/asCH_3 as a measure of trans-to-gauche isomerization of lipid tail groups, (D) symCH_2/symCH_3 as a measure of increased polar headgroup association with water due to membrane packing order decrease, and (E) asCH_2/symCH_2 as an indicator of decreasing acyl chain packing order. *indicates $p < 0.05$

vitro neurons and have been used in the past successfully to study electrodynamics evoked by IR stimulation (19,20,38). **Figure 4.8A** shows a maximum intensity projection of an hsSRS spectral image stack to highlight the morphology of NG-108 cells. Successful stimulation with pulsed IR light were verified in separate experiments (unpublished) of NG108 cells loaded with a calcium-sensitive dye, Fluo-4-AM at 1µM in balanced saline for 45 minutes. Two-photon fluorescence and SRS centered at 2880 cm^{-1} – an asymmetric sp^3 CH_2 resonance dominantly from lipids –images were acquired simultaneously during IR stimulation of NG108s at a range of IR doses until noticeable increases in calcium-dependent fluorescence responses were evoked (>2% increase in dF/F). Levels of IR evoking consistent intracellular calcium responses across the microscope's field of view were referred to as threshold levels of exposure. Cells were imaged with hsSRS during IR stimulation with threshold and subthreshold (about half of threshold levels) doses of IR light.

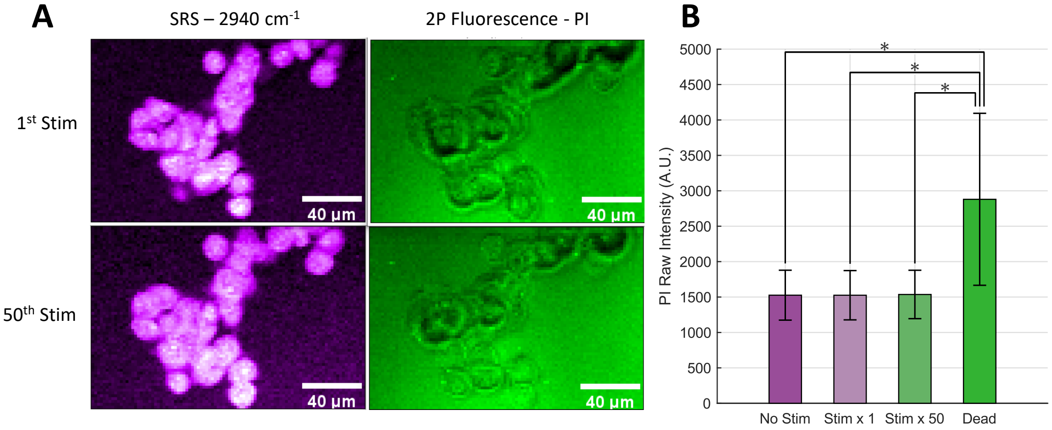

Figure 4.9: NG108 Cell Viability following hsSRS and repeated INS
(A) Representative average intensity projection images of NG108 cells with SRS (left, magenta) and 2P fluorescence (green, right, identical intensity image scaling) of a cell viability indicator, propidium iodide (PI). Slight differences in cell morphology appear after 50 rounds of INS (bottom) compared to 1 round of INS (top). No substantial update of PI was observable. Scale bars are all 40 µm in width. (B) Intensity level comparison of PI fluorescence in cells exposed to different amounts of threshold INS events. No significant differences observed between non-stimulated and stimulated conditions. Significantly lower fluorescence compared to positive control of dead cells across all conditions. Asterisk indicates $p < 0.05$ based on a 2-sided student's t-test comparisons of cell intensity means and standard deviations across all measured cells (n = 38).

The resultant area-normalized hsSRS spectra of NG108 cells under baseline (unstimulated), subthreshold, and threshold stimulation conditions are shown in **Figure 4.8B**. Relevant spectral band assignments for biological samples in the CH-stretch region are summarized in **Table 4.1**. Shoulders appearing at 2850 cm-1 during stimulation are indicative of relatively increased vibrational resonant activity from symmetric aliphatic C-H stretching in lipid tail chains. Decreases in the relative intensity ratio between 2940 and 2885 cm^{-1} (**Figure 4.8C**) suggest a decrease in packing order within the hydrocarbon tails of the lipid molecules due to *trans-gauche* isomerization of sp^3 hydrocarbon chains. Interestingly, the 2850 cm^{-1} shoulder appears to increase in spectral intensity relative to the associated Fermi resonance at 2880 cm^{-1}, possibly suggesting a reduction of intermolecular steric hindrance between aliphatic lipid tails, or more rotational freedom of hydrocarbon chains. These observations were quantified by calculating the intensity ratio between 2850 and 2940 cm^{-1} (**Figure 4.8D**), as well as 2880 and 2850 cm^{-1} (**Figure 4.8E**). These metrics respectively offer a quantification of lipid tail chain packing order – which was previously hypothesized to decrease during IR stimulation (3). **Figure 4.8C-E** shows these intensity ratios from NG-108 whole cell spectra obtained at baseline, sub-threshold, and threshold levels of INS previously established to elicit calcium transients. Statistically significant differences ($p < 0.05$, indicated with asterisk) in these ratios suggest decreased hydrocarbon tail chain packing in cellular lipid membranes. Notably, in each comparison, the ratios calculated for subthreshold exposure fall between unstimulated and stimulated conditions. Of particular note, the shoulder around 3030 cm^{-1} – which is a sp^2 CH (methylene) resonance assignable to CH bonds at points of unsaturation in lipid hydrocarbon tails – appears at the threshold stimulation but is reduced in the subthreshold and no stimulation cases (**Figure 4.8B**).

The hsSRS spectral acquisition as described above requires cells to be exposed to 50 different rounds of IR stimulation – possibly damaging the cells and yielding biologically irrelevant observations. Though no morphological changes were observed in the stimulation experiments, cell viability was verified after repeated IR exposure. Exposed NG108 cells were imaged with multiphoton fluorescence to track the uptake of a cell damage indicator – propidium iodide (PI) – simultaneously with SRS tuned to the 2940 cm^{-1} CH_3 resonance. Cells were imaged through 50 rounds of stimulation, using parameters similar to those used during a live cell hsSRS imaging experiment (**Figure 4.9A**). Some cell swelling was observed morphologically, but no uptake of PI was observed (**Figure 4.9B**)– suggesting that the repetitive nature of hsSRS acquisition did not have any immediate impact on acute cell viability.

4.4.4 Ratiometric fluorescence imaging of functional lipid dye during INS verify changes in lipid bilayer packing order

Ratiometric fluorescence of di-4-ANNEPS emission, a probe of membrane packing order, was employed to verify cellular lipid dynamics as observed in vibrational spectra (25). Di-4-ANNEPS rotoisomerization is known to be dependent on fatty acid tail chain packing order in lipid membranes. During IR stimulation, if lipid tail chain packing order is decreased, a similar decrease in general polarization (GP) metric should follow. In place of the conventional approach for calculating GP, intensity-invariant adaptation of GP was utilized to circumvent the defocusing effect during IR stimulation (detailed in Methods and **Figure 4.5**). **Figure 4.10A** depicts an intensity image of di-4-ANNEPS loaded NG-108 cells overlaid with color denoting GP calculation at each pixel. **Figure 4.10B** and **C** show the mean single cell GP time traces and their standard deviations for each dosing condition. The intensity-invariant GP of di-4-ANNEPS (**Figure 4.5**, see Methods) shows substantial decrease in GP as a function of IR stimulation dosage (**Figure 4.10C**). A decrease in GP suggests a decrease in lipid chain packing order during IR stimulation supporting the hsSRS observations.

4.5 Discussion

Our current understanding of label-free directed energy neuromodulation continues to raise questions about their mechanistic bases. An improved understanding of INS mechanisms provides a fundamental framework for the development of future innovative neuromodulation technologies. Here, we provide an approach that uses hsSRS microscopy to gain insight to the role of lipid dynamics in live neural

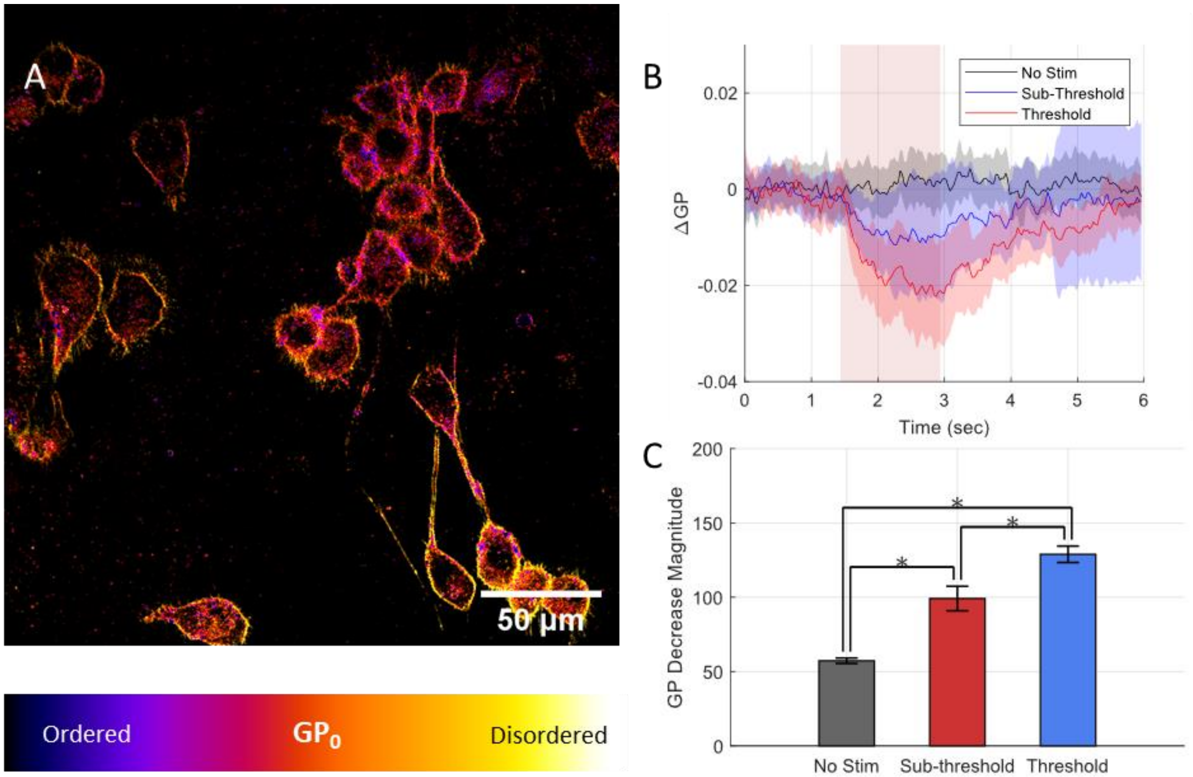

Figure 4.10: General polarization (GP) measurements in NG108 cells of di-4-ANNEPS during INS (A) Fluorescence intensity images overlaid with calculated initial GP values of NG108 cell cultures loaded with di-4-ANNEPS. (B) Relative changes in adapted general polarization metrics NG108 cells during varied doses of IR stimulation. Decreases in relative general polarization are indicative of decreases in relative extracellular lipid membrane packing order which agree with hsSRS observations. Error traces represent standard deviation across all cell responses [n = 50-109 cells]. (C) Magnitude of GP decreases across sub-threshold [5.02J/cm2] and threshold [10.63 J/cm2] levels of radiant exposure. Error bars represent SEM across all cells within each condition. * indicates $p < 0.05$

cells during INS. Most traditional methods to observe lipid-specific dynamics (e.g. isolated lipid preparations, electrophysiology, x-ray diffraction, neutron scattering) in cells in real time suffer from lack of specificity or biological compatibility. Methods that utilize fluorescent tags (e.g. fluorescence correlation spectroscopy, fluorescence recovery after photobleaching) provide insight into the dynamics of lipids in live cells but are inherently indirect. The goal of this work was to directly observe the biophysical dynamics of INS with a vibrational spectroscopic approach in live neural cells. Using the intrinsic Raman contrast of lipids, spectroscopic insight would help clarify the mechanistic role of lipid dynamics in INS. Our demonstration of characterizing and precompensating for dynamic defocus during INS with hsSRS is a novel approach in biomedical microscopy that is applicable to studying the molecular biophysics of live cell models more generally.

Photothermal events are notoriously difficult to address with biological microscopy due to the relationship between temperature and refractive index in water. While bulk changes in sample temperature can impact optical aberrations in microscopes, spatial thermal gradients that vary on the order of the microscope's field of view can have significant impacts on the refraction of light into the sample (**Figure 4.7B**). Accounting for defocusing actively on millisecond timescales may be possible with dynamic adaptive optics approaches but is far from trivial to implement. Instead, our approach to adjust for IR-induced defocusing of the fluorescence excitation empirically (**Figure 4.7**A**&C**) – though coarse compared to adaptive optics – enables us to gather useful insight to the biophysical phenomena associated with INS (**Figure 4.8**). The reliable timing of stimulation can be leveraged to employ a time-resolved spectroscopy approach to hsSRS imaging at high framerates. In doing so, we demonstrate that high-speed vibrational dynamics can be resolved in live cell preparations safely to yield biologically meaningful observations. In studying INS using high numerical aperture microscopy, where IR induced deflections in focal length can equal or exceed the depth of focus of a particular imaging objective, we urge others to interpret their results cautiously. Thermal defocusing can have a disproportionate impact on single-channel intensiometric-based measurements and need to be carefully accounted for (**Figure 4.5**). In cases where intensity noticeably changes during exposure, we encourage others to employ ratiometric or multi-spectral approaches to allow for defocusing artifacts to be readily accounted for. With fluorescence microscopy, where quantum yield, fluorescence intensity, and spectral profiles are well known to be sensitive to both heating and defocusing (39–41), having simultaneous or time-resolved multispectral reference bases will allow for such artifacts to be accounted for in post-processing.

There are several spectral changes in the CH-stretch region of the Raman spectrum (2800-3100 cm^{-1}) that one might expect to see if the current INS mechanistic model was valid. *Trans-gauche* isomerization, or rotoisomerization, of sp^3 hydrocarbon chains – primarily associated with lipid hydrophobic tail groups in Raman imaging – can give rise to a number of steric effects that drive lipid membrane deformations (36,37,42,43). Specifically, lipid packing order – or the ability for lipid molecules to stack neatly alongside each other within the membrane leaflets – was hypothesized to decrease with elevated temperature during INS. Rotoisomerization in membrane lipids geometrically shortens acyl tail groups, resulting in membrane thinning. While quantifying the absolute deformation of lipid membrane thickness with SRS would require additional calibration experiments, relative indicators of molecular interactions can be quantified with hsSRS. An increased quantity of gauche rotamer within the hydrophobic region of the membrane leads to geometric acyl tail shortening and sterically drives lipid molecules apart from each other. The result is a decrease in membrane packing order. In the CH-stretch region of the Raman spectrum, relative changes in symmetric (2850 cm^{-1}) and asymmetric (2880 cm^{-1}) aliphatic C-H stretching indicate shifts in molecular packing order due to changes in the rotational freedom of hydrocarbon chains in lipid tails. Raman signal at these resonances is largely attributed to biological lipids (**Figure 4.4**)(33). A decrease in the ratio of 2880 and 2850 cm^{-1} during INS (**Figure 4.8E**) is indicative of a ‘loose’ packing order between lipid molecules or an increase in trans-gauche isomerization (44,45). The rotoisomerization of lipid tails is well known to both decrease membrane thickness and increase the area of each lipid molecule’s solvent interactions (46–48). Changes in the ratio between 2940 and 2885 cm^{-1} offer insight to water interaction with lipid molecules, which should increase with temperature. The data show a decrease in the ratio between 2940 and 2885 cm^{-1} (**Figure 4.8C**), which is in line with the idea that lipid molecules expand within the membrane leaflets to leave room for more potential solvent interactions (e.g. hydrogen bonding) with elevated temperatures. The IR dose dependance of this observation further suggests that the relative degree of isomerization correlates with levels of IR exposure that would evoke neural activity *in vitro*. The observations of a progressive increase in isomerization with IR exposure support the existing mechanistic model of INS, where transient temperature changes are accompanied by changes in physical bilayer geometry.

The shoulder appearing around 2990 and 3030 cm^{-1} during INS in cells (**Figure 4.8B**) arise from relative increases in vinyl C-H resonances, which correspond to points of unsaturation in lipid tail acyl chains. Relative increases in vinyl C-H signal can arise from reduced steric hinderance of sp^2 C-H stretching as well as compositional or membrane potential related changes when the lipid bilayer undergoes thermal changes. Curiously, the appearance of the 3030 cm^{-1} shoulder in threshold stimulated cells was reduced in sub-threshold levels of stimulation. This resonance at 3030 cm^{-1} may provide a key marker for neural biophysics during INS.

The vinyl C-H portion (2980-3100 cm^{-1}) of the C-H stretch region does contain SRS signal contributions from proteins– particularly from amino acid residues such as tyrosine, phenylalanine, and tryptophan. These amino acids play a key structural role in stabilizing hydrophobic domains of transmembrane proteins in the cell membrane. Control experiments observing the IR-related dependance of BSA SRS spectra in solution (**Figure 4.4**) as well as evidence from others (36,37,49) reinforce that thermally-mediated changes in protein dynamics are not major contributors in the CH stretch region of the Raman spectrum. As such, we conclude protein signal contributes minimally to the photothermal mediated SRS changes that would be expected during INS. Others have attributed relative decreases in 2930 cm^{-1} signal to changes in cellular membrane potential, enabling the visualization of neuronal action potentials with SRS microscopy (18,32). These spectral changes were attributed to the decrease in positively-charge proteins electrostatically accumulating at the extracellular membrane surface when a cell is at its resting membrane potential. A reduction in membrane potential was suspected to reduce membrane-associated proteins in solution at the cell membrane surface. Our results show a considerable reduction in relative 2930-2940 cm^{-1} signal during INS (**Figure 4.8B**), thus electrostatic association of soluble proteins with cell surfaces may play some role in our results. Several experimental details suggest that membrane potential changes from electrostatic protein association would not be contributing to our spectra. Defocusing artifacts make it difficult to obtain conclusions about absolute molecular concentrations during INS (**Figure 4.7A-C**). Practically, our approach to region of interest selection, non-balanced detection, and imaging medium formulation confounds any comparability of our results with these previous studies. However, Lee et al. did employ a similar time-resolved approach for acquiring SRS spectra as a function of membrane potential – demonstrating the utility of such an approach for certain types of experiments beyond photothermal phenomena.

The physical changes in the lipid bilayer during rapid heating with IR light are thought to give rise – at least in part – to the cell capacitance increase that drives cellular depolarization during INS(2,3). Our results (**Figure 4.8**) support the idea that the lipid bilayer undergoes some thermally mediated chemo-physical change during INS that is observable via vibrational imaging and correlate with the level of delivered stimulus. While these findings are promising, they do not definitively support that bilayer deformation is directly causal to the stimulatory effect of INS. Though beyond the scope of this work, questions remain about how transmembrane ion channels may be independently sensitive to lipid membrane geometry and thermodynamics. Lipid thermodynamics are known to affect the conformational and functional properties of transmembrane ion channels (50–53). It is not clear whether the capacitive effect or the actual physical change in the lipid bilayers themselves give rise to stimulatory phenomenon. It is difficult to decouple chemo-physical and thermal electrodynamic changes in biologically relevant preparations. A preparation of lipid vesicles or cells expressing voltage gated ion channels loaded with a UV photo-switchable lipid analogue (e.g., containing an azobenzene moiety in the tail group) may be a useful experiment. The photo-switching property of such synthetic lipids would allow for optical control of membrane packing order with substantially reduced photothermal effects.

The current hypothesis for how INS occurs is that rapid heating causes a capacitive inward current that can depolarize neurons and lead to action potential generation (2). This capacitive current is thought to arise from biophysical changes within the extracellular membrane – namely *trans-gauche* isomerization of lipid acyl tail chains – that change the physical dimensions of the extracellular membrane due to temperature elevations (3). This deformation is accompanied by a movement of membrane-associated charge that – when hot and fast enough – can generate an inward current that depolarizes cells. The model of this phenomenon relies on steady-state chemical assessments of synthetic lipid bilayer geometry (54,55). The changes in bilayer geometry are used to inform a computational electrodynamic model that is compared against previous experimental work (2,38). While the model of chemo-physical and electrodynamic phenomena convincingly reproduces experimental data, capacitance changes and cellular electrodynamics are ultimately influenced by more than lipid dynamics alone *in vitro* and *in vivo*. Our work here provides direct evidence that lipid membrane dynamics are actively changing during INS in neural cells *in vitro*. The causality of this phenomena remains to be proven. But the insight provided by our work shows how lipid membrane dynamics can be leveraged to selectively modulate cellular physiology.

Our SRS spectral observations are supported by an additional gold standard means of measuring lipid dynamics in real-time – ratiometric fluorescence of a lipophilic dye, di-4-ANNEPS (**Figure 4.10**, **Figure 4.5**). The negative changes in GP during INS affirm the decrease in membrane packing order observed with hsSRS. The magnitude of the changes in GP scaled with the level of stimulus delivered (**Figure 4.10B&C**). The data further suggests that hsSRS can be leveraged as a complementary tool to study lipid biophysics alongside traditional fluorescence approaches. Others have applied hsSRS to observe lipid biophysics in synthetic preparations (16,17), or to study lipid metabolism at the biomolecular level (56,57). Stimulated Raman microscopy has not previously been applied to the study of biophysical thermodynamics at sub-second timescales. Our work explores a temporal regime of live cell biophysics that few have ventured into with SRS. This work provides a practical extension to the existing work around hsSRS development while shedding light on a question pertinent to the field of optical neuromodulation.

While the implementation of hsSRS here can resolve high speed spectral dynamics well below a second, it does take several minutes to build observations of events on a spectral basis. In situations where repeated perturbation of cells is not practical, the same approach can be implemented with a drastically reduced number of spectral channels. Alternatively, multispectral approaches leveraging simultaneous acquisition of multiple resonances would be advantageous. To account for the defocusing artifacts described here, at least two spectral channels need to be acquired to accurately draw conclusions – thus single-shot perturbations are not readily applicable with the demonstrated approach here. The fast rates of development in bioimaging with SRS show promise in pushing SRS based imaging methods to their limits. Our work shows that hsSRS can be applied to a range of lipid biophysics experiments as a complement to more conventional fluorescence-based approaches. In contrast to fluorescence-based approaches that rely on indirect readout from reporter molecules interacting with lipids in the cell membrane, vibrational contrast like that of hsSRS enables direct inference to be made specific to lipids at the intra- and intermolecular levels. As technology in coherent Raman imaging continues to improve with better lasers, detectors, and signal processing strategies, we can expect to see extensions of hsSRS to address many other areas of lipid biophysics and beyond. Currently, signal to noise limits the real-time performance of hsSRS in the fingerprint region of the Raman spectrum (400-1700 cm^{-1}). In future studies we propose to study the fingerprint region which provides more information about other biomolecules, such as DNA, RNA, and carbohydrates, which can be used to study macromolecular phase separation phenomena, chromatin dynamics, or glycogen metabolism directly without exogenous labeling. Furthermore, coherent Raman imaging can be readily performed simultaneously with other nonlinear microscopy modalities (22). Multiplexing modalities might enable studies into how lipid membrane biophysics can influence biological dynamics with conventionally accepted molecular reporters. With this in mind, hsSRS has promising potential for a diverse range of bioimaging applications.

Alternative approaches utilizing deuterated lipid preparations to shift lipid-specific resonances into the “silent window” of the Raman spectrum (1700-2700 cm^{-1}) may offer additional insight into the role of vinyl C-D resonances in the biophysics of INS (12,58–60). However, the applications of deuterated lipids may not be easily replicable in live cells as it can interfere with the hydrogen bonding dynamics crucial to cell membrane integrity. Currently, fast implementation of hsSRS is technically hampered by the signal-to-noise performance in the fingerprint window of the Raman spectrum (400-1700 cm^{-1}). Utilizing other features of the Raman spectrum that are more directly attributed to lipid tail chain rotoisomerization (e.g. the skeletal vibrational C-C modes between 1030 and 1150 cm^{-1}, as well as C=C stretching modes around 1650 cm^{-1}) might provide more direct mechanistic insight to INS once possible (44). Some promising newer spectroscopic and computational denoising methods that circumvent these noise issues are gaining popularity, but still require careful validation for high-speed imaging of cellular dynamics (61–64). Ongoing work continues to improve the technical capabilities of SRS such that real time imaging of fingerprint spectral features within live cells may be possible. Coherent anti-Stokes Raman scattering, or CARS - a similar contrast modality to SRS – has achieved considerably fast imaging throughput at high spectral resolution over the span of the CARS spectrum (5ms/px dwell times over >3000 cm^{-1} bandwidth) (61,65). While this approach was too slow for spatially resolving cellular dynamics in real time for our study, broadband CARS approaches may be suitable for numerous other biological applications with different instrument performance needs.

Though the data presented here offer support for the involvement of lipid dynamics in INS, it needs to be noted that focus precompensation and hsSRS does not readily show the absolute magnitude of deformation in the cell membrane during INS. With a molecular dynamic model of INS biophysics, simple bilayer geometry simulations may enable some degree of calibration to correlate observed hsSRS spectra with lipid bilayer physical properties. Without clear approximations of lipid bilayer physical or electrical properties, it becomes difficult to judge or estimate the cell capacitance changes postulated to depolarize cells from SRS data alone. Integrating voltage imaging or electrophysiology alongside our existing hsSRS experimental preparation may be helpful in identifying a relationship between lipid dynamics and capacitance. Imaging systems with framerates exceeding 1 kHz can provide a window into these dynamics – however we were unable to reach such high framerates with our system without damaging cells. More generally, our results provide supportive evidence of the role lipids play in INS however, the data does not show a causal relationship between lipid dynamics and INS. Further, our imaging approach does not differentiate between extracellular membranes and intracellular organelle membranes. Transmembrane protein sensitivity to INS phenomena is still not clear, though it is known that different molecular pathways can be actuated depending on cell phenotype (20,21,66–70). Despite these caveats, the provided data clearly demonstrates that lipid bilayer dynamics are changing during INS and these changes track with magnitude of stimulus. These results provide validation of the current mechanism's key assumptions in a live neural cell model. The understanding of this concept serves as a crucial basis for understanding of label free neuromodulation more broadly. Further, the general experimental framework presented here is readily applicable to other methods of directed energy neuromodulation as well as in the study of other dynamic processes.

The mechanistic basis of directed energy label-free neuromodulation has long been a question lacking complete answers (71,72). Having a better understanding of how directed energy in the optical domain can be used to modulate brain function opens the door for innovation in neuromodulation to improve spatial targeting, temporal accuracy, and long-term utility, optically or otherwise. Extending these understandings to the development of new neuromodulation methods, neural prostheses, and therapeutic interventions provides a promising outlook for directed energy approaches. Whether the mechanistic basis for methods of directed energy neuromodulation, such as infrared, ultrasonic, or radio frequency-based approaches, are shared remains to be demonstrated. Our approach may serve as a valuable benchmark for answering such questions in the future as technology in neuromodulation and hsSRS imaging continues to develop.

4.6 Conclusion

We have used hsSRS to experimentally demonstrate the mechanistic involvement of lipid dynamics in INS in live neural cells. Our results provide direct supportive evidence of lipid bilayer structural changes related to thermally induced *trans-gauche* isomerization of lipid tail hydrocarbon chains during INS. These experimental observations are in line with the currently proposed mechanistic model of INS. The implications from our results reinforce the idea that the photothermal basis of INS may be driving a general, nonspecific effect in live cells that evokes a multitude of physiological responses. The experimental framework also highlights the utility of hsSRS microscopy in addressing questions with high temporal resolution requirements and will continue to provide fruitful information about live cell biophysics beyond neuromodulation.

4.7 Funding

Funding for this work was provided by the following grants: AFOSR DURIP FA9550-15-1-0328, AFOSR FA9550-14-1-0303, AFOSR FA 9550-17-1-0374. Additional support was provided from funding through the Vanderbilt University Trans-Institutional Partnership (TIPS) Program. WRA was supported through the ASEE NDSEG Fellowship.

4.8 Acknowledgements

The authors wish to thank Dr. Manqing Wang, Dr. Paul Stoddart, Dr. William Patrick Roach, Dr. Mark Hutchinson, and Dr. Valentina Benfenati for their discussion and guidance that formed the early basis for this work. The authors would also like to thank Dr. Bruce Tromberg for his suggestions and guidance for the ratiometric fluorescence imaging experiments presented in this study. The authors also thank Dr. Bryan Millis for his input on the manuscript.

4.9 Author Contributions

AMJ, EDJ, and WRA conceived the idea for the manuscript. AMJ and EDJ secured funding support for the published work. AMJ, EDJ, GT, RG, and WRA designed the experiments. AL assisted in identifying, preparing, imaging the control samples for the study, and interpreting the results. AIBC assisted in preparing cell cultures, formulating experimental approaches, and data analysis. RG, AL, and GT contributed to data processing and analysis. BRJ, CD, AL, and WRA prepared the multilamellar vesicles. WRA assisted in all sample preparations, performed all imaging experiments, image processing, data analysis, data visualization, and wrote the manuscript. All authors contributed to editing manuscript.

4.10 Conflicts of Interest

The authors declare no conflicts of interest.

4.11 Data Availability

Any raw or processed data, processing, and analysis code are available upon request from the corresponding authors.

4.12 References

1. Wells J, Kao C, Konrad P, Milner T, Kim J, Mahadevan-Jansen A, et al. Biophysical mechanisms of transient optical stimulation of peripheral nerve. Biophys J. 2007 Oct 1;93(7):2567–2580.
2. Shapiro MG, Homma K, Villarreal S, Richter C-P, Bezanilla F. Infrared light excites cells by changing their electrical capacitance. Nat Commun. 2012 Mar 13;3:736.

3. Plaksin M, Shapira E, Kimmel E, Shoham S. Thermal Transients Excite Neurons through Universal Intramembrane Mechanoelectrical Effects. Phys Rev X. 2018 Mar 16;8(1):011043.
4. Throckmorton G, Cayce J, Ricks Z, Adams WR, Jansen ED, Mahadevan-Jansen A. Identifying optimal parameters for infrared neural stimulation in the peripheral nervous system. Neurophotonics. 2021 Jan;8(1):015012.
5. Wells J, Kao C, Mariappan K, Albea J, Jansen ED, Konrad P, et al. Optical stimulation of neural tissue in vivo. Opt Lett. 2005 Mar 1;30(5):504–506.
6. Moen EK, Beier HT, Ibey BL, Armani AM. The role of membrane dynamics in electrical and infrared neural stimulation. In: Wax A, Backman V, editors. Biophysics, Biology, and Biophotonics: the Crossroads. SPIE; 2016. p. 97190E.
7. Walsh AJ, Cantu JC, Ibey BL, Beier HT. Short infrared laser pulses increase cell membrane fluidity. In: Jansen ED, Beier HT, editors. Optical Interactions with Tissue and Cells XXVIII. SPIE; 2017. p. 100620D.
8. Nagle JF, Tristram-Nagle S. Structure of lipid bilayers. Biochimica et Biophysica Acta (BBA) - Reviews on Biomembranes. 2000 Nov;1469(3):159–195.
9. Lyatskaya Y, Liu Y, Tristram-Nagle S, Katsaras J, Nagle JF. Method for obtaining structure and interactions from oriented lipid bilayers. Physical review E, Statistical, nonlinear, and soft matter physics. 2001;63(1 Pt 1):011907–011907.
10. Kucerka N, Nagle JF, Sachs JN, Feller SE, Pencer J, Jackson A, et al. Lipid bilayer structure determined by the simultaneous analysis of neutron and X-ray scattering data. Biophys J. 2008 Sep;95(5):2356–2367.
11. Amaro M, Reina F, Hof M, Eggeling C, Sezgin E. Laurdan and Di-4-ANEPPDHQ probe different properties of the membrane. J Phys D, Appl Phys. 2017 Apr 5;50(13):134004.
12. Syed A, Smith EA. Raman Imaging in Cell Membranes, Lipid-Rich Organelles, and Lipid Bilayers. Annu Rev Anal Chem (Palo Alto, Calif). 2017 Jun 12;10(1):271–291.
13. Köhler M, Machill S, Salzer R, Krafft C. Characterization of lipid extracts from brain tissue and tumors using Raman spectroscopy and mass spectrometry. Anal Bioanal Chem. 2009 Mar;393(5):1513–1520.
14. Freudiger CW, Min W, Holtom GR, Xu B, Dantus M, Xie XS. Highly specific label-free molecular imaging with spectrally tailored excitation stimulated Raman scattering (STE-SRS) microscopy. Nat Photonics. 2011 Jan 16;5(2):103–109.
15. Lee HJ, Cheng J-X. Imaging chemistry inside living cells by stimulated Raman scattering microscopy. Methods. 2017 Sep 1;128:119–128.
16. Duboisset J, Berto P, Gasecka P, Bioud F-Z, Ferrand P, Rigneault H, et al. Molecular orientational order probed by coherent anti-Stokes Raman scattering (CARS) and stimulated Raman scattering (SRS) microscopy: a spectral comparative study. J Phys Chem B. 2015 Feb 19;119(7):3242–3249.
17. Cheng J-X, Pautot S, Weitz DA, Xie XS. Ordering of water molecules between phospholipid bilayers visualized by coherent anti-Stokes Raman scattering microscopy. Proc Natl Acad Sci USA. 2003 Aug 19;100(17):9826–9830.
18. Lee HJ, Zhang D, Jiang Y, Wu X, Shih P-Y, Liao C-S, et al. Label-Free Vibrational Spectroscopic Imaging of Neuronal Membrane Potential. J Phys Chem Lett. 2017 May 4;8(9):1932–1936.
19. Paviolo C, Haycock JW, Cadusch PJ, McArthur SL, Stoddart PR. Laser exposure of gold nanorods can induce intracellular calcium transients. J Biophotonics. 2014 Oct;7(10):761–765.
20. Tolstykh GP, Olsovsky CA, Ibey BL, Beier HT. Ryanodine and IP3 receptor-mediated calcium signaling play a pivotal role in neurological infrared laser modulation. Neurophotonics. 2017 Apr 5;4(2):025001.
21. Borrachero-Conejo AI, Adams WR, Saracino E, Mola MG, Wang M, Posati T, et al. Stimulation of water and calcium dynamics in astrocytes with pulsed infrared light. FASEB. 2020;
22. Adams WR, Mehl B, Lieser E, Wang M, Patton S, Throckmorton GA, et al. Multi-modal nonlinear optical and thermal imaging platform for label-free characterization of biological tissue. Sci Rep. 2021 Apr 13;11(1):8067.

23. Fu D, Holtom G, Freudiger C, Zhang X, Xie XS. Hyperspectral imaging with stimulated Raman scattering by chirped femtosecond lasers. J Phys Chem B. 2013 Apr 25;117(16):4634–4640.
24. Hellerer T, Enejder AMK, Zumbusch A. Spectral focusing: High spectral resolution spectroscopy with broad-bandwidth laser pulses. Appl Phys Lett. 2004 Jul 5;85(1):25–27.
25. Parasassi T, Gratton E, Yu WM, Wilson P, Levi M. Two-photon fluorescence microscopy of laurdan generalized polarization domains in model and natural membranes. Biophys J. 1997 Jun;72(6):2413–2429.
26. Schindelin J, Arganda-Carreras I, Frise E, Kaynig V, Longair M, Pietzsch T, et al. Fiji: an open-source platform for biological-image analysis. Nat Methods. 2012 Jun 28;9(7):676–682.
27. Hiner MC, Rueden CT, Eliceiri KW. SCIFIO: an extensible framework to support scientific image formats. BMC Bioinformatics. 2016 Dec 7;17(1):521.
28. Legland D, Arganda-Carreras I, Andrey P. MorphoLibJ: integrated library and plugins for mathematical morphology with ImageJ. Bioinformatics. 2016 Nov 15;32(22):3532–3534.
29. Owen DM, Rentero C, Magenau A, Abu-Siniyeh A, Gaus K. Quantitative imaging of membrane lipid order in cells and organisms. Nat Protoc. 2011 Dec 8;7(1):24–35.
30. Ford JB, Ganguly M, Poorman ME, Grissom WA, Jenkins MW, Chiel HJ, et al. Identifying the role of block length in neural heat block to reduce temperatures during infrared neural inhibition. Lasers Surg Med. 2020;52(3):259–275.
31. Schiebener P, Straub J, Levelt Sengers JMH, Gallagher JS. Refractive index of water and steam as function of wavelength, temperature and density. J Phys Chem Ref Data. 1990 May;19(3):677–717.
32. Liu B, Lee HJ, Zhang D, Liao C-S, Ji N, Xia Y, et al. Label-free spectroscopic detection of membrane potential using stimulated Raman scattering. Appl Phys Lett. 2015 Apr 27;106(17):173704.
33. Zhang D, Wang P, Slipchenko MN, Ben-Amotz D, Weiner AM, Cheng J-X. Quantitative vibrational imaging by hyperspectral stimulated Raman scattering microscopy and multivariate curve resolution analysis. Anal Chem. 2013 Jan 2;85(1):98–106.
34. Wang K, Zhang D, Charan K, Slipchenko MN, Wang P, Xu C, et al. Time-lens based hyperspectral stimulated Raman scattering imaging and quantitative spectral analysis. J Biophotonics. 2013 Oct;6(10):815–820.
35. Lu F-K, Basu S, Igras V, Hoang MP, Ji M, Fu D, et al. Label-free DNA imaging in vivo with stimulated Raman scattering microscopy. Proc Natl Acad Sci USA. 2015 Sep 15;112(37):11624–11629.
36. Pézolet M, Georgescauld D. Raman spectroscopy of nerve fibers. A study of membrane lipids under steady state conditions. Biophys J. 1985 Mar;47(3):367–372.
37. Taraschi T, Mendelsohn R. Lipid-protein interaction in the glycophorin-dipalmitoylphosphatidylcholine system: Raman spectroscopic investigation. Proc Natl Acad Sci USA. 1980 May;77(5):2362–2366.
38. Brown WGA, Needham K, Nayagam BA, Stoddart PR. Whole cell patch clamp for investigating the mechanisms of infrared neural stimulation. J Vis Exp. 2013 Jul 31;(77).
39. Walsh AJ, Masters DB, Jansen ED, Welch AJ, Mahadevan-Jansen A. The effect of temperature on the autofluorescence of scattering and non-scattering tissue. Lasers Surg Med. 2012 Nov;44(9):712–718.
40. Zaman RT, Rajaram N, Walsh A, Oliver J, Rylander HG, Tunnell JW, et al. Variation of fluorescence in tissue with temperature. Lasers Surg Med. 2011 Jan;43(1):36–42.
41. Moreau D, Lefort C, Burke R, Leveque P, O’Connor RP. Rhodamine B as an optical thermometer in cells focally exposed to infrared laser light or nanosecond pulsed electric fields. Biomed Opt Express. 2015 Oct 1;6(10):4105–4117.
42. Minamikawa T, Niioka H, Araki T, Hashimoto M. Real-time imaging of laser-induced membrane disruption of a living cell observed with multifocus coherent anti-Stokes Raman scattering microscopy. J Biomed Opt. 2011 Feb;16(2):021111.

43. Wu H, Volponi JV, Oliver AE, Parikh AN, Simmons BA, Singh S. In vivo lipidomics using single-cell Raman spectroscopy. Proc Natl Acad Sci USA. 2011 Mar 1;108(9):3809–3814.
44. Gaber BP, Peticolas WL. On the quantitative interpretation of biomembrane structure by Raman spectroscopy. Biochimica et Biophysica Acta (BBA) - Biomembranes. 1977 Mar;465(2):260–274.
45. Snyder RG, Scherer JR, Gaber BP. Effects of chain packing and chain mobility on the raman spectra of biomembranes. Biochimica et Biophysica Acta (BBA) - Biomembranes. 1980;601:47–53.
46. Szekely P, Dvir T, Asor R, Resh R, Steiner A, Szekely O, et al. Effect of temperature on the structure of charged membranes. J Phys Chem B. 2011 Dec 15;115(49):14501–14506.
47. Zhuang X, Makover JR, Im W, Klauda JB. A systematic molecular dynamics simulation study of temperature dependent bilayer structural properties. Biochim Biophys Acta. 2014 Oct;1838(10):2520–2529.
48. Kučerka N, Nieh M-P, Katsaras J. Fluid phase lipid areas and bilayer thicknesses of commonly used phosphatidylcholines as a function of temperature. Biochim Biophys Acta. 2011 Nov;1808(11):2761–2771.
49. Laroche G, Carrier D, Pézolet M. Study of the effect of poly(L-lysine) on phosphatidic acid and phosphatidylcholine/phosphatidic acid bilayers by raman spectroscopy. Biochemistry. 1988 Aug 23;27(17):6220–6228.
50. Startek JB, Boonen B, López-Requena A, Talavera A, Alpizar YA, Ghosh D, et al. Mouse TRPA1 function and membrane localization are modulated by direct interactions with cholesterol. Elife. 2019 Jun 11;8.
51. Antonov VF, Petrov VV, Molnar AA, Predvoditelev DA, Ivanov AS. The appearance of single-ion channels in unmodified lipid bilayer membranes at the phase transition temperature. Nature. 1980 Feb 7;283(5747):585–586.
52. Levi V, Rossi JPFC, Echarte MM, Castello PR, González Flecha FL. Thermal Stability of the Plasma Membrane Calcium Pump. Quantitative Analysis of Its Dependence on Lipid-Protein Interactions. Journal of Membrane Biology. 2000 Feb 1;173(3):215–225.
53. Cantu JC, Tarango M, Beier HT, Ibey BL. The biological response of cells to nanosecond pulsed electric fields is dependent on plasma membrane cholesterol. Biochim Biophys Acta. 2016 Jul 16;1858(11):2636–2646.
54. Lyatskaya Y, Liu Y, Tristram-Nagle S, Katsaras J, Nagle JF. Method for obtaining structure and interactions from oriented lipid bilayers. Phys Rev E, Stat Nonlin Soft Matter Phys. 2001 Jan;63(1 Pt 1):011907.
55. Kucerka N, Tristram-Nagle S, Nagle JF. Structure of fully hydrated fluid phase lipid bilayers with monounsaturated chains. J Membr Biol. 2005 Dec;208(3):193–202.
56. Zhang C, Li J, Lan L, Cheng J-X. Quantification of Lipid Metabolism in Living Cells through the Dynamics of Lipid Droplets Measured by Stimulated Raman Scattering Imaging. Anal Chem. 2017 Apr 18;89(8):4502–4507.
57. Li J, Condello S, Thomes-Pepin J, Ma X, Xia Y, Hurley TD, et al. Lipid desaturation is a metabolic marker and therapeutic target of ovarian cancer stem cells. Cell Stem Cell. 2017 Mar 2;20(3):303–314.e5.
58. Mendelsohn R, Maisano J. Use of deuterated phospholipids in raman spectroscopic studies of membrane structure. I. Multilayers of dimyristoyl phosphatidylcholine (and its -d54 derivative) with distearoyl phosphatidylcholine. Biochimica et Biophysica Acta (BBA) - Biomembranes. 1978 Jan;506(2):192–201.
59. Fu D, Yu Y, Folick A, Currie E, Farese RV, Tsai T-H, et al. In vivo metabolic fingerprinting of neutral lipids with hyperspectral stimulated Raman scattering microscopy. J Am Chem Soc. 2014 Jun 18;136(24):8820–8828.
60. Hu F, Lamprecht MR, Wei L, Morrison B, Min W. Bioorthogonal chemical imaging of metabolic activities in live mammalian hippocampal tissues with stimulated Raman scattering. Sci Rep. 2016 Dec 21;6:39660.

61. Camp CH, Lee YJ, Heddleston JM, Hartshorn CM, Hight Walker AR, Rich JN, et al. High-Speed Coherent Raman Fingerprint Imaging of Biological Tissues. Nat Photonics. 2014;8:627–634.
62. Liao C-S, Choi JH, Zhang D, Chan SH, Cheng J-X. Denoising stimulated raman spectroscopic images by total variation minimization. J Phys Chem C, Nanomater Interfaces. 2015 Aug 20;119(33):19397–19403.
63. Feizpour A, Marstrand T, Bastholm L, Eirefelt S, Evans CL. Label-free Quantification of Pharmacokinetics in Skin with Stimulated Raman Scattering Microscopy and Deep Learning. J Invest Dermatol. 2020 Jul 22;
64. Manifold B, Thomas E, Francis AT, Hill AH, Fu D. Denoising of stimulated Raman scattering microscopy images via deep learning. Biomed Opt Express. 2019 Aug 1;10(8):3860–3874.
65. Liu Y, Lee YJ, Cicerone MT. Broadband CARS spectral phase retrieval using a time-domain Kramers–Kronig transform. Opt Lett. 2009 May 1;34(9):1363.
66. Barrett JN, Rincon S, Singh J, Matthewman C, Pasos J, Barrett EF, et al. Pulsed infrared releases Ca2+ from the endoplasmic reticulum of cultured spiral ganglion neurons. J Neurophysiol. 2018 Aug 1;120(2):509–524.
67. Albert ES, Bec JM, Desmadryl G, Chekroud K, Travo C, Gaboyard S, et al. TRPV4 channels mediate the infrared laser-evoked response in sensory neurons. J Neurophysiol. 2012 Jun;107(12):3227–3234.
68. Lumbreras V, Bas E, Gupta C, Rajguru SM. Pulsed infrared radiation excites cultured neonatal spiral and vestibular ganglion neurons by modulating mitochondrial calcium cycling. J Neurophysiol. 2014 Sep 15;112(6):1246–1255.
69. McPheeters MT, Wang YT, Werdich AA, Jenkins MW, Laurita KR. An infrared optical pacing system for screening cardiac electrophysiology in human cardiomyocytes. PLoS One. 2017 Aug 24;12(8):e0183761.
70. Moreau D, Lefort C, Pas J, Bardet SM, Leveque P, O'Connor RP. Infrared neural stimulation induces intracellular Ca2+ release mediated by phospholipase C. J Biophotonics. 2018;11(2).
71. Blackmore J, Shrivastava S, Sallet J, Butler CR, Cleveland RO. Ultrasound neuromodulation: A review of results, mechanisms and safety. Ultrasound Med Biol. 2019 May 18;45(7):1509–1536.
72. Grossman N, Bono D, Dedic N, Kodandaramaiah SB, Rudenko A, Suk H-J, et al. Noninvasive deep brain stimulation via temporally interfering electric fields. Cell. 2017 Jun 1;169(6):1029–1041.e16.
73. Nandakumar P, Kovalev A, Volkmer A. Vibrational imaging based on stimulated Raman scattering microscopy. New J Phys. 2009 Mar 25;11(3):033026.
74. Kerdoncuff H, Pollard MR, Westergaard PG, Petersen JC, Lassen M. Compact and versatile laser system for polarization-sensitive stimulated Raman spectroscopy. Opt Express. 2017 Mar 6;25(5):5618–5625.
75. Czamara K, Majzner K, Pacia MZ, Kochan K, Kaczor A, Baranska M. Raman spectroscopy of lipids: a review. J Raman Spectrosc. 2015 Jan;46(1):4–20.

CHAPTER 5:

STIMULATION OF WATER AND CALCIUM DYNAMICS IN ASTROCYTES WITH PULSED INFRARED LIGHT

Text adapted from:

Ana I Borrachero-Conejo*, Wilson R Adams*, Emanuela Saracino, Maria Grazia Mola, Manqing Wang, Tamara Posati, Francesco Formaggio, Manuela De Bellis, Antonio Frigeri, Marco Caprini, Mark R. Hutchinson, Michele Muccini, Roberto Zamboni, Grazia Paola Nicchia, Anita Mahadevan-Jansen, Valentina Benfenati. *Stimulation of water and calcium dynamics in astrocytes with pulsed infrared light*. The FASEB Journal. 23 March 2020. https://doi.org/10.1096/fj.201903049R

*Shared first authorship

5.1 Abstract

Astrocytes are non-neuronal cells that govern the homeostatic regulation of the brain through ions and water transport, and Ca^{2+}-mediated signaling. As they are tightly integrated into neural networks, label-free tools that can modulate cell function are needed to evaluate the role of astrocytes in brain physiology and dysfunction. Using live-cell fluorescence imaging, pharmacology, electrophysiology, and genetic manipulation, we show that pulsed infrared light can modulate astrocyte function through changes in intracellular Ca^{2+} and water dynamics, providing unique mechanistic insight into the effect of pulsed infrared laser light on astroglial cells. Water transport is activated and, IP3R, TRPA1, TRPV4 and Aquaporin-4 (AQP4) are all involved in shaping the dynamics of infrared pulse-evoked intracellular calcium signal. These results demonstrate that astrocyte function can be modulated with infrared light. We expect that targeted control over calcium dynamics and water transport will help to study the crucial role of astrocytes in edema, ischemia, glioma progression, stroke, and epilepsy.

5.2 Introduction

The ability of the brain to receive and process information is critically dependent on regulation operated by non-neuronal cells called astrocytes (1, 2). Astrocytes sense variation of extracellular milieu composition that occur in the extracellular environment during and following neuronal activity. These variations trigger selective activation of transmembrane receptors and channels leading to ion, water, and Ca2+ fluxes amongst others across the cell membrane. The latter membrane dynamics can orchestrate processes such as energetic delivery, vascular activity, and even immune responses depending on the stimulus (1, 3, 4).

Various receptors and channels have been implicated in the mechanisms of astrocytes. Among others, plasma membrane cation channels belonging to the Transient Receptor Potential (TRP) superfamily have been shown to play a critical role in regulating homeostatic intracellular calcium ([Ca2+]i) signaling in astroglia (5–12). Water transport and distribution is facilitated by the water channel aquaporin-4 (AQP4) (8, 12–14). Together, TRP Vanilloid 4 (TRPV4) channels in conjunction with AQP4 are critical in controlling ion and water dynamics, thus driving regulatory volume mechanisms as shown in primary astrocytes (12, 15) and the retina in situ (14, 16). Dysfunction in this TRPV4-AQP4 cooperation causes brain swelling, most notably in ischemia, epilepsy and brain tumors, proving the importance of astrocytes in the homeostatic mechanism for normal brain physiology (13, 17, 18).

The narrow set of tools currently available to modulate ion fluxes, water dynamics, and numerous receptors and channels expressed in astrocytes have limited our ability to effectively study their importance in healthy and pathological brain function. Methods to study astrocytic processes have been confined to conventional pharmacology, genetic manipulation, fluorescence imaging of molecular sensors, and electrophysiology (3, 6, 12, 15, 19–21). Optical tools can provide precise, fast, label-free control of ions and water dynamics to study the cellular and molecular mechanisms of astrocytes function and to potentially treat dysfunction. However, despite recent advances in optogenetics approaches and optoelectronics device to study neurons (22, 23), there is a continued need for reliable methods for label-free control of ion flux and water dynamics in astrocytes (24–26).

Infrared stimulation is a label-free approach that can modulate neural activity in cells and tissues by transient delivery of pulsed infrared laser light (27–31). Mechanistically, infrared stimulation has been shown to rely on a transient spatial and temporal thermal gradient for neuronal depolarization and action potential initiation in the peripheral and central nervous system (32–34). Studies have also demonstrated the ability of infrared stimulation to modulate processes in different cells. However, the biophysical mechanisms by which this method modulates cells and tissues is not fully understood (32). Nonetheless, the direct effect of pulsed infrared light on non-neuronal cells such as astrocytes has not been previously reported.

The goal of this paper then is to study the effect of pulsed infrared light on astrocytes and to understand the mechanisms by which astrocytes may be modulated. Results show that infrared stimulation can drive Ca2+ dynamics, trigger water transport, and cell volume changes in rodent astrocytes. Based on our observations of the activation of TRP channels, Inositol-3-Phosphate Receptor (IP3R) and AQP4, we propose the molecular mechanisms by which astrocytes are modulated with infrared light. These findings suggest that infrared stimulation offers a transformative approach to study astrocytic homeostatic regulation and to study glial involvement in normal and diseased brain physiology as well as in the clinical care of brain disease.

5.3 Materials and Methods

5.3.1 Rat cortical astrocyte culture preparation, maintenance and plating

Primary astroglial cultures were prepared at the University of Bologna (UNIBO) and at the University of Bari (UNIBA), in concordance with the Italian and European law of protection of laboratory animals, with the approval of the local bioethical committee and under the supervision of the veterinary commission for animal care and comfort of UNIBO and UNIBA, with approved protocol from Italian Ministry of Health (no 360/2017 PR for UNIBO and 710/2017-PR for UNIBA). Astrocytes primary culture were prepared as described previously (3, 6, 12).

In brief, primary cultures of astrocytes were prepared from newborns of Rattus Norvegicus Wistar. Neural cortices were placed in cell culture flasks containing Dulbecco's Modified Eagle-glutamax medium with 15% fetal bovine serum (FBS) and penicillin/streptomycin (100 U/mL and 100 lg/mL, respectively). Cells were maintained in incubation at 37ºC and 5% of CO2 and 95% relative humidity levels for three weeks prior to experimentation. Cells were used between days 21 and 35 in vitro for experiments after re-plating. AQP4 KO (-/-) pups with a CD21 genetic background and aged-matched controls were used for preparation of primary cortical astrocytes as described previously (35). Primary astrocytes were plated on Glass coverslips coated with Poly-D-lysine (PDL) and uncoated hydrotalcite (HTlc) (36) samples and experiments were performed 48-72h after re-plating. Astrocytes were plated at a high density for calcium imaging and calcium quenching experiments. For single cell patch-clamp experiments cells were seeded at a low density.

5.3.2 Pulsed Infrared Laser Stimulation

To explore the effect of pulsed infrared light on astrocytes, an inverted epifluorescence microscope was fitted with a multimode fiber attached to a micromanipulator (Sutter Inc), ensuring tight control of optical fiber positioning at close proximity (230-250 µm) to primary astrocytes plated on a glass coverslip (**Figure 5.1A-B**). Laser light at 1875 nm from a pulsed diode laser (Capella, Lockheed Martin Aculight, Bothell, WA) was coupled to the fiber. The pulse duration was set to 8 ms which was calculated to be ~3 J/cm2 at the sample plane and was delivered 30s after the beginning of the experiment. The infrared laser output was estimated to be located ~240 µm from the center of the optical fiber face at a 45° angle to the cell-coverslip plane (**Figure 5.1B**). For pharmacological characterization of astrocyte responses, an exposure to elicit a target activation probability of 0.8 was used as a baseline for comparison across all experiments.

5.3.3 Transfection with siRNA

siRNA transfection was performed using Lipofectamine RNAiMAX and Opti-MEM according to manufacturer instructions (Invitrogen) and to protocols previously described (12). Briefly, Stealth RNAi siRNA select RNAi (ID RSS330373, designated "number 9") that respectively target nucleotides 1201–1225, of rat TRPV4 (GenBank accession no. NM_023970.1) were purchased from Invitrogen. Transfection was performed on two-three weeks-old primary rat astrocytes using Lipofectamine RNAiMAX and Opti-MEM I reduced serum medium according to the manufacturer's instructions (Invitrogen). The day before transfection, astrocytes were cultured using DMEM with 10% FBS without antibiotics. The final concentrations were 50 nM for the selected RNAi or scrambled control and 10 µL for Lipofectamine RNAiMAX in a 60-mm culture vessel. After 24h the medium was replaced with complete 10% FBS DMEM containing penicillin/streptomycin (100 U/mL and 100 µg/ mL, respectively) medium. Transfection efficiency was verified using a BLOCK-iT Alexa Fluor Red Fluorescent Oligo that is not homologous to any known genes. Five days after transfection we performed calcium imaging experiments as described above.

5.3.4 Calcium Imaging

Changes in intracellular Ca^{2+} concentration ($[Ca^{2+}]$i) were monitored by calcium imaging using the single-wavelength Ca^{2+} indicator Fluo-4-AM (Life Technologies). Experiments were performed 48h after cell plating. Astrocytes plated in glass+PDL and HTlc samples were incubated at room temperature for 45 min to 1h with Fluo-4-AM (1 uM) dissolved in control saline solution. Measurements of $[Ca^{2+}]_i$ were performed by using an epifluorescence microscope (Nikon Eclipse Ti-S) equipped with long-distance dry objective (40x, 0.4NA) and standard filters for GFP fluorescence. The excitation wavelength was 470nm, filtered from a broadband LED light source. Light pulse durations were set to 200ms, while camera exposure times were set to 100ms with a sampling rate of 2Hz. Data acquisition was controlled by MetaFluor software (Molecular Devices, Sunnyvale, CA, USA) or NIS Elements (Nikon Imaging Systems).

5.3.5 Electrophysiology

Current recordings were obtained with the whole-cell configuration of the patch-clamp technique as described previously (6). Patch pipettes were prepared from thin-walled borosilicate glass capillaries to obtain a tip resistance of 2–4 MΩ when filled with the standard internal solution. Membrane currents were amplified, filtered at 2 kHz and acquired at a sample rate of 5 kHz by Axopatch 200B amplifier in voltage-clamp mode. Responses were amplified, low-pass filtered at 1 kHz, digitised at 20 kHz, stored and analysed with pCLAMP 10. Liquid junction potential (7 mV) was calculated and corrected off-line; voltages indicated are those relative to the real transmembrane potentials. Experiments were carried out at room temperature (22–24 °C). When necessary, current values were plotted as current densities calculated by dividing the current values measured at each membrane potential by the cell capacitance obtained by the correction of the capacitive transient of the recorded cells by means of the digital circuit of the patch-clamp amplifier. To investigate whether astrocytic TRPV4 conductance was altered by INS, we performed whole-cell patch-clamp experiments, according to protocols described previously (6, 7) by holding the membrane potential (Vh) at 7 mV and stimulating the cells with a 400-ms-long step potential to -87 mV, followed by a voltage ramp from -87 mV to 73 mV for 600 ms. Potassium (K+) in the intra- and extra-cellular saline were replaced by cesium (Cs+) to isolate TRPV4 conductance from voltage-gated K+ currents expressed by astrocytes in vitro and in situ. Moreover, intracellular Cl- was partially replaced by gluconate to change reversal potential of Cl- and to distinguish chloride currents from cationic ones. The outward rectification profile, known to be dependent by [Ca2+]o, caused by Ca2+ blockage at membrane potentials negative to the reversal potential (Erev) was prevented by using 2mM [Ca2+]o. INS pulse was delivered when current profiles reached the steady-state.

5.3.6 Calcein self-quenching image acquisition

Changes in cell volume were assessed using calcein fluorescence quenching as described previously (15, 18). Experiments were performed 48-72h after cell re-plating. Astrocytes were loaded with Calcein-AM (10 μM) (Life Technologies, USA) dissolved in standard bath solution and they were incubated for 30 min at room temperature. Image acquisition was controlled by the NIS Elements (Nikon Imaging Systems) on a Nikon TI-Eclipse inverted epifluorescence microscope (Nikon Instruments). The excitation wavelength used was 470 nm filtered from a broadband source and fluorescence from calcein was filtered through a standard GFP filter cube (Nikon Instruments). Cells were imaged through a 20X/0.7NA air objective (Nikon) with a sCMOS camera (Hammamatsu Orca Flash 4.0). Camera exposure time of 10 ms and a sampling rate of 5Hz was employed.

Image processing and analysis were done in FIJI (37) and Matlab (Natick, MA, USA). Time course fluorescence data were analyzed with Prism (Graph Pad, San Diego, CA, USA) software. For each experimental curve, the time constant of cell swelling or shrinkage phase was obtained by fitting the data with an exponential function and a time constant calculated (18). Further details surrounding data analysis can be found in Supplemental Information.

5.3.7 Solutions and chemicals

Calcium imaging and calcein self-quenching analyses the control saline bath solution, named as control (CTRL) was composed of (mM): 140 NaCl, 4 KCl, 2 $MgCl_2$, 2 $CaCl_2$, 10 HEPES, 5 glucose, pH 7.4 with NaOH and osmolarity adjusted to ~318 mOsm with mannitol. Ca^{2+}-free extracellular solution (0 $[Ca^{2+}]_{out}$) contained (mM) 140 NaCl, 4 KCl, 4$MgCl_2$, 10 HEPES, 0.5 EGTA, pH 7.4 with NaOH and osmolarity adjusted to ~318 mOsm with mannitol. For electrophysiological experiments the standard bath saline was (mM) 140 NaCl, 4 KCl, 2 MgCl2, 2 CaCl2, 10 Hepes, 5 glucose, pH 7.4 with NaOH and osmolarity adjusted to 315 mOsm with mannitol. In order to eliminate potassium currents, K^+ was omitted by extracellular solution and pipette solutions was replaced with cesium (Cs). The intracellular (pipette) solution was composed of (mM): 100 Cs gluconate, 26 CsCl2, 2 MgCl2, 1 EGTA, 10 TES, pH 7.2 with CsOH and osmolarity 300 mOsm with mannitol.

Salts and chemicals used to prepare physiological solutions were the highest purity grade and obtained from Sigma (Milan, Italy). For details on the compositions of solutions and stock solutions of chemicals preparations see Supplementary Information.

5.3.8 Data analysis, representation and statistics

All data are expressed as mean of several cells (*n*) ± SEM. Statistical comparison of metrics is performed with a 2-sided student's T-test unless otherwise noted. A *p*-value < 0.05 was considered statistically significant. All analyses were performed in Matlab.

1.5.3.8 ***Calcium imaging analysis, representation and statistics***

Calcium imaging: on the basis of previous studies (1,5) , considering the consistency of the results obtained in previous works using the same culture preparation, we determinate that a minimum number of 4 recordings (n value) from 3 different animals with 2 replicates (coverslips) can be considered significant sample size to determine the response of astrocytes to INS and for the pharmacological manipulation. Accordingly, each cell culture preparation was prepared from one different newborns animal and each calcium imaging recording was considered as n (N). For each experimental condition a set of at least 2 different coverslips from each cell culture preparation were tested. For patch clamp experiments, a minimum of 10 cells recorded with the same ionic condition were considered significant sample size for testing the response to INS, and 4 when pharmacology was used TRP pharmacology (1,5). Somatic cellular fluorescence time series were manually extracted in both Metafluor (Molecular Devices, Sunnyvale, CA, USA) and with a custom-written FIJI script to accelerate data extraction. Extracted data was imported into analysis in MATLAB (Mathworks, Natick, MA, USA), where raw fluorescence traces are aligned relative to INS pulse delivery, normalized, and processed to extract different calcium response metrics. Alignment of traces relative to INS pulse delivery were performed by locating the peak second derivative for fluorescence intensity as a function of time for each imaging experiment's average time series. Defocusing due to the transient heating of the INS pulse delivery yields a sharp transient decrease in observed intensity for each image, with resulted in a relatively high peak in the fluorescence time series second derivative. Time series data for each cell was subsequently truncated to 5 seconds prior to INS exposure for analysis purposes. Each cell's raw fluorescence intensity was normalized with respect to the mean raw intensity of the 10 frames prior to IR exposure, which are reported and analyzed as fractions (dF/F).

Quantitative metrics extracted from each cell's time series trace included maximum change in relative fluorescence, elapsed time to peak fluorescence intensity, the full-width half-maximum of each cells response, and the numerically integrated area of each cell's response. A cell was deemed 'activated' if a 5% increase in normalized calcium fluorescence within 20 seconds of IR exposure. The fraction of activated cells relative to the total number of cells observed is reported as 'activation fraction' or 'fraction of responding cells. Statistical comparison of metrics is performed with a 2-sided student's T-test unless otherwise noted. Error bars reported are standard error of the mean (SEM) response between cells unless otherwise denoted. Plotting was performed in MATLAB with the 'superbar' package and native plotting functions. FIJI scripts for data compression / extraction as well as MATLAB processing scripts are available upon request.

*2.5.3.8**Calcein imaging data analysis***

Cells were selected, and time series were extracted through a custom FIJI script. Time series for each cell were imported into MATLAB for processing and analysis. Low-frequency fluorescence background subtraction from each time series was achieved by fitting a 6th-order polynomial function the time series points outside of our region of interest. Our determined area of interest was 5 frames prior to INS stimulus and 350 after stimulus. The initial 50 frames of data were excluded to avoid skewed fits due to initial photobleaching artifacts. We found that the 6th-order polynomial best accounted for photobleaching inconsistencies that arise from preparing each field of view for observation (e.g. fiber placement). Relative changes in calcein fluorescence due to INS exposure were calculated by dividing the difference of corrected fluorescence intensity 2 seconds (10 frames) prior to and following INS exposure by the pre-stimulated fluorescence intensity (dF/F). Negative changes in fluorescence indicate decreases in fluorescence intensity after INS exposure. Mean time traces are reported for each experimental condition as the central tendencies of observed responses, unless otherwise noted.

*3.5.3.8**Electrophysiology Data Analysis***

Electrophysiological data are expressed as mean± standard error mean (SEM) of several cells (n) in the various conditions. The statistical analysis was performed with two-tailed Student's t-test and a P-value 0.05 was taken as statistically significant. Steady state current density in response to ramp currents was calculated before and after the INS stimulation. Maximal current increase (pA/pF) is reported as the ratio of the maximal current density observed after INS at -87 mV and + 73 mV, divided by the current density recorded at the same voltages at the steady state before the stimulus.

5.4 Results and Discussion

5.4.1 Infrared pulsed stimulation evokes calcium signaling in primary astrocytes

To evaluate whether pulsed infrared light can modulate astrocytes, cortical primary rat astrocytes were plated on glass coverslips coated with Poly-D-lysine (PDL) and placed under an inverted fluorescence microscope while delivering 8 ms pulsed infrared light (λ=1875nm) using an optical fiber placed close to the cell from above as shown in **Figure 5.1**. The astrocytes were loaded with the calcium indicator Fluo-4-AM (2 μM) and calcium imaging was used to study the resulting cell dynamics. Changes in fluorescence intensity (dF/F) were directly related to intracellular levels of free Ca2+ ([Ca2+]i) in the cell soma. The observed responses were characterized by a rapid increase in [Ca2+]i that reached its peak intensity ~6.91±1.12 s (Tpeak) and had a duration (T1/2, reported as full-width half-maximum times) of 9.39±1.64

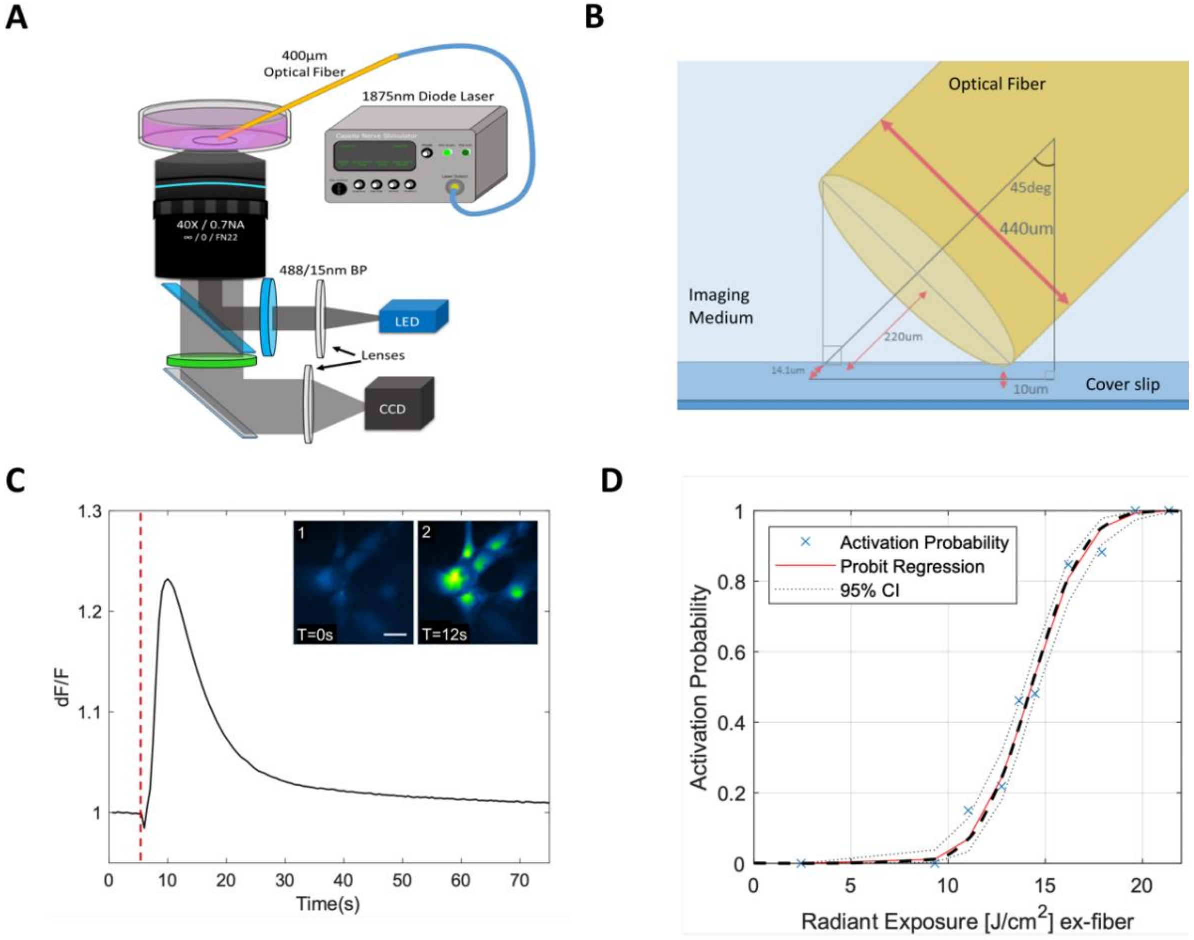

Figure 5.1. Pulsed infrared light can stimulate calcium imaging in cultured astrocytes
(A) Schematic representation of the experimental set-up for stimulation of astrocyte -(1875 nm). (B) To-scale illustration of fiber placement in proximity of cells during the experiments. (C) Representative trace depicting the normalized variation in cell fluorescence over time (dF/F) that reflects variation in [Ca^{2+}]i. Red dashed line marks the timepoint at which laser pulse was delivered. Inset. Fluorescent images of Fluo-4-AM loaded astrocytes captured before the stimulation (1, t=0s) and at the peak of fluorescence after stimulation (2, t=12s), scale bar is 40 μm. (D) Activation probability (P) as a function of radiant exposure delivered to rat astrocytes.

s, followed by a recovery of fluorescence to near initial baseline levels after 120s (Figure 5.1**C**). The time course of dF/F response of an individual cell were consistent across the cells observed with an average maximum fluorescence of 1.28 ± 0.02. The activation probability (P), or the fraction of cells responding to infrared light, was found to be dependent on radiant exposure (J/cm2) with a 50% activation probability occurring at 14.31 J/cm2 at the tip of the fiber (

Figure 5.1**D**), which translates to approximately 3 J/cm2 at the cell surface. Radiant exposures targeting an activation fraction of 0.8 was selected for the rest of the experiments described. We have performed

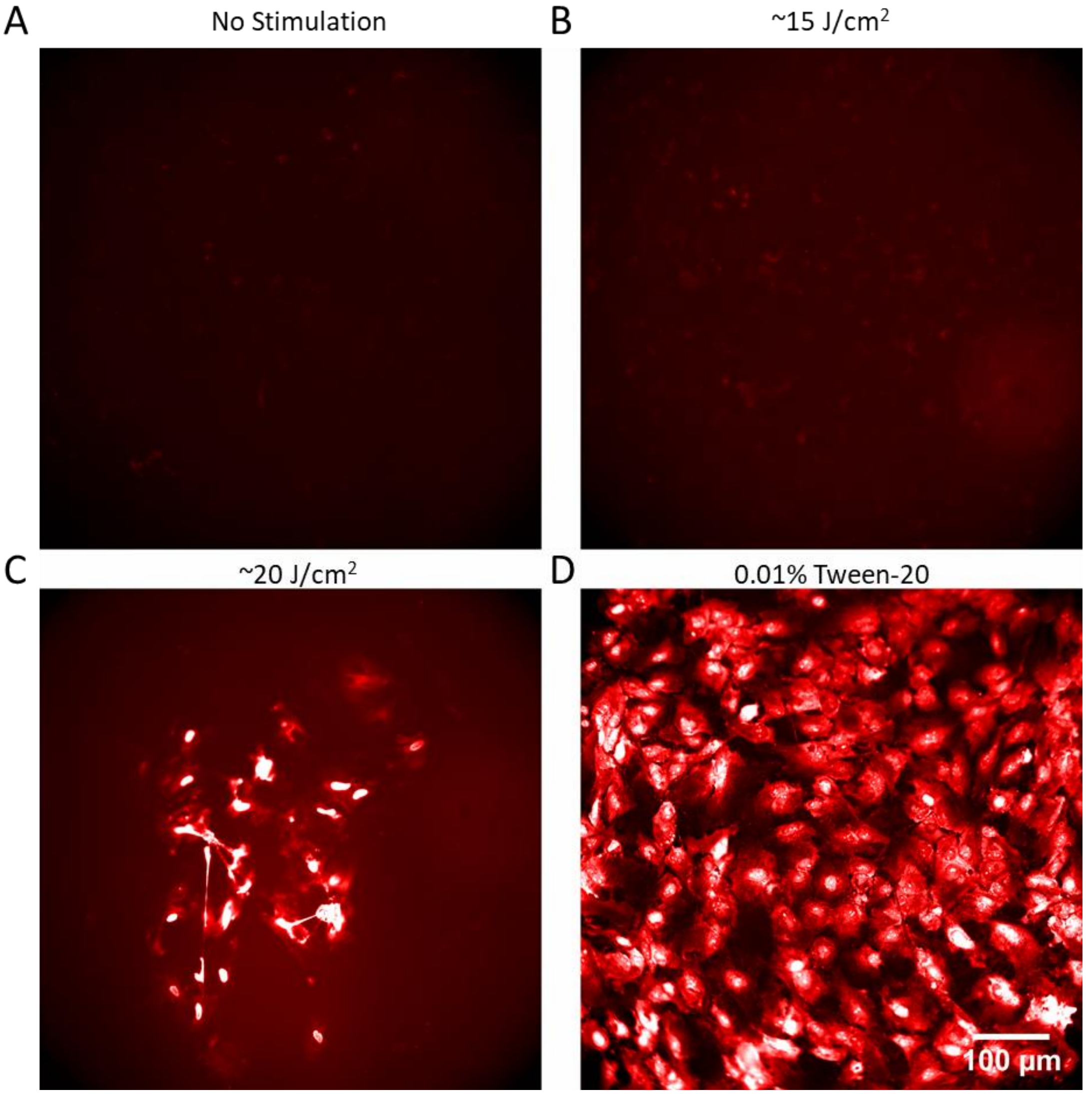

Figure 5.2: Cell damage with IR occurs above threshold levels of stimulation
Fluorescence images of primary rat astrocyte cultures in a solution containing 5uM Propidium Iodide (PI) captured A) before IR stimulation, B) after near threshold IR stimulation (~15 J/cm^2 *ex fiber*), C) over threshold (~20 J/cm^2 *ex fiber*) IR stimulation, and D) treatment with 0.01% Tween-20 detergent solution for 5 minutes that permeabilize the cell plasma membrane, causing cell death.

experiments to verify astrocytic viability during IR stimulation by assessing extracellular membrane integrity with propidium iodide (PI) uptake. By exposing cells to IR in the presence of PI-containing solution, positively stained cell nuclei would indicate extracellular membrane disruption by the IR pulse. Unstimulated (**Figure 5.2A**) and threshold-stimulated cells (**Figure 5.2B**) showed negligible levels of PI

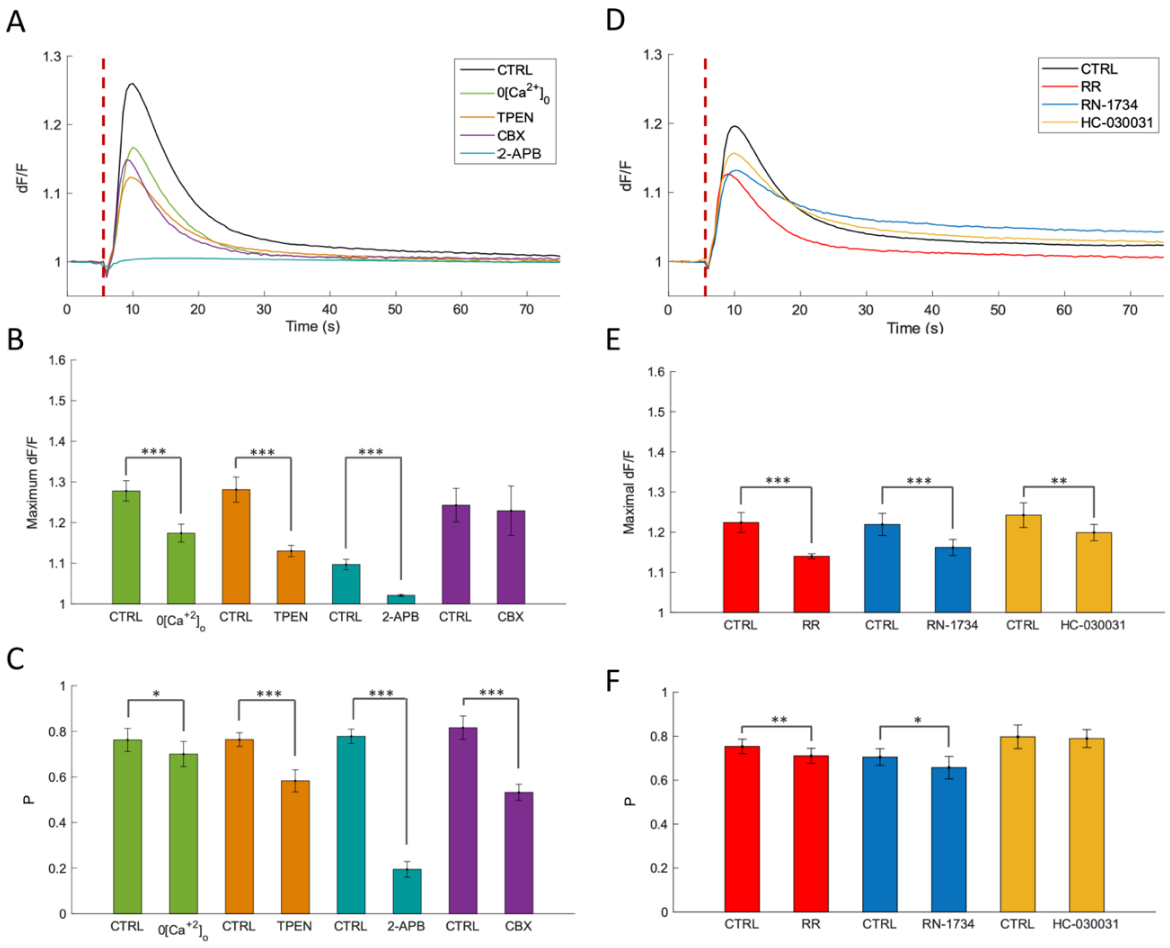

Figure 5.3. Pharmacology of the $[Ca^{2+}]$i response of astrocytes to infrared light
(A) Representative traces of experiments performed using extracellular standard solution (black, CTRL), extracellular solution not-containing Ca^{2+} ($0[Ca^{2+}]_o$, green trace) and by adding TPEN (2mM, orange trace), 2-APB (100 µM, blue trace) or CBX (50 µM, violet trace) to the CTRL saline. (B-C) Histogram plots depicting the averaged maximal dF/F (B) and activation probability (C) calculated for CTRL saline and $0[Ca^{2+}]_o$ solution (green columns), CTRL and CTRL+TPEN (orange columns), CTRL and CTRL+2-APB (blue columns), CTRL and CTRL+CBX (purple columns). D)Representative traces of experiments performed in CTRL saline (black), and CTRL+ Ruthenium Red (RR, 10 µM, red trace), CTRL+RN-1734 (10 µM, dark blue trace), CTRL+HC-030031 (40 µM, yellow trace). E-F) Histogram plots depicting the averaged maximal dF/F (E) and activation probability (F) calculated using CTRL saline and CTRL+RR (10 µM, red columns), CTRL and CTRL+RN-1734 (10 µM, dark blue columns), CTRL and CTRL+HC-030031 (40 µM, yellow columns). Data are reported as mean and SEM. Student's t-test, *: p<0,05; **: p<0,01; ***: p<0,001). Red dashed lines in A and D represent the time point at which the pulsed infrared light was delivered. All experiment performed using primary rat cortical astrocytes.

fluorescence, within 5 minutes of IR stimulation. On the contrary, exposure to IR at almost higher power (**Figure 5.2C**) and chemogenic permeabilization with a dilute detergent solution, 0.1% Tween-20 (Sigma-Aldrich, St. Louis, MO, USA) (**Figure 5.2D**) display strong PI fluorescent signal. Collectively, these results suggest that, within 5 minutes of IR stimulation, acute cellular damage is not a cause for concern at threshold radiant exposures for astrocytic modulation.

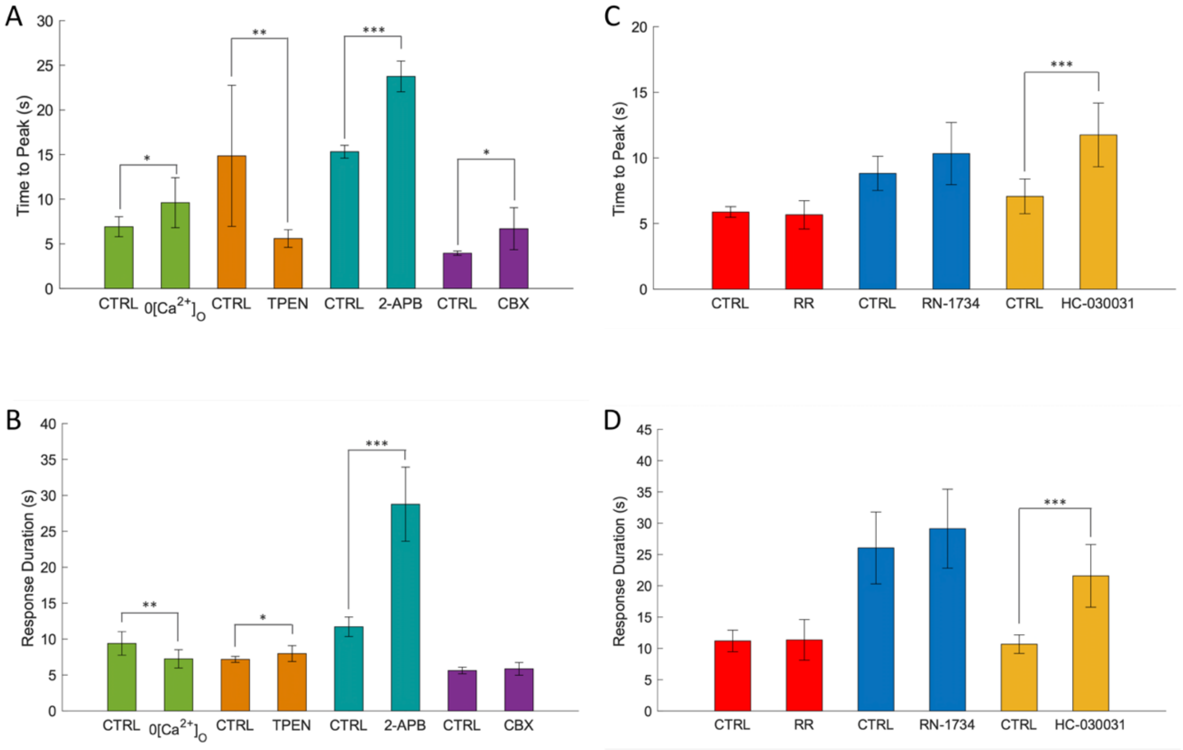

Figure 5.4: Calcium mobilization temporal dynamics
A) Histogram plot depicting the time to fluorescence peak calculated for each condition experiments performed in CTRL saline and in saline non containing Ca^{2+} ($0[Ca^{2+}]_{out}$, green columns), CTRL saline and CTRL+TPEN (orange columns), CTRL saline and CTRL+2APB (blue columns), CTRL saline and CTRL+CBX (violet columns). B) Response duration in experiments using CTRL saline and $0[Ca^{2+}]_{out}$ solution (green columns), CTRL saline and CTRL+TPEN (orange columns), CTRL+ 2APB (light blue columns), CTRL saline and CTRL+CBX (violet columns). C) Histogram plot depicting the time to fluorescence peak value using control saline solution added with RR (10 µM, red columns), RN1734 (10 µM, dark blue columns) and HC 030031 (40 µM, yellow columns). D) Histogram plot depicting the duration of the response to INS using CTRL saline and CTRL saline solution added with RR (10 µM, red columns), CTRL saline and CTRL saline +RN1734 (10 µM, dark blue columns), CTRL saline and CTRL saline + HC 030031 (40 µM, yellow columns). All histogram plots represents mean and error bars represent SEM. N= number of experiments; N=11 for CTRL and N=11 for $0[Ca^{2+}]_o$; N=9 for CTRL and N=11 for CTRL+TPEN; N=8 for CTRL and N=9 for CTRL+2-APB; N=4 for CTRL and N=5 for CTRL+CBX; N=11 for CTRL and N=15 for CTRL+RR; N=10 for CTRL and N=10 for CTRL+RN-1734; N=10 for CTRL and N=11 for CTRL+HC-030031; Student's t-test, *: $p<0.05$; **: $p<0.01$; ***: $p<0.001$).

Pharmacological methods were used to isolate the basis of intracellular Ca^{2+} rise observed with infrared stimulation. All the results, expressed as mean ± SEM and statistic p-values (pval), are reported in **Table 5.1**. Application of intracellular Ca^{2+} chelator (N,N,N′,N′-tetrakis(2-pyridinylmethyl)-1,2-ethanediamine, TPEN, 2mM) (38) (**Table 5.1**, Figure 5.3 and **Figure 5.4**) results in a significant reduction in activation probability and peak dF/F followed by alterations in response dynamics. Application of 2-Aminoethoxydiphenylborane (2-APB, 100 µM), an antagonist of Inositol-3-Phosphate (IP_3) receptors results in a near loss of the calcium response and a drastic reduction in activation probability. Substitution of control saline solution (CTRL) with a Ca^{2+}-free solution ($0[Ca^{2+}]_o$, (**Figure 5.3A-B**) results in a statistically significant decrease in dF/F and $T_{1/2}$ and a decrease in the activation probability as well as $<T_{peak}$ (**Table 5.1**, Figure 5.3, **Figure 5.4**) and shows that extracellular Ca^{2+} influx is needed for the amplification and maintenance of infrared-mediated $[Ca^{2+}]_i$ responses as well as the onset of Ca^{2+} response. We found that blocking gap junctions (essential for propagation of $[Ca^{2+}]_i$ through the syncytium (35, 39) does not alter the magnitude of $[Ca^{2+}]_i$ responses when compared to control, as observed with bath application of Carbenoxolone (CBX) although the activation probability is significantly reduced. Collectively, our results suggest that $[Ca^{2+}]_i$ responses to pulsed infrared light are initiated by IP_3R-dependent Ca^{2+} release from intracellular stores, sustained by $[Ca^{2+}]_o$ influx, and propagated across astroglia cellular networks through gap junction (35).

These observations align with the response to infrared stimulation seen in sensory and hippocampal neurons *in vitro* (40, 41). Pharmacology implicates IP_3R as a primary pathway for the release of $[Ca^{2+}]_i$ from intracellular stores and is believed to be critical in numerous astrocytic functions (1, 2). Recent work suggested that Ca^{2+} release via IP_3R activation is crucial for the release of signaling molecules from astrocytes that mediate astrocyte-neuronal communication and influence long term potentiation *in situ* (2, 42). Thus, our results with an approach that can trigger IP_3R pathways might offer the opportunity for probing communication between neuronal and glial cells.

5.4.2 TRPV4 and TRPA1 mediate influx of calcium and whole-cell conductance changes with infrared light

Using selective pharmacology and siRNA methodologies, the molecular basis for $[Ca^{2+}]_o$ influx was evaluated. Thermally sensitive TRPV4 has been shown to be involved in the response of spiral, vestibular, and dorsal root ganglion neurons to pulsed infrared light (43–45). Considering TRPV4's role in astrocyte physiology (6, 7, 14), we postulated that TRPV4 is involved in the Ca^{2+} dynamics of astrocytes during infrared stimulation. Results show that TRP superfamily member channels are broadly involved in Ca^{2+} influx. The magnitude of dF/F and activation probability is significantly reduced following the

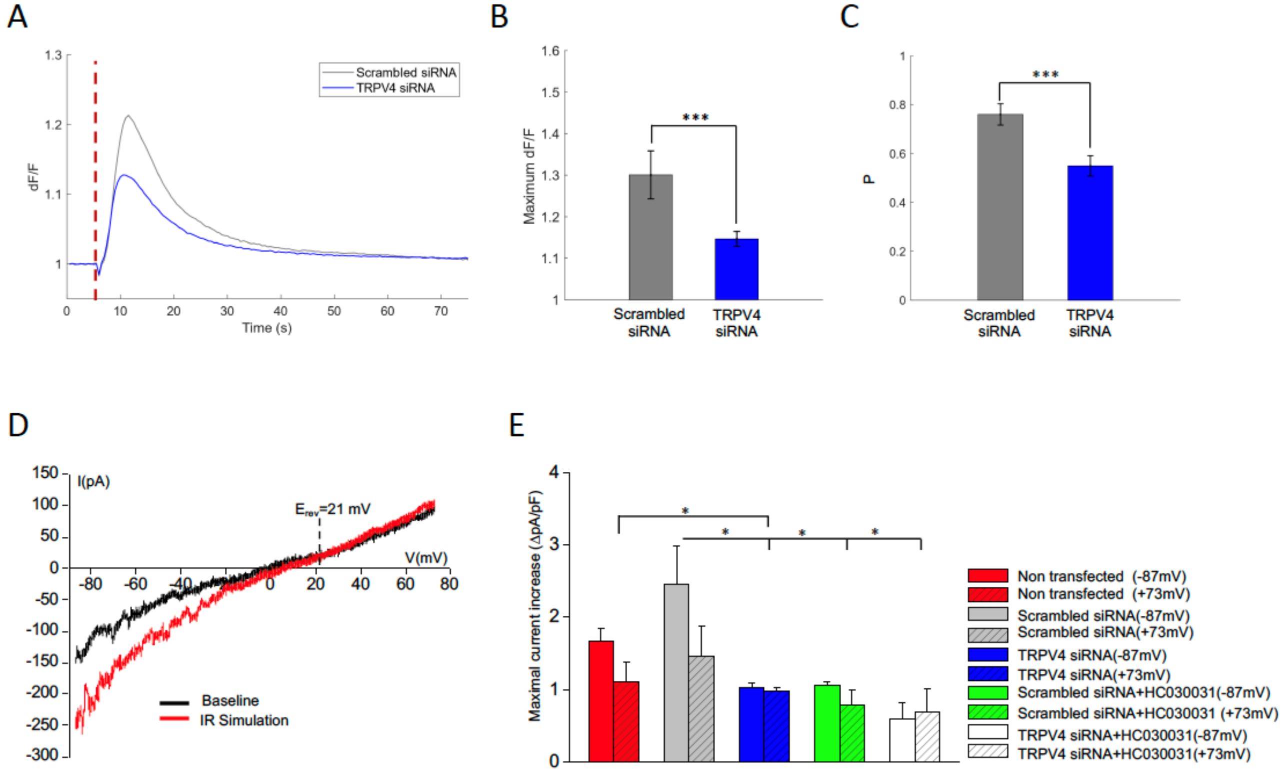

Figure 5.5. The role of TRPV4 in $[Ca^{2+}]_i$ and whole-cell conductance changes IR stimulation (A) Representative traces of $[Ca^{2+}]_i$ dynamics recorded in astrocytes transfected with scrambled siRNA and TRPV4 siRNA. Red dashed line represents the infrared stimulation time point. B-C) Bar plots showing the averaged maximal dF/F (B) and activation probability (C) in astrocytes transfected with scrambled siRNA (grey columns) and TRPV4 siRNA (blue columns). (D) Typical ramp current traces stimulated with a voltage ramp protocol (Supplementary methods) recorded in saline solution before (black trace) and at maximal current increase observed after pulsed infrared light (red trace). Dashed line depicts the reversal potential (E_{rev}) of the infrared stimulation-induced current. (E) Bar plot of averaged maximal current density, recorded at -87 mV and +73 mV after infrared stimulation, normalized with respect to the baseline current. Data were recorded in non-transfected primary rat astrocytes, (ΔpA/pF=1.12±0.26 at +73mV; ΔpA/pF=1.66±0.19 at -87mV red columns, n=11), in astrocytes transfected with scrambled siRNA, (ΔpA/pF=1.46±0.41 at +73 mV, ΔpA/pF=2.45±0.54 at -87mV, grey columns, n=6) or with TRPV4siRNA (ΔpA/pF=0.98±0.05 at +73mV, ΔpA/pF=1.03±0.05 at -87mV, blue columns, n=6, pval=0.016 Vs non transfected, pval=0.0101 Vs Scrambled siRNA). The plot also reported the averaged data in cells transfected with scrambled siRNA+40 µM HC-030031 (ΔpA/pF=1.06±0.06 at -87 mV, ΔpA/pF=0.79±0.2 at +73 mV green columns, n=4, pval=0.04) and TRPV4siRNA+40µM HC-030031 (ΔpA/pF=0.60±0.21 at -87 mV, ΔpA/pF=0.69±0.31 at +73 mV, white columns, n=4, pval=0.023). (Data are reported as mean and SEM. Student's t-test, n= number of cells, Student's t-test, *: p<0,05; **: p<0,01). All experiment performed using primary rat cortical astrocytes.

application of a broad-spectrum TRP channel antagonist, Ruthenium Red (RR, 10µM) (see **Figure 5.3**E-F). Additionally, RR did not alter the dynamics of Ca^{2+} responses, as T_{peak} and $T_{1/2}$ when using RR is comparable to values in control saline (**Figure 5.4C-D**). In the presence of selective TRPV4 antagonist RN1734 (RN, 10µM) (5), dF/F and activation probability were reduced but not eliminated, and it is not involved in shaping the response dynamics (**Figure 5.4C-D**). These findings indicate that TRPV4 is important in the observed response but is not the sole intermediary to the process. With the addition of HC030031 - a TRP Ankirin-1 (TRPA1)-specific antagonist - the peak dF/F was significantly attenuated, while T_{peak} and $T_{1/2}$ both increased (**Figure 5.4C-D**). On the other hand, activation probability was not significantly altered (**Figure 5.3D, F**). These results support that TRPA1 also plays a role in the magnitude and dynamics of the Ca^{2+} responses.

Figure 5.5 shows the results obtained in astrocytes transfected with scrambled siRNA and TRPV4 siRNA. Western blot experiments and densitometric analysis, indicated that the transfection with TRPV4 siRNA causes 73% (± 4%) of reduction of the band at 110 kDa, which correspond to the isoform that is expressed in the membrane of astrocytes (46). Reduced expression of TRPV4 alter Ca^{2+} responses with infrared stimulation. Slight but significant differences were observed in the T_{peak} (**Figure 5.6A**), while $T_{1/2}$ was significantly higher in TRPV4 knock down cells (**Figure 5.6B**). Both dF/F and activation probability are significantly lower in these cells (**Figure 5.5B-C**). Using a whole-cell patch-clamp rig, electrophysiology was also performed in transfected astrocytes as well as non-transfected cells (**Figure 5.5D-E**). The electrophysiological data further implicates the role of TRPV4, demonstrating that infrared-induced cationic current increases are attenuated upon knocking down the expression of TRPV4. Cationic currents are further abolished by additional blocking the function of TRPA1 (Figure 5.5**E**). Using saline solution and stimulation protocols described previously (6, 7), we recorded ramp baseline currents (see Methods for details) that changed polarity at positive potentials, consistently with a cation conductance (E_{rev} 22 ±7mV, n=11). Exposure to pulsed infrared light induced a fast increase in ramp currents that reaches its peak after 10s (T_{peak}=9.8±2s). An increase in current density was detected at both positive and negative

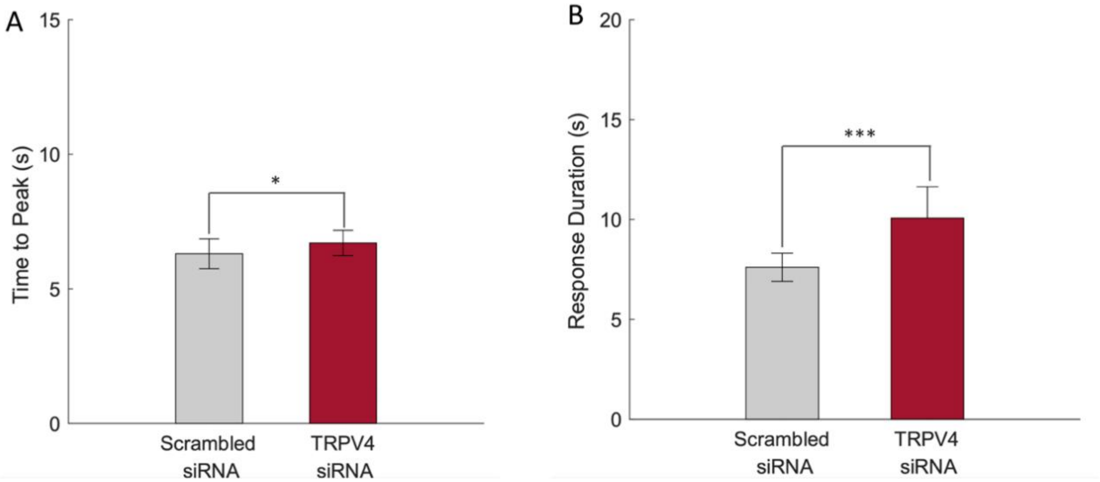

Figure 5.6: Effects of TRPV4 knockdown on IR-evoked calcium response dynamics
A) Histogram plot depicting the time to fluorescence peak calculated for astrocytes transfected with scrambled siRNA (grey columns) and TRPV4 siRNA (brown columns). B) Response duration in astrocytes transfected with scrambled siRNA (grey columns) and TRPV4 siRNA (brown columns). All histogram plots represent mean and error bars represent SEM. (N=number of experiments; N=11 for Scrambled siRNA and N=14 for TRPV4 siRNA) Student's t-test, *: $p<0.05$; **: $p<0.01$; ***: $p<0.001$).

potentials (**Figure 5.5E**, red columns) and reversed at voltages comparable with respect to controls (21±10 mV). Astrocytes transfected with scrambled siRNA showed current responses similar in magnitude (

Figure 5.5**E** grey columns) and dynamics (T_{peak}= 9.7±3s) to those observed in non-transfected cells. Infrared-evoked current responses were negligible for both inward and outward currents in TRPV4 siRNA astrocytes (**Figure 5.5E**, blue columns). The onset of the infrared evoked current was delayed in TRPV4 siRNA (T_{peak}=34±3s). Interestingly, the addition of HC-030031 (blocking TRPA1) decreased both inward and outward current density changes elicited by infrared stimulation in scrambled siRNA (**Figure 5.5E**, green columns) and nulled the residual responses in TRPV4 siRNA treated cells (**Figure 5.5E**, white columns). Collectively, these results suggest that TRPV4 and TRPA1 are both involved in mediating astrocytic extracellular Ca^{2+} influx and conductance increases in response to pulsed infrared light. The notion that TRPA1 is critical for regulation of basal $[Ca^{2+}]_i$ in astrocytes *in vitro* and *in* situ (47) may account for its involvement in the onset of the $[Ca^{2+}]_i$ responses and the relative decrease in dF/F magnitude when it is inhibited (**Table 5.1**, **Figure 5.3E**).

5.4.3 Water transport is triggered by infrared stimulation

Given the partnership of TRP channels with aquaporin-4 (AQP4) in astrocytes (12), we hypothesized that the activation of TRPV4 and TRPA1 may be related to AQP4 and related astrocytic cell volume changes. To validate this hypothesis, astrocytes from wildtype (WT) mice and AQP4 knockout (KO) mice were modulated with pulsed infrared light and compared. Calcium imaging results show that AQP4 expression is critical to the magnitude and dynamics of the response of astrocytes to infrared stimulation. When compared with WT, AQP4$^{(-/-)}$ astrocytes showed a decrease in both peak dF/F (**Figure 5.7A-B**) and activation probability (**Figure 5.9C**). Deletion of AQP4 caused a significantly delayed onset, with a nearly 50% increase in T_{peak} (**Figure 5.7C**) and a prolonged $T_{1/2}$ compared to WT astrocytes (**Figure 5.9D**). Accordingly, in differentiated astrocytes plated on nanostructured hydrotalcite (HTlc) films, where AQP4 expression and water permeability are increased (36), the peak dF/F and activation probability were increased with increased time to peak using infrared stimulation (**Table 5.1**, Figure 5.7, **Figure 5.9**).

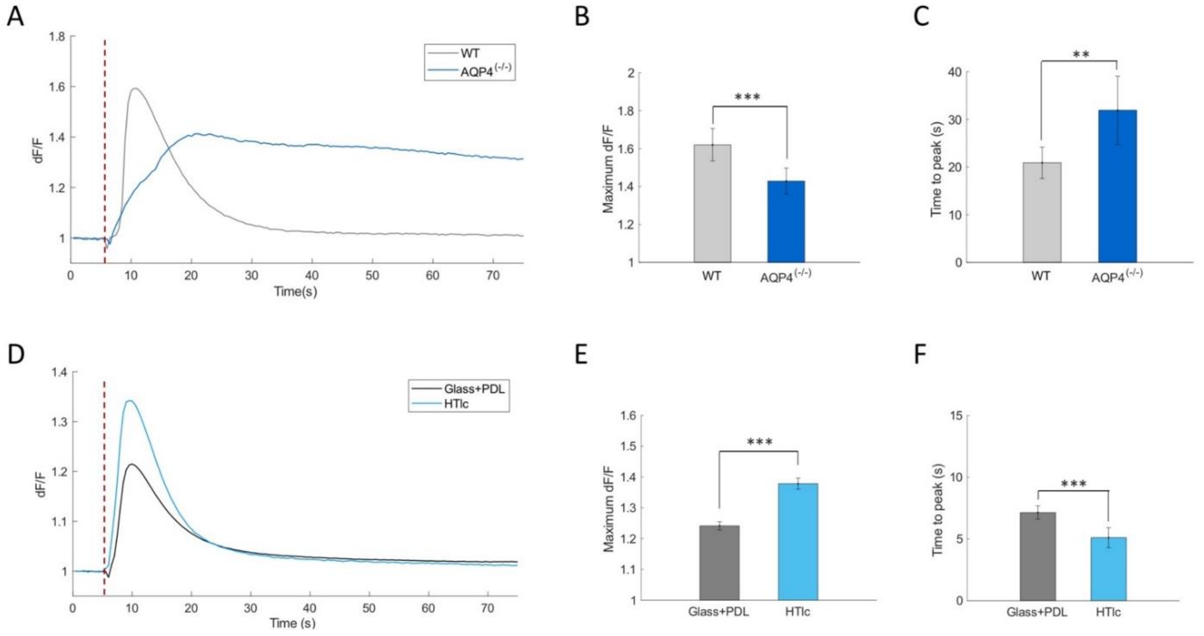

Figure 5.7. AQP4 expression is determinant for the dynamic of infrared-evoked calcium response (A) Representative traces of calcium fluorescence recorded in astrocytes from WT (light grey trace) and AQP4-KO ($^{-/-}$) mice (dark blue trace). (B-C) Histogram plots showing averaged maximal dF/F (B) and time to peak (C) in astrocytes from WT (light grey columns) and AQP4-KO ($^{-/-}$) astrocytes (dark blue columns). (D) Representative traces of calcium imaging experiments reporting dF/F dynamics performed on rat astrocytes grown on PDL (black trace) and on HTlc films (light blue trace). (E-F) Histogram plots showing averaged maximal dF/F (E) and time to peak (F) in rat primary astrocytes grown on PDL (grey columns) and HTlc films (light blue columns). All histogram plots represent mean and error bars represent SEM. Student's t-test, *: p<0,05; **: p<0,01; ***: p<0,001). Red dashed line in A and D represents the timepoint where pulsed infrared light was delivered.

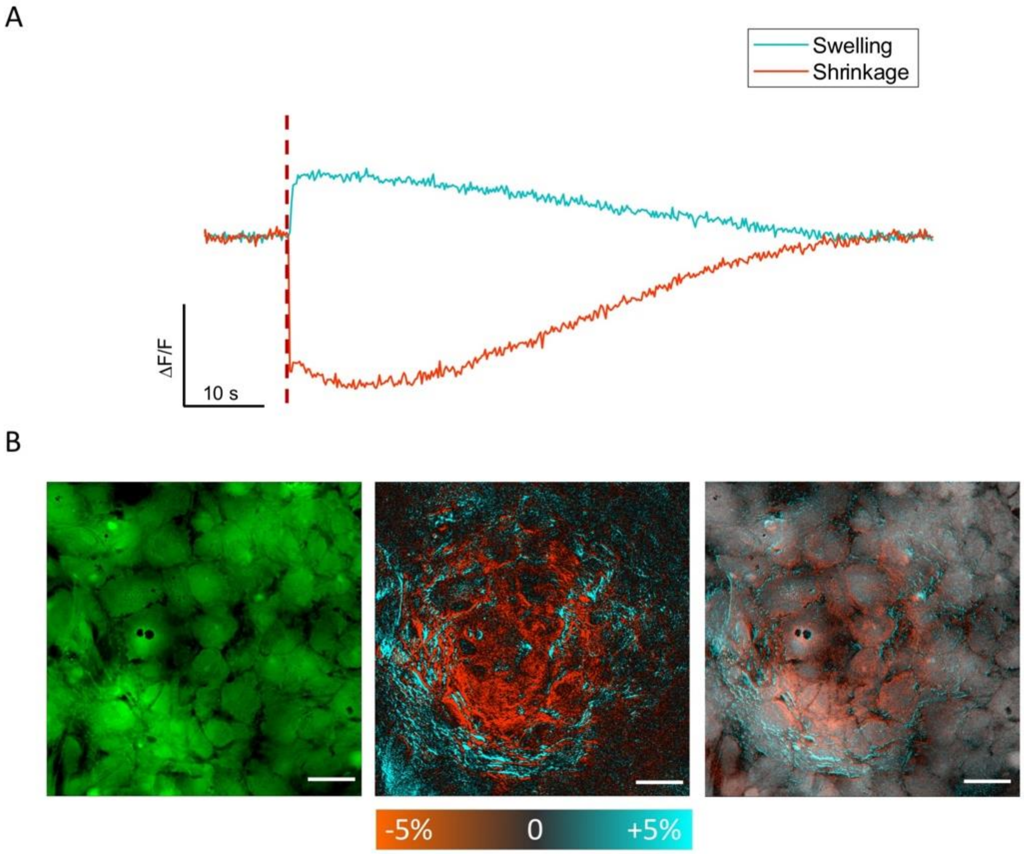

Figure 5.8. Water permeability is triggered by infrared pulses in rat astrocytes
(A) Representative traces of calcein fluorescence recorded in rat astrocytes representing fluorescence somatic response to an infrared pulse. Red dashed line represents the time point at which the pulse INS was delivered. B) left panel: image of dF/F recorded one second before the laser pulse, center panel: spatial map of fluorescence changes following infrared laser pulse exposure, merge of the images is indicative of the spatial distribution of the response. Scale bars are 50 μm.

Remarkably, by performing a calcein fluorescence self-quenching assay (18), we found that pulsed infrared light consistently induced water transport resulting in swelling and shrinkage of primary rat cortical astrocytes. Changes in cell volume appear in spatially distinct domains surrounding the site of stimulation. Nearly 50% of calcein-loaded astrocytes (505 responding, 526 non-responding, n=1031 cells) showed changes in levels of fluorescence immediately after the laser light was delivered (**Figure 5.8A**). About half of responding cells (n=255) responded with decrease in fluorescence (shrinking), while the remaining responded with fluorescence increase (swelling). Interestingly, the magnitude of swelling as demonstrated by the increase in fluorescence (0.57±0.38%) was different from that of shrinkage i.e. the decrease in fluorescence (-1.39±1.01%). The time constant of cell swelling was faster (0.44±0.04) than that observed for cell shrinkage (0.01±0.02).

The spatial map of change in fluorescence following infrared stimulation as shown in **Figure 5.8B**, indicates that the cells directly under the fiber delivering infrared light shrunk in volume, while those

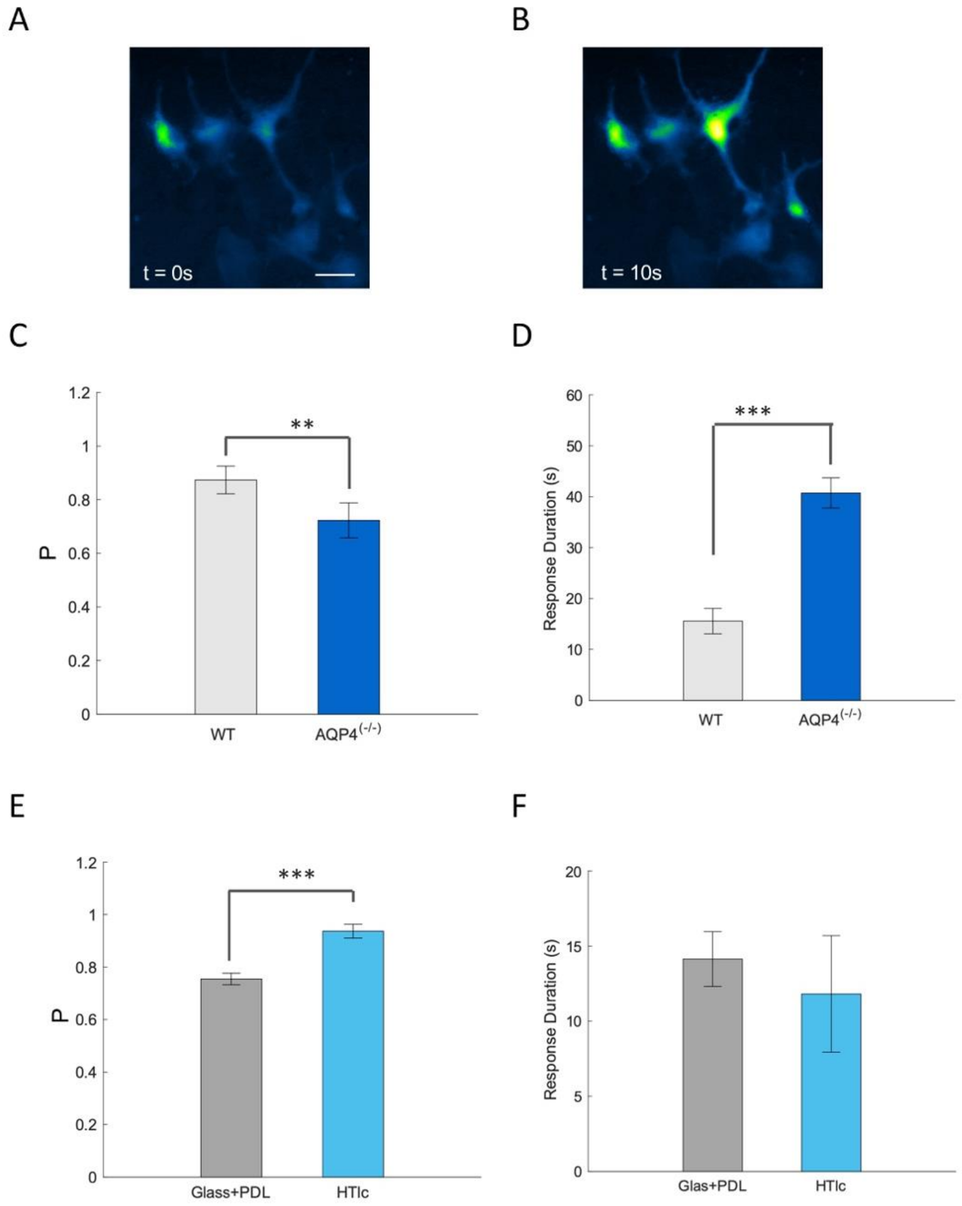

Figure 5.9: IR-evoked response dynamics are sensitive to AQP4 expression
(A-B) Sequential fluorescent images obtained from Fluo-4-AM loaded rat cortical astrocytes plated on HTlc. Images depicts fluorescent cells at time 0 (t=0), at the peak of fluorescence after INS stimulation (t=10s), scale bars are 40 µm. (C) Histogram plot showing percentage of responding cells in WT mouse astrocytes (grey columns) and AQP4-KO ($^{-/-}$) (blue columns). (D) Response duration recorded in mouse WT (grey columns) and AQP4-KO ($^{-/-}$) astrocytes (blue columns). (E) Histogram plot showing percentage of responding cells primary rat astrocytes grown on glass + PDL (grey columns) and HTlc (blue columns). (F) Response duration recorded in primary rat astrocytes grown on glass + PDL (grey columns) and HTlc (Blue columns). All histogram plots represent mean and error bars represent SEM. N=number of experiments; N=7 for WT; N=8 for AQP4(-/-); N=42 for Glass+PDL; N=7 for HTlc; Student's t-test, *: $p<0.05$; **: $p<0.01$; ***: $p<0.001$)

stimulation induces both swelling and shrinkage in primary rat cortical astrocytes in spatially distinct domains surrounding the site of stimulation. These changes suggest that homeostatic osmotic responses may be triggered by this method.

5.4.4 Proposed mechanisms

Various hypothesis can be proposed to explain the mechanisms underlying the effect of pulsed infrared light on astrocytes based on the experimental results described (**Figure 5.10**). Previous studies suggest that in neurons, infrared stimulation initiates a mechano-electrical effect at the cell plasma membrane, transiently modulating its thickness, capacitance, and its lipid bilayer structure (32, 34). If

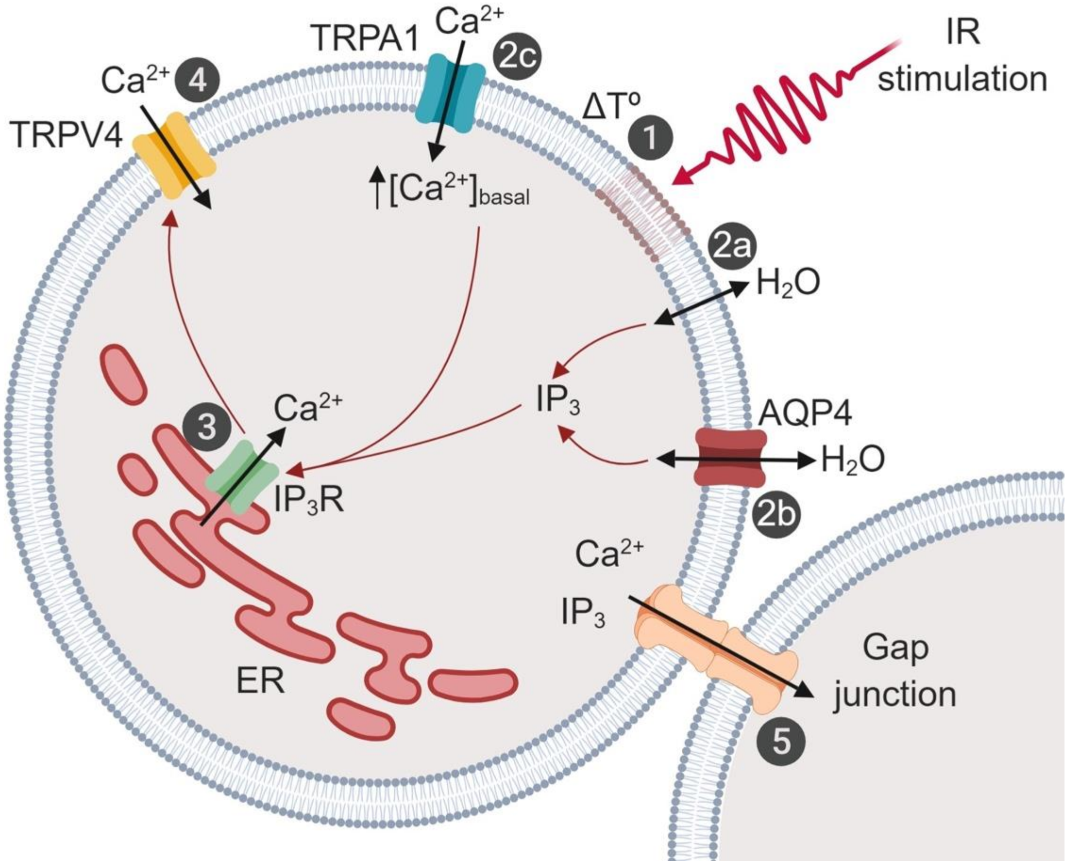

Figure 5.10. Possible mechanism underpinning the effects of infrared stimulation in astrocytes Infrared pulse effects a thermal increase that can alter astroglial plasma membrane structure (thickness, fluidity, permeability) or osmotic gradient, (1). The alteration can allow water fluxes through the plasma-membrane (2a) and through AQP4 (2b). Cell volume changes and/or mechanical membrane stress or incidental lipid release induced by infrared stimulation might activate TRPA1 (2a). Ca^{2+} influx through TRPA1 can elicit Ca^{2+} induced Ca^{2+} release via IP_3R (3). We hypothesize that $[Ca^{2+}]_i$ released via IP_3R can bind TRPV4 and sensitize it to cell volume changes to initiate RVD or RVI (4). Lastly, the Ca^{2+} signal can travel through gap junctions to spread to neighboring cells (5). Given that IP_3 pathway can also be activated by osmotic stress via the arachidonic acid path, we cannot rule out that the formation of IP_3 is triggered directly by cell volume changes.

direct gating of AQP4 by temperature rise is unlikely, the transient thermal gradient generated by infrared stimulation may spatially alter the kinetic energy of the water molecules around and within the cell (48), driving water transport through the cells. It is also possible that the laser light modulates the lipid bilayer composition or fluidity in the extracellular membrane (49), thus initiating water transport and swelling/shrinkage through AQP4-independent pathways. As a result, AQP4 may accelerate or add to an already infrared-initiated event that increases swelling/shrinkage rate.

Previous studies report the activation of TRPV4 by infrared stimulation in spiral and vestibular ganglion neuron (40, 43, 44). However, our data suggests that TRPV4 is not directly activated by pulsed infrared light in astrocytes, but rather as a secondary response to some additional effector. Function of TRPV4 is known to be dependent on osmotic stress (6, 12, 14), basal $[Ca^{2+}]_i$ (6, 47), that in the present case may be controlled in part by TRPA1 or IP_3R (50).

Given the known affinity and interaction between IP_3 and TRPV4 (50), it is possible that the activation of TRPV4 that we observed is dependent by the production of IP_3 induced by osmotic stress or by the increase in $[Ca^{2+}]_i$ (51). Accordingly, pulses of infrared light activated phospholipase-C mediated rises in $[Ca^{2+}]_i$ HT22 mouse hippocampal neurons and U87 human glioblastoma cells, suggesting the formation of IP_3 (40). However, our results do not provide evidence for IP_3 production by IR light in astrocytes, but only activation of IP_3R by pulsed IR light.

Direct thermal activation of TRPA1 is unlikely, as its debated thermal activation is prominently for cold stimuli rather than warm (8, 47, 52). However, recent evidence suggested a direct activation of TRPA1 by transient heat induced by ultra-fast infrared laser pulse (53) – although the temperature-time dynamics explored were quite different from those explored in this study. Interestingly, a recent study reported the implication of TRPA1 in osmotic-induced Ca^{2+} influx (52). While its activity and expression patterns is modulated by membrane lipid surrounding environment (8) which might explain the role of TRPA1 during infrared stimulation. In summary, we hypothesize that infrared stimulation induces transmembrane water transport or alteration in lipid membrane composition which in turn activates TRPA1. This activation initiates Ca^{2+} entry, promoting Ca^{2+} release via IP_3R, increased in $[Ca^{2+}]_i$ might bind to TRPV4 and sensitizes it to the cell volume changes triggered by pulsed infrared light (Figure 5.10).

5.5 Limitations

In this study, our experiments only addressed a narrow range of possible physiological responses that infrared stimulation may be driving in astrocytes. As a cell that is integral to so many dynamic processes in the brain, we cannot conclusively state that water transport and intracellular calcium dynamics are the only driving responses triggered in astrocytes. Further, our study only sought to understand acute astrocytic responses to IR exposure. Chronic effects of IR exposure on astrocytes are actively being studied. Nonetheless, our work provides a basis for how pulsed infrared light affects acute astrocyte physiology.

Activation of cortical astrocytes in conjunction with neuronal cells when using infrared stimulation has been previously demonstrated *in vivo* (31). However, questions remained on whether this response is a direct effect of this light on astrocytes or neurons with the other being affected indirectly. Here we show that astrocytes respond to pulsed infrared light, suggesting that we must consider how astrocytes might be affecting neuronal activity during infrared stimulation of the brain. On the other hand, previous studies have shown that neurons also respond to infrared light. Thus, future studies using co-cultures and controlled multicellular preparations must be conducted to evaluate the selectivity (or lack thereof) of this approach in different cell types and their interplay.

The specificity of laser parameters needed to modulate specific cell types remains to be determined. Moreover, our study only probed short, 8ms pulses of infrared light and delivered to a group of cells primarily targeting the cell body. However, pulsed infrared light has been demonstrated using a wide range of laser parameters (54). The spatial and temporal scale of calcium dynamics in astrocytes appears to vary depending on the initiation of Ca^{2+} signals in the cell body, processes, or endfeet (55, 56). By modifying the illumination geometry of the fiber as well as varying laser parameters, spatially and temporally, we may be able to trigger cellular or sub-cellular responses for tightly controlled multiscale probing and analyses of astrocytic $[Ca^{2+}]_i$ to study their function and dysfunction in various models.

5.6 Implications

Previous attempts from other groups to evoke astrocytic Ca^{2+} responses with light in cell cultures were only successful when used with cell-conjugated NIR-optimized plasmonic nanoparticles or label-free with high-intensity ultrafast NIR laser pulses (57, 58). Practically, our method of stimulation offers a label free, touchless strategy of glial and neural modulation - without exogenous effectors or genetic modification. A recent study indicates that commonly used visible light illumination protocols increase the temperature by 0.2–2°C and suppress spiking in multiple brain regions (59). Now, this work raises questions on the assumption that astrocyte functions are not altered by thermal or optical modulation such as that used during two-photon imaging of calcium dynamics imaging *in situ* and *in vivo,* This calls for detailed investigation of the impact of light on neural cell function. Regardless, infrared stimulation may be a useful tool for studying astrocytic water and ionic dynamics and the effect of homeostasis, neuro-vascular coupling and osmotic stress in healthy and pathological brain function.

5.7 Conclusion

In conclusion, we have demonstrated for the first time that astrocytes can directly and dynamically respond to pulsed infrared light. We provide clear and consistent evidence of the molecular mechanisms initiating the response, as well as downstream effects that have a direct impact on physiologically relevant astrocyte function. Specifically, we have i) characterized the initiation of Ca^{2+} responses in astrocytes from a label-free single 8ms pulse of infrared light in terms of $[Ca^{2+}]_i$ dynamics, whole-cell cationic conductance, and water permeability, ii) identified specific molecular players that underpin the effect of infrared stimulation on astroglial cells, highlighting that activation of IP_3R, TRPA1, TRPV4 and AQP4 are all involved in shaping the dynamics of infrared-evoked $[Ca^{2+}]_i$ activity, iii) demonstrated that infrared stimulation is a valuable tool to study Ca^{2+} and water dynamics as well as regulatory volume responses in cultured astrocytes, which may be useful in studying these processes during homeostatic dysregulation or exploring the effects of astrocyte activity on neuronal signaling. Such tools can probe the ionic and osmotic dynamics of the brain on a cellular and whole-organ scale and modulate homeostatic function in astrocytes at high spatial and temporal precision that would enable the study of healthy and diseased brain function.

5.8 Acknowledgements

This work was supported by EU Marie Curie Project OLIMPIA (GA 316832), the ASEE NDSEG Fellowship Program, and by the AFOSR Research Projects ASTROMAT, FA9550 16-1-0502 and ASTRONIR, FA9550-17-1-0502, 3D NEUROGLIA, DURIP FA9550-15-1-0328, FA9550-14-1-0303, FA 9550-17-1-0374. Calcium and calcein fluorescence imaging experiments were performed in part through the use of the Vanderbilt Cell Imaging Shared Resource (supported by NIH grants CA68485, DK20593, DK58404, DK59637 and EY08126). We are grateful to Dr Alessia Minardi from FABIT Dept. of the University of Bologna, for her help in the preparation and maintenance of astrocyte cultures.

5.9 Supplementary Data

Table 5.1: Calcium imaging experiments: data and statistics.
Mean values, Standard Error Mean (SEM) and p values (pval) calculated for maximal increase in fluorescence intensity (dF/F), time to peak (T$^{1/2}$), duration (d) and activation probability (P) for all the experimental conditions tested. The table shows also the number of experiments (N) and number of cells analysed for each experimental condition. p values were calculated with the Student’s t-test.

Calcium Source (Figure 2)														
	dF/F	SEM	pval	T$_{1/2}$ (sec)	SEM	pval	d (sec)	SEM	pval	P	SEM	pval	N	Number of cells
CTRL	1.28	0.02	7.45 x10^{-6}	6.91	1.12	1.05x10^{-2}	9.39	1.64	5.43x10^{-3}	0.76	0.05	0,014	11	140
$0[Ca^{2+}]_{out}$	1.17	0.02		9.61	2.80		7.24	1.27		0.70	0.06		11	86
CTRL	1.28	0.03	1.43 x10^{-6}	14.85	7.90	5.04x10^{-3}	7.17	0.40	0,03	0.76	0.03	9.24x10^{-6}	9	71
TPEN	1.13	0.01		5.59	0.99		7.99	1.10		0.58	0.05		11	91
CTRL	1.24	0.04	>0.05	3.96	0.24	1.81 x10^{-2}	5.63	0.46	>0.05	0.82	0.05	1.67x10^{-5}	4	57
CBX	1.23	0.06		6.69	2.35		5.86	0.89		0.54	0.04		5	50
CTRL	1.10	0.01	2.53x10^{-8}	15.31	0.71	1,45x10^{-7}	11.71	1.36	2.59x10^{-6}	0.78	0.03	2.14x10^{-11}	8	686
2-APB	1.02	0.002		23.76	1.73		28.77	5.15		0.19	0.03		9	634
TRP Pharmacology (Figure 2)														
	dF/F	SEM	pval	T$_{1/2}$ (sec)	SEM	pval	d (sec)	SEM	pval	P	SEM	pval	N	Number of cells
CTRL	1.22	0.02	3.52x10^{-7}	5.88	0.40	>0.05	11.19	1.73	>0.05	0.75	0.03	4.70x10^{-3}	11	122
RR	1.14	0.01		5.66	1.07		11.36	3.24		0.71	0.03		15	223
CTRL	1.22	0.03	1.66x10^{-4}	8.82	1,30	>0.05	26.06	5.74	>0.05	0.71	0.04	1.93x10^{-2}	10	107
RN	1.16	0.02		10.32	2,37		29.14	6.32		0.66	0.05		10	90
CTRL	1.24	0.03	1.83x10^{-3}	7.07	1,32	1.22x10^{-4}	10.68	1.48	2,06x10^{-5}	0.80	0.05	>0.05	10	118
HC030031	1.19	0.02		11.75	2,43		21.60	5.00		0.79	0.04		11	134
TRPV4 Knock Down (Figure 3)														
	dF/F	SEM	pval	T$_{1/2}$ (sec)	SEM	pval	d (sec)	SEM	pval	P	SEM	pval	N	Number of cells
Scrambled siRNA	1.30	0.06	1.79x10^{-6}	6.30	0.55	4.14x10^{-2}	7.61	0.70	1.35x10^{-4}	0.76	0.04	5.01x10^{-8}	11	97
TRPV4 siRNA	1.15	0.02		6.70	0.47		10.07	1.57		0.55	0.04		14	80
AQP4$^{(-/-)}$ (Figure 4)														
	dF/F	SEM	pval	T$_{1/2}$ (sec)	SEM	pval	d (sec)	SEM	pval	P	SEM	pval	Number of trials	Number of cells
WT	1.62	0.09	1.60x10^{-3}	20.91	3.31	0.004	15.58	2.48	9.77x10^{-7}	0.87	0.05	1.20x10^{-3}	7	135
AQP4$^{(-/-)}$	1.43	0.07		31.92	7.19		40.73	2.96		0.72	0.07		8	101
HTLC (Figure 4)														
	dF/F	SEM	pval	T$_{1/2}$ (sec)	SEM	pval	d (sec)	SEM	pval	P	SEM	pval	Number of trials	Number of cells
Glass+PDL	1.24	0.01	4.44x10^{-16}	7.13	0.55	8.74x10^{-7}	14.14	1.81	>0.05	0.75	0.02	1.20x10^{-3}	42	487
HTLC	1.38	0.02		5.11	0.81		11.82	3.87		0.9	0.03		7	100

5.10 References

1. Verkhratsky, A. and Nedergaard, M. (2018) Physiology of Astroglia. *Physiol. Rev.* 98, 239–389
2. Santello, M., Toni, N., and Volterra, A. (2019) Astrocyte function from information processing to cognition and cognitive impairment. *Nat. Neurosci.* 22, 154–166
3. Formaggio, F., Saracino, E., Mola, M. G., Rao, S. B., Amiry-Moghaddam, M., Muccini, M., Zamboni, R., Nicchia, G. P., Caprini, M., and Benfenati, V. (2019) LRRC8A is essential for swelling-activated chloride current and for regulatory volume decrease in astrocytes. *FASEB J.* 33, 101–113
4. Benfenati, V. and Ferroni, S. (2010) Water transport between CNS compartments: functional and molecular interactions between aquaporins and ion channels. *Neuroscience* 168, 926–940
5. Vincent, F., Acevedo, A., Nguyen, M. T., Dourado, M., DeFalco, J., Gustafson, A., Spiro, P., Emerling, D. E., Kelly, M. G., and Duncton, M. A. J. (2009) Identification and characterization of novel TRPV4 modulators. *Biochem. Biophys. Res. Commun.* 389, 490–494
6. Benfenati, V., Amiry-Moghaddam, M., Caprini, M., Mylonakou, M. N., Rapisarda, C., Ottersen, O. P., and Ferroni, S. (2007) Expression and functional characterization of transient receptor potential vanilloid-related channel 4 (TRPV4) in rat cortical astrocytes. *Neuroscience* 148, 876–892
7. Butenko, O., Dzamba, D., Benesova, J., Honsa, P., Benfenati, V., Rusnakova, V., Ferroni, S., and Anderova, M. (2012) The increased activity of TRPV4 channel in the astrocytes of the adult rat hippocampus after cerebral hypoxia/ischemia. *PLoS One* 7, e39959
8. Startek, J. B., Boonen, B., López-Requena, A., Talavera, A., Alpizar, Y. A., Ghosh, D., Van Ranst, N., Nilius, B., Voets, T., and Talavera, K. (2019) Mouse TRPA1 function and membrane localization are modulated by direct interactions with cholesterol. *Elife* 8
9. Garcia-Elias, A., Mrkonjic, S., Pardo-Pastor, C., Inada, H., Hellmich, U. A., Rubio-Moscardó, F., Plata, C., Gaudet, R., Vicente, R., and Valverde, M. A. (2013) Phosphatidylinositol-4,5-biphosphate-dependent rearrangement of TRPV4 cytosolic tails enables channel activation by physiological stimuli. *Proc. Natl. Acad. Sci. USA* 110, 9553–9558
10. Nilius, B., Vriens, J., Prenen, J., Droogmans, G., and Voets, T. (2004) TRPV4 calcium entry channel: a paradigm for gating diversity. *Am. J. Physiol. Cell Physiol.* 286, C195–205
11. Startek, J. B., Boonen, B., Talavera, K., and Meseguer, V. (2019) TRP Channels as Sensors of Chemically-Induced Changes in Cell Membrane Mechanical Properties. *Int. J. Mol. Sci.* 20
12. Benfenati, V., Caprini, M., Dovizio, M., Mylonakou, M. N., Ferroni, S., Ottersen, O. P., and Amiry-Moghaddam, M. (2011) An aquaporin-4/transient receptor potential vanilloid 4 (AQP4/TRPV4) complex is essential for cell-volume control in astrocytes. *Proc. Natl. Acad. Sci. USA* 108, 2563–2568
13. Thrane, A. S., Rappold, P. M., Fujita, T., Torres, A., Bekar, L. K., Takano, T., Peng, W., Wang, F., Rangroo Thrane, V., Enger, R., Haj-Yasein, N. N., Skare, Ø., Holen, T., Klungland, A., Ottersen, O. P., Nedergaard, M., and Nagelhus, E. A. (2011) Critical role of aquaporin-4 (AQP4) in astrocytic Ca2+ signaling events elicited by cerebral edema. *Proc. Natl. Acad. Sci. USA* 108, 846–851
14. Jo, A. O., Ryskamp, D. A., Phuong, T. T. T., Verkman, A. S., Yarishkin, O., MacAulay, N., and Križaj, D. (2015) TRPV4 and AQP4 channels synergistically regulate cell volume and calcium homeostasis in retinal müller glia. *J. Neurosci.* 35, 13525–13537
15. Mola, M. G., Sparaneo, A., Gargano, C. D., Spray, D. C., Svelto, M., Frigeri, A., Scemes, E., and Nicchia, G. P. (2016) The speed of swelling kinetics modulates cell volume regulation and calcium signaling in astrocytes: A different point of view on the role of aquaporins. *Glia* 64, 139–154
16. Nicchia, G. P., Pisani, F., Simone, L., Cibelli, A., Mola, M. G., Dal Monte, M., Frigeri, A., Bagnoli, P., and Svelto, M. (2016) Glio-vascular modifications caused by Aquaporin-4 deletion in the mouse retina. *Exp. Eye Res.* 146, 259–268

17. Noell, S., Wolburg-Buchholz, K., Mack, A. F., Ritz, R., Tatagiba, M., Beschorner, R., Wolburg, H., and Fallier-Becker, P. (2012) Dynamics of expression patterns of AQP4, dystroglycan, agrin and matrix metalloproteinases in human glioblastoma. *Cell Tissue Res.* 347, 429–441
18. Solenov, E., Watanabe, H., Manley, G. T., and Verkman, A. S. (2004) Sevenfold-reduced osmotic water permeability in primary astrocyte cultures from AQP-4-deficient mice, measured by a fluorescence quenching method. *Am. J. Physiol. Cell Physiol.* 286, C426–32
19. Nicchia, G. P., Nico, B., Camassa, L. M. A., Mola, M. G., Loh, N., Dermietzel, R., Spray, D. C., Svelto, M., and Frigeri, A. (2004) The role of aquaporin-4 in the blood-brain barrier development and integrity: studies in animal and cell culture models. *Neuroscience* 129, 935–945
20. Yool, A. J., Brown, E. A., and Flynn, G. A. (2010) Roles for novel pharmacological blockers of aquaporins in the treatment of brain oedema and cancer. *Clin. Exp. Pharmacol. Physiol.* 37, 403–409
21. Mederos, S., Hernández-Vivanco, A., Ramírez-Franco, J., Martín-Fernández, M., Navarrete, M., Yang, A., Boyden, E. S., and Perea, G. (2019) Melanopsin for precise optogenetic activation of astrocyte-neuron networks. *Glia* 67, 915–934
22. Fenno, L., Yizhar, O., and Deisseroth, K. (2011) The development and application of optogenetics. *Annu. Rev. Neurosci.* 34, 389–412
23. Yizhar, O., Fenno, L. E., Davidson, T. J., Mogri, M., and Deisseroth, K. (2011) Optogenetics in neural systems. *Neuron* 71, 9–34
24. Ji, Z.-G. and Wang, H. (2015) Optogenetic control of astrocytes: is it possible to treat astrocyte-related epilepsy? *Brain Res. Bull.* 110, 20–25
25. Takata, N., Sugiura, Y., Yoshida, K., Koizumi, M., Hiroshi, N., Honda, K., Yano, R., Komaki, Y., Matsui, K., Suematsu, M., Mimura, M., Okano, H., and Tanaka, K. F. (2018) Optogenetic astrocyte activation evokes BOLD fMRI response with oxygen consumption without neuronal activity modulation. *Glia* 66, 2013–2023
26. Cho, W.-H., Barcelon, E., and Lee, S. J. (2016) Optogenetic glia manipulation: possibilities and future prospects. *Exp. Neurobiol.* 25, 197–204
27. Wells, J., Kao, C., Konrad, P., Milner, T., Kim, J., Mahadevan-Jansen, A., and Jansen, E. D. (2007) Biophysical mechanisms of transient optical stimulation of peripheral nerve. *Biophys. J.* 93, 2567–2580
28. Wells, J., Kao, C., Mariappan, K., Albea, J., Jansen, E. D., Konrad, P., and Mahadevan-Jansen, A. (2005) Optical stimulation of neural tissue in vivo. *Opt. Lett.* 30, 504–506
29. Cayce, J. M., Kao, C. C., Malphrus, J. D., Konrad, P. E., Mahadevan-Jansen, A., and Jansen, E. D. (2010) Infrared neural stimulation of thalamocortical brain slices. *IEEE J. Select. Topics Quantum Electron.* 16, 565–572
30. Cayce, J. M., Wells, J. D., Malphrus, J. D., Kao, C., Thomsen, S., Tulipan, N. B., Konrad, P. E., Jansen, E. D., and Mahadevan-Jansen, A. (2015) Infrared neural stimulation of human spinal nerve roots in vivo. *Neurophotonics* 2, 015007
31. Cayce, J. M., Bouchard, M. B., Chernov, M. M., Chen, B. R., Grosberg, L. E., Jansen, E. D., Hillman, E. M. C., and Mahadevan-Jansen, A. (2014) Calcium imaging of infrared-stimulated activity in rodent brain. *Cell Calcium* 55, 183–190
32. Shapiro, M. G., Homma, K., Villarreal, S., Richter, C.-P., and Bezanilla, F. (2012) Infrared light excites cells by changing their electrical capacitance. *Nat. Commun.* 3, 736
33. Ebtehaj, Z., Hatef, A., Malekmohammad, M., and Soltanolkotabi, M. (2018) Computational modeling and validation of thermally induced electrical capacitance changes for lipid bilayer membranes irradiated by pulsed lasers. *J. Phys. Chem. B* 122, 7319–7331
34. Plaksin, M., Shapira, E., Kimmel, E., and Shoham, S. (2018) Thermal Transients Excite Neurons through Universal Intramembrane Mechanoelectrical Effects. *Phys. Rev. X* 8, 011043
35. Benfenati, V., Caprini, M., Nicchia, G. P., Rossi, A., Dovizio, M., Cervetto, C., Nobile, M., and Ferroni, S. (2009) Carbenoxolone inhibits volume-regulated anion conductance in cultured rat cortical astroglia. *Channels* 3, 323–336

36. Posati, T., Pistone, A., Saracino, E., Formaggio, F., Mola, M. G., Troni, E., Sagnella, A., Nocchetti, M., Barbalinardo, M., Valle, F., Bonetti, S., Caprini, M., Nicchia, G. P., Zamboni, R., Muccini, M., and Benfenati, V. (2016) A nanoscale interface promoting molecular and functional differentiation of neural cells. *Sci. Rep.* 6, 31226
37. Schindelin, J., Arganda-Carreras, I., Frise, E., Kaynig, V., Longair, M., Pietzsch, T., Preibisch, S., Rueden, C., Saalfeld, S., Schmid, B., Tinevez, J.-Y., White, D. J., Hartenstein, V., Eliceiri, K., Tomancak, P., and Cardona, A. (2012) Fiji: an open-source platform for biological-image analysis. *Nat. Methods* 9, 676–682
38. Hofer, A. M., Fasolato, C., and Pozzan, T. (1998) Capacitative Ca2+ entry is closely linked to the filling state of internal Ca2+ stores: a study using simultaneous measurements of ICRAC and intraluminal [Ca2+]. *J. Cell Biol.* 140, 325–334
39. Scemes, E. (2000) Components of astrocytic intercellular calcium signaling. *Mol. Neurobiol.* 22, 167–179
40. Moreau, D., Lefort, C., Pas, J., Bardet, S. M., Leveque, P., and O'Connor, R. P. (2018) Infrared neural stimulation induces intracellular Ca2+ release mediated by phospholipase C. *J. Biophotonics* 11
41. Tolstykh, G. P., Olsovsky, C. A., Ibey, B. L., and Beier, H. T. (2017) Ryanodine and IP3 receptor-mediated calcium signaling play a pivotal role in neurological infrared laser modulation. *Neurophotonics* 4, 025001
42. Sherwood, M. W., Arizono, M., Hisatsune, C., Bannai, H., Ebisui, E., Sherwood, J. L., Panatier, A., Oliet, S. H. R., and Mikoshiba, K. (2017) Astrocytic IP3 Rs: Contribution to Ca2+ signalling and hippocampal LTP. *Glia* 65, 502–513
43. Barrett, J. N., Rincon, S., Singh, J., Matthewman, C., Pasos, J., Barrett, E. F., and Rajguru, S. M. (2018) Pulsed infrared releases Ca2+ from the endoplasmic reticulum of cultured spiral ganglion neurons. *J. Neurophysiol.* 120, 509–524
44. Lumbreras, V., Bas, E., Gupta, C., and Rajguru, S. M. (2014) Pulsed infrared radiation excites cultured neonatal spiral and vestibular ganglion neurons by modulating mitochondrial calcium cycling. *J. Neurophysiol.* 112, 1246–1255
45. Paris, L., Marc, I., Charlot, B., Dumas, M., Valmier, J., and Bardin, F. (2017) Millisecond infrared laser pulses depolarize and elicit action potentials on in-vitro dorsal root ganglion neurons. *Biomed. Opt. Express* 8, 4568–4578
46. Vriens, J., Watanabe, H., Janssens, A., Droogmans, G., Voets, T., and Nilius, B. (2003) Cell swelling , heat , and chemical agonists use distinct pathways for the activation of the cation channel TRPV4. *PNAS* 101, 396–401
47. Shigetomi, E., Jackson-Weaver, O., Huckstepp, R. T., O'Dell, T. J., and Khakh, B. S. (2013) TRPA1 channels are regulators of astrocyte basal calcium levels and long-term potentiation via constitutive D-serine release. *J. Neurosci.* 33, 10143–10153
48. Nicchia, G. P., Frigeri, A., Liuzzi, G. M., Santacroce, M. P., Nico, B., Procino, G., Quondamatteo, F., Herken, R., Roncali, L., and Svelto, M. (2000) Aquaporin-4-containing astrocytes sustain a temperature- and mercury-insensitive swelling in vitro. *Glia* 31, 29–38
49. Walsh, A. J., Cantu, J. C., Ibey, B. L., and Beier, H. T. (2017) Short infrared laser pulses increase cell membrane fluidity. presented at the SPIE BiOS
50. Fernandes, J., Lorenzo, I. M., Andrade, Y. N., Garcia-Elias, A., Serra, S. A., Fernández-Fernández, J. M., and Valverde, M. A. (2008) IP3 sensitizes TRPV4 channel to the mechano- and osmotransducing messenger 5'-6'-epoxyeicosatrienoic acid. *J. Cell Biol.* 181, 143–155
51. Garcia-Elias, A., Lorenzo, I. M., Vicente, R., and Valverde, M. A. (2008) IP3 receptor binds to and sensitizes TRPV4 channel to osmotic stimuli via a calmodulin-binding site. *J. Biol. Chem.* 283, 31284–31288
52. Fujita, F., Uchida, K., Takayama, Y., Suzuki, Y., Takaishi, M., and Tominaga, M. (2018) Hypotonicity-induced cell swelling activates TRPA1. *J Physiol Sci* 68, 431–440

53. Ermakova, Y. G., Lanin, A. A., Fedotov, I. V., Roshchin, M., Kelmanson, I. V., Kulik, D., Bogdanova, Y. A., Shokhina, A. G., Bilan, D. S., Staroverov, D. B., Balaban, P. M., Fedotov, A. B., Sidorov-Biryukov, D. A., Nikitin, E. S., Zheltikov, A. M., and Belousov, V. V. (2017) Thermogenetic neurostimulation with single-cell resolution. *Nat. Commun.* 8, 15362
54. Thompson, A. C., Stoddart, P. R., and Jansen, E. D. (2014) Optical Stimulation of Neurons. *Curr. Mol. Imaging* 3, 162–177
55. Dunn, K. M., Hill-Eubanks, D. C., Liedtke, W. B., and Nelson, M. T. (2013) TRPV4 channels stimulate Ca2+-induced Ca2+ release in astrocytic endfeet and amplify neurovascular coupling responses. *Proc. Natl. Acad. Sci. USA* 110, 6157–6162
56. Bindocci, E., Savtchouk, I., Liaudet, N., Becker, D., Carriero, G., and Volterra, A. (2017) Three-dimensional Ca2+ imaging advances understanding of astrocyte biology. *Science* 356
57. Lu, Y., Li, T., Zhao, X., Li, M., Cao, Y., Yang, H., and Duan, Y. Y. (2010) Electrodeposited polypyrrole/carbon nanotubes composite films electrodes for neural interfaces. *Biomaterials* 31, 5169–5181
58. Choi, M., Yoon, J., Ku, T., Choi, K., and Choi, C. (2011) Label-free optical activation of astrocyte in vivo. *J. Biomed. Opt.* 16, 075003
59. Owen, S. F., Liu, M. H., and Kreitzer, A. C. (2019) Thermal constraints on in vivo optogenetic manipulations. *Nat. Neurosci.* 22, 1061–1065

CHAPTER 6:

DIFFERING APPROACHES TO INFRARED NEURAL STIMULATION CAN MODULATE DISTINCT PHYSIOLOGICAL RESPONSES OF ASTROCYTES *IN VITRO*

Text adapted from:

Wilson R. Adams*[1], Ana I Borrachero-Conejo*[1], Emanuela Saracino[3], Roberto Zamboni[3], E Duco Jansen[1,2], Valentina Benfenati[3,4], Anita Mahadevan-Jansen[1,2]. *Differing approaches to infrared neural stimulation can modulate distinct physiological responses of astrocytes in vitro*. [In Preparation]

*Authors contributed equally to work

6.1 Abstract

Label-free optical stimulation of brain cells with infrared (IR) light provides a powerful tool for spatially targeted neuromodulation. However, lingering questions about the off-target effects of IR stimulation on non-neuronal cells remain sparsely explored. The variation in IR dosing strategies across IR neuromodulation studies further complicates interpreting results. We have previously shown that rat astroglial cultures are independently sensitive to single pulses of infrared light, evoking osmoregulatory phenomena *in vitro.* Previous work *in vivo* showed astrocyte calcium responses to bursts of multiple shorter pulses. To better understand how astrocytes respond to different dosing strategies of IR stimulation, we systematically explored the impact of three different IR stimulation time courses on astrocyte calcium and water transport dynamics with widefield fluorescence microscopy and pharmacology. Results show that different stimulation methods can evoke similar shaped calcium responses in astrocytes, though their responses result from distinct biomolecular signaling processes. This work has crucial implications for interpreting previous work in the IR neuromodulation literature. Despite these implications, we also show the utility of leveraging label-free optical modulation techniques to drive astroglial water transport, a crucial process in healthy brain function that lacks tools for spatially precise modulation. More broadly, our results demonstrate the need to consider off-target effects with neuromodulation strategies and how to use such effects to study brain physiology.

6.2 Introduction

Neuromodulation with pulses of strongly absorbed infrared (IR) light, or infrared neural stimulation (INS), evokes neural activity in a wide variety of model systems (1–17). The nonspecific nature of infrared light heating water to trigger cell signaling raises how it may be impacting non-neuronal cells in the brain. Glial cells are receiving growing recognition for their role in neural circuitry and brain function, yet optical tools to modulate their physiology are underdeveloped. Label-free glial modulation methods with light would provide a helpful tool to study the brain in unique ways.

Prior work shows astrocytes are involved in the initial responses of rat somatosensory cortex to INS *in vivo* (4). As a follow-up to that work, we showed that astrocytes are independently sensitive to single 8-millisecond pulses of IR light, which evoke physiological effects such as IP3R-mediated Ca^{2+} release and water transport processes (18). Astrocytes play a crucial role in supporting and modulating neuronal function on a wide range of timescales by altering the extracellular fluid constituents (e.g., ions, water molecules, neuromodulators, metabolic waste) (19–21). Hydrosaline homeostasis can profoundly affect synaptic plasticity, neural network dynamics, and animal behavior (22–24). Astrocytes play a crucial role in regulating local energetic demand and facilitating immunological reactivity across the entire brain (25). Recently, a surge of tools to modulate and study astrocyte function chemically, optically, and genetically have been developed to study their role in brain function and behavior (26, 27). Though many tools are repurposed from those developed for neurons, these tools often drive substantially different physiology in astrocytes. Understanding the cell-type specific effects on tissue physiology is critical for new neuromodulation technologies' research and clinical utility.

A key remaining question about INS concerns how dosing cells differently with light impacts their physiological responses. Studies using INS employ a broad range of stimulation parameters. Previous *in vivo* studies in rats and non-human primates used a rapid burst of lower energy IR pulses to evoke neural activity to avoid tissue damage (1, 3, 28–31). Similar bursts of pulses at even shorter pulse widths drive auditory activity in guinea pigs and cats (10, 12, 13). Conventionally, single IR pulses between 1 and 10 milliseconds long excite *in vitro* neuronal and *in vivo* peripheral nerve preparations (7–9, 14–16, 32–34). The lack of consistency with IR dosing parameters (35, 36) naturally raises questions about their comparability. Research addressing this question remains unavailable.

INS's mechanistic models suggest that the heat generated by water's IR absorption properties depolarizes neurons (7, 17, 32, 37, 38). However, cells of different phenotypes respond differently to INS downstream at the biomolecular level. Groups have shown that different molecular pathways can be affected by similar IR exposure conditions in different model systems (8, 14–16, 39, 40). No study has compared IR dosing conditions to cell physiological responses. Such a study would provide a practical basis for deploying label-free neuromodulation technologies for broader questions in neuroscience.

To begin addressing these points, we hypothesize that different dosing parameters of pulsed infrared light can evoke distinct biochemical pathways and physiological processes in primary cortical astrocyte cultures. We carry out *in vitro* calcium imaging experiments with pharmacology on rat-derived primary cortical astrocytes. Water transport dynamics are evaluated by calcein-fluorescence-quenching microscopy. Results across three IR exposure conditions were compared: a single IR pulse (SP), a short train of stronger short IR pulses (SMP), and a longer train of lower energy short IR pulses (LMP). Furthermore, we offer insight into how these findings may help study astrocyte function and disfunction in the broader context of brain physiology.

6.3 Methods

6.3.1 Rat Cortical Astrocyte Culture Isolation

Primary astroglial cultures were prepared in accordance with animal use protocols approved by the Vanderbilt University Institute for Animal Care and Use Committee (VU-IACUC, Protocol M1600084). Astrocyte primary cultures were prepared as described previously (41). In brief, astrocytes were isolated from day 0-2 postnatal Sprague-Dawley rat pups (Envigo/Harlan, Indianapolis, IN, USA). The superficial-most portions of neural cortices were mechanically dissected and placed in 1mL of Dulbecco's Modified Eagle Medium supplemented with 5mM L-glutamine, 15%v/v fetal bovine serum (FBS), and penicillin/streptomycin (100 U/mL and 100 µg/mL, respectively). Tissues were mechanically dissociated by shearing tissue samples through a disposable pipette tip in their respective media and straining the medium suspension with a 40 µm cell strainer (Falcon, BD Bioscience, Bedford, MA). Strained cells in suspension were plated on culture flasks containing the previously described medium formulation. Cells were maintained in incubation at 37ºC with 5% CO_2 and 95% relative humidity levels for at least three weeks before imaging. After three days *in vitro*, culture flasks were periodically gently shaken, when necessary, to remove microglial, fibroblasts, and fibrous astrocyte growth in the flask. After 14 days *in vitro*, medium concentrations of FBS were reduced to 10%v/v. Cells were used between days 21 and 35 *in vitro* for experiments upon re-plating. Primary astrocytes were detached using a 0.025% trypsin/EDTA solution for 5 minutes at 37ºC and 5% CO2 to plate cells for live imaging experiments. Cells were reseeded on glass-bottom 35mm cell culture dishes (#1.5 coverglass, 10-17 mm diameter, Mattek, Waltham, MA, USA) coated with Poly-D-lysine (PDL) at a concentration of about 30,000 cells/cm^2. Imaging experiments were performed between 48-72 hours of re-plating.

6.3.2 Widefield Calcium Fluorescence Imaging

To image intracellular calcium dynamics of rat cortical astrocyte cultures, cells seeded on glass-bottom imaging dishes were rinsed and incubated with physiological saline solution containing 1 µM of Fluo-4-AM and Pluronic-127 for 1 hour at room temperature (Molecular Probes, Thermo-Fisher, St. Louis, MO, USA). After dye loading, cells were rinsed with and maintained in a standard bath solution for the duration of imaging sessions (<60 minutes). Cells were imaged on a Nikon Ti-S inverted epifluorescence microscope (Figure 6.1**A**). Fluorescence excitation was provided by a broadband light source (Lumencore Sola or Aura III) bandpass filtered to a wavelength range centered around 488nm. Average powers measured at the sample were maintained at about 1.3 mW across all experiments. Fluorescence detection was achieved through a 525 nm bandpass filter and an air objective (Nikon Instruments, 20 X Plan Apo, 0.8 NA) onto an sCMOS camera (Hamamatsu Orca Flash 3.0). Camera sensor exposure times were held constant at 200 ms, with a 50 ms fluorescence illumination buffer for stable illumination intensities across all widefield fluorescence images.

During an imaging experiment, fluorescence images of dye-loaded astrocytes were acquired at a 2Hz framerate for 300 frames (i.e., two and a half minutes). Approximately 30 seconds into the recording period, cells were stimulated with infrared light as described in the ***Pulsed Infrared Stimulation*** methods. The evoked calcium signal was observed for the remaining two minutes of the experiment interval. Bath application of pharmacological agents was employed to study the influence of molecular signaling pathways involved in IR-evoked calcium dynamics, with agents and working concentrations described in ***Solutions and Chemicals*** and **Table 6.1.** All images were acquired in NIS Elements (Nikon Imaging Systems, Melville, NY, USA) and analyzed using custom processing and analysis workflows with Fiji (42) and Matlab (Mathworks, Natick, MA, USA).

6.3.3 Calcein Self-Quenching Imaging

To assess cell volume changes in rat astrocytes *in vitro*, we used the calcein fluorescence quenching method as previously described (43). Cells plated on glass-bottom dishes were loaded with Calcein-AM (Life Technologies, Thermo Fisher, USA) by incubating cells with 10 μM of dye in standard bath solution for 30 min at room temperature. Experiments were performed 48-72h after re-plating cells on imaging dishes. Image acquisition was controlled by NIS Elements (Nikon imaging Systems, Melville, NY, USA) on a Nikon Ti-S inverted epifluorescence microscope using identical acquisition parameters from calcium imaging. All images were analyzed using custom processing and analysis workflows in Fiji (42) and Matlab (Mathworks, Natick, MA, USA).

6.3.4 Pulsed Infrared Stimulation

Pulsed infrared light was delivered to astrocytes via a multimode optical fiber (400 µm diameter, Ocean Optics, Jupiter, FL, USA) coupled to an 1875nm diode laser system (Capella, Aculight | Lockheed-Martin, Bothell, WA, USA). The bare output was positioned within the microscope's field of view using a micromanipulator (MPC-1000, Sutter Instruments). The optical fiber was aimed at a 45-degree angle relative to the microscope's sample plane. The fiber was positioned laterally in the field of view, where the fiber edge was approximately 10 µm above the coverslip surface. The lateral position of the fiber was adjusted such that the central region of the evoked calcium responses in the observed cells were central to

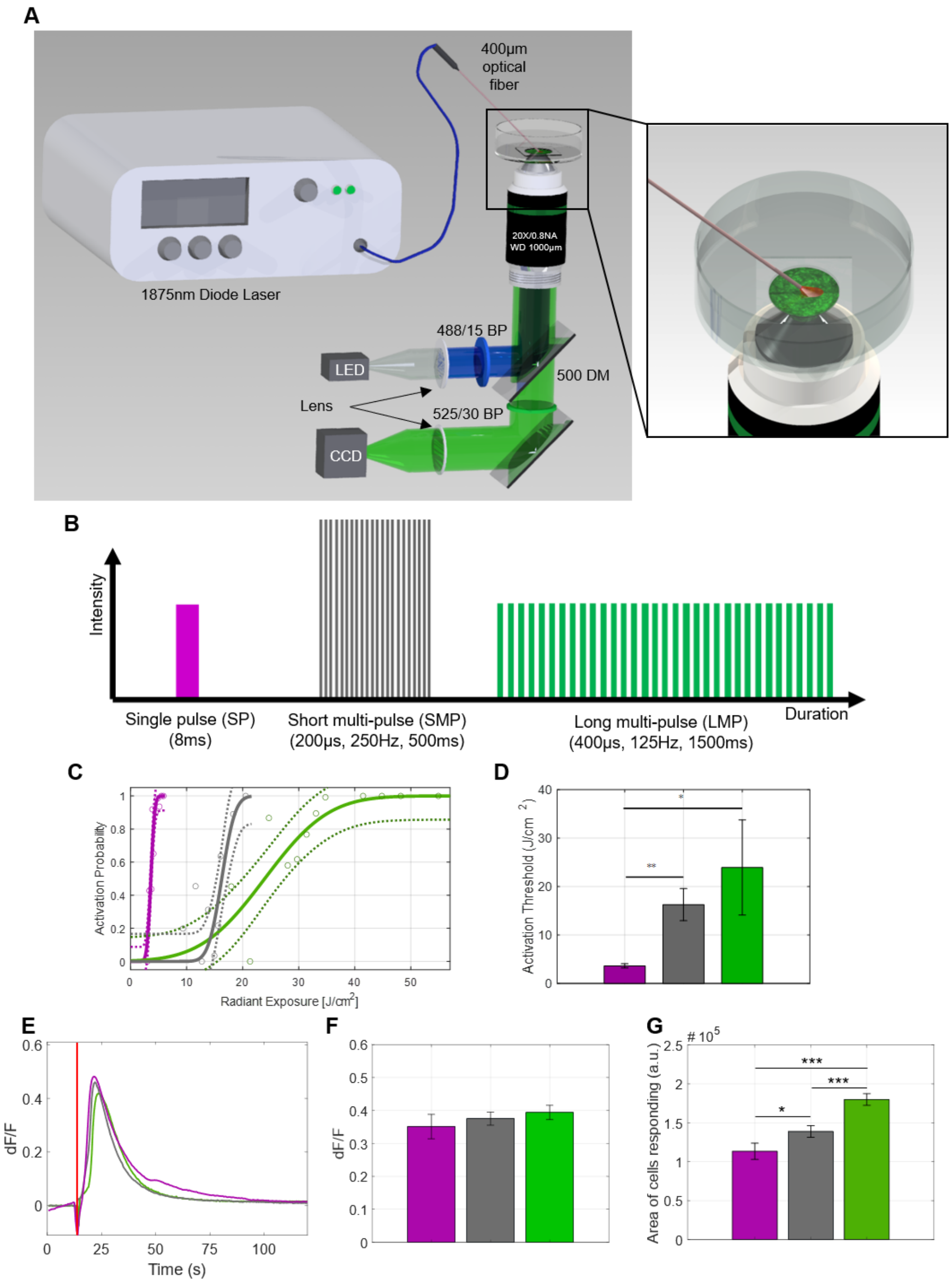

Figure 6.1: Experimental setup and dose-dependent Ca^{2+} responses to IR stimulation
(A) Schematic representation of the experimental set-up for astrocyte stimulation. (B) Schematic representation of the different pulse protocols used to stimulate astrocytes. (C) Activation probability as a function of radiant exposure delivered to rat primary astrocytes with an 8ms single pulse, a SMP, and LMP stimulation. (D) Bar graph showing the average values of radian exposure for the 50% of activation. (E) Representative traces depicting the normalized variation in cell fluorescence over time (dF/F) that reflects variation in $[Ca^{2+}]_i$. The red lines mark the timepoint at which the laser pulse was delivered. (F) Bar plot showing the average dF/F for the different pulse protocols. (G) Bar plot depicting the average area of astrocytic activation for the different stimulation protocols. N=32 for SP, N=61 for SMP and N=59 for LMP. N represents the number of plates. Data are reported as mean and SEM. Student's unpaired t-test,* $p < .05$,**$p < .01$, ***$p < .001$.

observed to elicit a large, slow-spreading calcium response amongst cells in the imaging dish. The effort was taken to avoid mechanical stimulation of the cells by locking the lateral micromanipulator position between experiments and repositioning the fiber axially to minimize shearing of the medium around the cells when navigating fields of view to stimulate.

Astrocytes were given one of three different irradiation/stimulation protocols (**Figure 6.1B**): an 8 ms long single pulse (SP), a shorter 500 ms-duration burst of 250 μs-long pulses at a 200Hz repetition rate (SMP), or a longer 1500 ms-duration burst of 400 μs-long pulses at a 125 Hz repetition rate (LMP). The radiant exposure delivered to the cells under each stimulation protocol was adjusted by changing each pulse's pulse peak power. Peak power was controlled by adjusting the current delivered to the laser diode. The activation probability as a function of radiant exposure was fit to a cumulative distribution function for each stimulation protocol. The dosage eliciting 50% cell activation was reported as the stimulation threshold. The 95% confidence interval was reported as the error in estimating the stimulation threshold. For pharmacological experiments, the radiant exposure that activated 75-80% of cells in an imaging control experiments field of view was used.

Energy doses of IR pulses are calculated based on the externally measured optical power from a constant temporal train of optical pulses. Measured power output was divided by the duty cycle of the pulse train (5%) to calculate the average peak power of each IR pulse. Multiplying the IR pulse peak power by the pulse duration yields an average pulse energy value. Calculated pulse energies can be divided across the 400 μm fiber area to output an average radiant exposure value delivered to the imaging medium at the fiber exit per pulse. The radiant exposure per pulse multiplied by the number of pulses delivered to the cells yields the total radiant exposure delivered to the medium at the optical fiber face. Extrapolating the exponential decay of this energy as a function of the distance between the fiber face and the coverslip surface, assuming an absorption coefficient of the stimulation laser in water as 26 cm^{-1} (44), yields an approximate radiant exposure experienced by the imaged cells. There is a spatial variation to the radiant exposure of IR light - and thus temperature change – experienced by the cells during stimulation across the microscope's field of view. The observed stimulation areas always appeared to fall within the entire field of view of the microscope. For the sake of simplicity, the average approximated radiant exposure at the coverslip surface was used consistently to describe the experimental condition for each imaging experiment.

6.3.5 Electrophysiology Methods

Currents were recorded with the whole-cell configuration of the patch-clamp technique as described previously (41). Patch pipettes were prepared from thin-walled borosilicate glass capillaries to obtain a tip resistance of 2–4 MΩ when filled with the standard internal solution. Membrane currents were amplified, filtered at 2 kHz and acquired at a sample rate of 5 kHz by Axopatch 200B amplifier in voltage-clamp mode. Responses were amplified, low-pass filtered at 1 kHz, digitised at 20 kHz, stored and analysed with pCLAMP 10. Liquid junction potential (7 mV) was calculated and corrected off-line; voltages indicated are those relative to the real transmembrane potentials. Experiments were carried out at room temperature (22–24 °C). Steady state current density in response to ramp currents was calculated before and after INS. Maximal current increase (pA/pF) is reported as the ratio of the maximal current densities after INS at -80mV and +80 mV to those measured at steady state prior to INS. Electrophysiological data are expressed as mean +/- standard error of the mean, where the number of cells patched was the number of samples. Potassium (K^+) in the intra- and extra-cellular saline were replaced by cesium (Cs^+) to isolate non-K^+ currents in astrocytes *in vitro*.

6.3.6 Solutions and Chemicals

Standard bath solution is composed of the following salts in deionized water (in mM): 140 NaCl, 4 KCl, 2 $MgCl_2$, 2 $CaCl_2$, 10 HEPES, 5 glucose, pH 7.4 with NaOH, and osmolarity adjusted to ~318 mOsm with mannitol. Ca^{2+}-free extracellular solution (0 $[Ca^{2+}]_{out}$) is formulated with deionized water containing the following salt concentrations (mM): 140 NaCl, 4 KCl, 4 $MgCl_2$, 10 HEPES, 5 glucose, 0.5 EGTA, pH 7.4 with NaOH and osmolarity adjusted to ~318 mOsm with mannitol. Stock solutions of pharmacological agents were prepared from vendors by solubilizing them in their appropriate diluent solutions. Stock aliquot concentrations and diluents are summarized in **Table 6.1**. Stock aliquots of carbenoxolone (CBX, 50mM) 4-(Phosphonomethyl)-2-piperazinecarboxylic acid (PMPA, 10mM), (3-Aminopropyl) (diethoxymethyl) phosphinic acid (CGP-35348, 100 mM), Suramin (100 mM), (Brilliant Blue G (BBG, 10 mM), Verapamil (5mM) and Ruthenium red (RR, 10mM) were prepared in water and stored at -20 ºC. Aliquots of 2-Aminoethoxydiphenylborane (2-APB, 100 mM), 2,3-Dioxo-6-nitro-1,2,3,4-tetrahydrobenzo[*f*]quinoxaline-7-sulfonamide disodium salt (BNQX, 10mM), RN-1734 (14.7 mM), HC-030031 (40 mM) capsazepine (5mM) and A425619 (1mM) were prepared by dissolving in DMSO and stored as aliquots at -20 ºC. Aliquots of N,N,N′,N′-tetrakis(2- pyridinylmethyl)-1,2-ethanediamine (TPEN,100 mM) were prepared in ethanol and stored at -20 ºC. Aliquots of DL-2-Amino-3-phosphonopropionic acid (DL-AP3, 300mM) were prepared in a 1eq NaOH solution in water. Working

Table 6.1: Summary of pharmacological agents used in study.

Drug	Abbreviation	Targeted Effect	Working Concentration	Stock Concentrati
N,N,N',N’ – Tetrakis (2-pyridylmethyl) ethylenediamine	TPEN	Intracellular Ca^{2+} chelator	2 mM	100 mM
2-Aminoethoxydiphenylborane	2-APB	IP_3R and RyR Antagonist	100 µM	50 mM
Carbenoxolone	CBX	Connexin/Pannexin Antagonist	50 µM	50 mM
DL-AP3	DL-AP3	Grp I mGluR Antagonist	300 µM	100 mM
BNQX	BNQX	AMPA (iGluR) Antagonist	10 mM	10 µM
PMPA	PMPA	NMDA (mGluR) Antagonist	10mM	10 µM
CGP-35348	CGP	$GABA_B$ Antagonist	100 µM	100 mM
Suramin	Suramin	P2Y Antagonist	100 µM	100 mM
Brilliant Blue G	BBG	P2X7 Antagonist	1 µM	10 mM
Verapamil	VPM	Voltage Gated Calcium Channel Antagonist	5 µM	10 mM
Ruthenium Red	RR	Nonspecific TRPV group antagonist	10 µM	10 mM
RN-1734	RN	TRPV4 Antagonist	10 µM	14.7 mM
HC030031	HC	TRPA1 Antagonist	40 µM	40 mM
Capsazepine	CZP	Selective TRPV Antagonist	5 µM	5 mM
A425619	A425619	Selective TRPV1 Antagonist – heat sensitivity	1 µM	1 mM

concentrations of pharmacological agents for imaging experiments were as follows: CBX 50 µM, PMPA 10 µM, CGP-35348 100 µM, Suramin 100 µM, BBG 1 µM, Verapamil 5 µM, RR 10 µM, 2-APB 100 µM, BNQX 10 µM, RN-1734 10 µM, HC-030031 40 µM, capsazepine 5µM, A425619 at 1 µM, TPEN 2 mM, DL-AP3 300 µM in physiological saline solution. For electrophysiological experiments the standard bath saline was (mM) 140 NaCl, 4 KCl, 2 MgCl2, 2 CaCl2, 10 Hepes, 5 glucose, pH 7.4 with NaOH and osmolarity adjusted to 315 mOsm with mannitol. In order to eliminate potassium currents, K^+ was omitted by extracellular solution and pipette solutions was replaced with cesium (Cs). The intracellular (pipette) solution was composed of (mM): 126 CsCl, 2 MgCl2, 1 EGTA, 10 TES, pH 7.2 with CsOH and osmolarity 300 mOsm with mannitol. Salts and chemicals used to prepare physiological solutions were the highest purity grade available from Sigma (Milan, IT).

6.3.7 Image processing

Somatic cellular fluorescence time series were obtained with a custom-written Fiji script to repeatably and reliable segment cells with a modified seeded watershed segmentation approach (42, 45). Raw time-series images were imported into Fiji using the Bioformats plugin (46). An average intensity projection of the first 30 frames before IR stimulation was calculated as a baseline image to identify cell soma. A rolling ball filter (diameter approximately 50% of image width) was applied to reduce low spatial frequency variations attributable to illumination inconsistencies. Contrast-enhanced adaptive histogram equalization (CLAHE) with a local block size of 20% of the image's largest dimension was applied to the average intensity projection image to reduce cell-to-cell variability in baseline somatic fluorescence intensity across the field of view. A 2-to-6-pixel gaussian kernel was convolved with the processed image to reduce high-frequency noise that impeded local maxima identification. Local maxima in the processed average intensity projection were found to locate nuclear features indicative of single-cell soma. The local maxima points were was used to seed a watershed segmentation algorithm. A binary mask was generated with Huang segmentation to restrict the extent of watershed segmentation. The identified local maxima, binary mask, and a distance-transformed edge map of the binary mask were fed into a seeded watershed segmentation workflow (45) to yield a segmented single-cell map in a particular field of view. These regions of interest for each cell were applied to raw time-series images to extract individual cellular raw fluorescence signals to IR stimulation. Mean fluorescence intensity and relative cell centroid positions exported from Fiji for further processing, analysis, and visualization using a custom workflow implemented in MATLAB (Mathworks, Natick, MA, USA). This workflow was streamlined into a semi-automated pipeline facilitating rapid data extraction with minimal user input. The described calcium imaging segmentation workflow is available as a Fiji macro script from the authors upon request.

6.3.8 Fluorescence Timeseries Analysis

Raw fluorescence traces are temporally aligned, intensity normalized, and processed to extract different calcium and calcein response metrics. Alignment of traces relative to INS pulse delivery was performed by locating a decrease in fluorescence due to the stimulation lasers thermally induced defocusing. Each cell's raw fluorescence intensity was normalized to the mean raw intensity of the 10 frames preceding IR exposure, then reported and analyzed as fractions (dF/F). For calcein experiments only, fluorescence time-series traces were background-subtracted with a 6th order iterative polynomial algorithm to account for the high photobleaching rate of calcein over data acquisition periods (47). Due to temporal variation in image background from the endogenous fluorescence of the stimulation fiber, the dark signal offset was omitted from relative fluorescence signal calculations. Quantitative metrics extracted from each cell's Ca^{2+} time series trace included maximum change in relative fluorescence (peak dF/F), elapsed time-to-peak fluorescence intensity (time-to-peak, in seconds), the full-width half-maximum of each cell's response (response duration, in seconds). A cell was deemed activated if a 5% increase in relative calcium fluorescence within 15 seconds of IR exposure was measured. The fraction of activated cells relative to the total number of cells observed is reported as "activation fraction" or "fraction of responding cells" on a per-imaging-experiment basis. The responding cells area is approximated as the area of pixels in which an activated cell is likely to be during IR stimulation. Delaunay triangulation between centroids of activated cells for a given experiment was used to calculate the activation area empirically. The reported area values are in units of pixels^2, with each square pixel representing 0.1037 μm^2 (0.322 μm / px sampling density). Plotting was performed in Matlab with the "superbar" package and native plotting functions. Fiji scripts for image segmentation and data extraction and Matlab processing scripts are available upon request.

6.3.9 Statistical Analysis

Statistical comparison of metrics is performed with a 2-sided unpaired student's T-test. Error bars reported are standard error-of-the-mean (SEM) between imaging experiments. For subthreshold stimulation analyses, response times between pooled cell populations were compared with a Wilcoxon Rank Sum test. Statistical significance is denoted graphically with asterisks, where * represents $p < 0.05$, ** represents $p < 0.01$, and *** represents $p < 0.001$.

6.4 Results

6.4.1 Multipulse stimulation thresholds are higher than single-pulse stimulation thresholds.

The three stimulation protocols studied are illustrated in **Figure 6.1B**. Both short (SMP, 16.26 J/cm^2, CI +/- 1.65 J/cm^2) and long multipulse (LMP, 23.93 J/cm^2, CI +/- 4.91 J/cm^2) stimulation conditions required substantially higher radiant exposures to elicit concerted calcium responses than to single pulse (SP, 3.61 J/cm^2, CI +/- 0.22 J/cm^2) stimulation **(Figure 6.1C&D)**. The shapes of the calcium responses are similar across all stimulation types (**Figure 6.1E,** representative traces), showing no statistically significant difference in peak fluorescence nor time-to-peak (**Figure 6.2**). However, the area of cells exhibiting responding to SMP and LMP stimulation in an experiment – spatially – was significantly higher than that of SP stimulation (**Figure 6.1G)**, with LMP stimulation showing the largest average response area. Peak powers per pulse required for threshold stimulation were highest for SMP stimulation (1.51 W, CI +/- 0.15 W), followed by SP (1.05W, CI +/- 0.06W) and LMP stimulation (0.74 W, CI +/- 0.15 W).

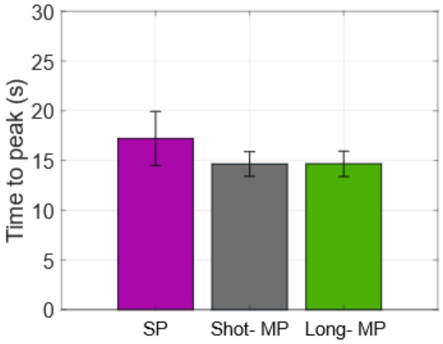

Figure 6.2: Time-to-peak average comparison from SP, SMP, and LMP stimulation –
Bar plot representing the time to reach the maximum fluo-4 AM dF/F (time-to-peak) for single pulse, short multipulse, and long multipulse stimulations. Data are reported as mean and SEM.

6.4.2 Sub-threshold levels of multipulse stimulation evoke stochastic activation of astrocyte Ca^{2+} dynamics

In observing Ca^{2+} responses obtained during stimulation threshold experiments, activation of astrocytes with SMP and LMP stimulation with sub-threshold levels of radiant exposure displayed more random spatiotemporal activation dynamics. An example of these observations is represented graphically as temporal color-coded maximum intensity projections and temporal Ca^{2+} traces for threshold (**Figure 6.3A&B)** and subthreshold (**Figure 6.3C&D**) from an example SMP stimulation experiment. The variation in the arrival of astrocytes to their peak Ca^{2+} responses appeared more pronounced in the subthreshold stimulation conditions than the threshold stimulation conditions for SMP and LMP stimulation. Comparing the time-to-peak distributions for each stimulus condition provided a rough response randomness metric. SP stimulation at below and above threshold radiant exposures showed no statistically significant difference in time-to-peak distribution medians (**Figure 6.3E**, $p > 0.05$, Wilcoxon rank-sum). However, SMP (**Figure 6.3F**) and LMP (**Figure 6.3G**) showed a significant increase in subthreshold time-to-peak distribution medians over threshold stimulation levels ($p < 0.05$, Wilcoxon rank-sum). The response probability to SMP and LMP stimulation was higher for threshold levels of stimulation. Similarly, subthreshold stimulation was more likely to yield Ca^{2+} responses peaking well after IR exposure. While IR stimulation is dose-dependent, this work focused on understanding INS bioeffects at threshold stimulation levels moving forward.

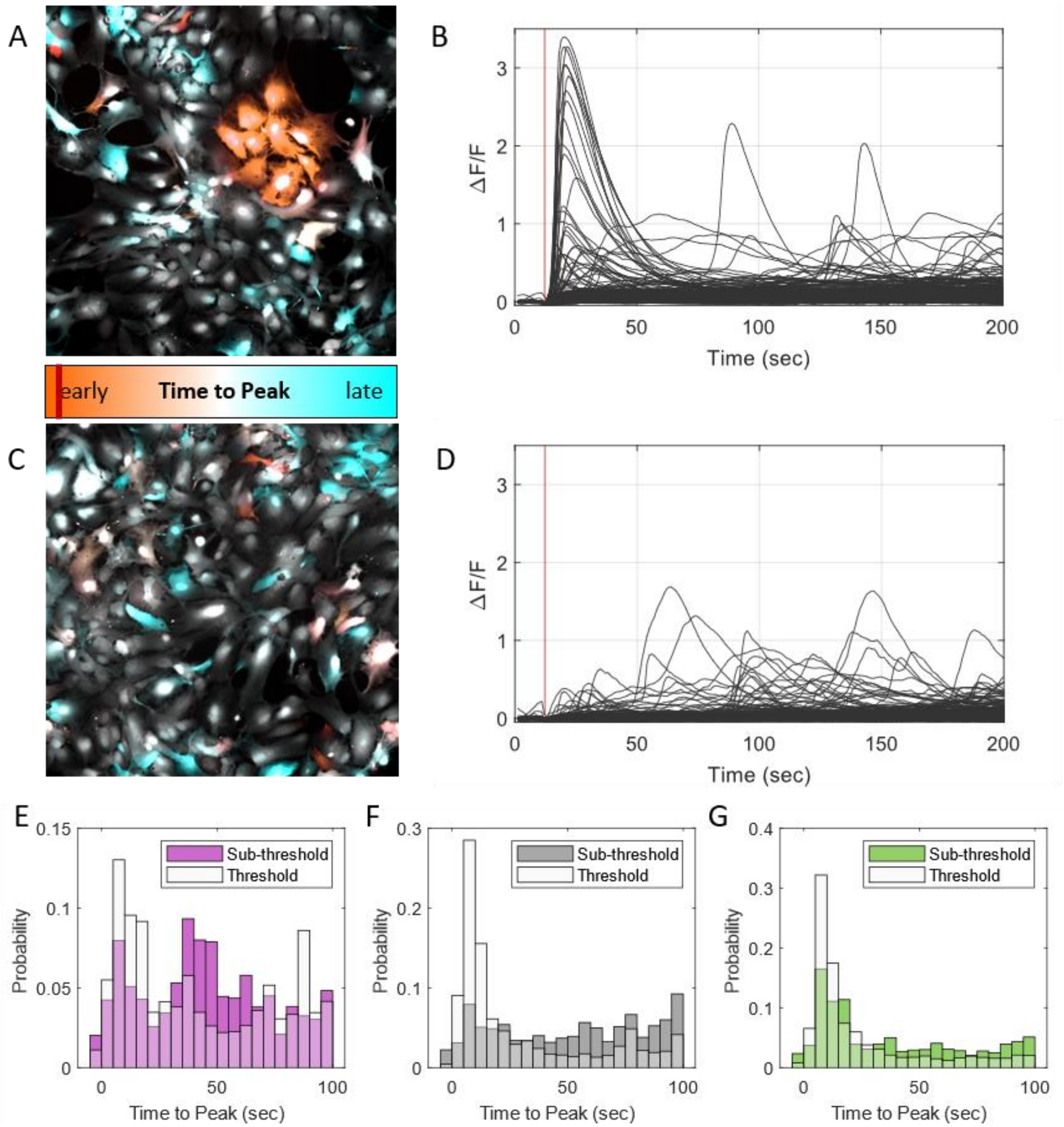

Figure 6.3: Stochastic activation of astrocyte Ca^{2+} dynamics with subthreshold multipulse stimulation

(A) Representative image from one imaging experiment of SMP threshold-stimulated astrocytes with (B) representative Ca^{2+} fluorescence time traces across 3 experiments. (C) Representative image from one imaging experiment of SMP subthreshold-stimulated astrocytes with (D) representative Ca2+ fluorescence time traces across 3 experiments. Histograms of individual cell subthreshold and threshold stimulation with (E) SP, (F) SMP, and (G) LMP stimulation.

6.4.3 Multipulse stimulation of astrocytes primarily mediates extracellular Ca^{2+} entry.

Pharmacological and calcium imaging experiments helped identify the primary route for cytosolic Ca^{2+} concentration ($[Ca^{2+}]_i$) increase from IR stimulation. **Figure 6.4A, D, and F** show representative calcium dynamic traces evoked with SP, SMP, and LMP stimulation under control and pharmacological perturbation, respectively. Data shown for SP stimulation was previously published (18).

Increasing Ca^{2+} signals evoked by SP stimulation were attenuated by perturbing Ca^{2+} release from intracellular stores with N,N,N′,N′-tetrakis(2- pyridinylmethyl)-1,2-ethanediamine (TPEN, 2mM) (48), an intracellular Ca^{2+} store chelator at 2 mM. Application of TPEN showed a significant decrease in fluorescence intensity, relative activation fraction, and time-to-peak (**Figure 6.4B&C; Figure 6.6A**). This observation implicated IP_3R activation in astrocytic Ca^{2+} responses to SP stimulation. Application of the IP_3R antagonist 2-aminoethoxydiphenylborane (2-APB, 100 µM) significantly attenuates Ca^{2+} response magnitude and activation probability to SP stimulation while increasing the response time-to-peak (**Figure 6.4B&C, Figure 6.6A**) (49). Extracellular calcium entry appears to shape SP-evoked responses. Calcium-free imaging medium ($0[Ca^{2+}]_o$) significantly decreases Ca^{2+} response magnitude and activation probability (**Figure 6.4B&C**) while increasing time-to-peak (**Figure 6.6A**). Intracellular Ca^{2+} release through IP3R activation primarily mediates astrocyte Ca^{2+} responses to SP stimulation. Intercellular communication mediates the spread of SP-evoked Ca^{2+} responses. Blocking intercellular Ca^{2+} release with carbenoxolone (CBX, 50µM) (50) decreases activation probability and increases response time-to-peak for SP stimulation (**Figure 6.4C**; **Figure 6.6A**). Meanwhile, CBX had no significant effect on peak calcium responses (**Figure 6.4B**).

In contrast to SP stimulation, extracellular Ca^{2+} entry primarily mediates astrocyte responses to SMP and LMP stimulation. Using a Ca^{2+}-free imaging medium significantly attenuates Ca^{2+} responses and decreases activation probability while increasing response time-to-peak after SMP stimulation (**Figure 6.4E, F, H** & **I; Figure 6.6B**&**C**). Applying TPEN insignificantly reduced Ca^{2+} responses, decreased activation probability, and did not alter the time-to-peak evoked by SMP stimulation (**Figure 6.4E**&**F**, **Figure 6.6B**). Applying 2-APB to block IP3R activation yielded a significant decrease in Ca^{2+} response magnitude and a significant increase in the time-to-peak, but did not affect activation probability to SMP stimulation (**Figure 6.4E**&**F**, **Figure 6.6 B**).

Unlike SMP observations, TPEN yielded a significant decrease in response magnitude and activation fraction while yielding no change in the time-to-peak after LMP stimulation (**Figure 6.4H**&**I**, **Figure 6.6C**). Applying 2-APB attenuated the Ca^{2+} response magnitude and activation probability to LMP

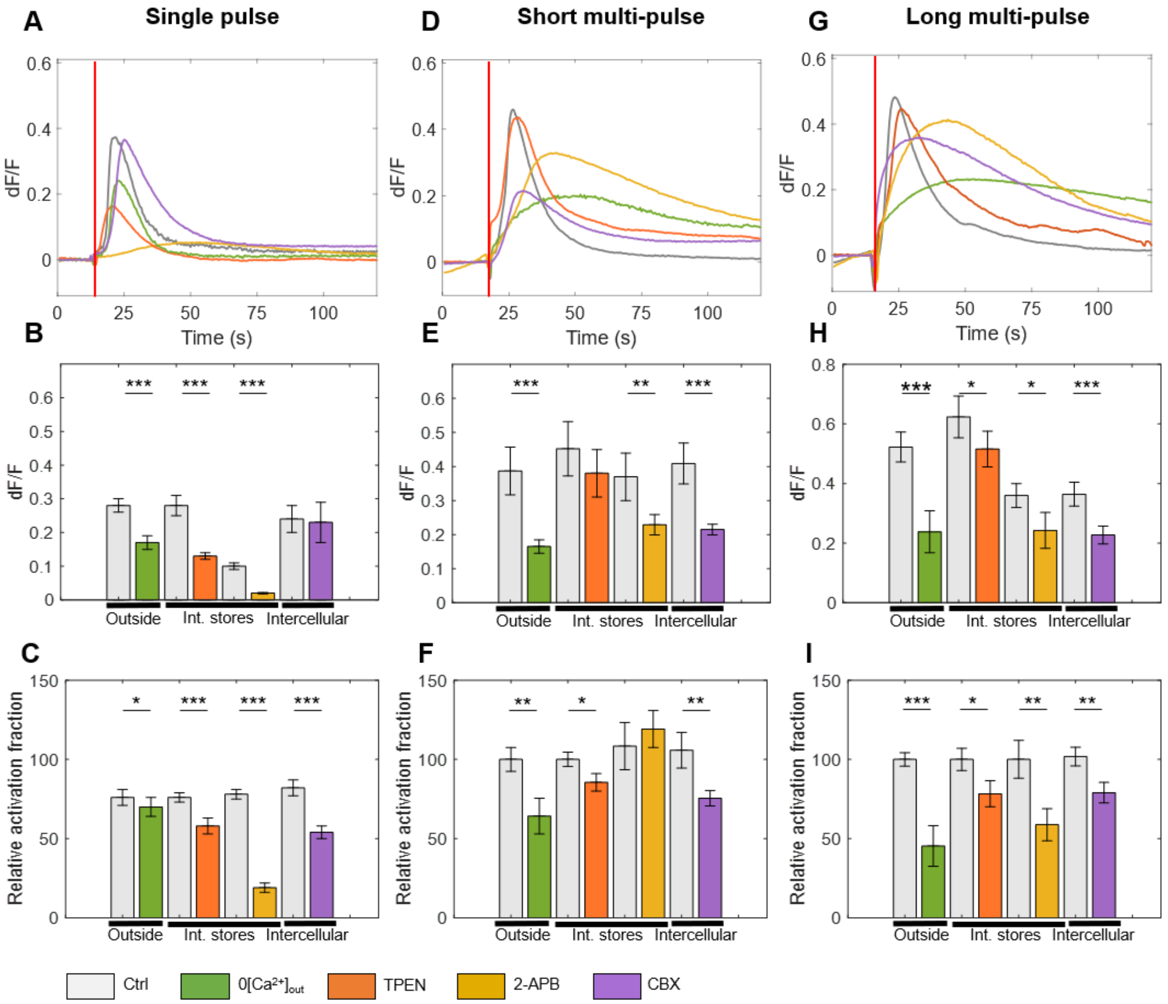

Figure 6.4: Pharmacological study of calcium mobilization in astrocytes
(A, B and C) Calcium imaging results for SP stimulation. (A) Representative traces using extracellular standard solution (Ctrl), extracellular solution not-containing Ca^{2+} ($0[Ca^{2+}]_o$), and by adding TPEN (2mM), 2-APB (100 µM) or CBX (50 µM) to the Ctrl saline. (B) Bar plots showing average maximum dF/F for $0[Ca^{2+}]_o$ solution, TPEN, 2-APB and CBX compared with their own Ctrl. (C) Bar plots depicting relative activation fraction for $0[Ca^{2+}]_o$ solution, TPEN, 2-APB and CBX compared with their own Ctrl for SP. (D, E and F) Calcium imaging results for SMP stimulation. Representative traces using Ctrl solution, $0[Ca^{2+}]_o$, and adding TPEN, 2-APB or CBX to the Ctrl saline (E). Bar plots showing average maximum dF/F for $0[Ca^{2+}]_o$ solution, TPEN, 2-APB and CBX compared with their own Ctrl. (F) Bar plots depicting relative activation fraction for $0[Ca^{2+}]_o$ solution, TPEN, 2-APB and CBX compared with their own Ctrl for SP. (G, H and I) Calcium imaging results for LMP stimulation. (G) Representative traces using Ctrl solution, $0[Ca^{2+}]_o$, and adding TPEN, 2-APB or CBX to the Ctrl saline. (H) Bar plots showing average maximum dF/F for $0[Ca^{2+}]_o$ solution, TPEN, 2-APB and CBX compared with their own Ctrl. (I). Bar plots depicting relative activation fraction for $0[Ca^{2+}]_o$ solution, TPEN, 2-APB and CBX compared with their own Ctrl for LMP stimulation. SP number of experiments N=11 for $0[Ca^{2+}]_{o,}$ N=11 for TPEN, N=9 for 2-APB, N=5 for CBX. SMP number of experiments N=13 for $0[Ca^{2+}]_{o\,,}$ N=11 for TPEN, N=9 for 2-APB, N=8 for CBX LMP number of experiments N=13 for $0[Ca^{2+}]_{o\,,}$ N=11 for TPEN, N=10 for 2-ABP, N=11 for CBX. N represents the number of plates. Data are reported as mean and SEM. Student's t test,* p < .05,**p < .01 ***p < .001.

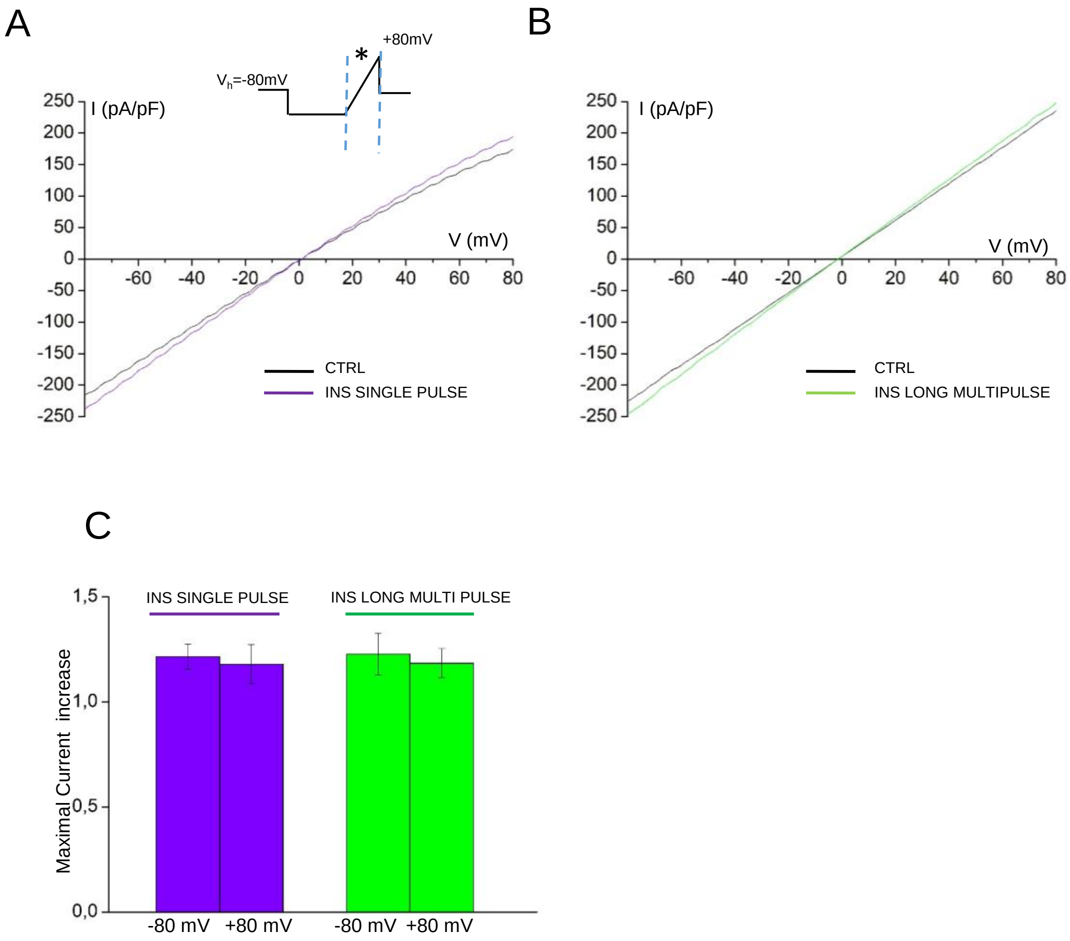

Figure 6.5: LMP-evoked whole-cell conductance changes in astrocyte cultures
(A-B) Typical ramp current traces stimulated with a voltage ramp protocol (inset) recorded in Cs-saline solution, before (A, B, black trace) at maximal current increase observed after pulsed infrared (IR) light (A, single pulse violet trace, and B, multi pulse, green trace). C) Bar plot of averaged maximal current density, recorded at −80mV and +80mV after INS, normalized with respect to the baseline current. Data are reported as mean and SE. (n=4 single pulse, left bar and n=5 multi pulse right side). $p<0,05$; ANOVA

stimulation. In contrast, 2-APB showed a significant increase in response time-to-peak to LMP stimulation – which was not observed with TPEN application.

Both multipulse protocols show higher contributions from extracellular Ca^{2+} influx relative to intracellular Ca^{2+} release. Perturbing gap junction signaling with CBX reduced Ca^{2+} response magnitude and activation probability to SMP and LMP stimulations (**Figure 6.4E**, **F**, **H & I**). However, CBX increased time-to-peak with the LMP stimulation, not SMP stimulation (**Figure 6.6B&C**). In comparison, CBX did not affect SP-evoked response magnitudes. This result raised whether SMP and LMP stimulation might drive modulatory molecule release (51).

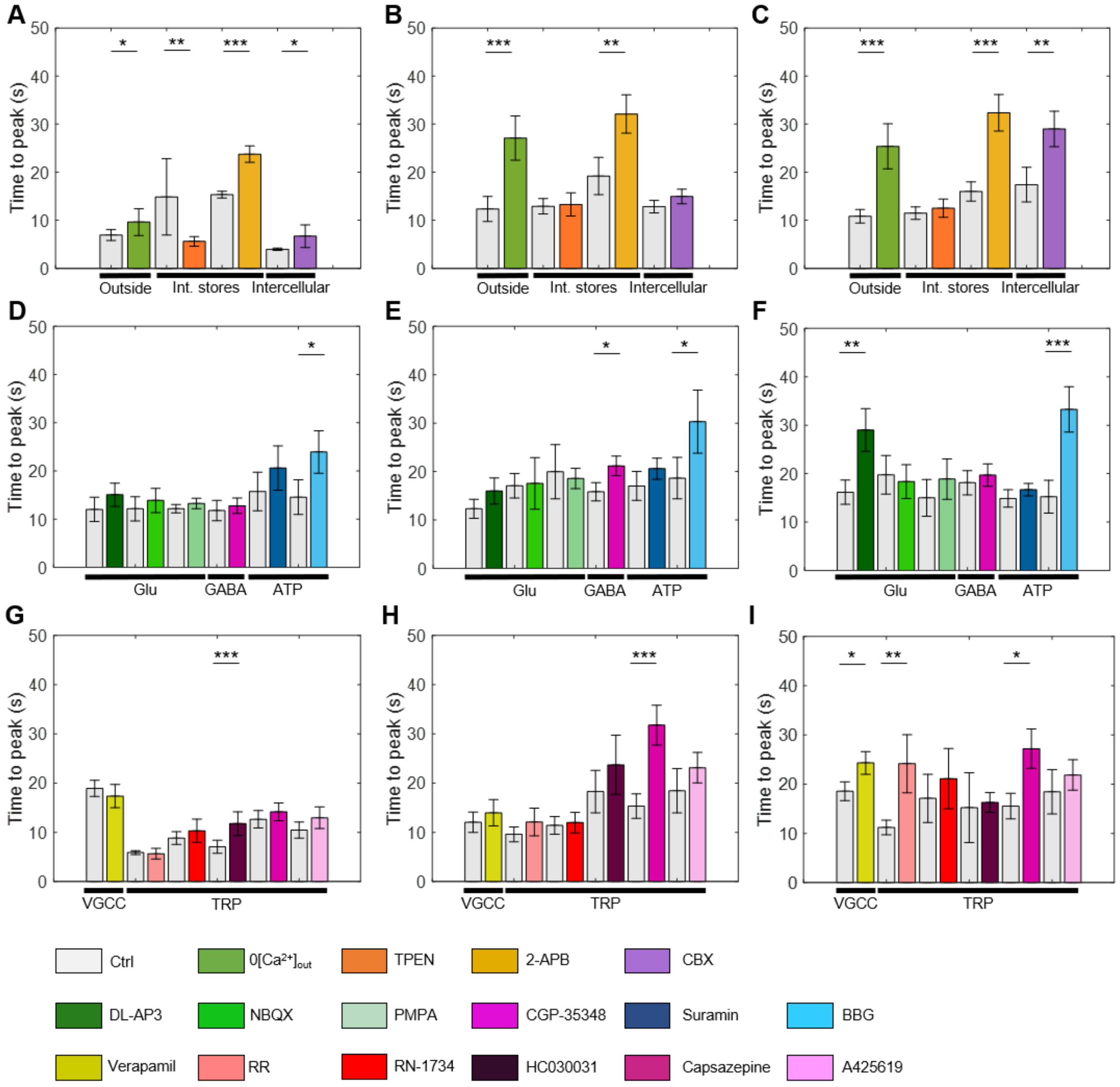

Figure 6.6: Pharmacological effects on single and multipulse stimulation Ca^{2+} dynamics – (A, B and C) Bar plots showing average time-to-peak for 0[Ca2+]o solution, TPEN (2mM), 2-APB (100 µM) and CBX (50 µM) compared with their own Ctrl for single pulse (A) short multipulse (B), and long multipulse (C). D, E and F) Bar plot depicting time-to-peak for DL-AP3 (300 µM) , NBQX (µM) , PMPA (µM), CGP-35348 (µM) , suramin (100 µM) and BBG (1 µM) compared with their own Ctrl for single pulse (D) short multipulse (E), and long multipulse (F). G, H and I) Bar plots depicting time-to-peak for for verapamil (5 µM) , RR (10 µM), RN-1734 (10 µM), HC030031 (40 µM), Capsazepine (5 µM) and A425619 (1 µM) compared with their own Ctrl for single pulse (G) short multipulse (H), and long multipulse (I). Data are reported as mean and SEM. Student's unpaired t-test,* p < .05,**p < .01, ***p < .001.

To analyze the effect of SP and LMP INS on astrocytes whole-cell currents, we used intra- and extra-cellular saline containing CsCl and astrocytes were clamped at the holding potential (Vh) of 0 mV and stimulated with voltage ramps from -80 to 80 mV of 1-s duration (**Figure 6.5A**, inset *). The exposure to pulsed infrared light induced an increase in ramp currents when cells were stimulated with single and with LMP. A significant increase in inward current was observed in single and multi-pulse (**Figure 6.5C**); however, the magnitude of the increase was not significantly different. The data is in agreement with calcium imaging experiments. Indeed, at steady-state, the magnitude of the calcium signaling responses were comparable in response to single and long multipulse.

6.4.4 Membrane receptor activation underlies astroglial Ca^{2+} responses to multipulse stimulation.

Modulatory receptor's impact on IR-evoked Ca^{2+} responses was assessed with pharmacology and widefield Ca^{2+} fluorescence imaging. Applying Brilliant Blue G (BBG, 1 μm) – a selective P2X7 antagonist with nanomolar affinity (52) – significantly decreased calcium response magnitudes and significantly increased time-to-peak (**Figure 6.7A-C; Figure 6.6D**). Antagonists against glutamate, GABA, and ATP receptors had no significant impact on SP-evoked Ca^{2+} responses and activation probabilities (**Figure 6.7A-C; Figure 6.6D**).

For both SMP and LMP stimulation, interrupting receptor activity affected IR-evoked Ca^{2+} response. Blocking group-I metabotropic glutamate, AMPA, and NMDA receptors with DL-AP3 (53), NBQX (54), and PMPA (55), respectively, significantly attenuated Ca^{2+} responses magnitude and reduced activation probability without changing temporal dynamics of SMP-evoked responses (**Figure 6.7D-F; Figure 6.6E**). Applying CGP-35348, a selective antagonist for $GABA_B$ receptors (56), reduced cell activation probability to SMP stimulation. Using suramin, a non-selective P2Y blocker (57), and BBG, a P2X7 receptor antagonist, significantly decreased Ca^{2+} response magnitude to SMP stimulation (**Figure 6.7D&E**). However, changes in the number of cells responding and time-to-peak were affected only by BBG (**Figure 6.7E&F; Figure 6.6E**). Using DL-AP3, NBQX, and PMPA during LMP stimulation reduced the magnitude of Ca^{2+} responses (**Figure 6.7G&H)**. The same drugs reduced activation fractions to LMP stimulation except for PMPA (**Figure 6.7I**). DL-AP3 was the only glutamate receptor antagonist to significantly alter Ca^{2+} response time-to-peak after LMP stimulation (**Figure 6.7G; Figure 6.6 F**). $GABA_B$ antagonist CGP-35348 and P2 antagonist suramin did not show any significant change to LMP response magnitude or activation probability (**Figure 6.7G; Figure 6.6F**). Similar to SP and SMP observations, the use of BBG caused a significant decrease in response magnitude and activation fraction after LMP stimulation (**Figure 6.7G-I)**. Applying BBG also significantly increased response time-to-peak following LMP stimulation (**Figure 6.7G; Figure 6.6F**).

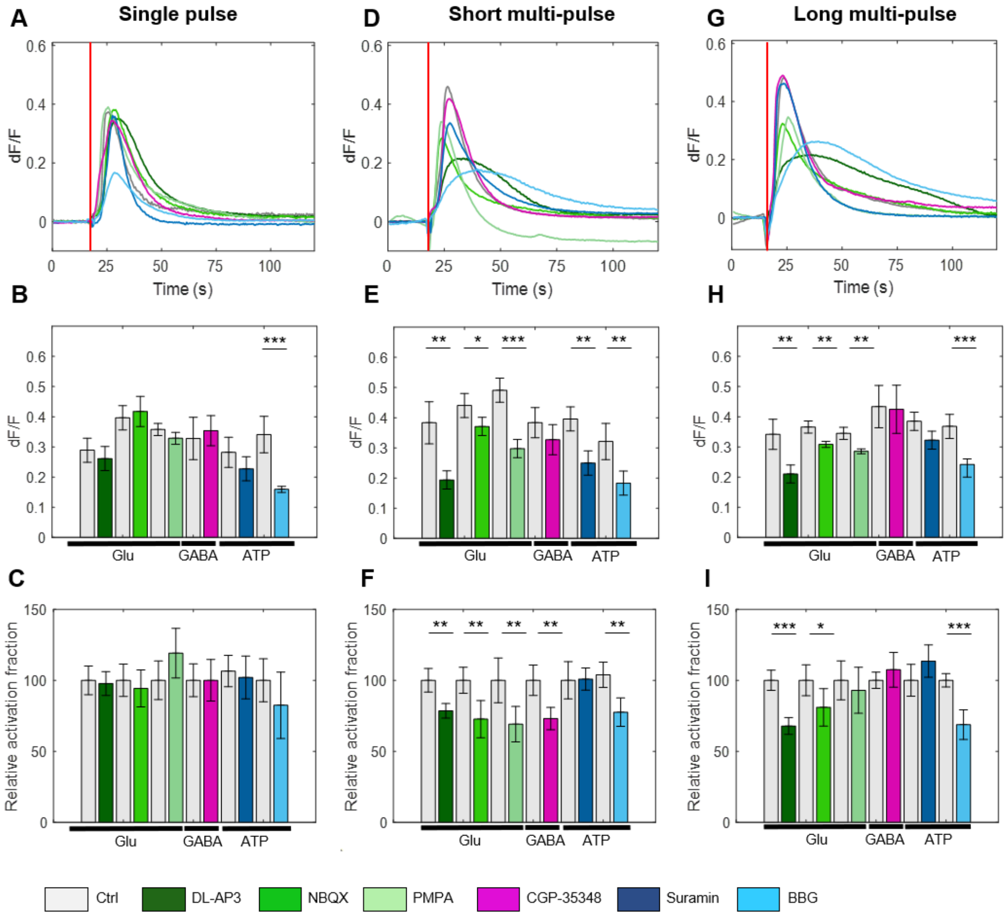

Figure 6.7: Pharmacological study of receptor involvement on intracellular calcium concentration increases

(A, B and C) Calcium imaging results for SP stimulation. (A) Representative traces using extracelular standard solution (Ctrl), and Ctrl with DL-AP3 (300 µM), NBQX (10µM), PMPA (10µM), CGP-35348 (10µM), suramin (100 µM) and BBG (1 µM) added to the Ctrl solution. (B) Bar plots showing average maximum dF/F for DL-AP3, NBQX, PMPA, CGP-34348, Suramin and BBG compared with their own Ctrl. (C) Bar plots depicting relative activation fraction for DL-AP3, NBQX, PMPA, CGP-34348, Suramin and BBG compared with their own Ctrl. (D, E and F) Calcium imaging results for SMP stimulation. (D) Representative traces using extracelular standard solution (Ctrl), and Ctrl with DL-AP3, NBQX, PMPA, CGP-35348, Suramin and BBG added to the Ctrl solution. (E) Bar plots showing average maximum dF/F for DL-AP3, NBQX, PMPA, CGP-34348, Suramin and BBG compared with their own Ctrl. (F). Bar plots depicting relative activation fraction for DL-AP3, NBQX, PMPA, CGP-34348, Suramin and BBG compared with their own Ctrl. (G, H and I) Calcium imaging results for LMP stimulation. (G) Representative traces using extracelular standard solution (Ctrl), and Ctrl with DL-AP3, NBQX, PMPA, CGP-35348, Suramin and BBG added to the Ctrl solution. (H) Bar plots showing average maximum dF/F for DL-AP3, NBQX, PMPA, CGP-34348, Suramin and BBG compared with their own Ctrl. (I). Bar plots depicting relative activation fraction for DL-AP3, NBQX, PMPA, CGP-34348, Suramin and BBG compared with their own Ctrl. SP number of experiments N=11 for DL-AP3, N=8 for NBQX, N=8 for PMPA, N=8 for CGP-35348, N=7 for Suramin, N=10 for BBG. SMP number of experiments N=11 for DL-AP3, N=8 for NBQX, N=8 for PMPA, N=8 for CGP-35348, N=10 for Suramin, N=10 for BBG. LMP number of experiments N=12 for DL-AP3, N=8 for NBQX, N=8 for PMPA, N=8 for CGP-35348, N=10 for Suramin, N=10 for BBG. N represents the number of plates. Data are reported as mean and SEM. Student's unpaired t-test,* p < .05,**p < .01, ***p < .001.

6.4.5 Transient Receptor Protein (TRP) family channels and Voltage-Gated Calcium Channels (VGCC) are involved in shaping Ca^{2+} responses to multipulse stimulation.

We next studied the involvement of astroglial ion channels in the evoked responses given the role of Ca^{2+} efflux from the extracellular environment in shaping the response for the three stimulation protocols. We previously showed that TRP channels impact SP-evoked Ca^{2+} responses (18). **Figure 6.8A-C** summarizes the results of this SP stimulation study (18). Broadly blocking TRP channel function with RR (58) significantly attenuated Ca^{2+} response magnitude and reduced response probability (**Figure 6.8B&C**). However, RR did not affect the temporal dynamics of SP-evoked Ca^{2+} responses (**Figure 6.6G**). Applying RN-1734, a selective inhibitor for TRPV4 (59), significantly decreased SP-evoked response magnitude and activation probability without affecting response time-to-peak (**Figure 6.8B&C; Figure 6.6G**). Using HC030031, a selective blocker for TRPA1 (60), significantly reduced SP-evoked Ca^{2+} response magnitude and significantly increased time-to-peak without affecting the response probability (**Figure 6.8 B&C; Figure 6.6G**). Applying capsazepine – a vanilloid antagonist for TRPV1 (61) – and A425619 – a selective inhibitor of TRPV1 that blocks its heat-sensitive activation explicitly (El Kouhen et al., 2005) – did not impact SP-evoked Ca^{2+} dynamics (**Figure 6.8B&C; Figure 6.6G**). Applying verapamil to target L- and T-type voltage-gated calcium channels (VGCC)s (62) did not noticeably affect astrocyte Ca^{2+} responses to SP stimulation (**Figure 6.8A-C; Figure 6.6G**).

Ion channels shape SMP-evoked Ca^{2+} responses differently than SP stimulation. Applying RR reduced Ca^{2+} response magnitude to SMP stimulation significantly without affecting activation fraction and time-to-peak (**Figure 6.8E&F; Figure 6.6H**). Using RN-1734 did not affect SMP-evoked Ca^{2+} responses (**Figure 6.8E&F; Figure 6.6H**). Applying HC030031 decreased Ca^{2+} response magnitude significantly but did not affect activation fraction or time-to-peak (**Figure 6.8E&F; Figure 6.6H**). Capsazepine significantly reduced SMP-evoked response magnitude and activation fraction while significantly increasing the response time-to-peak (**Figure 6.8E&F; Figure 6.6H**). Using A425619 did not affect response magnitude or time-to-peak, though significantly increased response probability to SMP stimulation (**Figure 6.8E&F; Figure 6.6H**). Verapamil attenuated SMP-evoked Ca^{2+} responses and reduced activation probability without affecting response time-to-peak (**Figure 6.8E&F; Figure 6.6H**).

Ion channel influences on LMP-evoked Ca^{2+} showed notable differences from SP and SMP stimulation. Using RR attenuation of response magnitude and increased in the time-to-peak significantly but did not alter activation probability. Applying RN1734 decreased LMP-evoked response magnitude significantly without affecting the activation fraction or the time-to-peak (**Figure 6.8H&I; Figure 6.6I**). Using HC030031 reduced response magnitude and – intriguingly – increased activation probability significantly without changing time-to-peak (**Figure 6.8H&I; Figure 6.6H**). Capsazepine reduced response

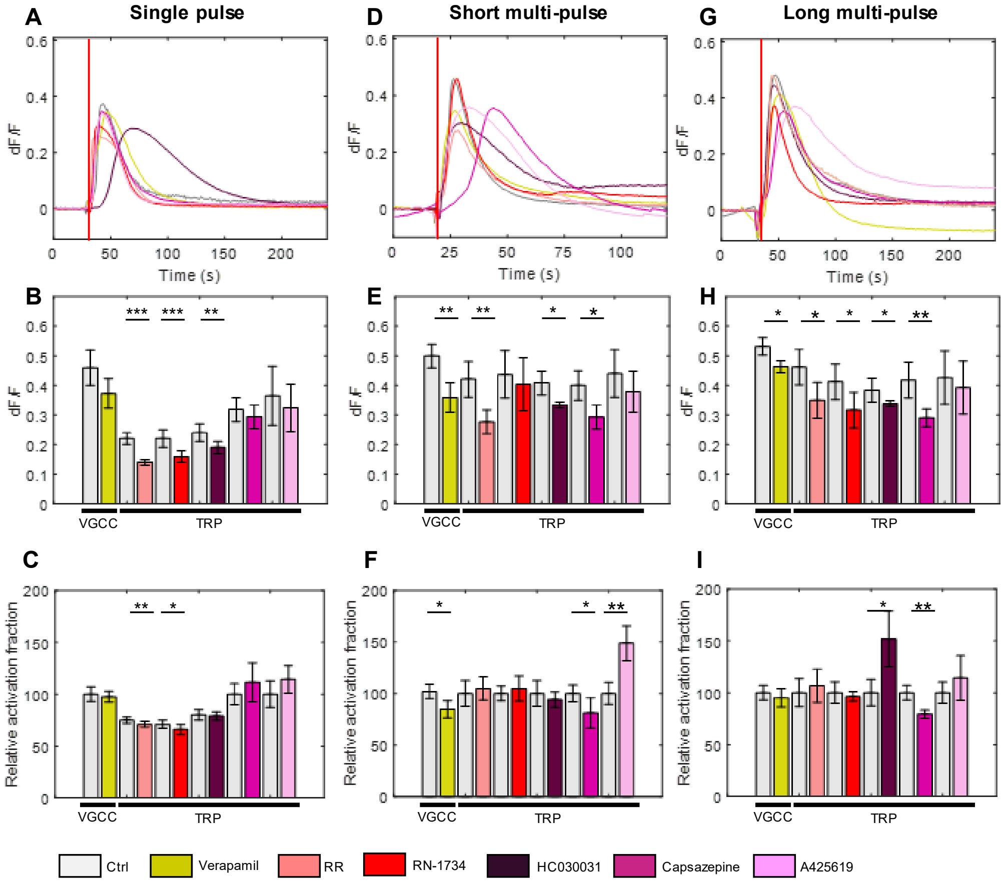

Figure 6.8: Pharmacological study of ion channel involvement on intracellular calcium concentration increases

(A, B and C) Calcium imaging results for SP stimulation. (A) Representative traces using extracellular standard solution (Ctrl), and Ctrl with Verapamil (5 µM), RR (10µM), RN-1735 (10µM), HC030031 (40µM), Capsazepine (10 µM) and A425619 (1 µM) added to the Ctrl solution. (B) Bar plots showing average maximum dF/F for Verapamil, RR, RN-1734, HC030031, Capsazepine and A425619 compared with their own Ctrl. (C) Bar plots depicting relative activation fraction for Verapamil, RR, RN-1734, HC030031, Capsazepine and A425619 compared with their own Ctrl. (D, E and F) Calcium imaging results for SMP stimulation. (D) Representative traces using extracellular standard solution (Ctrl), and Ctrl with Verapamil, RR, RN-1735, HC030031, Capsazepine and A425619 added to the Ctrl solution. (E) Bar plots showing average maximum dF/F for Verapamil, RR, RN-1734, HC030031, Capsazepine and A425619 compared with their own Ctrl. (F) Bar plots depicting relative activation fraction for Verapamil, RR, RN-1734, HC030031, Capsazepine and A425619 compared with their own Ctrl. (G, H and I) Calcium imaging results for LMP stimulation. Representative traces using extracellular standard solution (Ctrl), and Ctrl with Verapamil, RR, RN-1735, HC030031, Capsazepine and A425619 added to the Ctrl solution. (H). Bar plots showing average maximum dF/F for Verapamil, RR, RN-1734, HC030031, Capsazepine and A425619 compared with their own Ctrl. (I) Bar plots depicting relative activation fraction for Verapamil, RR, RN-1734, HC030031, Capsazepine and A425619 compared with their own Ctrl. SP number of experiments N=8 for Verapamil, N=15 for RR, N=10 for RN-1734, N=11 for HC030031, N=8 for Capsazepine, N=8 for A425619. SMP number of experiments N=9 for Verapamil, N=10 for RR, N=7 for RN-1734, N=6 for HC030031, N=8 for Capsazepine, N=8 for A425619. LMP number of N=10 for Verapamil, N=10 for RR, N=7 for RN-1734, N=6 for HC030031, N=8 for Capsazepine, N=8 for A425619. N represents the number of plates. Data are reported as mean and SEM. Student's unpaired t-test,* p < .05,**p < .01, ***p < .001.

magnitude and increased the time-to-peak significantly without impacting activation fraction (**Figure 6.8H&I; Figure 6.6H**). A425619 had no impact on LMP-evoked Ca^{2+} dynamics (**Figure 6.8H&I; Figure 6.6H**). Verapamil decreased response magnitude and increased time-to-peak significantly without affecting the activation fraction (**Figure 6.8H&I; Figure 6.6H**).

6.4.6 Multipulse IR stimulation preferentially triggers astrocyte swelling

A major SP-evoked physiological response in astrocytes was cell volume modulation (18). The same calcein quenching assay (63) adapted for optical microscopy was used to compare the water transport effects of SP, SMP, and LMP stimulation. SP stimulation evoked location-dependent cell swelling and shrinking processes in astrocyte cultures (**Figure 6.9B**) (18). Stimulating cells with SMP and LMP protocols disproportionately drove cell swelling (**Figure 6.9A, C-E**). SP stimulation drove swelling in 75.14 ± 3.22% of exposed cells and 21.20 ± 4.26% shrinking (**Figure 6.9E**). SMP and LMP stimulation resulted in 99.56 ± 0.3% and 98.84 ± 0.71% of irradiated cells swelling, respectively (**Figure 6.9E**). The magnitude of IR-evoked volume changes with SP-induced cell shrinking is not significantly different from SMP or LMP-evoked swelling (**Figure 6.9F)**. SP-evoked cell swelling was significantly less than that of multipulse stimulation (**Figure 6.9F**). SMP and LMP stimulation yielded too few shrinking cells to compare to SP-evoked shrinking magnitudes rigorously. However, the magnitude of cell swelling and shrinking for SMP and LMP stimulation were not significantly different (**Figure 6.10&B**).

The time-to-peak of cell swelling is significantly lower (i.e., faster) than that of cell shrinking across all stimulation protocols (**Figure 6.9G & Figure 6.10C&D**). The stimulation protocol evokes a different area of cells responding, with SP stimulation activating the smallest and LMP activating the largest area of cells (**Figure 6.9H)** – similar to observations with Ca^{2+} responses. However, water transport responses' activation area was significantly larger than Ca^{2+} responses across all stimulation conditions (**Figure 6.11B**). Swelling responses showed significantly faster response times (i.e., lower time-to-peak) than their Ca^{2+} responses across all stimulation protocols (**Figure 6.11A**). Except for LMP stimulation, SP and SMP stimulation showed no significant difference in response dynamics between shrinking and intracellular Ca^{2+} response speeds (**Figure 6.11A**).

6.5 Discussion

This study aims to compare astrocyte physiological responses to different pulsed IR stimulation protocols *in vitro*. We previously published the effect of 8 ms single pulse stimulation, or SP, on rodent primary astroglial cultures (18). With SP stimulation, cells respond with transient increases in $[Ca^{2+}]_i$; IP3R and TRP channels were the molecular mediators identified. Expression of AQP4 shaped SP-evoked $[Ca^{2+}]_i$ responses. SP stimulation drove bidirectional cell volume changes *in vitro*. Prior work from our group

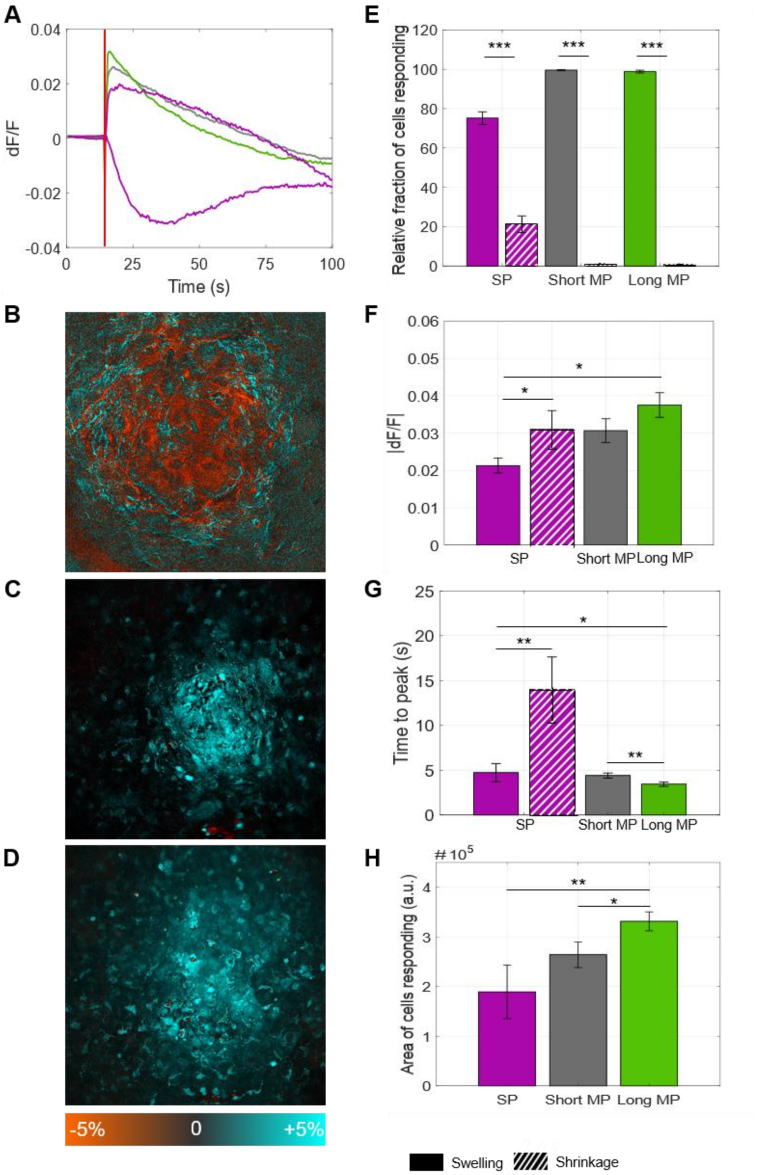

Figure 6.9: Cell swelling and shrinking triggered by different stimulation protocols
(A) Representative traces of calcein fluorescence recorded in rat astrocytes representing fluorescence somatic response to an infrared pulse. Red line marks the timepoint at which laser pulse was delivered. (B, C and D) Spatial map of fluorescence changes following a (B) single pulse, (C) short multipulse, and (D) long multipulse. (E) Bar plot depicting relative number of cells responding with increases in calcein fluorescence associated with cell swelling (flat bars) and decreases in calcein fluorescence associated with cell shrinkage (patterned bars) for single pulse, short multipulse and long multipulse. (F) Bar plot showing the absolute value of average maximum dF/F for single pulse (flat bar: swelling, patterned bar: shrinkage) short multipulse, and long multipulse stimulations. (G) Bar plot presenting the time to reach the maximum dF/F (time-to-peak) for single pulse (flat bar: swelling, patterned bar: shrinkage) short multipulse, and long multipulse stimulations. (H) Bar plot representing the total area of cell responding with increases and decreases in calcein fluorescence to single pulse, short multipulse and long multipulse stimulations. Data are reported as mean and SEM. Student's unpaired t-test,* $p < .05$,** $p < .01$, *** $p < .001$.

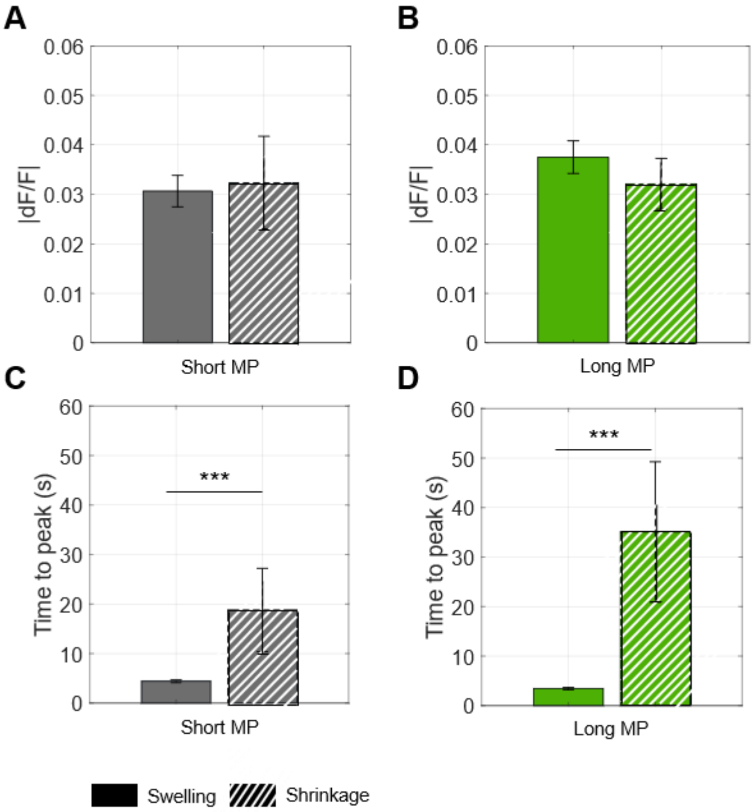

Figure 6.10: Cell volume regulation dynamics evoked from multipulse stimulation
(A) Bar plot showing the absolute value of average maximum calcein dF/F for short multipulse for Calcein fluorescence increase (flat bar) and calcein fluorescence decreases (patterned bar). (B) Bar plot showing the absolute value of average maximum calcein dF/F for long multipulse for Calcein fluorescence increase (flat bar) and calcein fluorescence decreases (patterned bar). (C) Bar plot depicting average time-to-peak for cells swelling (flat bar) and cells shrinking (patterned bar) for short multipulse. (D) Bar plot depicting average time-to-peak for cells swelling (flat bar) and cells shrinking (patterned bar) for long multipulse. Data are reported as mean and SEM. Student's unpaired t-test,* p < .05,**p < .01, ***p < .001.

detailed SMP-evoked Ca^{2+} signals in rat somatosensory cortex *in vivo* (4). SP stimulation could not elicit calcium responses *in vivo* without damaging tissue. Developing the SMP stimulation sought to target heating neuronal cell bodies in deeper cortical layers without superficial tissue damage. Current *in vivo* rat and non-human-primate brain studies continue to use SMP stimulation (1, 3, 4, 28, 29, 31).

Prior work described SMP-evoked Ca^{2+} responses *in vivo* with a fast and a slow component sensitive to a glutamate receptor antagonist and aerobic metabolism inhibitor, respectively (4). Neuronal Ca^{2+} responses were attributed to faster signals, while astrocyte responses were attributed to slower signals. Astrocyte sensitivity to SMP stimulation remained unclear from this work. Our results show that different IR dosing strategies act through distinct molecular signaling pathways in astrocytes.

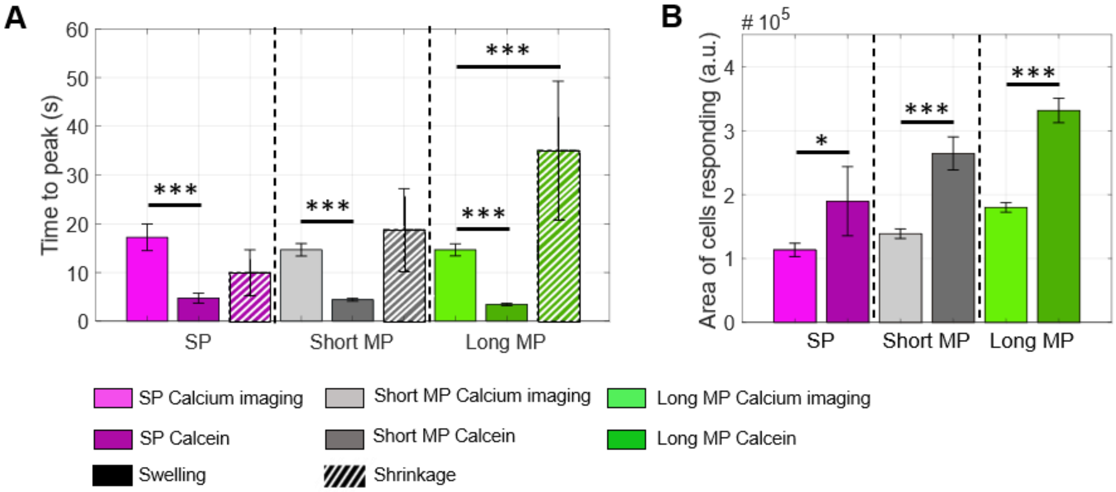

Figure 6.11: Comparison of astrocyte Ca2+ responses and regulatory volume dynamics evoked by single and multipulse IR stimulation
(A) Bar plot showing time-to-peak for calcium imaging (light) and calcein (dark) experiments (flat: swelling, patterned; shrinking) for single pulse, short multipulse, and long multipulse stimulations. (B) Bar plot depicting total area of cells responding for calcium imaging (light) and calcein (dark) experiments. Data are reported as mean and SEM. Student's unpaired t-test,* p < .05,**p < .01, ***p < .001.

SMP and LMP stimulation of astrocytes revealed a unique dose-dependent response not observed with SP stimulation. More stochastic activation (i.e., increase median and variance of peak response times **- Figure 6.3**) after subthreshold SMP and LMP stimulation leaves questions to address. While this work focused on threshold-level bioeffects that elicit concerted Ca^{2+} responses, subthreshold response dynamics were not fully explored. Pharmacology and electrophysiology would address whether this phenomenon acts through similar pathways to threshold stimulation. Driving different signaling pathways with subthreshold SMP and LMP stimulation would suggest additional INS applications in studying astroglial physiology. More work is needed to address such questions. However, stochastic astrocyte calcium dynamics may be a powerful tool to drive astrocytic physiology for specific research questions. Subthreshold activation of astrocytes with SMP and LMP stimulation still required substantially higher radiant exposures than threshold SP stimulation. This discrepancy may be attributable to the added inter-pulse cooling and thermal diffusion involved in SMP and LMP stimulation, but a biomolecular explanation warrants additional experiments.

While the general shapes of astrocyte Ca^{2+} responses to SP, SMP, and LMP stimulations were nearly indistinguishable (**Figure 6.1E&F**), numerous differences became clear with pharmacology. SP stimulation primarily drives the release of intracellular Ca^{2+} stores with comparatively minor contributions from extracellular Ca^{2+} entry (**Figure 6.4B&C**). Both SMP and LMP stimulation primarily drive extracellular Ca^{2+} entry (**Figure 6.4E-F, H-I**). This is further reflected by the increased conductance at positive holding potentials after LMP stimulation, implicating Ca^{2+} or Na^{+} currents. Intracellular Ca^{2+} release shapes SMP and LMP Ca^{2+} responses. The delayed time-to-peak in SMP and LMP responses with $0[Ca^{2+}]_o$ solution suggests extracellular Ca^{2+} involved in initiating responses (**Figure 6.6B&C**). Use of 2-APB delayed multipulse time-to-peak responses. However, 2-APB can sensitize TRPV1 activation, leading to delayed Ca^{2+} responses (64). Sensitization would not impact SP stimulation results as TRPV1 seems uninvolved in SP-evoked Ca^{2+} responses (**Figure 6.8A-C**). Activating IP3R cannot be entirely ruled out in initiating SMP and LMP evoked responses, but the results differ from SP stimulation. Off-target activation of TRPV1 by 2-APB could contribute to the MP-evoked response magnitude decrease by sensitizing cells to respond through TRPV1. Sensitization of TRPV1 could also explain the non-significant increase in the number of cells responding to SMP stimulation (**Figure 6.4F**). Nevertheless, IP3Rs partly mediate SMP and LMP evoked responses in astrocytes (**Figure 6.4E&H**). The sensitivity of different TRP isoforms to different temperature dynamics may also influence evoked Ca^{2+} responses.

Modulatory receptor antagonists on cell calcium responses to SMP and LMP stimulation further implicates IP3R activation (**Figure 6.7E-F&H-I**). Blocking gap junctions and hemichannels with CBX had a limited impact on SP Ca^{2+} response dynamics, though it did have a substantial impact on SP activation probability (**Figure 6.4B&C**). Conversely, the fluorescence intensity attenuation with CBX on SMP and LMP stimulation was substantial (**Figure 6.4E&H**). CBX can block modulatory molecule release from hemichannels and P2X7 (51). The results suggested that SMP and LMP may be driving modulatory receptor activation or possibly molecule release. In this respect, it should be noted that CBX can block volume-regulated anion channel (VRAC) currents that are known to mediate gliotransmitter release (50, 65, 66). INS-evoked volume changes could activate VRACs. In this set of patch-clamp experiments, we used intracellular saline with CsCl, which fails to distinguish if chloride conductance is changed concomitantly with the cationic ones. Patch-clamp experiments with Cs-gluconate or knock down of Leucine-reach Repetitive Containing 8-A (LRRC8-A) channel unit of VRAC (65) are needed to clarify VRAC contributions to the observed effects.

Blocking P2X7 receptors with BBG decreased response magnitude across all stimulation methods (**Figure 6.7B, E&H**) and reduced activation probability to SMP and LMP stimulation only (**Figure 6.7C, F&I**). P2X7Rs activate phospholipase-C (PLC) directly and indirectly in rodent cerebellar astrocytes *in vitro* (67). Activating PLC could explain how intracellular Ca^{2+} release is implicated in all three stimulation protocols. SMP and LMP stimulation activated multiple types of membrane receptors (**Figure 6.7D-I**). Conversely, SP-evoked responses were only sensitive to receptor antagonists for P2X7R – an ATP receptor sensitive to many known stimuli (68, 69). Cholesterol presence affects the activation and sensitization in human and rodent P2X7 by altering cell membrane properties to allow pore formation (69). Neuronal INS nonspecifically evokes an inward capacitive current by increasing cell capacitance, decreasing cell membrane thickness, and altering cell membrane physical properties (17, 37, 38). Lipid bilayer dynamics would explain P2X7R involvement in all three stimulation protocols. Blocking P2X7R delayed response time-to-peak across all stimulation protocols (**Figure 6.6D-F**), suggesting its role in initiating Ca^{2+} responses. SMP-evoked response sensitivity to suramin suggests that other P2 family receptors may be involved. However, ATP activated receptors are not the only receptors implicated in SMP and LMP stimulation responses. Blocking mGluI, AMPA, and NMDA receptors attenuated responses to SMP and LMP stimulation (**Figure 6.7E-F&H-I**). These results support the role of modulatory molecule release due to MP stimulation. However, we cannot rule out their activation by other means. AMPA and NMDA receptor activation from supports the observation of MP-evoked extracellular Ca^{2+} influx. Blocking $GABA_B$ receptors reduced SMP-evoked activation probability, but not for SP or LMP stimulation (**Figure 6.7F**). Further studies are necessary to validate the release of molecules with SMP and LMP stimulation protocols. Activating modulatory receptors with multipulse stimulation has major implications for targeted control of astrocyte physiology.

Several TRP family ion channels shape SP, SMP, and LMP evoked responses. TRP channels act as cellular sensors for a broad spectrum of physical such as voltage changes, temperature changes, mechanical stimuli, and chemical stimuli (70). Several mechanisms could explain the activation of this superfamily of ion channels with infrared stimulation from temperature changes and lipid dynamics to changes in cell volume.

The TRPV4 and TRPA1 channels shape SP-evoked Ca^{2+} responses (18). Since blocking TRPA1 delayed SP-evoked responses, it may help initiate responses. TRPA1-mediated Ca^{2+} entry raises $[Ca^{2+}]_i$ and can drive Ca^{2+}-induced-Ca^{2+}-released through IP3R. Activating IP3R could further sensitize TRPV4 to cell volume changes driven by infrared light (18). Activation of TRPV1 by SP stimulation was not observed (**Figure 6.8B&C**). TRPA1 and TRPV1 shape SMP-evoked responses (**Figure 6.8E&F**). However, TRPV1 seems to help initiate the response to SMP stimulation - capsazepine delays SMP-evoked responses (**Figure 6.6H**). Applying HC030031 to block TRPA1 delays SMP-evoked responses slightly (**Figure 6.6H**). Interestingly, applying A425619 to block TRPV1 vanillin and heat activation does not attenuate SMP-evoked responses. This observation was surprising considering the thermal effects of IR stimulation. While capsazepine significantly reduced SMP activation probability, A425619 and 2-APB significantly increased SMP activation probability (**Figure 6.8F**, **Figure 6.4C**). Activating TRPV1 is a unique effect of SMP stimulation, suggesting IR light can act through distinct molecular signaling pathways in cultured astrocytes.

LMP stimulation was sensitive to blocking TRPV4, TRPA1, and TRPV1. Similar to SMP stimulation, capsazepine increased LMP-evoked time-to-peak (**Figure 6.6I**), suggesting TRPV1 helps initiate LMP-driven Ca^{2+} responses. Capsazepine also reduced LMP activation probability (**Figure 6.8I**). However, applying A425619 did not change response dynamics and non-significantly increased LMP activation probability (**Figure 6.8H&I**). Interestingly, using HC030031 to block TRPA1 significantly increased LMP activation probability (**Figure 6.8I**) – similar to A425619 affecting SMP responses. Given TRP channels' polymodal sensitivity, it is difficult to answer how exactly infrared stimulation will act on them; additional methods and further experiments would be necessary. However, the power of multipulse stimulation of driving calcium responses is apparent. Acting through TRP ion channels positions MP stimulation as a promising tool to study astroglial microdomain activity *in vivo*, where TRP channels have a crucial role. Using SP, SMP, or LMP to recruit different TRP activities provides a valuable tool in studying these channel's roles in astrocyte physiology more broadly.

Using SMP and LMP recruits VGCCs, but SP stimulation was unaffected by verapamil. This finding was curious, as it was initially suspected that the well-characterized electrodynamics of SP stimulation (17) would more likely actuate voltage-gated channels. However, the electrical properties of astrocytes differ greatly from neurons (25); thus, fast capacitive currents from SP stimulation may not impact astrocyte physiology like they do neurons. Much like P2X7 (69), VGCCs are sensitive to membrane composition and physical properties (71). The current biophysical model of IR stimulation suggests that membrane physics is crucial to how IR light can depolarize charged lipid membranes (37, 38). Despite SP-evoked depolarization, intracellular Ca^{2+} release blocks VGCC function (72). The sensitivity of VGCCs to $[Ca^{2+}]_i$ could explain verapamils differing effects on different IR-evoked responses (**Figure 6.8B&C**). Infrared-mediated nonspecific heating effects on molecular biophysics is a topic that warrants further exploration.

Astrocytes are critical players in the regulation of the extracellular milieu composition and space. They can adjust their cytosolic volume via water transport in response to various stimuli (73), impacting neuronal communication. SP stimulation evokes swelling and shrinking in astrocyte cultures with strong spatial dependence (**Figure 6.9C&D**) (18). Meanwhile, SMP and LMP stimulation overwhelmingly drove cell swelling (**Figure 6.9E-H**). Selectively modulating cell volume dynamics – both swelling and shrinking – optically with such spatial precision is unprecedented, and it is the major novelty of the present work.

Interestingly, the swelling and shrinking responses substantially outpace Ca^{2+} signals (i.e., lower time-to-peak), particularly for cell swelling (**Figure 6.11A**). The latter result is in line with calcium and water dynamics observed when astrocytes are exposed to hypotonic and hypertonic solutions (43, 58, 63).

Water transport may precede or induces calcium signaling. These results align with the proposed biomolecular mechanism for SP stimulation, where water flux into the cell drove astrocyte responses to IR light (18). The mechanisms of water transport evoked by INS are not clear. Stimulation could evoke passive or active water transport; however, discerning between the two is not trivial. Water molecules could passively transit the extracellular membrane as water temperature increases and the cell membrane thinning with heating (37, 38). However, the breadth of water transport processes in astrocytes suggests these effects are likely to be multifaceted (19). We could rule out the possibility that the SP, SMP, or LP cause membrane poration to allow for water flux. Typically, dynamics mediated by simple diffusion of water across the plasma membrane are slower than those observed here (43, 63). We have previously shown that the expression of AQP4 can critically alter the onset of calcium responses to SP (18). However, AQP-4 effects on SMP and LMP stimulation were not tested. Experiments targeted to address these questions would help clarify the water transport processes triggered by IR stimulation. For SMP and LMP stimulation, we hypothesize that water entry is triggering the Ca^{2+} response of astroglial cells. Selectively modulating cell volume dynamics – both swelling and shrinking – optically with such spatial precision is unprecedented. High spatial control over water transport in astrocytes provides a potentially powerful tool in studying osmoregulatory processes in the brain, which have implications for high burden neurological conditions associated with traumatic brain injury, Alzheimer's disease, or epilepsy (74).

Our results demonstrate that simply changing the irradiation-time profile of IR stimulation can bias astrocyte water transport and Ca^{2+} responses through different molecular pathways – free of genetic manipulation or the need for changing stimulation wavelength. Label-free optical modulation approaches offer practical advantages. For example, optogenetically driving astrocyte extracellular and intracellular Ca^{2+} flux currently requires distinct channelrhodopsin and melanopsin-based modulators (75). Transfecting astrocytes with two optically sensitive cationic channels reduces the spectral bandwidth for using functional fluorescent probes. With a label-free approach to astrocytic modulation, the entire visible spectrum becomes available for multiplexing a broad palette of functional fluorescent probes. With the growing palette of fluorogenic reporters available, moving optical stimulation methods outside the visible spectrum opens the door to answer new neuroscience and glial biology questions. Many aspects of IR stimulation on non-neuronal cell types in the brain (e.g., oligodendrocytes, microglia) remain unstudied. Nonetheless, IR stimulation provides a promising tool to study multicellular brain function.

IR stimulation may be a helpful tool for studying multicellular communication *in vivo*. In the brain, microglia, oligodendrocytes, and neurovascular-associated cells will influence tissue responses to IR stimulation. In the peripheral nervous system, Schwann cells' role in axonal responses to INS remains unstudied. However, the primary drawback of label-free neuromodulation tools like INS is the lack of cell-type specificity – which must occur through spatial targeting or dosing. Isolated cultures like those in this work provide a fruitful opportunity to explore dosing considerations, though they differ substantially from *in vivo* conditions. Phenotypic differences between astrocyte cell cultures and tissue models are well documented and warrant consideration (25). There is no guarantee that our observations will be consistent *in vivo* – there are too many variables to speculate.

The stark differences in pharmacological effects across stimulation types suggest that SP, SMP, and LMP stimulation recruit different mechanisms. The nature of the direct and latent effects of IR light remains unclear. Physically, the temperature elevation from SMP and LMP stimulation is higher than that of SP stimulation. However, the temperature rise of SP stimulation takes place over 8 ms, while the heating dynamics of SMP and LMP stimulation are orders of magnitude slower. Studying temperature-time dynamics on cells and tissue remains challenging because of the breadth of parameter space. There could be effects of temperature on cell membrane structure, ion/solvent interactions, reaction kinetics, metabolism, protein expression, and many more unexplored factors. Despite the lingering questions, the presented work clarifies that these different approaches to stimulation are not the same.

If our observations are consistent *in vivo*, neurological signals may present differently based on anatomic location. While activation of neurons directly with pulsed IR light is likely (4, 31), it appears plausible that glial release of modulatory molecules could suppress, exaggerate, or even wholly alter baseline neuronal responses and downstream circuitry. Excitatory and inhibitory effects are documented with INS *in vivo* (1). SMP stimulation evokes hemodynamic responses *in vivo* (3, 76). While our results offer additional clarity to the involvement of astrocytes *in vivo*, we provide substantial motivation to study INS-evoked glial dynamics *in vivo*. It is unclear whether neurons, astrocytes, or other brain cells are the primary drivers of neurological responses to INS *in vivo*. Similarly, aspects of astrocyte physiology remain entirely unstudied. Hemodynamic responses, metabolic changes, and immune reactivity may influence acute and chronic tissue responses to INS. These questions emphasize the importance of considering other cell types in the brain. The translational impact of neuromodulation technology relies on a deep physiological understanding of the brain. INS may provide a useful approach for such investigations moving forward.

While our results raise some new observations in the INS research, there are several limitations to consider. Apart from the lack of cell selectivity previously discussed, the lack of commercially available turn-key IR stimulation systems is a leading barrier. Laboratories currently need to build laser systems in-house, which leads to substantial variability between systems based on different budgets, diode form factors, output wavelengths, spectral bandwidths, power overhead, and thermal load management. When power overhead is severely lacking, illumination duty cycles are limited for thermal stability. Here we show that different stimulation approaches might evoke different physiological phenomena. The data shown here serves as a caution to users when comparing studies from different groups utilizing different stimulation approaches. Consideration must be given to the electrical, thermal, and biomolecular dynamics driven by different stimulation protocols. Furthermore, INS parameter space is widely tunable. Control over peak power, wavelength, pulse widths, temporal pulse shape, number of pulses delivered, and laser output bandwidth exponentially scale optimization potential. Computational models of INS biophysical and biomolecular dynamics will provide invaluable resources for optimizing the INS parameter space for different applications (77). Several models currently exist to study specific biophysical aspects of INS. Leveraging these model combinations to optimize neuromodulation deployment remains to be demonstrated. Our results highlight the need to characterize the parameter space available to dosing pulsed IR light for neuromodulation. Furthermore, we show that stimulation with SP, SMP, and LMP protocols are not interchangeable – as they act through distinct molecular pathways in astrocytes. Frameworks for dosing considerations and a thorough understanding of IR dosing on cell physiology are needed.

6.6 Conclusion

Changing dosing strategies of pulsed infrared light drive distinct biomolecular signaling pathways in cultured rat astroglia. Optically targeting different biomolecular pathways in a label-free manner offers a unique opportunity to study astroglial physiology in a spatially targeted fashion. Cell swelling and shrinking dynamics were observed with different IR dosing strategies, suggesting potential in studying osmoregulatory processes in astroglia. Different stimulation strategies preferentially evoke intracellular release or extracellular influx of calcium in astrocytes. Multipulse stimulation uniquely drives modulatory receptor activation in astrocytes. Despite its flexibility, our results suggest that the disparity in IR stimulation paradigms across the INS literature warrants careful consideration. Furthermore, this work emphasizes the need to consider how neuromodulation impacts non-neuronal cell function. Much work remains to realize a complete understanding of IR stimulation's physiological effects on the brain. Nonetheless, label-free optical stimulation of brain cells with infrared light provides a powerful research tool towards understanding the brain from a multicellular perspective.

6.7 Funding

Funding for this work was provided by the following grants: AFOSR FA9550-14-1-0303, AFOSR FA 9550-17-1-0374, AFOSR ASTRONIR, ASTROLIGHT FA9550-20-1-0386, and the Vanderbilt University Trans-Institutional Partnership (BIOMIID). WRA was supported through the ASEE NDSEG Fellowship. Widefield fluorescence imaging experiments were performed in part through the use of the

Vanderbilt Cell Imaging Shared Resource (supported by NIH grants CA68485, DK20593, DK58404, DK59637 and EY08126).

6.8 Acknowledgements

The authors wish to thank the Vanderbilt Cell Imaging Shared Resource staff, particularly Dr. Nicholas Mignemi and Dr. Kari Seedle, for their guidance and support during the imaging that made this work possible. The authors would also like to thank Logan Jenkins, Graham Throckmorton, and Jeremy Ford for their input throughout the process of this work.

6.9 Author Contributions

AIBC, WRA, EDJ, AMJ, and VB conceived the idea for the study and planned the experimental approach. AIBC performed cell culture isolation and maintenance, most of the pharmacological experiments and analyses and wrote the manuscript. WRA performed cell culture isolation, pharmacological experiments, IR dose response experiments, data analysis, and wrote the manuscript. ES performed electrophysiology experiments and related data analyses. AMJ, VB, RZ, and EDJ secured funding for the project. All authors contributed to editing the manuscript.

6.10 Conflicts of Interest Statement

AMJ and EDJ are coinventors on patents pertaining to applications of pulsed infrared light for neuromodulation. The remaining authors report no conflicts of interest.

6.11 References

1. Cayce, J. M., Friedman, R. M., Jansen, E. D., Mahavaden-Jansen, A., and Roe, A. W. (2011) Pulsed infrared light alters neural activity in rat somatosensory cortex in vivo. Neuroimage 57, 155–166
2. Cayce, J. M., Wells, J. D., Malphrus, J. D., Kao, C., Thomsen, S., Tulipan, N. B., Konrad, P. E., Jansen, E. D., and Mahadevan-Jansen, A. (2015) Infrared neural stimulation of human spinal nerve roots in vivo. Neurophotonics 2, 015007
3. Cayce, J. M., Friedman, R. M., Chen, G., Jansen, E. D., Mahadevan-Jansen, A., and Roe, A. W. (2014) Infrared neural stimulation of primary visual cortex in non-human primates. Neuroimage 84, 181–190
4. Cayce, J. M., Bouchard, M. B., Chernov, M. M., Chen, B. R., Grosberg, L. E., Jansen, E. D., Hillman, E. M. C., and Mahadevan-Jansen, A. (2014) Calcium imaging of infrared-stimulated activity in rodent brain. Cell Calcium 55, 183–190
5. Cayce, J. M., Kao, C. C., Malphrus, J. D., Konrad, P. E., Mahadevan-Jansen, A., and Jansen, E. D. (2010) Infrared neural stimulation of thalamocortical brain slices. IEEE J. Select. Topics Quantum Electron. 16, 565–572
6. Wells, J., Kao, C., Jansen, E. D., Konrad, P., and Mahadevan-Jansen, A. (2005) Application of infrared light for in vivo neural stimulation. J. Biomed. Opt. 10, 064003

7. Wells, J., Kao, C., Konrad, P., Milner, T., Kim, J., Mahadevan-Jansen, A., and Jansen, E. D. (2007) Biophysical mechanisms of transient optical stimulation of peripheral nerve. Biophys. J. 93, 2567–2580
8. Tolstykh, G. P., Olsovsky, C. A., Ibey, B. L., and Beier, H. T. (2017) Ryanodine and IP3 receptor-mediated calcium signaling play a pivotal role in neurological infrared laser modulation. Neurophotonics 4, 025001
9. Walsh, A. J., Tolstykh, G. P., Martens, S., Ibey, B. L., and Beier, H. T. (2016) Action potential block in neurons by infrared light. Neurophotonics 3, 040501
10. Izzo, A. D., Walsh, J. T., Ralph, H., Webb, J., Bendett, M., Wells, J., and Richter, C.-P. (2008) Laser stimulation of auditory neurons: effect of shorter pulse duration and penetration depth. Biophys. J. 94, 3159–3166
11. Tan, X., Young, H., Matic, A. I., Zirkle, W., Rajguru, S., and Richter, C.-P. (2015) Temporal properties of inferior colliculus neurons to photonic stimulation in the cochlea. Physiol. Rep. 3
12. Matic, A. I., Robinson, A. M., Young, H. K., Badofsky, B., Rajguru, S. M., Stock, S., and Richter, C.-P. (2013) Behavioral and electrophysiological responses evoked by chronic infrared neural stimulation of the cochlea. PLoS One 8, e58189
13. Tan, X., Rajguru, S., Young, H., Xia, N., Stock, S. R., Xiao, X., and Richter, C.-P. (2015) Radiant energy required for infrared neural stimulation. Sci. Rep. 5, 13273
14. Moreau, D., Lefort, C., Pas, J., Bardet, S. M., Leveque, P., and O'Connor, R. P. (2018) Infrared neural stimulation induces intracellular Ca2+ release mediated by phospholipase C. J. Biophotonics 11
15. Albert, E. S., Bec, J. M., Desmadryl, G., Chekroud, K., Travo, C., Gaboyard, S., Bardin, F., Marc, I., Dumas, M., Lenaers, G., Hamel, C., Muller, A., and Chabbert, C. (2012) TRPV4 channels mediate the infrared laser-evoked response in sensory neurons. J. Neurophysiol. 107, 3227–3234
16. Lumbreras, V., Bas, E., Gupta, C., and Rajguru, S. M. (2014) Pulsed infrared radiation excites cultured neonatal spiral and vestibular ganglion neurons by modulating mitochondrial calcium cycling. J. Neurophysiol. 112, 1246–1255
17. Shapiro, M. G., Homma, K., Villarreal, S., Richter, C.-P., and Bezanilla, F. (2012) Infrared light excites cells by changing their electrical capacitance. Nat. Commun. 3, 736
18. Borrachero-Conejo, A. I., Adams, W. R., Saracino, E., Mola, M. G., Wang, M., Posati, T., Formaggio, F., Bellis, M., Frigeri, A., Caprini, M., Hutchinson, M. R., Muccini, M., Zamboni, R., Nicchia, G. P., Mahadevan-Jansen, A., and Benfenati, V. (2020) Stimulation of water and calcium dynamics in astrocytes with pulsed infrared light. FASEB
19. Benfenati, V. and Ferroni, S. (2010) Water transport between CNS compartments: functional and molecular interactions between aquaporins and ion channels. Neuroscience 168, 926–940
20. Amiry-Moghaddam, M. and Ottersen, O. P. (2003) The molecular basis of water transport in the brain. Nat. Rev. Neurosci. 4, 991–1001
21. Jessen, N. A., Munk, A. S. F., Lundgaard, I., and Nedergaard, M. (2015) The glymphatic system: A beginner's guide. Neurochem. Res. 40, 2583–2599
22. Martin-Fernandez, M., Jamison, S., Robin, L. M., Zhao, Z., Martin, E. D., Aguilar, J., Benneyworth, M. A., Marsicano, G., and Araque, A. (2017) Synapse-specific astrocyte gating of amygdala-related behavior. Nat. Neurosci. 20, 1540–1548
23. Corkrum, M., Covelo, A., Lines, J., Bellocchio, L., Pisansky, M., Loke, K., Quintana, R., Rothwell, P. E., Lujan, R., Marsicano, G., Martin, E. D., Thomas, M. J., Kofuji, P., and Araque, A. (2020) Dopamine-Evoked Synaptic Regulation in the Nucleus Accumbens Requires Astrocyte Activity. Neuron 105, 1036–1047.e5
24. Gomez, J. A., Perkins, J. M., Beaudoin, G. M., Cook, N. B., Quraishi, S. A., Szoeke, E. A., Thangamani, K., Tschumi, C. W., Wanat, M. J., Maroof, A. M., Beckstead, M. J., Rosenberg, P. A., and Paladini, C. A. (2019) Ventral tegmental area astrocytes orchestrate avoidance and approach behavior. Nat. Commun. 10, 1455
25. Verkhratsky, A. and Nedergaard, M. (2018) Physiology of Astroglia. Physiol. Rev. 98, 239–389

26. Yu, X., Nagai, J., and Khakh, B. S. (2020) Improved tools to study astrocytes. Nat. Rev. Neurosci. 21, 121–138

27. Kastanenka, K. V., Moreno-Bote, R., De Pittà, M., Perea, G., Eraso-Pichot, A., Masgrau, R., Poskanzer, K. E., and Galea, E. (2020) A roadmap to integrate astrocytes into Systems Neuroscience. Glia 68, 5–26

28. Roe, A. W., Chernov, M. M., Friedman, R. M., and Chen, G. (2015) In Vivo Mapping of Cortical Columnar Networks in the Monkey with Focal Electrical and Optical Stimulation. Front. Neuroanat. 9, 135

29. Chernov, M. M., Chen, G., and Roe, A. W. (2014) Histological assessment of thermal damage in the brain following infrared neural stimulation. Brain Stimulat. 7, 476–482

30. Zhang, Y., Yao, L., Yang, F., Yang, S., Edathodathil, A., Xi, W., Roe, A. W., and Li, P. (2020) INS-fOCT: a label-free, all-optical method for simultaneously manipulating and mapping brain function. Neurophotonics 7, 015014

31. Xu, A. G., Qian, M., Tian, F., Xu, B., Friedman, R. M., Wang, J., Song, X., Sun, Y., Chernov, M. M., Cayce, J. M., Jansen, E. D., Mahadevan-Jansen, A., Zhang, X., Chen, G., and Roe, A. W. (2019) Focal infrared neural stimulation with high-field functional MRI: A rapid way to map mesoscale brain connectomes. Sci. Adv. 5, eaau7046

32. Brown, W. G. A., Needham, K., Nayagam, B. A., and Stoddart, P. R. (2013) Whole cell patch clamp for investigating the mechanisms of infrared neural stimulation. J. Vis. Exp.

33. Throckmorton, G., Cayce, J., Ricks, Z., Adams, W. R., Jansen, E. D., and Mahadevan-Jansen, A. (2021) Identifying optimal parameters for infrared neural stimulation in the peripheral nervous system. Neurophotonics 8, 015012

34. Wells, J., Kao, C., Mariappan, K., Albea, J., Jansen, E. D., Konrad, P., and Mahadevan-Jansen, A. (2005) Optical stimulation of neural tissue in vivo. Opt. Lett. 30, 504–506

35. Thompson, A. C., Wade, S. A., Cadusch, P. J., Brown, W. G. A., and Stoddart, P. R. (2013) Modeling of the temporal effects of heating during infrared neural stimulation. J. Biomed. Opt. 18, 035004

36. Thompson, A. C., Stoddart, P. R., and Jansen, E. D. (2014) Optical Stimulation of Neurons. Curr. Mol. Imaging 3, 162–177

37. Plaksin, M., Shapira, E., Kimmel, E., and Shoham, S. (2018) Thermal Transients Excite Neurons through Universal Intramembrane Mechanoelectrical Effects. Phys. Rev. X 8, 011043

38. Adams, W. R., Gautam, R., Locke, A. K., Borrachero-Conejo, A. I., Dollinger, B. R., Throckmorton, G. A., Duvall, C., Jansen, E. D., and Mahadevan-Jansen, A. (2021) Visualizing the Role of Lipid Dynamics during Infrared Neural Stimulation with Hyperspectral Stimulated Raman Scattering Microscopy. BioRxiv

39. Barrett, J. N., Rincon, S., Singh, J., Matthewman, C., Pasos, J., Barrett, E. F., and Rajguru, S. M. (2018) Pulsed infrared releases Ca2+ from the endoplasmic reticulum of cultured spiral ganglion neurons. J. Neurophysiol. 120, 509–524

40. Feng, H.-J., Kao, C., Gallagher, M. J., Jansen, E. D., Mahadevan-Jansen, A., Konrad, P. E., and Macdonald, R. L. (2010) Alteration of GABAergic neurotransmission by pulsed infrared laser stimulation. J. Neurosci. Methods 192, 110–114

41. Benfenati, V., Amiry-Moghaddam, M., Caprini, M., Mylonakou, M. N., Rapisarda, C., Ottersen, O. P., and Ferroni, S. (2007) Expression and functional characterization of transient receptor potential vanilloid-related channel 4 (TRPV4) in rat cortical astrocytes. Neuroscience 148, 876–892

42. Schindelin, J., Arganda-Carreras, I., Frise, E., Kaynig, V., Longair, M., Pietzsch, T., Preibisch, S., Rueden, C., Saalfeld, S., Schmid, B., Tinevez, J.-Y., White, D. J., Hartenstein, V., Eliceiri, K., Tomancak, P., and Cardona, A. (2012) Fiji: an open-source platform for biological-image analysis. Nat. Methods 9, 676–682

43. Solenov, E., Watanabe, H., Manley, G. T., and Verkman, A. S. (2004) Sevenfold-reduced osmotic water permeability in primary astrocyte cultures from AQP-4-deficient mice, measured by a fluorescence quenching method. Am. J. Physiol. Cell Physiol. 286, C426–32

44. Hale, G. M. and Querry, M. R. (1973) Optical Constants of Water in the 200-nm to 200-microm Wavelength Region. Appl. Opt. 12, 555–563

45. Legland, D., Arganda-Carreras, I., and Andrey, P. (2016) MorphoLibJ: integrated library and plugins for mathematical morphology with ImageJ. Bioinformatics 32, 3532–3534

46. Moore, J., Linkert, M., Blackburn, C., Carroll, M., Ferguson, R. K., Flynn, H., Gillen, K., Leigh, R., Li, S., Lindner, D., Moore, W. J., Patterson, A. J., Pindelski, B., Ramalingam, B., Rozbicki, E., Tarkowska, A., Walczysko, P., Allan, C., Burel, J.-M., and Swedlow, J. (2015) OMERO and Bio-Formats 5: flexible access to large bioimaging datasets at scale. presented at the SPIE Medical Imaging

47. Lieber, C. A. and Mahadevan-Jansen, A. (2003) Automated method for subtraction of fluorescence from biological Raman spectra. Appl Spectrosc 57, 1363–1367

48. Hofer, A. M., Fasolato, C., and Pozzan, T. (1998) Capacitative Ca2+ entry is closely linked to the filling state of internal Ca2+ stores: a study using simultaneous measurements of ICRAC and intraluminal [Ca2+]. J. Cell Biol. 140, 325–334

49. Wu, D. C., Chen, R. Y.-T., Cheng, T.-C., Chiang, Y.-C., Shen, M.-L., Hsu, L.-L., and Zhou, N. (2018) Spreading depression promotes astrocytic calcium oscillations and enhances gliotransmission to hippocampal neurons. Cereb. Cortex 28, 3204–3216

50. Benfenati, V., Caprini, M., Nicchia, G. P., Rossi, A., Dovizio, M., Cervetto, C., Nobile, M., and Ferroni, S. (2009) Carbenoxolone inhibits volume-regulated anion conductance in cultured rat cortical astroglia. Channels 3, 323–336

51. Suadicani, S. O., Brosnan, C. F., and Scemes, E. (2006) P2X7 receptors mediate ATP release and amplification of astrocytic intercellular Ca2+ signaling. J. Neurosci. 26, 1378–1385

52. Jiang, L. H., Mackenzie, A. B., North, R. A., and Surprenant, A. (2000) Brilliant blue G selectively blocks ATP-gated rat P2X(7) receptors. Mol. Pharmacol. 58, 82–88

53. Tan, Z., Liu, Y., Xi, W., Lou, H.-F., Zhu, L., Guo, Z., Mei, L., and Duan, S. (2017) Glia-derived ATP inversely regulates excitability of pyramidal and CCK-positive neurons. Nat. Commun. 8, 13772

54. Mathiesen, C., Varming, T., and Jensen, L. H. (1998) In vivo and in vitro evaluation of AMPA receptor antagonists in rat hippocampal neurones and cultured mouse cortical neurones. Eur. J. Pharmacol. 353, 159–167

55. Feng, B., Morley, R. M., Jane, D. E., and Monaghan, D. T. (2005) The effect of competitive antagonist chain length on NMDA receptor subunit selectivity. Neuropharmacology 48, 354–359

56. Olpe, H. R. and Karlsson, G. (1990) The effects of baclofen and two GABAB-receptor antagonists on long-term potentiation. Naunyn Schmiedebergs Arch. Pharmacol. 342, 194–197

57. Bianchi, B. R., Lynch, K. J., Touma, E., Niforatos, W., Burgard, E. C., Alexander, K. M., Park, H. S., Yu, H., Metzger, R., Kowaluk, E., Jarvis, M. F., and van Biesen, T. (1999) Pharmacological characterization of recombinant human and rat P2X receptor subtypes. Eur. J. Pharmacol. 376, 127–138

58. Benfenati, V., Caprini, M., Dovizio, M., Mylonakou, M. N., Ferroni, S., Ottersen, O. P., and Amiry-Moghaddam, M. (2011) An aquaporin-4/transient receptor potential vanilloid 4 (AQP4/TRPV4) complex is essential for cell-volume control in astrocytes. Proc. Natl. Acad. Sci. USA 108, 2563–2568

59. Vincent, F., Acevedo, A., Nguyen, M. T., Dourado, M., DeFalco, J., Gustafson, A., Spiro, P., Emerling, D. E., Kelly, M. G., and Duncton, M. A. J. (2009) Identification and characterization of novel TRPV4 modulators. Biochem. Biophys. Res. Commun. 389, 490–494

60. Shigetomi, E., Tong, X., Kwan, K. Y., Corey, D. P., and Khakh, B. S. (2012) TRPA1 channels regulate astrocyte resting calcium and inhibitory synapse efficacy through GAT-3. Nat. Neurosci. 15, 70–80

61. Ho, K. W., Lambert, W. S., and Calkins, D. J. (2014) Activation of the TRPV1 cation channel contributes to stress-induced astrocyte migration. Glia 62, 1435–1451

62. Bergson, P., Lipkind, G., Lee, S. P., Duban, M.-E., and Hanck, D. A. (2011) Verapamil block of T-type calcium channels. Mol. Pharmacol. 79, 411–419

63. Mola, M. G., Sparaneo, A., Gargano, C. D., Spray, D. C., Svelto, M., Frigeri, A., Scemes, E., and Nicchia, G. P. (2016) The speed of swelling kinetics modulates cell volume regulation and calcium signaling in astrocytes: A different point of view on the role of aquaporins. Glia 64, 139–154

64. Colton, C. K. and Zhu, M. X. (2007) 2-Aminoethoxydiphenyl borate as a common activator of TRPV1, TRPV2, and TRPV3 channels. Handb Exp Pharmacol 173–187

65. Formaggio, F., Saracino, E., Mola, M. G., Rao, S. B., Amiry-Moghaddam, M., Muccini, M., Zamboni, R., Nicchia, G. P., Caprini, M., and Benfenati, V. (2019) LRRC8A is essential for swelling-activated chloride current and for regulatory volume decrease in astrocytes. FASEB J. 33, 101–113

66. Wilson, C. S., Bach, M. D., Ashkavand, Z., Norman, K. R., Martino, N., Adam, A. P., and Mongin, A. A. (2019) Metabolic constraints of swelling-activated glutamate release in astrocytes and their implication for ischemic tissue damage. J. Neurochem.

67. Carrasquero, L. M. G., Delicado, E. G., Sánchez-Ruiloba, L., Iglesias, T., and Miras-Portugal, M. T. (2010) Mechanisms of protein kinase D activation in response to P2Y(2) and P2X7 receptors in primary astrocytes. Glia 58, 984–995

68. Borrachero-Conejo, A. I., Saracino, E., Natali, M., Prescimone, F., Karges, S., Bonetti, S., Nicchia, G. P., Formaggio, F., Caprini, M., Zamboni, R., Mercuri, F., Toffanin, S., Muccini, M., and Benfenati, V. (2019) Electrical stimulation by an organic transistor architecture induces calcium signaling in nonexcitable brain cells. Adv Healthc Mater 8, e1801139

69. Robinson, L. E., Shridar, M., Smith, P., and Murrell-Lagnado, R. D. (2014) Plasma membrane cholesterol as a regulator of human and rodent P2X7 receptor activation and sensitization. J. Biol. Chem. 289, 31983–31994

70. Zheng, J. (2013) Molecular mechanism of TRP channels. Compr. Physiol. 3, 221–242

71. Roberts-Crowley, M. L., Mitra-Ganguli, T., Liu, L., and Rittenhouse, A. R. (2009) Regulation of voltage-gated Ca2+ channels by lipids. Cell Calcium 45, 589–601

72. Kim, D.-I., Kweon, H.-J., Park, Y., Jang, D.-J., and Suh, B.-C. (2016) Ca2+ controls gating of voltage-gated calcium channels by releasing the β2e subunit from the plasma membrane. Sci. Signal. 9, ra67

73. Wilson, C. S. and Mongin, A. A. (2018) Cell volume control in healthy brain and neuropathologies. Curr Top Membr 81, 385–455

74. Boison, D. and Masino, S. A., eds. (2015) Homeostatic control of brain function. Oxford University Press

75. Mederos, S., Hernández-Vivanco, A., Ramírez-Franco, J., Martín-Fernández, M., Navarrete, M., Yang, A., Boyden, E. S., and Perea, G. (2019) Melanopsin for precise optogenetic activation of astrocyte-neuron networks. Glia 67, 915–934

76. Chernov, M. and Roe, A. W. (2014) Infrared neural stimulation: a new stimulation tool for central nervous system applications. Neurophotonics 1, 011011

77. Ganguly, M., Jenkins, M. W., Jansen, E. D., and Chiel, H. J. (2019) Thermal block of action potentials is primarily due to voltage-dependent potassium currents: a modeling study. J. Neural Eng. 16, 036020

CHAPTER 7:

SUMMARY AND CONCLUDING REMARKS

7.1 Summary of Dissertation and Major Conclusions

7.1.1 Summary of Dissertation Findings

The goal of this dissertation was to gain mechanistic insight into how infrared light modulates neural cells. Understanding INS phenomena paves the way for studying directed energy neuromodulation methods while laying the groundwork for future innovations in the field.

Previous evidence about astroglial sensitivity to INS raised questions about its cellular specificity and research utility (1). Part of this dissertation provides the first demonstration of direct astroglial sensitivity to SWIR light pulses. Astrocyte biology research currently lacks sufficient tools to control cell function with high spatial and temporal specificity. Latent effects from infrared light differentially drives water transport processes in astroglia by changing dosing parameters. This work highlights just one example of applying INS towards studying astroglial physiology in new ways with improved temporal and spatial control. The direct and latent effects of IR light known on neurons and now astrocytes provide important mechanistic insight into the mechanistic basis of INS. The lack of cell-type specificity in driving cellular activity suggests a mechanism that reaches beyond cell phenotype and protein expression.

The hypothesized direct effects of INS on extracellular membrane dynamics explain why many different cell types could respond to INS. Modulating cell membrane physical properties alters cellular function in ways that are cell-type dependent and difficult to predict. In neurons, IR modulation on cell electrodynamics drives action potentials. Though in another cell type, the electrodynamic effects of IR light may be secondary to latent evoked molecular processes. While different cell types perform their functions based on their phenotype, the cell membrane provides a universal route for modulation of cell function. Still, much of today’s understanding of live-cell lipid dynamics draws from biomimetic preparations and destructive experimental methods. Traditional techniques to study lipid dynamics directly in live neural cell models are limited in their application to INS because of its high spatial and temporal dynamics. This dissertation demonstrates the novel applications of multimodal nonlinear microscopy to directly study the biomolecular dynamics of lipids in live neural cells during INS. The data shown in this dissertation highlights the nonspecific mechanism of INS and the crucial influence it can have on a range of physiological responses in neuronal and non-neuronal cells.

All cells have lipid bilayers that serve crucial structural and functional roles. Photothermally mediated cellular modulation can impact virtually any cell type. Previous work demonstrated this idea electrodynamically and functionally (2–5), but the molecular implications of INS beyond that of neurons remain unknown. The currently accepted mechanistic model of INS hinges on critical assumptions about phospholipid dynamics derived from observations in idealized lipid bilayer preparations (6–14). These chemo-physical changes informed a computational model to deduce photothermal-induced electrodynamics in live cells (15). The computational model accurately predicted experimental measurements (2). The critical assumptions of this model remain to be validated in live-cell models – let alone neural cells. Standard techniques for measuring lipid membrane dimensions (e.g., x-ray diffraction, small-angle neutron scattering) are nonspecific in biological contexts and are not live-cell compatible (11, 16, 17). Live-cell fluorescent probes with lipid-sensitive photophysical properties are widely available but inherently provide an indirect readout of lipid interaction with exogenous fluorescent molecules (18–20). Methods for directly measuring real-time lipid dynamics in live cells exist but have yet to be widely adopted for live-cell imaging.

The work outlined in Chapter 3 describes a multimodal microscopy platform with high spatial and temporal resolution capable of integrating vibrational spectroscopic, functional fluorescence, and black-body thermal imaging on a flexible range of neurological samples. Vibrational spectroscopic contrasts provide a direct characterization of biochemical dynamics – particularly of lipids – in live cells. Meanwhile, fluorescence provides a functional readout of cellular physiology with commercial molecular probes. Thermal imaging offers direct physical thermodynamic information correlated in space and time with other optical measurements. The MANTIS platform is a multimodal optical microscopy system that integrates practically incompatible contrast mechanisms without sample repositioning. The MANTIS platform combines nonlinear optical contrast from CARS, SRS, MPF, and SHG microscopy in the NIR wavelength regime with black-body thermal imaging in the SWIR wavelength regime. MANTIS is the first system to integrate thermal and nonlinear contrasts into a common microscopy platform, which provides a unique opportunity to study the effects of temperature and functional biological dynamics with high temporal resolution. Chapter 3 demonstrates the utility of combining functional cellular information, biochemistry, and black body thermal imaging to study photothermal damage related to INS. Multimodal imaging of neurologically relevant model systems highlights the breadth of structural and functional information combined by nonlinear and thermal imaging. Such a platform offers the powerful potential to combine functional, biomolecular, and physical measurements across *in vitro* and *in vivo* model systems. The inherent flexibility of MANTIS enables users to adapt the platform to suit unique research needs. This work also describes practical considerations for biological black-body thermal imaging, which remains sparsely available in the literature.

Chapter 4 presents work that employs the MANTIS imaging system from Chapter 3 to study the effects of lipid dynamics in differentiated immortalized neuronal cells, NG108-15. Hyperspectral stimulated Raman scattering (hsSRS) microscopy in the C-H stretch band provided insight into lipid-specific molecular interactions. To obtain hsSRS imaging data, the characterization and circumvention of thermally induced defocusing artifacts with high-numerical-aperture microscopy were necessary. By combining a novel focus precompensation approach with hsSRS, we obtained vibrational spectra of NG108 cells during INS at sub-second resolution. Spectral signatures highlight shifts in resonances primarily attributable to *trans-gauche* isomerization of alkyl chains of fatty acid tail groups in lipids. Spectral changes correlated with the level of radiant exposures delivered to cells for INS, suggesting that these chemical dynamics are likely involved in the underlying biophysics of INS. A modified intensity-insensitive general polarization metric for di-4-ANNEPS ratiometric fluorescence was developed to validate vibrational spectral observations. These observations provide direct support for the chemo-physical deformations in the lipid membrane suspected to drive INS. Additionally, the methodologies laid out in this work provide a valuable framework for directly studying high-speed lipid dynamics in biological models. These observations emphasize the role of lipids in the biophysical mechanisms of INS which are broadly generalizable to cell types beyond neurons. Such an experimental approach provides another valuable tool for studying lipid biophysics. As the methodological and technical development of hsSRS continues, the potential value of the information afforded by such experiments is likely to grow.

Previous work shows that astrocyte calcium dynamics are involved in rat somatosensory cortex responses to INS but stopped short of clarifying the basis of astrocyte calcium responses (1). Chapter 5 leveraged pharmacology and widefield calcium-sensitive fluorescence microscopy to characterize the calcium responses of rat primary cortical astrocytes to INS, independent of the influence of neuronal and vascular dynamics. Astrocytes are independently sensitive to single 8 ms pulses of infrared light *in vitro*. Infrared light drives the release of intracellular calcium stores through IP_3R activation, with cation channels TRPV4 and TRPA1 shaping calcium dynamics. These molecular signaling processes are latent effects that manifest after IR exposure. Critically, IR light forced both astrocyte swelling and shrinking in a spatially dependent manner. Water transport is a crucial physiological function of astrocytes in the healthy brain. Tools to study water transport in a spatially selective manner are currently lacking. The work in Chapter 5 demonstrates the potential utility of INS for driving astrocyte water transport to investigate their functional involvement in healthy and diseased brain tissue.

Building on the findings in Chapter 5, Chapter 6 studied how different dosing strategies commonly employed for INS by other groups drove astrocyte physiological responses. In the INS literature, different model systems respond differently to similar stimulation conditions. Different methods of IR stimulation can be more or less effective in different model systems. For example, short multipulse stimulation (SMP) evoked vascular, calcium, and electrical signals in rat and nonhuman primate cortical tissue *in vivo* (1, 21). Similar pulse parameters over longer timeframes stalled neural signal propagation in the rat and *Aplysia* peripheral nervous systems (22, 23). Furthermore, stimulation parameters used across various studies and laboratories appear to evoke a convincing variety of neural activity despite their dissimilarities in approach. Intense single pulses of infrared light, typically 1-10 ms in duration, are employed *in vitro* and peripheral nerve stimulation *in vivo* (4, 24–32). In the brain, brief (~500 ms long) bursts of intense but short (~250 µs long at a 200Hz repetition rate), IR pulses typically evoke functional responses *in vivo* (21, 33–36). In the feline and guinea pig cochlea, trains of even shorter (<100 µs) pulses of IR light drove audition *in vivo* (37–41). No published study has sought to compare the effects of these different stimulation conditions on the physiological dynamics of a particular model system, let alone at the biomolecular signaling level. Given the crucial role of astrocytes and their abundance in the brain, Chapter 6 focused on characterizing astrocyte physiological responses to INS. Pharmacology and widefield fluorescence imaging of calcium and cell volume-sensitive reporters were used to compare multiple types of IR stimulation. Multipulse stimulation strategies typically employed for *in vivo* brain models appear to drive extracellular calcium entry into astrocytes primarily – the opposite of that observed with single pulse stimulation in Chapter 5. Furthermore, neuromodulatory receptors activation (e.g., glutamate, GABA, ATP) impacted astrocytic responses to multipulse stimulation approaches. Blocking neuromodulatory receptors did not affect single-pulse stimulation responses. Multipulse stimulation was sensitive to blocking hemichannels with carbenoxolone. Collectively, the astrocytic release of neurotransmitter molecules due to INS is a possible explanation. Critically, multipulse stimulation disproportionately drove cell swelling – rather than both shrinking and swelling with single-pulse stimulation. The onset times of cell swelling were noticeably quicker than calcium dynamics. This work highlights the curious but critical role INS parameter space plays in evoking physiological dynamics. The ability to bidirectionally drive cell volume changes in a spatially selective manner suggests that pulsed IR modulation of astrocyte physiology could play a crucial role in studying water transport physiology with unprecedented spatial and temporal precision. These results position INS as a powerful research tool for brain and glial physiology. However, these results also raise concern for the broad range of stimulation parameters used across the INS literature which may not be driving identical physiological processes. This comparison of stimulation conditions had yet to be demonstrated in any live cell model until now, and the results critically highlights the need for its consideration in interpreting experimental results.

In summary, this dissertation describes three overarching core advancements. First, a novel multimodal imaging system was developed for studying photothermal and biophysical phenomena of fast manipulations like INS. Using this multimodal imaging platform – specifically with vibrational spectroscopic contrast – the second advancement this dissertation provides is the first direct observations of lipid dynamics occurring in live neural cells during INS. Third, the later portions of this dissertation describe the latent molecular basis for astrocytic sensitivity to pulsed infrared light. Collectively, these ideas highlight the importance of considering the intersection of thermodynamics and molecular biology towards shaping cell and tissue physiology. With INS, neuronal and astrocytes sensitivity to infrared light demonstrates this. Lipid dynamics of cell membranes serve as the vital concept linking these two schools of thought. While interest in the role of lipid membrane dynamics on biological processes is rapidly growing, there is a clear need to improve our collective understanding of such phenomena. The work in this dissertation provides a glimpse of how manipulating such properties of biological systems could be used for research or therapeutic purposes.

7.1.2 Implications

The core finding of this dissertation affirms the involvement of lipid bilayer biophysics in the underlying mechanism of INS. These findings provide the groundwork to compare future translatable neuromodulation technologies. Developing methods to leverage lipid dynamics specifically may be invaluable in improving existing label-free neuromodulation capabilities. High spatial resolution neuromodulation with INS enables the study of high-resolution brain connectivity. Optical neuromodulation methods provide a valuable set of tools to study neural models in a fast and targeted way. The more we understand the biophysical basis of neuromodulation technologies, the more potential there is for innovation and applications that can push neuroscience research and clinical neurology forward in meaningful ways. The ideal system of optical neuromodulation would have stimulation capabilities approaching subcellular resolution deep into live tissue and millisecond-level temporal resolution. Adding similar capabilities to readout cell electrodynamics further complicates these goals. While no current technologies offer such capabilities, parts of these capabilities exist in isolation. Directed energy neuromodulation with RF or ultrasound can noninvasively target deep brain structures in humans. These methods currently lack the high spatial and temporal resolution offered by electrical and optical means. Meanwhile, optical and electrical methods that achieve high spatial and temporal resolution rapidly become invasive to interrogate beyond the most superficial portions of the cortex. However, it is conceivable to target deep brain structures with a systemically deliverable and safe subcellular switch that is orders of magnitude more sensitive to optical energy than current opsin-based molecules. Optimizing switches to be more sensitive to deeper penetrating forms of energy like NIR light, RF, or ultrasound could be used to generate focal heating of molecular actions that force cell depolarization via cell membrane deformations. Groups have designed hyper-sensitive opsins to facilitate deep brain optical stimulation *in vivo* (42). Others have leveraged localized heating of nanoparticles conjugated to neuronal cell membranes with NIR light to achieve cellular stimulation (43, 44). Nanoparticle-assisted NIR stimulation can stimulate brain activity deeper or more noninvasively than previously (45). Groups have used RF-sensitive opsin derivatives to modulate aspects of cellular physiology (46). Research into pharmacological interventions with deep-brain ultrasound stimulation is actively underway (47). Many of the pieces of knowledge to make an ideal neuromodulation tool are available. It may only be a matter of time before we can tease apart complex behaviors in animals at the cellular and connectome levels in the brain. Such capabilities would continue to revolutionize the way neuroscience research is currently done. Extending this further into label-free methods of neuromodulation could change the face of clinical psychology and neuroscience research.

The ability to independently modulate astrocytes has implications for research and clinical use. The nature of the photothermal basis of INS suggests that tissues are susceptible to collateral heating effects. Astrocytic sensitivity to INS is a crucial consideration to have for *in vivo* deployment of INS. Additionally, the results in Chapter 5 begs the question of the potential impacts on neurovasculature, neuroimmune cells, and neural progenitor cells. In a way, this work highlights many remaining questions towards dealing with the nonspecificity of INS. Though the lack of cell-type specificity may be a drawback in many cases, the counterpoint that IR light has the potential to modulate various cell types may be a powerful practical tool for different areas of biomedical research. Label-free IR modulation may have some exciting applications in epithelial and gastrointestinal biology, where cell membrane potential changes and water transport drive many vital physiological processes. Nonetheless, the sensitivity of astrocytes to INS suggests that IR light is a powerful tool to study specific physiological processes, such as water transport, that warrant a crucial investment of research effort for its societal impact.

Using different IR dosing parameters to modulate distinct biochemical signaling pathways in astrocytes is a crucial finding. Further investigation into the flexible parameter space INS offers is needed. The implications of glia releasing neuromodulators are relevant to the ongoing debate around gliotransmission. While modulation of IP_3Rs with single IR pulses is an important lever in driving astrocyte physiology (48–51), knocking out IP3R2 expression from astrocytes in mice nearly abolished astrocytic somatic calcium responses. Animals without IP3R2 expression did not significantly impact neuronal excitability, plasticity, or animal behavior (48–50). This work failed to consider the critical role of astrocyte morphology and how calcium dynamics in distal projections of the cell operate distinctly from cell soma. The calcium dynamics in distal microdomains of astrocytes appear to shape neuronal signaling (52–55). Still, the possible release of neurotransmitters from astrocytes is a phenomenon that remains heavily debated regarding its physiological relevance (51, 55). The release of neuromodulatory molecules from astrocytes can undoubtedly have significant impacts on neuronal excitability. Since multipulse stimulation is mainly applied *in vivo* to rats and nonhuman primates (1, 21, 33, 35, 36), the community must consider the implications of astrocytes on neural tissue responses *in vivo*. The same logic applies to modulating vascular and immune activity through other non-neuronal cells (e.g., microglia, neural progenitor cells, pericytes). While astrocytes are a vital mediator in vascular, immunological, and glymphatic physiology in the brain, they are a small piece of the larger puzzle of brain structure and function. Though the findings discussed here are *in vitro,* it provides the motivation to seriously consider multicellular responses to INS in an *in vivo* context.

The work in this dissertation supports the role of lipid biophysics in INS but likely does not provide a complete picture of the biophysics at play. The mechanistic basis of IR-based neuronal stimulation appears to rely on the electrodynamics that results from thermally driven deformations of charged lipid membranes. This mechanism fails to consider the tertiary effects of lipid biophysics on the structure and function of transmembrane proteins. These proteins can include ion channels that may or may not be sensitive to cell electrodynamics, as well as initiators of signaling cascades (e.g., GPCRs, G-proteins, catalytic enzymes, structural support proteins). The structure of transmembrane proteins molecularly interfaces with water molecules and extracellular membrane to allow for them to function adequately. The biophysical properties of the membrane and surrounding water can directly impact the function of transmembrane proteins independently of electrodynamics. The degree to which these effects impact protein function will vary extensively depending on a protein's structure and expression in a particular cell type. Effects of IR light are difficult to anticipate, as it calls for combining molecular dynamics simulations of biological membranes with structural and molecular biology. Further manipulating and expressing these isolated transmembrane proteins in a way that leaves them accessible to studying their properties as a function of temperature is not trivial. Multiplying this approach by the thousands of membrane proteins that exist, the number of cell types of interest, the phenotypic variation in those cell types, and the underexplored field of cellular lipid composition, the problem quickly becomes a daunting one to tackle. This knowledge may be necessary for understanding some aspects of IR modulation in neural cells but are likely to take some time before current research methodologies address these types of questions. Until then, we must rely on empirical observation, understanding that our picture of the mechanism is likely to be incomplete. Though as technology continues to advance, this knowledge may be accessible someday in the future.

7.2 Recommendations and Future Directions

Throughout completing the work for this dissertation, numerous roadblocks were encountered and addressed. Naturally, considering limitations is important in interpreting this work. Such limitations provide an opportunity for future research to address the many questions as a logical extent of this dissertation. The following sections detail some lines of questioning that would add to the biophotonics and neuroscience communities.

7.2.1 Technical implementations of spectral coherent Raman imaging

The spectral focusing approach detailed in Chapter 4 is inherently slow in the spectral dimension- limiting its application of hsSRS to perturbations that are consistently repeatable. The published approach works to obtain useful data for INS with limited observable hysteresis. However, using a time-resolved spectral acquisition approach cannot visualize single-shot events like those of destructive perturbations. An ideal implementation of spectral coherent Raman imaging would allow for a single-shot or near-single-shot collection of coherent Raman spectra per pixel. There are some implementations of coherent Raman imaging that would allow for such real-time data throughput. Techniques that use rapid optical path length modulation hardware, temporal dispersion multiplexing, spectrographic, and frequency modulation could improve data throughput capabilities for our approach (56–61). Each approach has benefits, but all are substantially more complex and have yet to be implemented in biological models. Such hardware adaptations without an idea for the applicability to biological models presents risks. However, more plug-and-play solutions are likely to become available as the technology around bioimaging with coherent Raman techniques continues to grow in popularity.

7.2.2 Expanded Contrast Modalities of MANTIS Platform

As it currently stands, performing CARS, SRS, MPF, SHG, and Thermal microscopies with video-rate imaging capabilities are possible with MANTIS. Unpublished but tested capabilities of MANTIS show that sum-frequency generation, transient absorption, three-photon fluorescence, and third-harmonic generation microscopy are all possible with optimized optics. There are several additional modalities that MANTIS could perform. This section details some of those potential avenues, their utility, and the practical details to implementing such modalities with a focus on high-speed imaging.

Fluorescence lifetime microscopy (FLIM) is a method of contrast that measures the times at which a fluorophore emits fluorescent photons following a photon absorption event. Biologically speaking, FLIM is used primarily for measuring autofluorescence from metabolic cofactors NAD(P)H and FAD, as well as Forster resonant energy transfer (FRET) probes that give insight into molecular interactions in live cells. Single or multiphoton excited fluorescence configurations of FLIM are possible. Recent advances in electronics hardware and photodetector technology have rapidly made FLIM more accessible than ever. Traditional methods of FLIM rely on time-correlated single-photon counting (TCSPC) – it is still regarded as the gold standard FLIM methodology. However, TCSPC remains relatively slow in practice. Using similar hardware, direct sampling FLIM (dsFLIM) timestamps the detected photons via a high-speed field-programmable gate array (FPGA). Integrating dsFLIM onto MANTIS could be achieved on the existing nonlinear imaging arm. Hardware additions would need to include high-speed photon-counting detectors equipped with high-frequency bandpass filters, an FPGA-based data acquisition (DAQ) interface capable of multichannel GHz sampling rates, and the software to control the data acquisition. Thorlabs does offer a dsFLIM add-on compatible with MANTIS and readily interfaces with the existing image acquisition software familiar to users. Capabilities for FLIM on MANTIS would offer a unique chance to study the effects of INS on aerobic metabolism in neural cells. Neurons and astrocytes are inter-reliant on each other for energetic needs, and the metabolic effects of INS have not been extensively studied. Furthermore, FRET probes of cell physical properties and neurotransmitter binding could address the hypothesis of INS driving gliotransmission phenomena that affect neurons.

Interferometric detection methods provide a powerful opportunity to image samples at high spatial and temporal resolutions. Several groups have deployed interferometric approaches for observing biophysical dynamics related to neural stimulation (62–64). However, much of these interferometric approaches use nonspecific scattering contrast in live neural cells. Molecularly specific validations of these observations have not been demonstrated. The hardware for interferometric methods of contrast (e.g., optical coherence tomography, quantitative phase imaging) are generally different from nonlinear optical microscopy. The MANTIS platform offers an opportunity to directly correlate nonlinear and interferometric imaging approaches by modifying the third imaging arm. Such an approach amounts to effectively building an independent microscope and registering images in post-processing but may become helpful in addressing specific biological questions.

The current iteration of MANTIS utilizes point-detectors in conjunction with laser scanning to produce images on the nonlinear imaging arm. In many cases, full spectroscopic contrast may address a particular research question that is not straightforward to adapt with point-based detectors. Replacing one of the three point-based detectors with a fiber optic terminal connected to a dispersive spectrometer would be the most obvious approach to obtaining spectral contrast on MANTIS. The need to extend pixel dwell times to accommodate the reduced photon flux and detection efficiency with dispersive spectrometers would be necessary. However, groups have performed broadband CARS spectroscopy in similar configurations with 5ms pixel dwell times – 3 orders of magnitude slower than point-based detectors. Spectrometer parameters can be optimized to improve detection speeds at the sacrifice of spectral resolution. Nonetheless, these are all factors to consider when adapting MANTIS to address such research questions. Creative experimental design in conjunction with expanded hardware capabilities can make MANTIS a sort of “swiss-army knife” of optical imaging platforms that improves imaging capabilities in a confined footprint.

Single-photon fluorescence imaging is not readily adaptable to MANTIS in its current configuration. Often, single-photon fluorescence is better suited for addressing scientific questions where multiphoton approaches are not straightforward (e.g., NIR fluorescence). The main limiting factors for this are the illumination sources, detector configurations, detector sensitivities, and optical filter configurations. The ultrafast laser sources used to generate nonlinear fluorescence can technically be repurposed for single-photon fluorescence. The amount of single-photon excited fluorescence signal generated from ultrafast laser excitation is too large to detect with MANTIS's GaAsP PMTs. Laser scanning single-photon fluorescence with continuous-wave laser excitation and confocal detection reduces photon flux at the detector by orders of magnitude. Since the current configuration of MANTIS uses nondescanned detection, single-photon confocal laser scanning fluorescence is not feasible. A detection module could be constructed and placed behind the existing scanning optics MANTIS to allow for confocal single-photon detection – which would need to be accompanied by exchanging dichroic mirrors for short-pass variants specific to the detection wavelengths of interest. These additions quickly become costly - comparable to the price of a standalone entry-level confocal microscope from a commercial manufacturer. Single-photon excited fluorescence imaging capabilities would be a valuable addition in alignment with the multimodal functionality of MANTIS.

7.2.3 Thermal Imaging in Biological Models

As demonstrated in Chapter 3 and Appendix A, water absorption in the spectral window of detection limits biological applications of black-body thermal imaging. This problem makes imaging in water-dominant environments like cell cultures difficult – but far from useless. Having spatially and temporally resolved thermodynamics of optical events with nonlinear contrasts remains a powerful tool to study laser-cell interactions. Some limitations prohibit the direct observation of single-shot perturbations (e.g., photoablation, photodamage). However, INS gentle and reliable enough where registering thermal and live-cell imaging data is both possible and potentially powerful.

Chapter 3 demonstrates the ability to combine thermal, SRS, and MPF microscopy to observe cell damage during INS at stimulating and damaging levels. This methodology is readily extendable to calcium imaging, fluorescence lifetime microscopy, voltage imaging, and many other functional biological phenomena as a direct function of temperature-time and temperature-space dynamics. Combining this with Raman contrast to visualize lipid and DNA perturbations readily allow for a new physical regime of photothermal cellular modulation to be explored. Combining thermal with nonlinear contrasts helps bridge a gap between physical thermodynamics and molecular biology. As the research community's interest in subjects such as biomolecular condensates continues to grow, these sorts of multimodal imaging approaches have enormous potential to offer biological insight.

7.2.4 hsSRS spectral evaluation of water band and fingerprint spectral features during INS

Using spectral CARS or SRS imaging in the O-H stretch regime (3400-3800 cm^{-1}) would help visualize the thermodynamic effects of INS on water hydrogen bonding networks in live neural cells during INS. Water is the primary chromophore attributed to driving heating for INS. As the kinetic energy of water molecules during INS increases, the association of partial charges in water molecules with the extracellular membrane may also be changing. These molecular associations could play a crucial role in how INS mediates lipid membrane dynamics during INS. Experiments that look at the effects of INS on neural cells in mixed saline-deuterium solutions may provide some insight into the role of water molecule association with cell membranes in INS. Similar approaches may apply to SRS imaging in the O-D stretching band spanning 2200-2800 cm^{-1}. Preliminary unpublished experiments on MANTIS have shown that it is possible to perform O-H stretching band SRS on live astrocyte cultures during INS. However, our results remain inconclusive due to some practical calibration concerns. The utility of water imaging in astrocytes is potentially advantageous to study water transport processes better. As discussed in Chapters 5 and 6, water transport is crucial in the brain's homeostatic regulation. Quantitative imaging of water in any biological sample – let alone the brain – is a notoriously difficult problem that would significantly impact biomedical research. SRS has the potential to fulfill this role, as already demonstrated (65–67). Much work remains on imaging biological water quantitatively and is poised to be a high-impact research front.

Recent work has utilized a creative implementation of dual-resonance SRS to probe the hydrogen-bonding effects on the O-H stretch vibrations in and around live cells (67). The work deploys this technique to spatially resolve temperature with microscopic resolution in live cells – which on its own is impressive compared to our results with black-body thermal imaging. The hydrogen bonding dynamics of water change with temperature as water molecules increase kinetic energy. Adapting this methodology to high-speed imaging would allow us to visualize water-cell interaction at the extracellular boundary during INS in real-time. This method of dual-resonance detection also is more amenable to single-shot perturbations with simultaneous dual-resonance measurements. Multispectral approaches would help in studying perturbations that are more prone to hysteresis than INS. Adapting multispectral approaches onto the MANTIS imaging platform would require another resonant electro-optical modulator, a parabolic fiber amplifier, an improved function generator, and a lock-in amplifier with some form of split amplitude/phase output (e.g., R/θ, X/Y). Further integration of FPGA-based detection electronics could even extend such multispectral functionality beyond just two resonances in real-time.

Accessing the fingerprint region of the Raman spectrum with SRS remains sparsely demonstrated. Not that fingerprint SRS is impossible, but it is generally weak. Stronger fingerprint signals are obtainable, such as the Amide III band and the C-H bending region. The result is a need for pixel dwell times that make video-rate image acquisition unfeasible (>30 μs). Some work has sought to get around this computationally with deep-learning-enabled image denoising. Until there is a substantial improvement in the ability to generate fingerprint Raman signal coherently, the outlook for video-rate SRS in the fingerprint region of the Raman spectrum remains bleak.

7.2.5 Molecular dynamic simulations of biomimetic lipid membranes and transmembrane proteins

At the atomic and molecular levels, biology becomes immensely complicated. Understanding the interplay of free ions and water molecules with lipid bilayers and proteins at different temperatures is still being studied. Simulating these molecular interactions is both powerful and exceptionally computationally intensive – but possible with open-source software packages. Computational approaches to guide spectroscopic and electrophysiology experiments would be valuable to understanding the effects of INS on charged lipid bilayers and transmembrane proteins. Similar approaches can be employed to intracellular biochemical signaling pathways with receptors localized to intracellular lipid-bound organelles – such as IP3Rs in the endoplasmic reticulum. Molecular dynamic simulations from first principles would help quantify parameters to more accurately model biological membranes at INS-relevant timescales. The results of molecular dynamics simulations can guide experimental inference and inform neurophysiological signaling models to optimize INS.

7.2.6 Modeling and parametric characterization of INS in neuronal and non-neuronal cells

As demonstrated in Chapter 6, different dosing parameters of INS can evoke different biochemical signaling pathways in astrocytes. Dose-dependant responses remain to be shown for neurons and other non-electrically-excitable neural cell types. There is a need to understand the effects of the IR dosing parameter space on physiological responses, neuronal and beyond. The dosing parameter space of INM is seemingly infinite. Currently, in-house laser systems (Capella, Aculight | Lockheed-Martin) readily allow for the temporal modulation of IR dosing, pulse widths, repetition rates, and peak laser powers between 0 and 5% duty cycles. Commercially available fiber geometries have limited exploring spatial patterning INS. Within the temporal and spatial parameter space, unexplored parameters include the effects of pulse intensity shapes, illumination duty cycles beyond 5 or 10%, and beam scanning geometries for the arbitrary spatial patterning of IR illumination. All of these capabilities are now available in the Biophotonics Center, with custom diode laser systems from IPS Inc., C-coated optical elements, and scanning galvanometer mirror pairs. Despite the hardware availability, the number of experiments needed to sample the INS parameter space adequately is prohibitive.

Parametric testing of the existing parameter space would require considerable time and effort, likely yielding substantial redundancies. Adding the previously mentioned unexplored parameters adds even more complexity to experimental evaluations. Efforts towards computational modeling of photothermal and neural signaling dynamics associated with INM would mitigate the need for redundant parametric evaluations. Model development requires substantial effort and time. However, a computational framework would reduce the need for experimental evaluation of a handful of crucial parameter combinations to reduce the number of animals and the amount of time needed for validation. A combined biophysical and neural signaling model would be readily applicable to other methods of directed energy neuromodulation. Such a flexible model would provide a basis to innovate on new technologies in neuromodulation.

7.2.7 Multicellular and *in vivo* effects of INS

While it is now clear that INS can impact more than just neuronal cells in brain tissue, what remains unclear is how the impact of INS on non-neuronal cells in the brain affects neuronal function. There are many ways to approach this from the angle of vascular, immune, and glial neurobiology. As an example, this section details multicellular considerations *in vivo* from the standpoint of astrocyte-neuron communication.

Astrocytes can have a crucial influence on neuronal function, which can shape neuronal excitability and animal behavior in various neural circuits and behavioral contexts (68–70). The physiological dynamics examined in Chapters 5 and 6 only detail a fraction of the pathways that influence astrocyte physiology. From these observations, it makes sense that single-pulse stimulation in the brain could not drive acute neural responses. In contrast, multipulse stimulation drove both neural excitability, suppression, and hemodynamic response (1, 21, 33). Single-pulse stimulation primarily forced IP3R activation in astrocytes. Genetic ablation of IP3R2 in mice had no noticeable impact on synaptic plasticity, neuronal excitability, or behavior (49, 50). Taken together, it makes sense that SP stimulation did not elicit noticeable acute responses in the rat cortex. Chapter 5 shows how SP stimulation can drive water transport phenomena in astrocytes *in vitro*. This observation remains to be confirmed *in vivo*. Chronic effects from long-term repeated IR exposure need to be assessed. The concentration of ions and molecules in the extracellular space progressively increasing over repeated stimulation (due to water transport) might drive excitotoxicity responses long term. Conversely, SP-mediated water transport could transiently mediate synaptic plasticity with high spatial precision. Additional work in acute brain slices or *in vivo* with neuroscience collaborators would be well suited to explore these ideas.

Multipulse stimulation appeared to drive activation of astrocyte-expressed neuromodulatory receptors. It is unclear whether MP stimulation directly activates receptors or mediates the release of neuromodulatory molecules. There is substantial reason to suggest that neurons can be affected by the glial release of neuromodulatory molecules under particular conditions. Astrocyte release of GABA into regions of the brain with neurons expressing GABA receptors could give rise to suppression of downstream neural activity. Similarly, the release of glutamate or ATP could bias neurons expressing receptors for those molecules towards activation. It is also unclear which cell type is driving the physiological responses evoked by INS *in vivo*. Acute brain slices might provide the most suitable model system to test these hypotheses – as pharmacological perturbations *in vivo* would present substantial difficulties due to collateral physiological effects. Selectively driving astrocyte swelling *in vivo* or brain slice models could provide a powerful tool for studying real-time osmotic and glymphatic dynamics, for which spatially selective tools are lacking. The impact of these tools on studying diseases linked to water transport dysfunction such as epilepsy, Alzheimer's disease, or brain edema associated with traumatic brain injury and ischemia could be meaningful. Groups should heed these considerations when applying MP stimulation *in vivo*.

An acute brain slice model would be ideal for identifying whether neurons or astrocytes are primarily driving brain tissue responses to MP INS. Pharmacology and calcium imaging targeting neuromodulatory receptors are practically suited for acute brain slice approaches. Validating experimental conditions transferrable to *in vivo* models should be a secondary approach to brain slice experiments. Slice preparation must be carefully considered to understand the slice orientation and region of the brain where INS is deployed. The fraction of excitatory and inhibitory neurons in a brain region, their spatial arrangement, and slice dead cell layers thicknesses will be of substantial importance.

7.2.8 In silico modeling of multicellular network impacts of INS on brain tissue

The seemingly infinite parameter space of INS remains largely unstudied. Multipulse stimulation in astrocytes appears to modulate cell swelling and neuromodulatory receptor activation. Meanwhile, sustained exposure to the same pulse settings blocks neuronal action potential propagation (22, 23, 71, 72). There remains a disconnect between the knowledge of the physical and molecular mechanisms of IR neuromodulation. Brute-force evaluation of these parameters would be time-consuming, costly, and potentially wasteful. A model that captures brain cell networks' electrical, thermal, and molecular dynamics would provide a valuable tool for optimizing IR neuromodulation in impactful ways.

Focused effort is warranted to fully understanding the effects of temperature-time dynamics in both neurons and astrocytes. All eukaryotic cells have some form of the cell membrane and transmembrane proteins essential for physiological function. How temperature-time dynamics influence molecular interactions needs to be considered. Detailed understandings of these effects can yield biophysical models to predict cellular responses to many thermal stimuli. Moving beyond modeling of single cells, realistic simulations of brain networks and cell intercommunication will provide a powerful computational framework to refine the applications of INS. Most of the in-house neurophysiological modeling on the single-cell level uses a Hodgkin-Huxley-derived model of neural signaling with the NEURON software package (73). The Allen Institute for Brain Science has developed a publicly available brain modeling toolkit (BMTK) that utilizes the NEURON framework to build biophysical models of *in vivo* neural networks (74). Modeling brain network responses to INS will be testable using the BMTK in concert with a refined temperature-sensitive NEURON model of neuronal and glial signaling. The BMTK does not currently include astrocytic physiology in its base package –. Aspects of astrocyte neurophysiology are available in the NEURON library and readily expandable. Appending these capabilities into both NEURON and the BMTK will simulate the relevant effects of INS in brain cell networks. The current base version of the BMTK does not incorporate astrocyte biophysics and morphology, nor are any public datasets of 3D astrocyte structure currently available. Additionally, the BMTK has a heavy focus on modeling the mouse visual cortex structure. The circuitry between visual and somatosensory cortices in mice is different. Some of the morphological and genotypic simulation features in the BMTK will be limited compared to the experimental models commonly used to study INS *in vivo*. Nonetheless, computational models that span the brain's molecular and connectome levels will play a critical role in understanding directed energy neural modulation.

7.2.9 Impacts of INS on astrocyte microdomain calcium dynamics, immunoreactivity, and hemodynamic signaling

Morphology is essential to *in vivo* cell function. Recreating natural dell morphologies *in vitro* is difficult. For example, astrocytes present completely different phenotypes *in vitro* and *in vivo,* both morphologically and genetically (75). Astrocytes are highly dendritic – with extremely high surface area compared to their intracellular volume based on the number of branches protruding from their processes (52). Many generations of branches extend from astrocytes, making them appear" bushy" *in vivo*. Astrocytes *in vitro* are flat and often not dendritic in appearance. Changes in membrane properties such as s line or surface tension, mean free path of diffusion within the membrane, or the intermolecular association between membrane lipids and transmembrane proteins can influence cell physiology. These are a few of many reasons why it is difficult to speculate the similarities between *in vitro* and *in vivo* INS responses from astrocytes. Tissue-based model systems provide a crucial window into identifying relevant responses and the physiological impact of INS.

Consistent with the idea of morphological variation to cell responses, astrocytes are well known to display distinct calcium dynamics within processes and microdomains than those observed in their soma (54). These projections and microdomains are the functional components that drive astrocyte physiology at synapses; thus, it is vital to consider their calcium dynamics to study their influence on neuronal dynamics following INS. Morphological effects on calcium dynamics are challenging to study *in vitro* without obtaining differentiated astrocytes in a 2D culture. *In vivo* observations of astrocytes are difficult due to the resolution needed to visualize astrocyte microdomains. Furthermore, sample motion in live animals often occludes microdomain structures in time-lapse imaging. Acute and organotypic brain slice models combined with high-speed, high-resolution 3D imaging of astrocyte dynamics would be the most promising approach to address these questions. Modern implementations of single objective light-sheet microscopy readily allow high-resolution video-rate volumetric imaging suitable to study these calcium dynamics. Characterizing INS *in vivo* with calcium imaging and pharmacology will provide invaluable insight into its influence on different cell types in the brain.

The immunoreactivity of astrocytes in the brain is a broadly studied topic in glial biology. The effects of IR exposure on astrocyte reactivity remain entirely unexplored. Considering the importance of astrocyte immune function in the healthy brain, understanding the impact of INS on astrocytes reactivity is vital. Reactive astrocytes can have chronic impacts on neuronal and neurological function spanning the synaptic and whole-organ scales. For safe and effective deployment for research and clinical neuromodulation, the effects of INS on astrocyte reactivity would be a crucial line of questioning to explore.

Astrocytes are also critically involved in mediating hemodynamic responses throughout the brain. Brain vasculature delivers energy, nutrients, and endocrine signaling molecules to the brain while tightly regulating the molecules that enter the brain's extracellular space. The vasculature serves as the physical barrier between the brain and the rest of the body. Long-term brain health and cognitive performance rely on healthy brain vasculature (69, 70, 76, 77). Astrocytes facilitate coordinated action between neurons and the brain vasculature for optimal brain tissue health. INS can elicit both astrocytic signaling and hemodynamic responses. These responses can occur through several avenues. 1) INS may be modulating neurons directly and causing astrocytes to signal for blood flow to maintain homeostatic balance. 2) INS could be modulating astrocytes directly to release neuromodulatory molecules that cause neuronal activation that drive Route 1 or directly drive the release of vascular signaling pathways to increase local blood flow – independent of neuronal firing. 3) INS may modulate vascular endothelium or pericytes directly and evoke hemodynamic responses. Currently, the evidence available suggests that any of these three routes could be involved in tissue responses to INS. Nonetheless, there remains a need to understand the collateral effects of INS on non-neuronal cells and their tertiary influences on neuronal activity. Future research towards these efforts would prove helpful for both current and future work deploying INS for clinical and research applications.

7.2.10 A general mechanistic model of IR neuromodulation

Pulsed IR light impacts the brain between the quantum, atomic, molecular, cellular, physiological, and behavioral levels. Current research methods let each of these levels be probed in specific ways, but a conceptual framework linking all of these levels together appears to be missing. It is clear that temperature changes are crucial to INS mechanisms at the physical level. At the atomic and molecular levels, temperature elevations impact how biomolecules like proteins and lipids interact and function. At the cellular level, the expression and function of proteins (e.g., ion channels, receptors, kinases) depends on the genetics and physiological role of a particular cell type. The role of a particular cell in an organisms physiological system and behavior can be shaped by many components (e.g., anatomic location, afferent and efferent connections, collateral interactions, epigenetics, environmental stimuli). Understanding each part of the INS mechanistic picture is vital to it's utility and adoption. The breadth of fields INS can impact is expansive. The work in this dissertation demonstrates how international collaborative efforts between academic physicists, engineers, neuroscientists, glial biologists, chemists, industrial organizations, and federal research teams can clarify INS mechanisms at the former levels previously listed. Many questions remain and would benefit from the combined expertise of neuroscientists, molecular biologists, behavioral neuroscientists, psychologists, and clinical neurological specialists. A completely clear understanding of INS mechanisms across all levels may be out of reach currently. That does not minimize the impact of detailed mechanistic models might have on INS' translational impact.

7.3 Contributions and Societal Impacts

Throughout the completion of the work in this dissertation, I have made numerous contributions scientifically in my field of research and, more broadly, with impacts on society. The imaging system described in Chapter 3 was the first imaging platform to integrate nonlinear and thermal microscopy on a platform capable of imaging samples ranging from fixed histology slides to the brains of live animals. The development of MANTIS provides a key advancement to the field of biomedical microscopy and biophotonics. With this sort of multimodal flexibility, the world now has a powerful tool to directly tie our functional understanding of physiology to the chemical and physical measurements that were previously difficult to combine. Furthermore, the developed imaging platform combining three independent imaging arms leaves immense flexibility to adapt hardware capabilities to suit targeted research needs. Such a concept can have a reverberating impact on research in biomedicine and beyond. Additionally, the MANTIS framework provides space-constrained laboratories the possibility to configure advanced microscopy infrastructure into smaller footprints. The demonstration of multiplexed SRS, MPF, and Thermal microscopy to study photothermal dynamics associated with INS in neural cell cultures was the first of its kind to register high-speed thermal, functional, and biochemical contrast. Multimodal imaging approaches to study the effects of INS on cell physiology (e.g., calcium dynamics, voltage changes, neurotransmitter release, metabolism, immunoreactivity) with chemical and thermal contrast at sub-micron, sub-second resolution opens the door to study biophysical dynamics.

Towards the fields of biophotonics and biophysics, this dissertation was the first to demonstrate the use of hsSRS microscopy towards observing spectroscopic signatures of sub-second processes in live neural cells. Observations of this kind typically rely on the indirect readout of molecular reporters that exhibit physical changes that are tertiary to the phenomenon of interest. Vibrational spectroscopic contrast offers a more direct way of visualizing lipid biophysics in live cells and provides valuable metabolic, structural, and compositional information. The results in this dissertation offer support for the experimental (2) and theoretical (15) mechanistic basis of INS. Additionally, this dissertation suggests the potential for coherent Raman imaging to offer further insight into the role of other chemical dynamics, including water hydrogen bonding and molecular condensates. Spectral coherent Raman continues to hold the potential to push the field of biophysics forward as methodologies become more refined and accessible.

In the fields of biophotonics, neuromodulation, and glial biology, this dissertation was the first to show the sensitivity of astrocytes to INS directly. Additionally, the ability to distinctly modulate physiological signaling in astrocytes based on the dosing of IR light emphasizes the need to understand better the broader bioeffects of laser irradiation on neural tissue. Astrocytes play a crucial role in supporting brain function and are traditionally overlooked in the design of neuromodulatory devices. Disruption in astrocyte physiology is well known to lead to severe neurological issues such as epilepsy, Alzheimer’s disease, brain swelling, and cognitive decline. Though the tools for studying astrocyte function are improving, there is still a need for tools and methods to drive and study their function. INS provides a valuable method of astrocytic modulation with distinct physiological responses to varying stimulation paradigms. Driving such physiology gives researchers a powerful investigative tool to improve our understanding of astrocytes’ role in healthy brain function.

The broader research goals of biomedical engineering aim to combine and apply a diverse set of scientific approaches to facilitate scientific discovery in biomedical research or improve clinical outcomes. The work in this dissertation combines knowledge from the fields of thermodynamics, biophotonics, systems engineering, nonlinear optics, molecular biology, biophysics, neuroscience, and glial biology to reveal molecular mechanisms of INS and add to its scientific utility. The direct evidence of lipid biophysical dynamics that underly INS are generalized to a variety of cell types provides a novel framework to approaching INS to make it potentially useful for applications beyond the nervous system. This work also demonstrates the potential of coherent Raman imaging as a tool for directly studying aspects of biophysical dynamics in live cells. Additionally, this dissertation presents the first characterization of different approaches to INS on astrocyte physiology *in vitro*, demonstrating its potential as a tool to study glial physiology on brain function. Glial physiology is a rapidly growing field in need of tools to drive cellular function. This dissertation demonstrates that INS may help study certain aspects of glial biology, such as water transport. Our understanding of these processes and others beyond that of neurons and astrocytes remains critical to understanding how to deploy neuromodulation tools for clinical and societal benefit. The work in this dissertation collectively brings the field of neuroscience and neuromodulation one step closer to realizing such impact.

7.4 References

1. Cayce, J. M., Bouchard, M. B., Chernov, M. M., Chen, B. R., Grosberg, L. E., Jansen, E. D., Hillman, E. M. C., and Mahadevan-Jansen, A. (2014) Calcium imaging of infrared-stimulated activity in rodent brain. Cell Calcium 55, 183–190
2. Shapiro, M. G., Homma, K., Villarreal, S., Richter, C.-P., and Bezanilla, F. (2012) Infrared light excites cells by changing their electrical capacitance. Nat. Commun. 3, 736
3. Walsh, A. J., Cantu, J. C., Ibey, B. L., and Beier, H. T. (2017) Short infrared laser pulses increase cell membrane fluidity. presented at the SPIE BiOS
4. Beier, H. T., Tolstykh, G. P., Musick, J. D., Thomas, R. J., and Ibey, B. L. (2014) Plasma membrane nanoporation as a possible mechanism behind infrared excitation of cells. J. Neural Eng. 11, 066006
5. Moen, E. K., Beier, H. T., Ibey, B. L., and Armani, A. M. (2016) The role of membrane dynamics in electrical and infrared neural stimulation. presented at the SPIE BiOS
6. Nagle, J. F. and Tristram-Nagle, S. (2000) Lipid bilayer structure. Curr. Opin. Struct. Biol. 10, 474–480
7. Nagle, J. F. and Tristram-Nagle, S. (2001) Structure and interactions of lipid bilayers: role of fluctuations. In Lipid Bilayers pp. 1–23, Springer Berlin Heidelberg, Berlin, Heidelberg
8. Mills, T. T., Toombes, G. E. S., Tristram-Nagle, S., Smilgies, D.-M., Feigenson, G. W., and Nagle, J. F. (2008) Order parameters and areas in fluid-phase oriented lipid membranes using wide angle X-ray scattering. Biophys. J. 95, 669–681
9. Mathai, J. C., Tristram-Nagle, S., Nagle, J. F., and Zeidel, M. L. (2008) Structural determinants of water permeability through the lipid membrane. J. Gen. Physiol. 131, 69–76
10. Greenwood, A. I., Tristram-Nagle, S., and Nagle, J. F. (2006) Partial molecular volumes of lipids and cholesterol. Chem Phys Lipids 143, 1–10
11. Pan, J., Tristram-Nagle, S., Kucerka, N., and Nagle, J. F. (2008) Temperature dependence of structure, bending rigidity, and bilayer interactions of dioleoylphosphatidylcholine bilayers. Biophys. J. 94, 117–124
12. Tristram-Nagle, S. and Nagle, J. F. (2004) Lipid bilayers: thermodynamics, structure, fluctuations, and interactions. Chem Phys Lipids 127, 3–14
13. Gaber, B. P., Yager, P., and Peticolas, W. L. (1978) Interpretation of biomembrane structure by Raman difference spectroscopy. Nature of the endothermic transitions in phosphatidylcholines. Biophys. J. 21, 161–176
14. Gaber, B. P. and Peticolas, W. L. (1977) On the quantitative interpretation of biomembrane structure by Raman spectroscopy. Biochimica et Biophysica Acta (BBA) - Biomembranes 465, 260–274
15. Plaksin, M., Shapira, E., Kimmel, E., and Shoham, S. (2018) Thermal Transients Excite Neurons through Universal Intramembrane Mechanoelectrical Effects. Phys. Rev. X 8, 011043
16. Nagle, J. F. and Tristram-Nagle, S. (2000) Structure of lipid bilayers. Biochimica et Biophysica Acta (BBA) - Reviews on Biomembranes 1469, 159–195

17. Lyatskaya, Y., Liu, Y., Tristram-Nagle, S., Katsaras, J., and Nagle, J. F. (2001) Method for obtaining structure and interactions from oriented lipid bilayers. Physical review. E, Statistical, nonlinear, and soft matter physics 63, 011907–011907

18. Amaro, M., Reina, F., Hof, M., Eggeling, C., and Sezgin, E. (2017) Laurdan and Di-4-ANEPPDHQ probe different properties of the membrane. J. Phys. D, Appl. Phys. 50, 134004

19. Chapman, C. F., Liu, Y., Sonek, G. J., and Tromberg, B. J. (1995) The use of exogenous fluorescent probes for temperature measurements in single living cells. Photochem. Photobiol. 62, 416–425

20. Owen, D. M., Rentero, C., Magenau, A., Abu-Siniyeh, A., and Gaus, K. (2011) Quantitative imaging of membrane lipid order in cells and organisms. Nat. Protoc. 7, 24–35

21. Cayce, J. M., Friedman, R. M., Chen, G., Jansen, E. D., Mahadevan-Jansen, A., and Roe, A. W. (2014) Infrared neural stimulation of primary visual cortex in non-human primates. Neuroimage 84, 181–190

22. Duke, A. R., Jenkins, M. W., Lu, H., McManus, J. M., Chiel, H. J., and Jansen, E. D. (2013) Transient and selective suppression of neural activity with infrared light. Sci. Rep. 3, 2600

23. Ford, J. B., Ganguly, M., Poorman, M. E., Grissom, W. A., Jenkins, M. W., Chiel, H. J., and Jansen, E. D. (2020) Identifying the role of block length in neural heat block to reduce temperatures during infrared neural inhibition. Lasers Surg Med 52, 259–275

24. Wells, J., Kao, C., Mariappan, K., Albea, J., Jansen, E. D., Konrad, P., and Mahadevan-Jansen, A. (2005) Optical stimulation of neural tissue in vivo. Opt. Lett. 30, 504–506

25. Wells, J. D., Thomsen, S., Whitaker, P., Jansen, E. D., Kao, C. C., Konrad, P. E., and Mahadevan-Jansen, A. (2007) Optically mediated nerve stimulation: Identification of injury thresholds. Lasers Surg Med 39, 513–526

26. Wells, J., Kao, C., Konrad, P., Milner, T., Kim, J., Mahadevan-Jansen, A., and Jansen, E. D. (2007) Biophysical mechanisms of transient optical stimulation of peripheral nerve. Biophys. J. 93, 2567–2580

27. Albert, E. S., Bec, J. M., Desmadryl, G., Chekroud, K., Travo, C., Gaboyard, S., Bardin, F., Marc, I., Dumas, M., Lenaers, G., Hamel, C., Muller, A., and Chabbert, C. (2012) TRPV4 channels mediate the infrared laser-evoked response in sensory neurons. J. Neurophysiol. 107, 3227–3234

28. Lumbreras, V., Bas, E., Gupta, C., and Rajguru, S. M. (2014) Pulsed infrared radiation excites cultured neonatal spiral and vestibular ganglion neurons by modulating mitochondrial calcium cycling. J. Neurophysiol. 112, 1246–1255

29. Moreau, D., Lefort, C., Pas, J., Bardet, S. M., Leveque, P., and O'Connor, R. P. (2018) Infrared neural stimulation induces intracellular Ca2+ release mediated by phospholipase C. J. Biophotonics 11

30. Troyanova-Wood, M., Musick, J. D., Ibey, B. L., Thomas, R. J., and Beier, H. T. (2014) Observation of changes in membrane fluidity after infrared laser stimulation using a polarity-sensitive fluorescent probe. presented at the SPIE BiOS

31. Walsh, A. J., Tolstykh, G. P., Martens, S., Ibey, B. L., and Beier, H. T. (2016) Action potential block in neurons by infrared light. Neurophotonics 3, 040501

32. Throckmorton, G., Cayce, J., Ricks, Z., Adams, W. R., Jansen, E. D., and Mahadevan-Jansen, A. (2021) Identifying optimal parameters for infrared neural stimulation in the peripheral nervous system. Neurophotonics 8, 015012

33. Cayce, J. M., Friedman, R. M., Jansen, E. D., Mahavaden-Jansen, A., and Roe, A. W. (2011) Pulsed infrared light alters neural activity in rat somatosensory cortex in vivo. Neuroimage 57, 155–166

34. Xu, A. G., Qian, M., Tian, F., Xu, B., Friedman, R. M., Wang, J., Song, X., Sun, Y., Chernov, M. M., Cayce, J. M., Jansen, E. D., Mahadevan-Jansen, A., Zhang, X., Chen, G., and Roe, A. W. (2019) Focal infrared neural stimulation with high-field functional MRI: A rapid way to map mesoscale brain connectomes. Sci. Adv. 5, eaau7046

35. Zhang, Y., Yao, L., Yang, F., Yang, S., Edathodathil, A., Xi, W., Roe, A. W., and Li, P. (2020) INS-fOCT: a label-free, all-optical method for simultaneously manipulating and mapping brain function. Neurophotonics 7, 015014

36. Roe, A. W., Chernov, M. M., Friedman, R. M., and Chen, G. (2015) In Vivo Mapping of Cortical Columnar Networks in the Monkey with Focal Electrical and Optical Stimulation. Front. Neuroanat. 9, 135
37. Izzo, A. D., Walsh, J. T., Ralph, H., Webb, J., Bendett, M., Wells, J., and Richter, C.-P. (2008) Laser stimulation of auditory neurons: effect of shorter pulse duration and penetration depth. Biophys. J. 94, 3159–3166
38. Moreno, L. E., Rajguru, S. M., Matic, A. I., Yerram, N., Robinson, A. M., Hwang, M., Stock, S., and Richter, C.-P. (2011) Infrared neural stimulation: beam path in the guinea pig cochlea. Hear. Res. 282, 289–302
39. Young, H. K., Tan, X., Xia, N., and Richter, C.-P. (2015) Target structures for cochlear infrared neural stimulation. Neurophotonics 2, 025002
40. Tan, X., Young, H., Matic, A. I., Zirkle, W., Rajguru, S., and Richter, C.-P. (2015) Temporal properties of inferior colliculus neurons to photonic stimulation in the cochlea. Physiol. Rep. 3
41. Matic, A. I., Robinson, A. M., Young, H. K., Badofsky, B., Rajguru, S. M., Stock, S., and Richter, C.-P. (2013) Behavioral and electrophysiological responses evoked by chronic infrared neural stimulation of the cochlea. PLoS One 8, e58189
42. Chen, R., Gore, F., Nguyen, Q.-A., Ramakrishnan, C., Patel, S., Kim, S. H., Raffiee, M., Kim, Y. S., Hsueh, B., Krook-Magnusson, E., Soltesz, I., and Deisseroth, K. Deep brain optogenetics without intracranial surgery. Nat. Biotechnol. 39, 161–164
43. Palankar, R., Pinchasik, B.-E., Khlebtsov, B. N., Kolesnikova, T. A., Möhwald, H., Winterhalter, M., and Skirtach, A. G. (2014) Nanoplasmonically-induced defects in lipid membrane monitored by ion current: transient nanopores versus membrane rupture. Nano Lett. 14, 4273–4279
44. Carvalho-de-Souza, J. L., Treger, J. S., Dang, B., Kent, S. B. H., Pepperberg, D. R., and Bezanilla, F. (2015) Photosensitivity of neurons enabled by cell-targeted gold nanoparticles. Neuron 86, 207–217
45. Wu, X., Jiang, Y., Rommelfanger, N. J., Yin, R., Liu, J., Cai, S., Ren, W., Shin, A., Ong, K. S., Pu, K., and Hong, G. (2020) Through-scalp deep-brain stimulation in tether-free, naturally-behaving mice with widefield NIR-II illumination. BioRxiv
46. Schmidt, M. S., Hussain, S. M., Dennis, P., Farajollahi, S., and Pachter, R. (2020) The development of radiogenetically-controlled signaling proteins for novel applications to optogenetics. presented at the Optogenetics and Optical Manipulation 2020
47. Rabut, C., Yoo, S., Hurt, R. C., Jin, Z., Li, H., Guo, H., Ling, B., and Shapiro, M. G. (2020) Ultrasound technologies for imaging and modulating neural activity. Neuron 108, 93–110
48. Petravicz, J., Boyt, K. M., and McCarthy, K. D. (2014) Astrocyte IP3R2-dependent Ca(2+) signaling is not a major modulator of neuronal pathways governing behavior. Front. Behav. Neurosci. 8, 384
49. Srinivasan, R., Huang, B. S., Venugopal, S., Johnston, A. D., Chai, H., Zeng, H., Golshani, P., and Khakh, B. S. (2015) Ca(2+) signaling in astrocytes from Ip3r2(-/-) mice in brain slices and during startle responses in vivo. Nat. Neurosci. 18, 708–717
50. Petravicz, J., Fiacco, T. A., and McCarthy, K. D. (2008) Loss of IP3 receptor-dependent Ca2+ increases in hippocampal astrocytes does not affect baseline CA1 pyramidal neuron synaptic activity. J. Neurosci. 28, 4967–4973
51. Fiacco, T. A. and McCarthy, K. D. (2018) Multiple Lines of Evidence Indicate That Gliotransmission Does Not Occur under Physiological Conditions. J. Neurosci. 38, 3–13
52. Bindocci, E., Savtchouk, I., Liaudet, N., Becker, D., Carriero, G., and Volterra, A. (2017) Three-dimensional Ca2+ imaging advances understanding of astrocyte biology. Science 356
53. Di Castro, M. A., Chuquet, J., Liaudet, N., Bhaukaurally, K., Santello, M., Bouvier, D., Tiret, P., and Volterra, A. (2011) Local Ca2+ detection and modulation of synaptic release by astrocytes. Nat. Neurosci. 14, 1276–1284
54. Volterra, A., Liaudet, N., and Savtchouk, I. (2014) Astrocyte Ca^{2+} signalling: an unexpected complexity. Nat. Rev. Neurosci. 15, 327–335

55. Savtchouk, I. and Volterra, A. (2018) Gliotransmission: Beyond Black-and-White. J. Neurosci. 38, 14–25
56. Zhang, D., Wang, P., Slipchenko, M. N., and Cheng, J.-X. (2014) Fast vibrational imaging of single cells and tissues by stimulated Raman scattering microscopy. Acc. Chem. Res. 47, 2282–2290
57. Zhang, C., Zhang, D., and Cheng, J.-X. (2015) Coherent raman scattering microscopy in biology and medicine. Annu. Rev. Biomed. Eng. 17, 415–445
58. Yang, W., Li, A., Suo, Y., Lu, F.-K., and Sunney Xie, X. (2017) Simultaneous two-color stimulated Raman scattering microscopy by adding a fiber amplifier to a 2 ps OPO-based SRS microscope. Opt. Lett. 42, 523–526
59. Bae, K., Zheng, W., Lin, K., Lim, S. W., Chong, Y. K., Tang, C., King, N. K., Ti Ang, C. B., and Huang, Z. (2018) Epi-Detected Hyperspectral Stimulated Raman Scattering Microscopy for Label-Free Molecular Subtyping of Glioblastomas. Anal. Chem. 90, 10249–10255
60. Alshaykh, M. S., Liao, C.-S., Sandoval, O. E., Gitzinger, G., Forget, N., Leaird, D. E., Cheng, J.-X., and Weiner, A. M. (2017) High-speed stimulated hyperspectral Raman imaging using rapid acousto-optic delay lines. Opt. Lett. 42, 1548–1551
61. Wang, K., Zhang, D., Charan, K., Slipchenko, M. N., Wang, P., Xu, C., and Cheng, J.-X. (2013) Time-lens based hyperspectral stimulated Raman scattering imaging and quantitative spectral analysis. J. Biophotonics 6, 815–820
62. Batabyal, S., Satpathy, S., Bui, L., Kim, Y.-T., Mohanty, S., Bachoo, R., and Davé, D. P. (2017) Label-free optical detection of action potential in mammalian neurons. Biomed. Opt. Express 8, 3700–3713
63. Ling, T., Boyle, K. C., Zuckerman, V., Flores, T., Ramakrishnan, C., Deisseroth, K., and Palanker, D. (2020) High-speed interferometric imaging reveals dynamics of neuronal deformation during the action potential. Proc. Natl. Acad. Sci. USA 117, 10278–10285
64. Ling, T., Boyle, K. C., Goetz, G., Zhou, P., Quan, Y., Alfonso, F. S., Huang, T. W., and Palanker, D. (2018) Full-field interferometric imaging of propagating action potentials. Light Sci Appl 7, 107
65. Duboisset, J., Berto, P., Gasecka, P., Bioud, F.-Z., Ferrand, P., Rigneault, H., and Brasselet, S. (2015) Molecular orientational order probed by coherent anti-Stokes Raman scattering (CARS) and stimulated Raman scattering (SRS) microscopy: a spectral comparative study. J. Phys. Chem. B 119, 3242–3249
66. Cheng, J.-X., Pautot, S., Weitz, D. A., and Xie, X. S. (2003) Ordering of water molecules between phospholipid bilayers visualized by coherent anti-Stokes Raman scattering microscopy. Proc. Natl. Acad. Sci. USA 100, 9826–9830
67. Figueroa, B., Hu, R., Rayner, S. G., Zheng, Y., and Fu, D. (2020) Real-Time Microscale Temperature Imaging by Stimulated Raman Scattering. J. Phys. Chem. Lett. 11, 7083–7089
68. Santello, M., Toni, N., and Volterra, A. (2019) Astrocyte function from information processing to cognition and cognitive impairment. Nat. Neurosci. 22, 154–166
69. Corkrum, M., Covelo, A., Lines, J., Bellocchio, L., Pisansky, M., Loke, K., Quintana, R., Rothwell, P. E., Lujan, R., Marsicano, G., Martin, E. D., Thomas, M. J., Kofuji, P., and Araque, A. (2020) Dopamine-Evoked Synaptic Regulation in the Nucleus Accumbens Requires Astrocyte Activity. Neuron 105, 1036–1047.e5
70. Martin-Fernandez, M., Jamison, S., Robin, L. M., Zhao, Z., Martin, E. D., Aguilar, J., Benneyworth, M. A., Marsicano, G., and Araque, A. (2017) Synapse-specific astrocyte gating of amygdala-related behavior. Nat. Neurosci. 20, 1540–1548
71. Ganguly, M., Jenkins, M. W., Jansen, E. D., and Chiel, H. J. (2019) Thermal block of action potentials is primarily due to voltage-dependent potassium currents: a modeling study. J. Neural Eng. 16, 036020
72. Lothet, E. H., Shaw, K. M., Lu, H., Zhuo, J., Wang, Y. T., Gu, S., Stolz, D. B., Jansen, E. D., Horn, C. C., Chiel, H. J., and Jenkins, M. W. (2017) Selective inhibition of small-diameter axons using infrared light. Sci. Rep. 7, 3275

73. Hines, M. L., Davison, A. P., and Muller, E. (2009) NEURON and Python. Front Neuroinformatics 3, 1

74. Dai, K., Gratiy, S. L., Billeh, Y. N., Xu, R., Cai, B., Cain, N., Rimehaug, A. E., Stasik, A. J., Einevoll, G. T., Mihalas, S., Koch, C., and Arkhipov, A. (2020) Brain Modeling ToolKit: An open source software suite for multiscale modeling of brain circuits. PLoS Comput. Biol. 16, e1008386

75. Benfenati, V., Caprini, M., Dovizio, M., Mylonakou, M. N., Ferroni, S., Ottersen, O. P., and Amiry-Moghaddam, M. (2011) An aquaporin-4/transient receptor potential vanilloid 4 (AQP4/TRPV4) complex is essential for cell-volume control in astrocytes. Proc. Natl. Acad. Sci. USA 108, 2563–2568

76. Martín, R., Bajo-Grañeras, R., Moratalla, R., Perea, G., and Araque, A. (2015) Circuit-specific signaling in astrocyte-neuron networks in basal ganglia pathways. Science 349, 730–734

77. Fields, R. D., Araque, A., Johansen-Berg, H., Lim, S.-S., Lynch, G., Nave, K.-A., Nedergaard, M., Perez, R., Sejnowski, T., and Wake, H. (2014) Glial biology in learning and cognition. Neuroscientist 20, 426–431